DECIPHERING THE MOLECULAR DETERMINANTS OF MEMBRANE

ASSOCIATION BY PHOSPHOLIPID-BINDING DOMAINS


A Dissertation

by

SACHIN S KATTI


Submitted to the Office of Graduate and Professional Studies of
Texas A&M University
in partial fulfillment of the requirements for the degree of

DOCTOR OF PHILOSOPHY


| | |
|---|---|
| Chair of Committee, | Vytas A. Bankaitis |
| Committee Members, | Tatyana I. Igumenova |
| | Hays S. Rye |
| | Jae-Hyun Cho |
| Head of Department, | A. Joshua Wand |


August 2020

Major Subject: Biochemistry

ABSTRACT


Assemblies of enzymes and adaptor complexes at the membranes relay the external signals to the cellular machineries in order to induce physiological responses. As a result, controlled and transient translocation of signaling complexes to the membranes is indispensable to signal transduction. Nature has designed a limited number of specialized phospholipid-binding domains to achieve such translocation. These domains are ubiquitous among modular protein complexes and respond to specific effectors and second messengers.

Among these membrane-targeting modules, the diacylglycerol-binding C1 domains and $Ca^{2+}$-sensitive C2 domains represent some of the most abundant classes in eukaryotes. These domains were first identified on protein kinase C (PKC), the membrane-activated kinase of AGC family that regulates cell proliferation, survival and apoptosis. The ligand/agonist preferences of most PKC-type C1 and C2 domains are known, yet their respective mechanisms of membrane association are not completely understood. Deciphering the molecular determinants that govern the membrane interactions of these domains is essential to fully realize how they modulate the host signaling complexes. That is the primary goal of the work presented here. Towards this goal, we systematically studied the tandem C1 domains (C1A and C1B) of PKCδ isoform and tandem C2 domains (C2A and C2B) of synaptic $Ca^{2+}$ sensor protein, Synaptotagmin 1 (Syt1).

The novel structural features along with the agonist-binding studies reported here reveal that C1A domain has a weak dependence on diacylglycerol but sensitive towards tumor-promoting phorbol esters and PtdIns(4,5)P$_2$. These findings combined with the existing knowledge provide a mechanistic model of diacylglycerol recognition by C1 domains. On the other hand, our work on C1B domain provides unprecedented atomic-resolution insight into the agonist-induced membrane insertion of C1 domains.

The determinants of membrane association for Syt1 C2 domains were studies using xenobiotic divalent cations, Cd$^{2+}$ and Pb$^{2+}$. These metal ions provided unique advantage over Ca$^{2+}$ due to their high affinities. Using them, we were able to identify the changes in C2 domains necessary for effective membrane association. Together, the results presented here contribute significantly to our understanding of these conserved domains and their roles in signal transduction.

# ACKNOWLEDGEMENTS

I thank my principle investigator, Dr. Tatyana I. Igumenova for providing me the opportunity, training, constant support, and more importantly the operational freedom throughout my time as a graduate student in her lab. I am equally fortunate to have Dr. Vytas Bankaitis as my committee chair, who was very encouraging as a mentor during my rotation in his lab as a first-year student. His constant guidance since then has kept me on track, and I am grateful for that.

I thank Dr. Hays Rye for his valuable suggestions on how to improve and present my research. He was a great mentor during my very first rotation in this department and exceptionally engaging as an instructor. I am grateful to Dr. Jae-Hyun Cho for providing a different perspective on the NMR experiments, and his continued support as a valuable member of the committee. The clarity I obtained on some of the NMR concepts while attending his class is also very much appreciated.

I would also like to express my gratitude towards the members of the Igumenova lab, past and present, for their support.

Finally, I want to thank my family members for their support and encouragement throughout this time, particularly my parents who made sure I got every opportunity necessary to accomplish what I wanted.

CONTRIBUTORS AND FUNDING SOURCES

TABLE OF CONTENTS

LIST OF FIGURES

xii

LIST OF TABLES

CHAPTER I INTRODUCTION

Membrane association of catalytic protein complexes is integral to signaling events that ultimately dictate cell survival, communication, and proliferation.[1-3] Plasma as well as internal membranes can be viewed as crossroads where second messengers, enzymes, cofactors, and substrates are converged in response to certain stimuli to exert their respective functions.[2] Dysregulation of membrane proteins often coincides with carcinogenesis, and neurodegenerative disorders, making them instinctive targets for corrective drug design strategies.[4] Since regulated localization of various protein activities at the membranes is what sparks signal transduction, understanding how these events initiate is necessary to exploit them therapeutically.

The sheer number of membrane-activated signaling proteins with dedicated activities and roles makes it difficult to study them individually. Fortunately, the membrane translocation of these proteins is mediated by only a limited number of specialized phospholipid-binding domains.[1] From the perspective of drug design, this scenario is desirable as any therapeutic agents designed to modulate these domains can in turn be used to control the activities of numerous host signaling complexes. The occurrence and importance of such domains was first realized beginning with Yasutomi Nishizuka's discovery of protein kinase C (PKC) in 1977,[5] a fascinating membrane-activated enzyme that is regarded as a nexus between the fields of lipid-mediated signaling and tumorigenesis.[6]

PKC is comprised of multiple isoforms of serine/threonine protein kinases that collectively belong to the AGC subfamily (PK<u>A</u>, PK<u>G</u>, and PK<u>C</u>).[7, 8] Upon recognition

1

of PKC as a signal transduction protein of GPCR (G-protein coupled receptor) and growth factor-stimulated signaling pathways; also dysregulated by non-endogenous phorbol esters leading to formation of tumors,[9-11] considerable interest was induced in studying the obligatory dependence of its activation on the membrane translocation. It was soon realized that the architecture of PKC is multi-modular with a conserved "regulatory" region responsible for its $Ca^{2+}$ and diacylglycerol (DAG) mediated transient membrane association (**Figure I.1A**).[12] In conventional PKC isoforms, this region is made up of tandem diacylglycerol/phorbol ester-binding conserved homology-1 (C1) and $Ca^{2+}$-dependent phospholipid-binding conserved homology-2 (C2) domains (**Figure I.1B and C**).[7] In addition to PKC, we now know that these domains occur on multitude of signaling protein classes such as Synaptotagmins (C2) and Unc-13s (C1 and C2).[13, 14] PKC-type C1 and C2s along with pleckstrin homology (PH) domains constitute three dominant classes of phospholipid binding modules that exhibit maximum occurrence on lipid-activated proteins in humans.[1]

In the subsequent sections of this chapter, an attempt is made to briefly describe structural and mechanistic aspects pertaining to membrane-association of C1/C2 domains along with the current limitations in our knowledge. Furthermore, the ligand promiscuity exhibited by these domains and the resulting implications on their membrane association is also discussed in the context of how it can be exploited to study them. The information presented in this chapter will serve as a segue into the findings that contribute to the better understanding of these domains and their host signaling proteins.
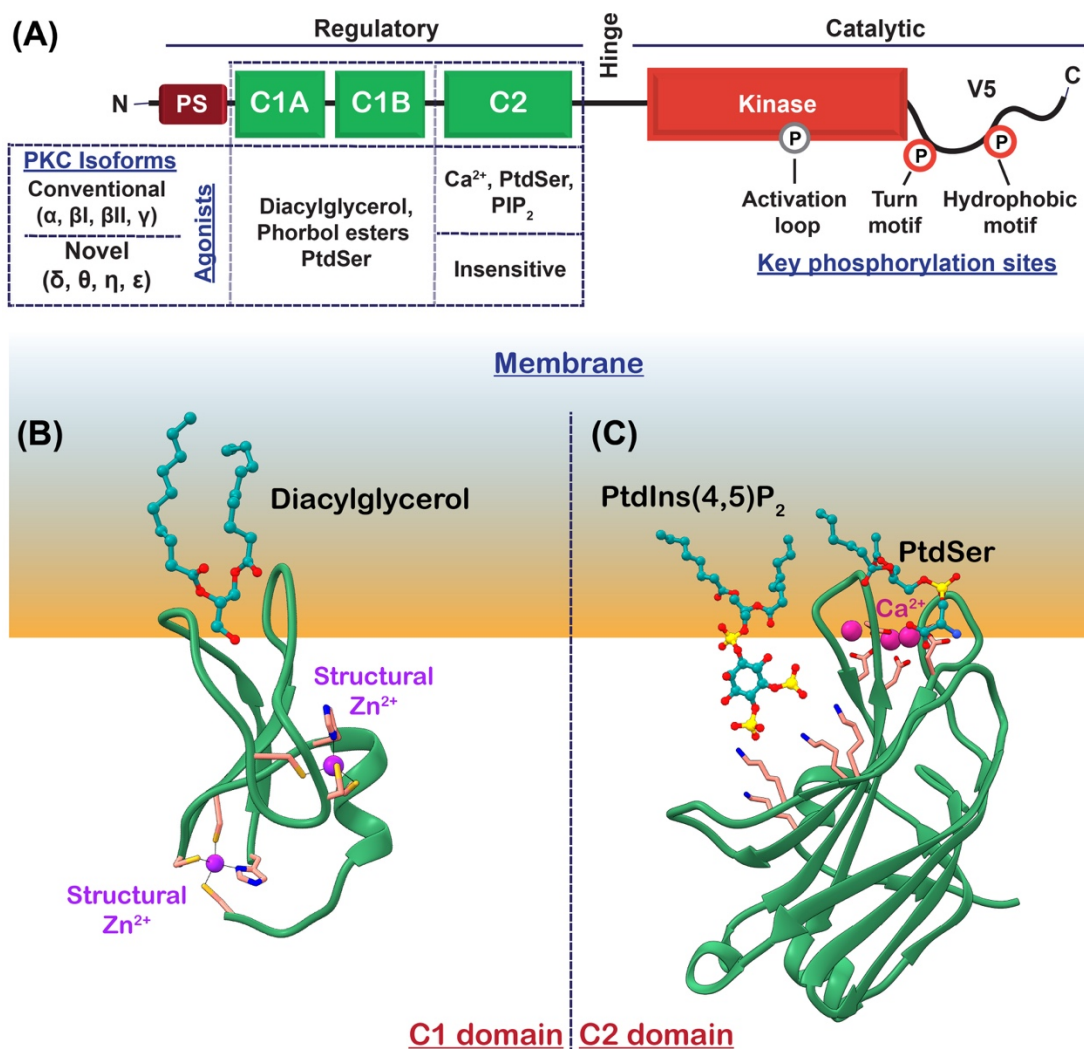
**Figure I.1 Occurrence of the conserved phospholipid-binding C1 and C2 domains was first discovered on Protein kinase C (PKC)**

(A) General schematic of the modular architecture of conventional and novel PKC isoforms is depicted. Phospholipid-binding C1 and C2-type domains were first identified on the regulatory region of PKC that is responsible for membrane translocation of the enzyme. The translocation is guided by a combination of second messengers and agonists listed in the tabular format. (B) Schematic model depicting the membrane interactions of C1 domains in response to the agonist diacylglycerol (applicable to the C1 domains of both conventional and novel isoforms) (C) Schematic model depicting the membrane interactions of C2 domains in response to $Ca^{2+}$ and anionic lipids: PtdSer and PtdIns(4,5)P$_2$ (applicable to C2 domains of conventional PKC isoforms)

**C1 domains: Diacylglycerol (DAG)/Phorbol ester binding modules**

Both C1 and C2 domains trace their origin to conventional PKC isoforms, as discussed in the previous section of this chapter. Unlike C2 domains however, C1 domains are small, ~50 residue modules that depend upon structural $Zn^{2+}$ ions to fold (**Figure I.2B**).[15, 16] These domains occur on >50 mammalian proteins; RasGRPs, chimaerins, DAG kinases, and UNC-13s to name a few (in addition to the PKCs).[15] On PKC isoforms, these domains appear in tandem (referred to as C1A and C1B).[7] The endogenous agonist of "typical" C1 domains is the physiological *sn*-1,2 isomer of the second messenger diacylglycerol (DAG), which has two acyl chains linked to glycerol backbone but no phosphate group (**Figure I.2C**).[17] Since DAG is a phosphate group short of being a "real" phospholipid, C1 domains can be seen mentioned as "honorary" phospholipid-binding modules.[1] The other important agonists of C1 domains are tumor-promoting phorbol esters, linking these domains to the aberrant activation of PKC in tumor formation.[10, 11] Incidentally, there are C1 domains that cannot bind to DAG or phorbol esters, referred to as "atypical" type C1 domains.[7]

With the discovery of more C1 domains, following questions started emerging: What structural features determine the differential DAG-sensitivity of various C1 domains? Do they possess the ability to interact with other phospholipids without DAG/phorbol esters, making them more than "honorary" phospholipid-binding modules? Are there any differences in the DAG vs phorbol ester binding modes of these domains? Why do proteins like PKCs need two C1 domains?
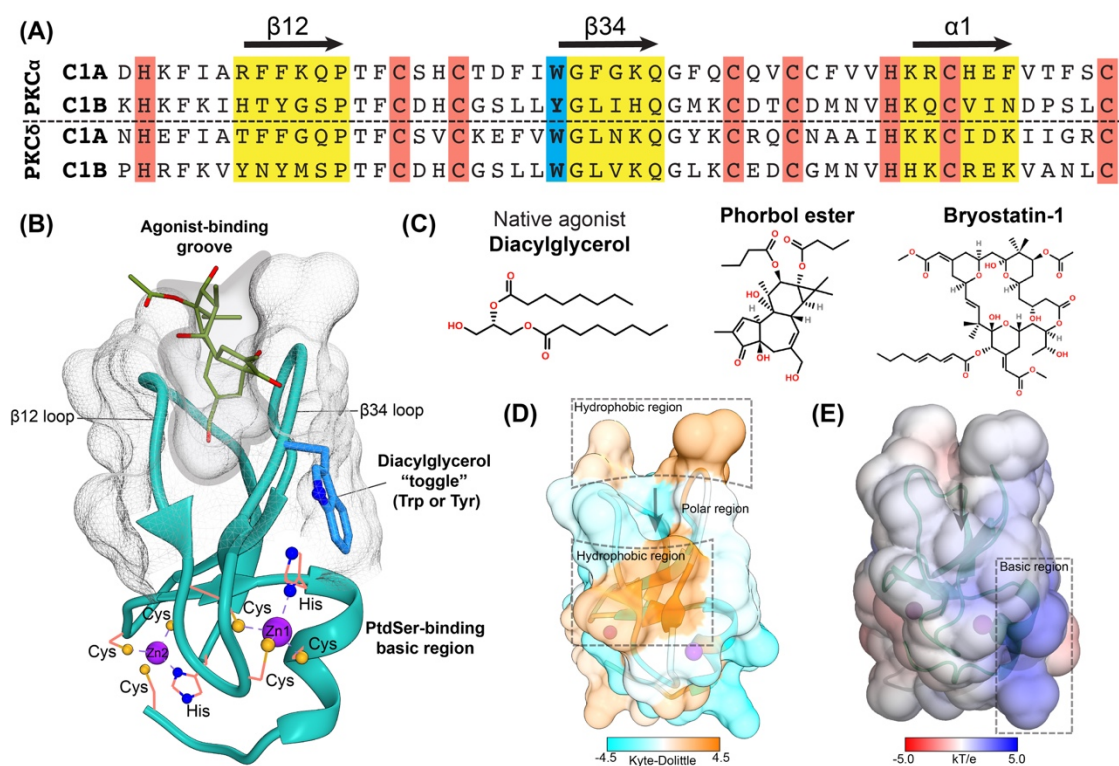
**Figure I.2 Distinct structural features and agonists of PKC C1 domains.**
(A) The amino acid sequences of 4 different C1 domains are compared (two per conventional PKCα and novel PKCδ isoforms). The two agonist-binding loops and a putative PtdSer sensitive helical segment are highlighted in yellow. The conserved and indispensable $Zn^{2+}$ coordinating residues are highlighted in red. The "DAG toggle" residue is highlighted in blue. (B) Crystal structure of PKCδ C1B domain (1PTQ)[18] is shown with the features noted in (A). The agonist-binding groove is the interaction site for several structurally diverse ligands shown in (C). One of the soluble analogs of the agonist phorbol esters, phorbol 13-acetate is depicted (from 1PTR, X-ray).[18] (D) The hydrophobic surface map of the PKCδ C1B domain is depicted using the Kyte-Dolittle scale. The relatively hydrophilic agonist-binding groove is flanked by the hydrophobic regions. (E) The electrostatic surface map (APBS) also of the PKCδ C1B domain is shown to identify the basic region (α1 helix) potentially responsible for the PtdSer targeting.

The first representative structures of these domains that started shining light on

C1-agonist interactions came out in 1994-95, as Marcel Luyten and James H. Hurley's

groups published the very first NMR (PKCα, C1B) and crystal (PKCδ, C1B) structures

respectively of the C1 domains (one of those depicted in **Figure I.2B**).[18, 19] These

structures were not only instrumental in sparking the research associated with C1

domains but also had special relevance to how the conventional and novel PKC isoforms

function.  Although several advances were made since then to identify other agonists of

C1 domains,[16, 20] the atomic resolution structural information of these interactions is

sadly lacking. For instance, no structure of C1 domain with its endogenous agonist DAG

is reported to date. The problem lies with the inherent hydrophobicity of most C1

agonists and thus requirement of a proper membrane mimic to partition them. To

overcome this obstacle, the need for novel approaches is apparent.

Subsequent sections of this chapter describe various aspects of C1 domains,

using the tandem C1 domains of PKCδ as examples. The information presented here will

be relevant in understanding the experimental work done on these domains and reported

in chapters II and III.

<div align="center">Structural features of C1 domains</div>

The core structural elements of all C1 domains are two $Zn^{2+}$ ions that are

coordinated by a highly conserved 3 cysteines-1 histidine cluster each (**Figure I.2A and

B**).[15] Two β sheets and an α helix form the globular fold around the $Zn^{2+}$ clusters. The

DAG as well as phorbol ester binding region of C1 domains is formed by the flexible

loops at one tip of the domain. [18, 21] The arrangement of residues around the agonist-

binding region of these domains is intriguing. Immediately flanking the relatively polar

agonist-binding groove are some hydrophobic residues. In the absence of the agonist, the

hydrophobicity of this region is interrupted by the groove itself, explaining the affinity

<div align="center">6</div>

of the domains for the apolar ligands (**Figure I.2D**). Upon agonist binding, the resulting "hydrophobic switch" enables the domain to partition effectively into the membrane core.[18] In addition, C1 domains possess a belt of basic residues surrounding the agonist-binding region that adds electrostatic component to C1-membrane interactions (**Figure I.2E and Figure I.3**).[18]
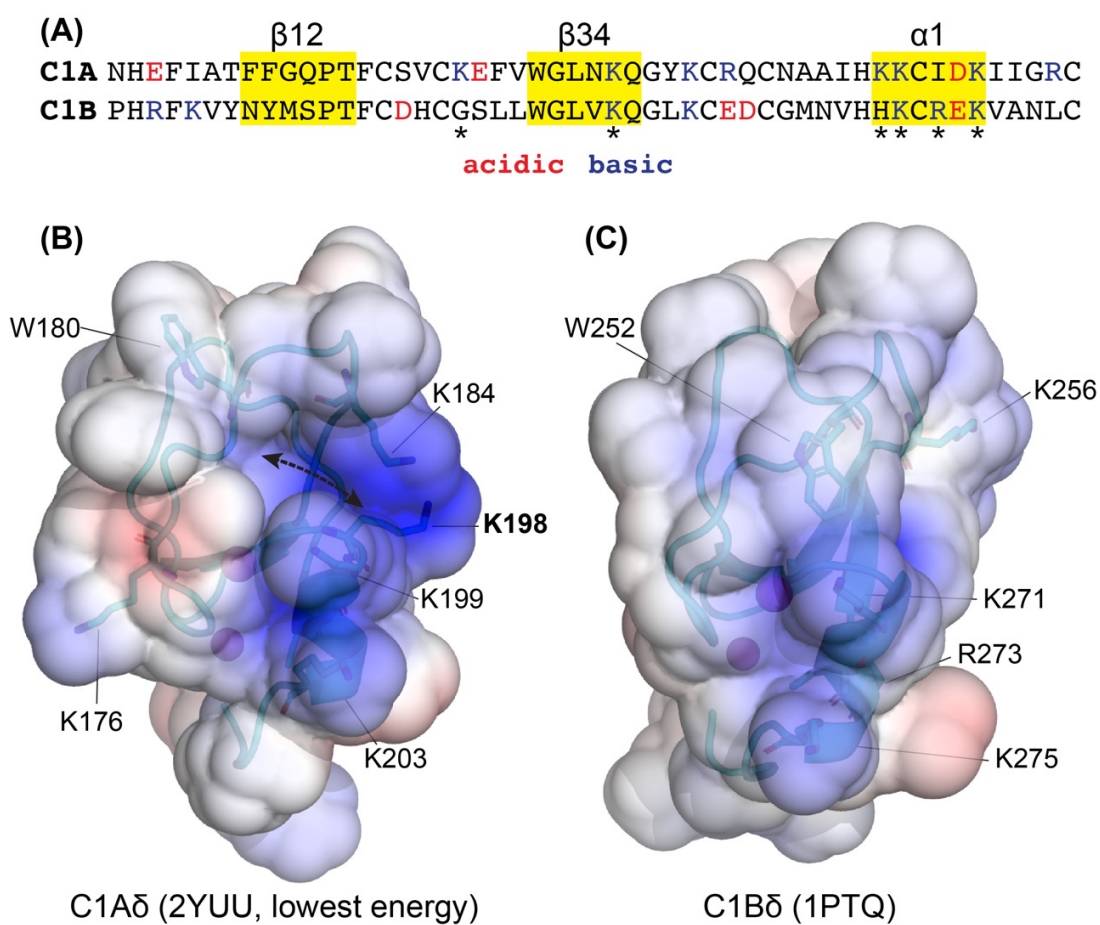


**Figure I.3 Distribution of charged residues among the two C1 domains of PKCδ.** (A) Amino acid sequence comparison of C1A and C1B domains of PKCδ, emphasizing the charged residues (color codes) and distinct differences (marked by asterisks). (B) Comparison of the surface electrostatic maps (APBS, ±kT/e) of the two C1 domains. The presence of an additional Lysine (K198, bold) on the helix of C1A increases the continuity of the basic region. In addition the differential Trp orientation (strictly applicable to the

depicted structural models) appears to open up a groove (marked by arrow) that can interact with anionic lipids like PtdSer, and potentially PtdIns(4,5)P$_2$. In comparison, the C1B basic region is less prominent. These differences could translate into the distinct anionic lipid preferences of these domains.

Other than these features, a single residue on the agonist-binding loops is reported to have a dominant influence on the behavior of these domains (**Figure I.2A and B**). This apparent "toggle" residue, depending upon whether its tryptophan or tyrosine, can modulate DAG sensitivity.[22, 23] The exact mechanism behind this distinction is not yet clear and more work is needed. Apart from importance of certain key residues on C1 domains, the dynamic nature of the agonist-binding region remains entirely enigmatic as the crystal structures cannot faithfully replicate the solution state ensemble of these regions. Therefore, to understand the C1 domains and their agonist preferences better, solution state methods such as solution Nuclear Magnetic Resonance (NMR) spectroscopy are uniquely suited and the field appears to transition in that direction.

<u>General mechanism of C1-membrane interactions</u>

The membrane association of "typical" C1 domains depends upon the presence of lipophilic agonists such as DAG, phorbol esters, macrocyclic lactones with great therapeutic potential: Bryostatin 1 (**Figure I.2C**) and its derivatives aptly termed as "Bryologs".[16, 24, 25] The striking differences in the structural features of these agonists suggest that the membrane binding mode of C1 domains with each one of them needs to be probed independently. The general model of C1-membrane interactions however is believed to have two common factors: First, the stereospecific recognition of the agonist

8

by relatively polar residues residing in the binding groove.[18] Due to lipophilicity of the agonists, this event likely occurs at the membrane interface. The initial membrane targeting pre-requisite for this could happen via electrostatic attraction between basic regions of the domain and the anionic lipids of the membranes (**Figure I.3A**). It is unclear whether the inherent differences in the charge density of this region between different C1 domains contribute to specificity towards certain anionic lipids (**Figure I.3B**). Second, the subsequent "hydrophobic switch" leading to creation of a single contiguous hydrophobic surface causes deeper membrane insertion supported by apolar contacts between the hydrophobic/aromatic residues with the acyl chains of the lipids.[18]
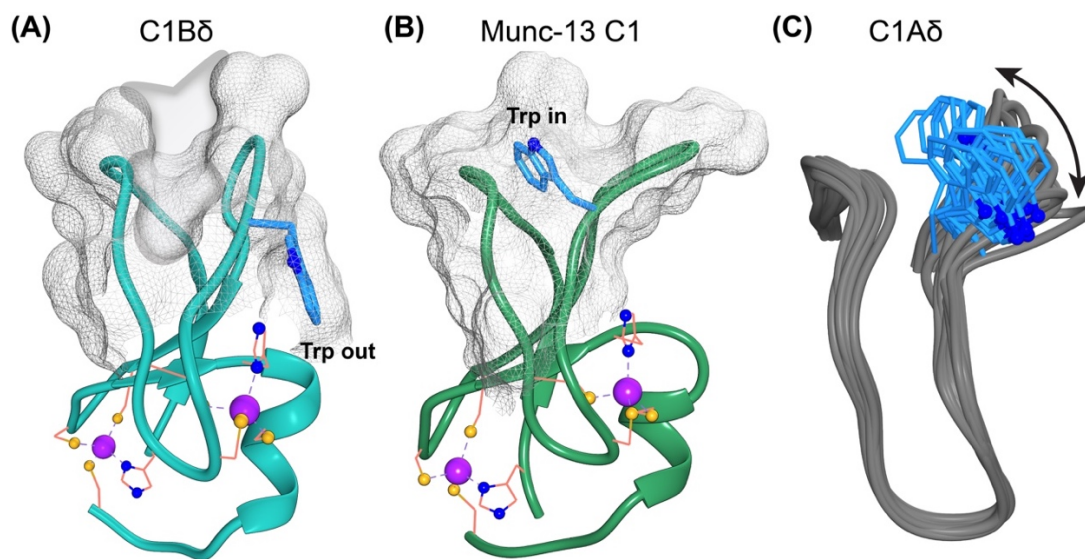


**Figure I.4 Correlation between orientational preferences of the "DAG toggle" residue with the respective DAG sensitivity.**
(A) In the crystal structures of C1B domain of PKCδ (1PTQ,1PTR)[18] the Trp is distinctly away from the intra-loop; agonist-binding region. This domain is highly sensitive towards DAG. (B) The lowest energy NMR conformer of Munc-13 C1 domain (1Y8F)[26] shows a distinct Trp state occluding the agonist-binding region. This orientation is consistent over the entire ensemble (not shown), attributed to the clear NMR-detected restrains reported. This domain has relatively weak affinity for DAG.

(C) The NMR ensemble of the C1A domain from PKCδ (2YUU, only loop ensemble is depicted) shows Trp sampling different orientations, yet in proximity to the intra-loop space. The intrinsic dependence of this domain for DAG is unclear and needs further investigation.

With respect to DAG interactions, it is believed that the presence of a specific aromatic residue at the agonist-binding loops plays key role. In case of the C1B domain of PKCδ, it's been reported that this residue being tryptophan instead of tyrosine (as in the equivalent C1 domain of PKCα) greatly improves DAG affinity (**Figure I.2A and Figure I.4A**).[22] Ironically, the C1 domain of Munc-13 does have tryptophan in the analogous position, yet it is oriented in such a manner that it occludes the agonist-binding groove (**Figure I.4B**).[26] The result is that the DAG affinity of Munc13-C1 domain is expected to be weak.[26] This raises an interesting question about how DAG affinity is modulated in domains where the tryptophan orientation changes due to inherent dynamics or where this residue is only partially blocking the agonist-binding region. For instance, NMR-determined structural ensemble of the C1A domain of PKCδ (PDB ID 2YUU, unpublished) shows that the tryptophan predominantly samples conformations that tend to partially occlude the intra-loop region (**Figure I.4C**). Although this domain expected to prefer DAG-membranes,[27] it will be interesting to see how its DAG-dependence compares with other C1 domains.

Another aspect in relation to C1-DAG interactions that is underdeveloped is the role played by DAG-induced alterations in the phase properties of the membranes. It is well known observation that certain DAGs can create membrane distortions, including creation of inverted hexagonal phases.[28] These alterations can disrupt the integrity of the

typical membrane architecture which is polarized with respect to hydrophobicity. Since hydrophobic interactions between C1 residues and lipid acyl chains can be stabilizing, the phase alterations caused by DAGs can provide the protein easier access to the most hydrophobic parts of the membranes. This can in turn significantly reduce the energetic penalty the protein has to pay for membrane penetration. Subsequently, it is likely that the hydroxyls of DAG can simply participate (via H-bonding interactions) in the existing protein-bound solvent network (similar to certain other agonists) or displace this solvent entirely to anchor the C1 domain. Furthermore, the clustering of DAGs into potential "microdomains" can greatly augment this phenomenon.[29]

It is essential to point out that that the aforementioned membrane-altering effects of DAGs are concentration dependent and specific to certain DAG isomers (*sn*-1,2 isomer for instance has differential phase properties from other isomers),[28] explaining why they may not manifest under all experimental conditions reported in the literature. The alternative or complementary hypothesis can be made based on this information: the C1 domains are sensitive to DAGs not exclusively because of their direct interactions as ligands, but due to their membrane altering actions. This hypothesis suggests that C1 domains can sense DAGs in principle as indirect agonists, where the effects of DAG on a common scaffold i.e. membranes drive the process. Further exploration to test such hypothesis is needed, using an experimental setup where one can separately distinguish the inherent affinity of a given C1 domain for DAG as an agonist from the membrane-specific DAG effects.

Finally, it is currently unclear whether there are inherent differences in the membrane-bound states of C1 domains associated with different agonists. This is essential to determine as certain agonists such as Bryostatin-1 impart protective effects on PKC action while others like phorbol esters tend to dysregulate it.[30] This aspect is discussed in following section as it is also linked to ligand promiscuity of the C1 domains.

<u>Therapeutic potential behind ligand promiscuity of C1 domains</u>

The pharmacological potential of C1 domains is realized particularly in the context of PKC regulation.[20] The clear cause-effect relationship between PKC dysregulation and tumor formation/metastasis is not yet established.[6] But it is abundantly clear given the role of PKC is cell proliferation and apoptosis that by controlling PKC activation in cancer cells, one could in principle be able to hinder the disease progression. The current strategy to achieve this involves targeting the enzymatic activity of the PKC by designing the kinase inhibitory compounds,[31] an approach that relies entirely upon the assumption that it is the upregulation of the PKC activity that leads to disease progression. This approach has failed consistently over the course of numerous clinical trials and might have been misguided to begin with.[32]

The assumption that PKC is an oncogene has started to shift based on the findings that the PKC mutations seen in cancers are in fact loss-of-function type.[33, 34] This finding suggests that although transient upregulation of the PKC is evident in cancers, it is the subsequent degradation and loss of PKC pools that leads to cancer progression. Further implication is that the therapeutic agents should be designed to

12

stabilize the PKC pools and restore the activity. In stark contrast, in neurodegenerative disorders, PKC mutations typically exhibit enhanced activity.[33] Treating those would require controlled suppression of PKC activity. This is where C1 domains come into picture. As agonist-dependent C1 membrane association is directly coupled to PKC activation, one can design high-affinity modulators that either enhance or suppress its membrane binding depending upon the disease state being treated.

**C1-agonist-membrane ternary complex**

**Membrane**

2

**Agonist**

1

**C1 domain**

3

1. **Depth of insertion**
2. **Relative mobility**
3. **Lipid specificity**
4. **Availability for secondary interactions**

4
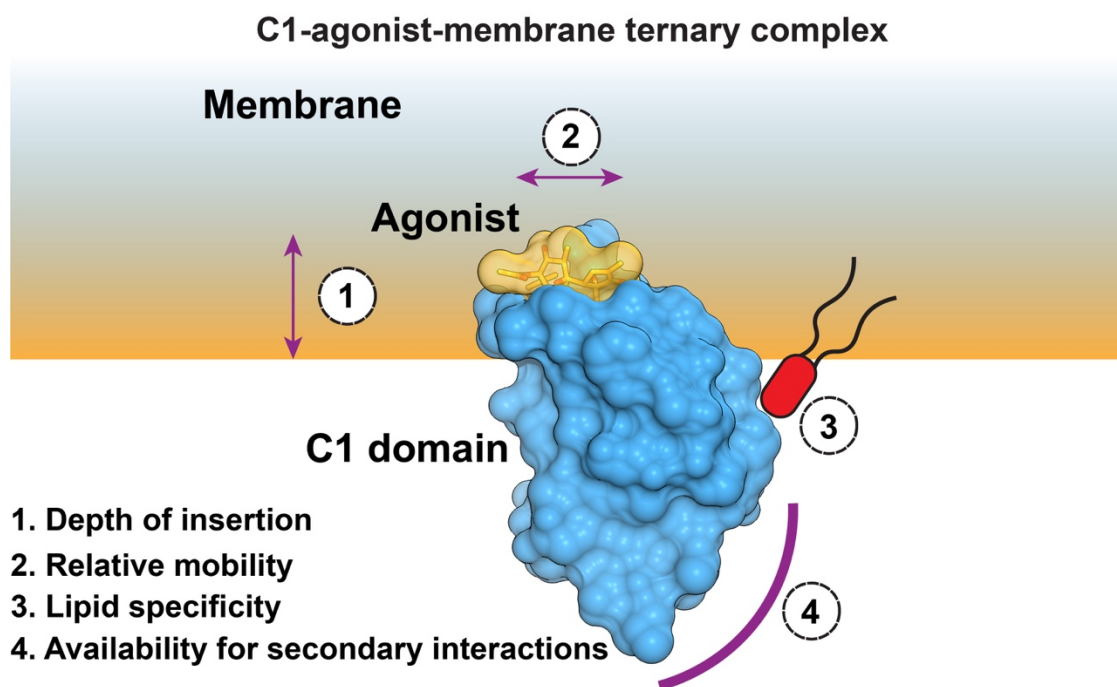
**Figure I.5 Essential factors that should be considered while designing and testing C1 agonists.**
These factors will ultimately determine the true therapeutic "potency" of the designed agonists. However, the lipophilic nature of most C1 agonists and the lack of suitable membrane mimics amenable to biochemical and biophysical approaches hinder such characterization of these ternary complexes.

In cancer therapy, it is lucrative to design agonists targeted for C1 domains that in turn modulate the PKC activation and slow down its eventual downregulation. Given the membrane association of C1 domains depends upon agonist-assisted hydrophobic shift, any hydrophobic ligand that has sufficient polarity to interact with the protein residues/solvent within the intra-loop groove can in principle serve as C1 agonist. Reflecting this assumption, several promising C1 ligands have been identified so far that show very high affinities towards the domain compared to endogenous agonist DAG.[16] But designing a potent ligand constitutes only the first half of the puzzle. The second half; that yet eludes us, is to determine how these ligands affect the membrane binding of C1 domains, as that is where the ultimate PKC enzymatic action resides. Biochemical and biophysical parameters such as thermodynamic "potency" of the ternary complex, depth of membrane insertion, lipid specificity, and relative mobility of the domain within the membrane could be critical determinants of how susceptible the resulting complexes are to inherent cellular countermeasures and dissociation (**Figure I.5**).

A potential way to approach this puzzle is to first determine a suitable and faithful membrane mimic that can be easily manipulated with respect to its composition yet remains amenable to atomic-resolution biophysical approaches like solution NMR and crystallography. In this regard, bicelles provide a promising middle ground to non-bilayer forming yet conveniently small micelles and bilayer-containing yet big liposomes.[35] We suggest an approach that involves the use of isotropically tumbling bicelles, C1 domains and variety of agonists with solution NMR spectroscopy as a method of choice (**Figure I.6**). The key advantage of this approach is that being solution

state, the inherent dynamics of the C1 domains can be factored into the analysis. Different isotope specific NMR experiments can allow probing of the protein backbone amides along with methyl containing and aromatic side chains at independent residue level. The presence of a bilayer environment that can be compositionally tailored is also useful to account for the membrane-altering effects of DAGs mentioned before. Furthermore, the experimental information obtained using strategy can be correlated and used to drive the *in silico* approaches that involve guided molecular dynamic simulations on this system. Although the molecular dynamics simulations reported on C1 domains so far have been informative,[36, 37] driving them further based on the atomistic restraints obtained using solution-state experiments would surely improve their reliability. The wealth of information obtained using such inclusive strategy can be subsequently used to revisit the agonist design iteratively. The direct application of this strategy is demonstrated in chapter III.
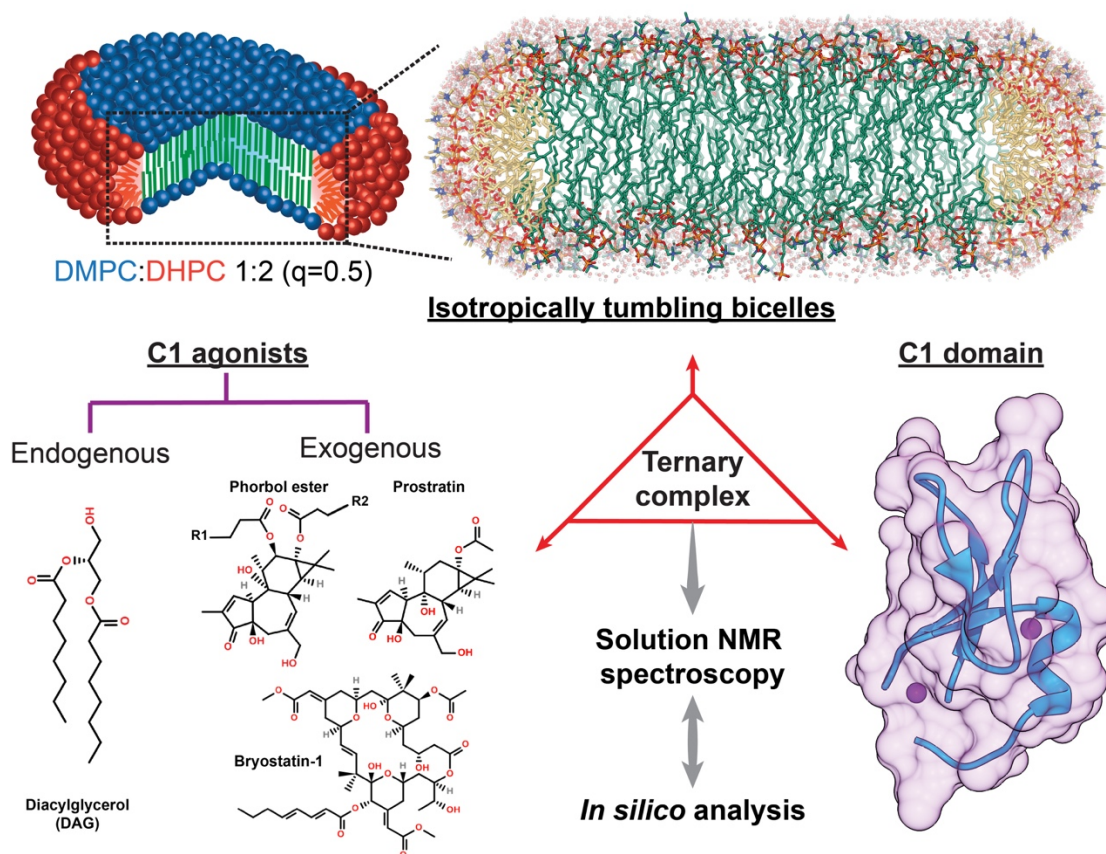
**Figure I.6 Proposed experimental approach to overcome the current difficulties associated with the characterization of C1 ternary complexes.**

This approach suggests the use of isotropically tumbling bicelles as membrane mimics to lead the formation of C1-agonist-membrane ternary complexes. Bicelles and the resulting complexes are amenable to solution state NMR spectroscopy, involved a set of techniques that would faithfully reflect the contributions of the inherent protein dynamics. The experimental readouts can in turn be used as restraints to drive the molecular dynamics simulations on the system. Conversely, the validity of the information obtained from the *in silico* approaches can also be tested using this approach.

## C2 domains: $Ca^{2+}$ dependent membrane-binding modules

C2 domains were first discovered as conserved modules of ~130 residues on conventional PKC isoforms, responsible for the $Ca^{2+}$ sensitive activation of these isoenzymes.[38-40] Subsequent studies identified the presence of these domains on proteins like Synaptotagmins, Rabphilin-3A, Perforin, and UNC-13s.[41] Their abundance is evident in eukaryotes attributed to the fact that $Ca^{2+}$-dependent signaling is fairly advanced compared to prokaryotes.[42] Incidentally, not all C2 domains appeared to be sensitive to $Ca^{2+}$ or capable of phospholipid interactions. A case in point being the C2 counterparts on novel PKC isoforms that are putative protein-protein interaction modules but do not possess the structural features to bind $Ca^{2+}$.[43] This raised three major questions: 1. Which factors determine the $Ca^{2+}$ binding ability of these domains? 2. Why do these domains specifically prefer acidic phospholipids in $Ca^{2+}$-dependent as well as independent manner? and 3. Are all C2 domains alike or have distinguishing features that "tune" them to their respective host signaling proteins?

The answers to some of these questions started emerging as the first crystal structure of C2 domain was solved in 1995 by Thomas Sudhof and Stephen Sprang's groups.[44] This pioneering work reported the apo and $Ca^{2+}$-complexed states of one of the two C2 domains (C2A) of Synaptotagmin 1 (Syt1), a neuronal $Ca^{2+}$ sensor that couples the action potential induced $Ca^{2+}$ influx to neurotransmitter release caused by SNARE-mediated vesicular fusion (**Figure I.7A and B**).[45, 46] Due to the direct importance of Syt1 C2 domains in controlling the process of synaptic exocytosis, these domains became one of the well-studied examples of lipid-binding modules in

calciomics. Reflecting that, following subsections are primarily focused on tandem C2

domains of Syt1 with their similarities and differences presented in the context of other

C2 domains when applicable.
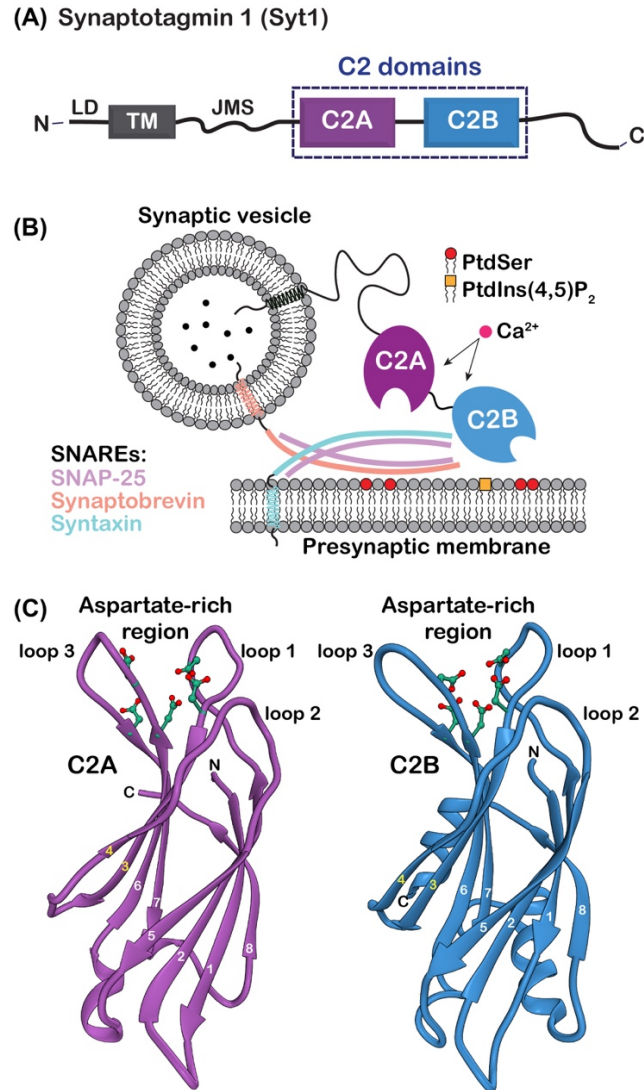


**Figure I.7 Some of the well-studied C2 domains belong to the neuronal Ca$^{2+}$ sensor, Synaptotagmin 1 (Syt1).**
(A) Schematic showing the modular architecture of Syt1, with C2 domains appearing in tandem. (B) The model shows the arrangement of fusogenic synaptic vesicle machinery with Syt1 C2 domains acting as Ca$^{2+}$-dependent triggers to cause exocytosis

and neurotransmitter release. (C) The three-dimensional structures of Syt1 C2 domains are shown. The C2A structure (1RSY, X-ray) represents the very first structure of the C2 domains solved.[44] The C2B structure (1K5W, NMR, lowest energy conformer) was subsequently solved.[47] There structures were instrumental in revealing the regions responsible for $Ca^{2+}$ and anionic lipid preferences of the C2 domains.

<div align="center">Structural features of C2 domains</div>

Structurally, most $Ca^{2+}$ sensitive C2 domains possess a β-sandwich fold that is made up of 8 anti-parallel β strands (**Figure I.7C**).[44] The strands are linked together by flexible loops on apical and basal ends of the domains. Three of these loops converged at one end form a region rich in aspartate residues that electrostatically attract and directly coordinate multiple $Ca^{2+}$ ions (**Figure I.8**).[48] In the absence of lipids or membranes, the intra-loop space of Syt1 C2A and C2B domains can accommodate upto three and two $Ca^{2+}$ ions respectively,[47, 49] while that of PKCα C2 domain can accommodate two.[50] The intrinsic $Ca^{2+}$ affinities of these domains appear weak in vitro, falling in µM-mM range.[47, 51-53] The oxygen atom ligands of the aspartate carboxylates are shared between the bound $Ca^{2+}$ ions, leading to depletion of the anionic charge density and subsequent basic shift in the surface electrostatic potential.[47, 54] This positive electrostatic shift in turn becomes the driving force that enables the C2 domains to interact with negatively charged membranes.
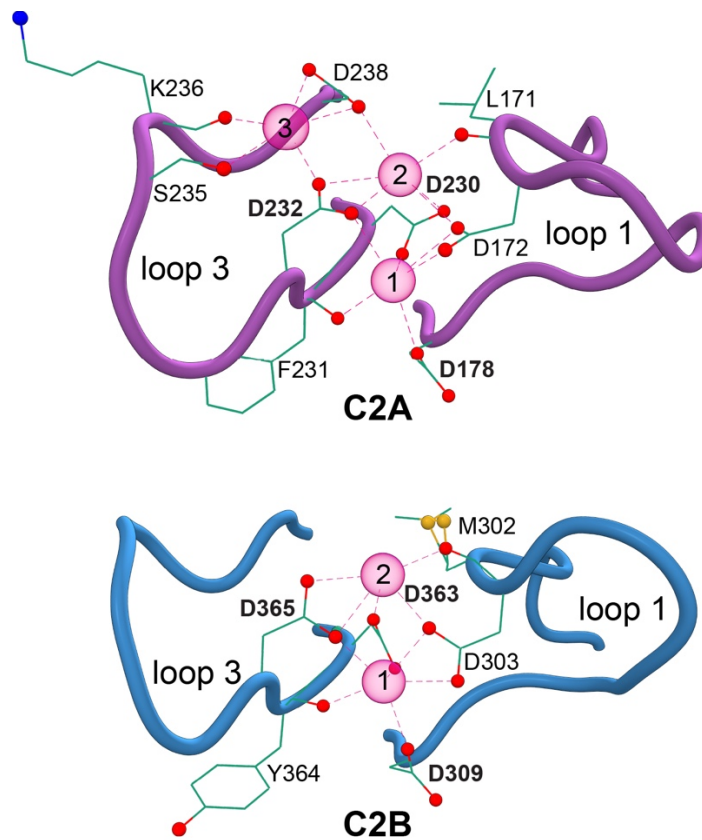
**Figure I.8 Ca$^{2+}$ is coordinated by the spatially clustered aspartate residues on the loops of the C2 domains, shown here in the context of Syt1.**
C2A domain can coordinate up to 3 Ca$^{2+}$ ions (1BYN, NMR, lowest energy conformer)[55] while C2B can coordinate up to 2 (1TJX, X-ray)[56] in the absence of anionic lipids. The carboxylates provided by the conserved aspartate residues are typically shared between different Ca$^{2+}$ ions, causing shift in the anionic charge density of the loop regions. The aspartates that can abolish the Ca$^{2+}$ binding are labelled in bold (tested by mutagenesis).

The residues involved in the metal ion coordination are conserved among the

Ca$^{2+}$ sensitive C2 domains (**Figure I.9A**).[48] Loss of some of these residues in certain C2

domains appears to be responsible for their that lack of Ca$^{2+}$ sensitivity. For instance, the

C2 domain of novel isoform PKCδ has a distinctly different loop region conformation

compared to Syt1 and PKCα C2 domains and lacks the equivalent aspartates accounting

for its inability to bind $Ca^{2+}$.[43] Mutagenesis studies done on Syt1 C2 domains are also

evident of the general consensus that these conserved residues are essential for $Ca^{2+}$

binding.[57, 58] Apart from the loops, C2 domains have other regions that can provide sites

for coulombic interactions of polyanionic lipid moieties. For instance, the Lysine-rich

cluster (LRC) located on the β3-β4 strands of Syt1 C2B creates a continuous basic

region at the concave void of the domain (**Figure I.9B**).[47] In addition, the "bottom"

region of Syt1 C2B possesses two consecutive arginine residues that in conjunction with

the LRC, significantly expand the positively charged surface of the domain.  Depending

upon the identity of other residues at or near these additional regions, the properties of

the given C2 domain can alter (as discussed in the next section). The loops along with

these variable regions determine the electrostatic makeup of various C2 domains (**Figure

I.10**), and by extension dictate their membrane interactions and lipid preferences.

**(A)**

| Domain | | loop 1 | loop 2 | loop 3 |
|---|---|---|---|---|
| Syt1 | C2A | ALDMGGTSD | HRKTLNP | YDFDRFSKHD |
| | C2B | KMDVGGLSD | KKNTLNP | LDYDKIGKND |
| PKC | C2α | PMDPNGLSD | IRSNLNP | WDWDRTTRND |

↑ Conserved acidic ↑ Conserved basic

**(B)** Syt1 C2B

Ca²⁺-binding loops
PtdSer/PtdCho interactions

loop 3    loop 1
          loop 2

Lys-rich cluster (LRC)
PtdIns(4,5)P₂ interactions

R322
K325
K321
K326
K324
K327

Syt1 C2A
PKC C2α
A271
V255
P270
H254

R399
R398
Arg-rich "bottom"
PtdSer interactions

**(C)**

| Domain | LRC: PtdIns(4,5)P₂ sensitivity |
|---|---|
| | β3-β4 |
| Syt1 C2A | PYVKVFLLP-- DKKKKFETKV: Insensitive |
| Syt1 C2B | PYVKIHLMQNG KRLKKKKTTI: Sensitive |
| PKC C2α | PYVKLKLIPDP KNESKQKTKT: Sensitive |
| | ↑ * * * * ↑ * |

↑ Conserved basic * Special differences

**Figure I.9 Comparison of the Ca²⁺ and other anionic phospholipid-binding regions of three representative Ca²⁺ sensitive C2 domains from Syt1 and PKCα.**
(A) The amino acid sequence of the Ca²⁺-binding regions formed by the three apical loops of the C2 domains is compared. The aspartates are conserved among them, indicating their importance for the Ca²⁺ sensitivity. Some of these residues are mutated in the C2 domains that do not sense Ca²⁺ (not shown here). Apart from the aspartates, there are conserved basic residues on loops 2 and 3 that can provide electrostatic

22

contribution to the membrane association. (B) The distinct regions of interest are depicted on the C2B domain of Syt1 as an example (2LHA, NMR lowest energy conformer).[59] In addition to $Ca^{2+}$ binding loops, a cluster of lysine residues on β3-4 is responsible for PtdIns(4,5)P$_2$ sensitivity. Inset: shows an arginine rich region exclusive to C2B domain that is not present on the other two C2 domains discussed. This region serves as a separate membrane/protein-protein binding site. (C) The amino acid sequences of the lysine-rich cluster (LRC) regions are compared. Although the LRC of C2A does have a stretch of lysines, this region is shorter and it is immediately flanked by the acidic residues. This distinction appears to make C2A insensitive to PtdIns(4,5)P$_2$.

<p style="text-align:center"><u>General mechanism of C2-membrane interactions</u></p>

The ability of C2 domains to selectively interact with anionic phospholipid membranes can be attributed to their characteristic electrostatic makeup prior to as well as after binding $Ca^{2+}$ ions. The loop region is negatively charged without $Ca^{2+}$ binding, and therefore cannot interact with anionic lipids due to coulombic repulsion. The shift of this opposing electrostatic surface potential is achieved by sequential $Ca^{2+}$ binding to the available sites, making the domains attract to anionic phosphatidyl serine (PtdSer/PS) or poly-anionic phosphatidyl inositol (PtdIns) headgroups.[60, 61] Although the interaction is driven by electrostatics, the stability at the membrane interface is reportedly achieved by additional H-bonding, cation-π and hydrophobic interactions between generic lipid moieties and various loop region residues (**Figure I.11A & B**).[54, 62] In addition, the anionic lipid headgroups can directly coordinate the protein-bound metal ions.[63] These lipid-metal ion interactions potentially provide additional ligands to augment the existing metal coordination spheres and in principle can create extra metal binding sites, increasing the apparent affinity of these domains towards $Ca^{2+}$.[51] Understanding the relative contribution and importance of each of the aforementioned factors is necessary

to grasp C2-membrane interactions mechanistically as addressed in the subsequent chapters.

Apart from the $Ca^{2+}$ binding loops, the LRC region of certain C2 domains can bind to the signaling lipid PtdIns(4,5)P$_2$.[64] Although the net abundance of PtdIns(4,5)P$_2$ in cellular plasma membranes is very low (<1%),[65] signaling events mediated by PKC as well as Syt rely heavily upon its presence. For instance, the $Ca^{2+}$ dependent interaction of PKCα C2 domains with PtdIns(4,5)P$_2$ help localize the kinase at the membrane, where the direct hydrolysis product of PtdIns(4,5)P$_2$; diacylglycerol, serves as a ligand for the specific membrane interactions of C1 domains.[66] Furthermore, the C2B domain of Syt1 has the PtdIns(4,5)P$_2$ sensitive LRC region that is coupled allosterically to its $Ca^{2+}$ affinities.[58, 67] It is observed that binding of PtdIns(4,5)P$_2$ to C2 domains via LRC increases their $Ca^{2+}$ affinities several fold, and vice versa.[58, 68] This observation is intriguing as the regions associated with $Ca^{2+}$ binding (the loops) and LRCs are several angstroms apart. Such mutual allosteric action is therefore likely achieved by shielding of the opposing charges of either regions by their respective ligands. Interestingly, although a distinct LRC region exists on the C2A domain of Syt1, it is insensitive towards PtdIns(4,5)P$_2$.[58] The arrangement of the four consecutive lysines on C2A LRC is distinct in a way that they are flanked on immediate ends by acidic residues (an aspartate and a glutamate), interrupting the continuity of the polybasic region (**Figure I.9C**).[64] The seemingly minor alteration in the LRC sequence that alters the electrostatic makeup seems sufficient to abolish the PtdIns(4,5)P$_2$ binding, highlighting the strictly coulombic nature of this particular interaction.
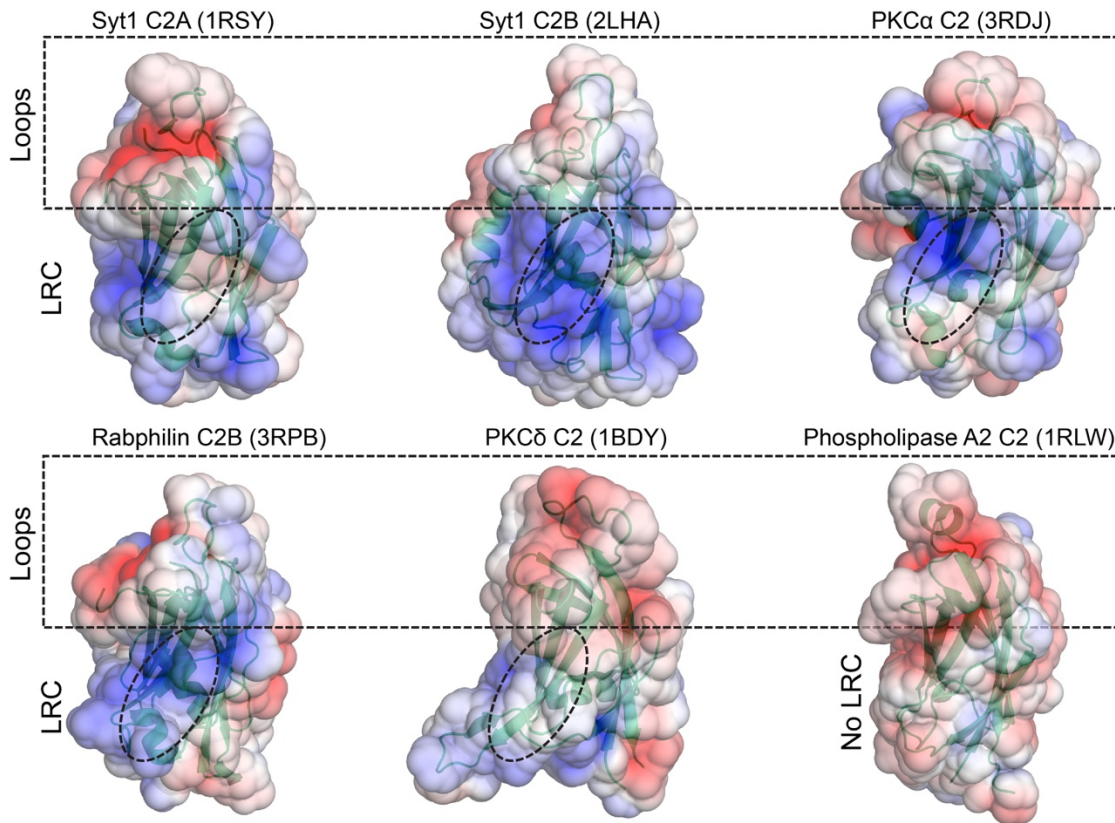
**Figure I.10 The electrostatic makeup of C2 domains have differences that are ultimately linked to their Ca²⁺ sensitivity and lipid preferences.**

The surface electrostatic maps (Adaptive Poisson-Boltzmann Solver, ±5 kT/e) of 6 C2 domains (Ca²⁺-free) is compared with respect to their Ca²⁺-binding and lysine-rich regions. The Syt1 C2A,[44] C2B,[59] PKCα C2,[69] Rabphilin C2B,[70] and Phospholipase A2 C2[71] all bind to Ca²⁺ ions via loops, but PKCδ C2[43] cannot (attributed to substitutions of certain conserved aspartates). Syt1 and Rabphilin C2Bs along with PKCα C2 can interact with PtdIns(4,5)P2 via their LRCs but the remaining three domains cannot.[64, 67] All the C2 domains depicted with the exceptions of those of PKCδ and Phospholipase A2 show preferences toward anionic lipid membranes. The PKCδ C2 does not appear to show membrane interaction at all while Phospholipase A2 C2 interacts with PtdCho.[62]

Apart from LRC, the two consecutive arginine residues at the basal loops of Syt1 C2B can interact with the anionic lipid membranes.[72, 73] These residues are not conserved on either the C2A counterpart of Syt1 or the PKCα C2 domain (**Figure I.9B, inset**). Due to this distinction, C2B possesses the unique ability to "bridge" the anionic phospholipid membranes through multivalent interactions.[73] As a result, C2B can interact with the factors involved in the fusogenic SNAREs machinery, and potentially the presynaptic as well as vesicular membranes simultaneously.[74, 75]
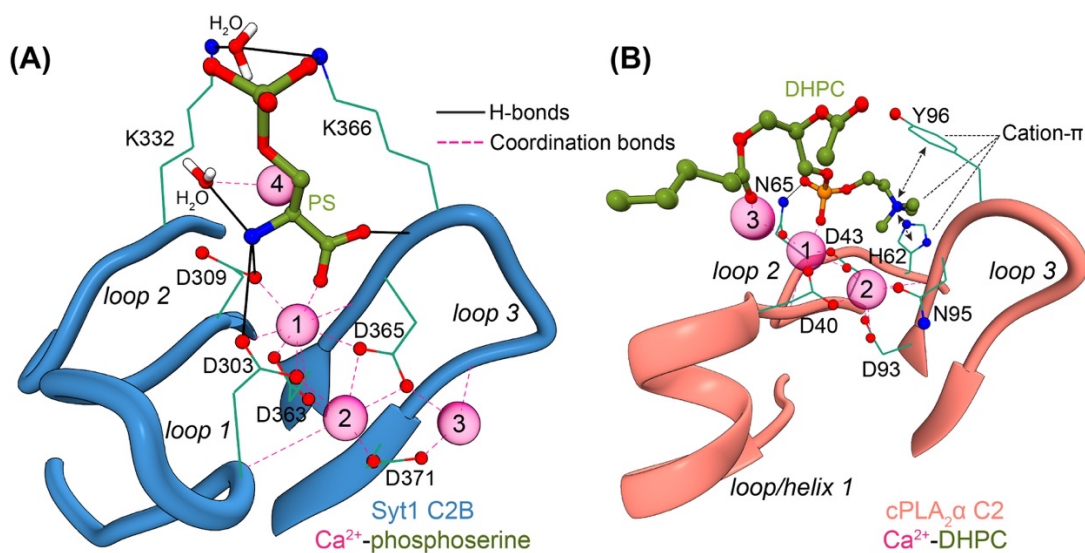


**Figure I.11 Stabilizing interactions of C2.Ca$^{2+}$ complexes with the lipids.**
(A) Interactions of phosphoserine, a soluble analog of PtdSer with Ca$^{2+}$ bound Syt1 C2B domain are depicted (2YOA, X-ray).[63] In addition to the sites 1 and 2 that get populated by Ca$^{2+}$ ions in the absence of lipids, additional ions seem to bind in the presence of phosphoserine. (B) Interactions of PtdCho (DHPC) with the Ca$^{2+}$ bound phospholipase A2 C2 domain are depicted (6IEJ, X-ray).[62] Due to the absence of basic residues on this domain, it prefers zwitterionic lipids like PtdCho and does not have unique preference for the anionic lipids (unlike Syt1 C2B and some other C2 domains shown in Fig I.5)

For the $Ca^{2+}$ insensitive C2 domains on the other hand, the membrane association is predicted to be achieved via polybasic regions and hydrophobic interactions.[76, 77] One way to look at their inability to bind $Ca^{2+}$ is by removing the aspartates that need $Ca^{2+}$ coordination to neutralize them, these domains have altogether eliminated the opposing negatively charged elements. As a result, they might be evolved to interact with anionic membranes or other proteins electrostatically via polybasic regions, without the need of $Ca^{2+}$ to bring about the necessary favorable changes. The C2 domain of PKCδ is a good example of this scenario, as it is believed to partake in protein-protein interactions while the C1 domains exclusively drive the kinase to anionic membranes.[43, 78] In conclusion, the key implication one can associate with these distinctions is that the lipid binding preferences are not identical for all C2 domains and they appear to be evolutionarily "tuned" to their context specific roles.

<u>Binding of non-native divalent cations to C2 domains</u>

The C2 domains that possess the conserved aspartates on the loops are selective towards $Ca^{2+}$ (**Figure I.12**), but have weak intrinsic $Ca^{2+}$ affinities. Further selectivity is likely achieved by their strategic cellular localization, which allows them to have better access to available $Ca^{2+}$ pools and sensitivity to the variations thereof. However, depending upon their affinities, other divalent cations can overcome these selectivity factors, bind to the C2 domains and potentially alter their functions (**Figure I.12**).[79, 80] This issue has been a focus of attention for several studies that address how non-native, toxic divalent cations affect $Ca^{2+}$ sensitive C2 domains.[52, 69, 81-83]

27
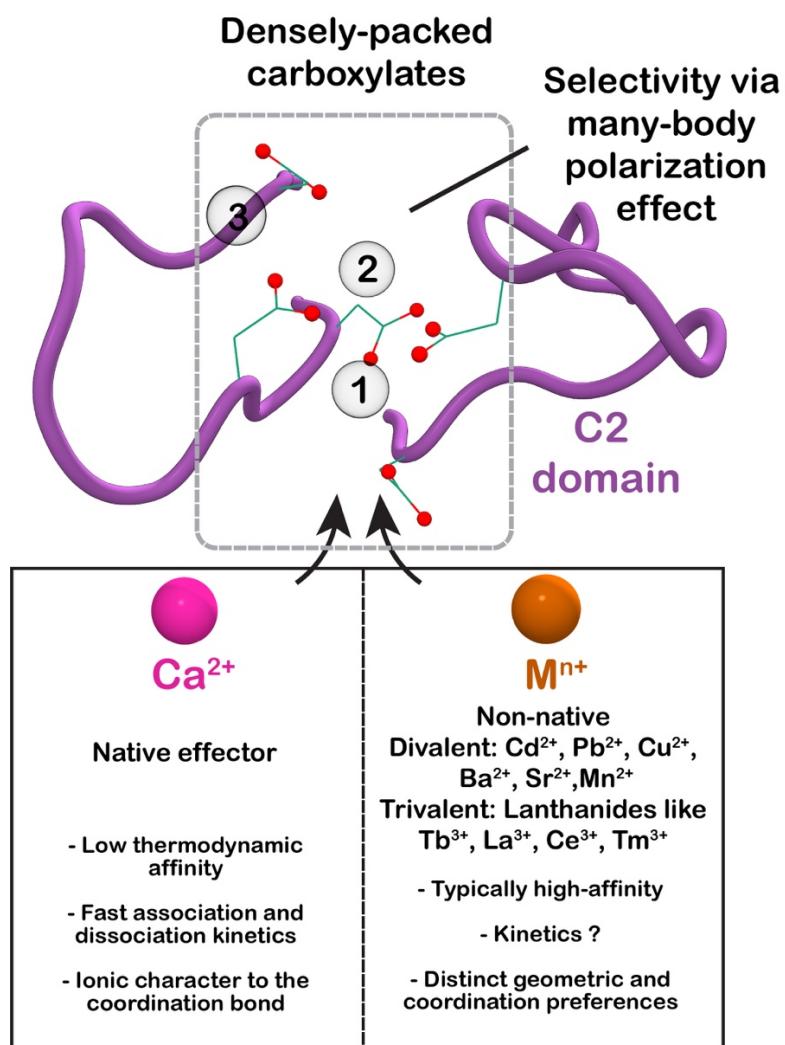
**Figure I.12 C2 domains can bind to several non-endogenous di- and tri-valent cations with distinct properties and potential functional outcomes.**
In contrast to $Ca^{2+}$, the other divalent cations reported to bind C2 domains typically show much higher affinities. However, the information about their binding kinetics is unclear. Although this wide gamut of metal ions gives the impression of non-selectivity, the C2 domains are highly selective. For instance, $Mg^{2+}$ being divalent, native, much higher in concentration, and better charge acceptor is not selected over $Ca^{2+}$. This is achieved via "many-body polarization effect".[84] Essentially by densely packing many anionic carboxylates around metal-ion, the protein creates geometric restrains that are selective towards $Ca^{2+}$. Although, the tabulated non-native metal ions are clearly able to overcome this selectivity barriers, the mechanisms are not clear.

Several examples of such ionic mimicry can be seen in the context of C2 domains and bio-toxic heavy metals like $Cd^{2+}$ and $Pb^{2+}$.[69, 82, 83] In case of PKCα C2 domain, the binding of $Cd^{2+}$ seems to inhibit its membrane localization, while $Pb^{2+}$ promotes it in vitro.[69, 82] The C2A domain of Syt1 is reported as a putative molecular target of $Pb^{2+}$, attributed to how $Pb^{2+}$ enhances its ability to bind anionic phospholipid vesicles.[81, 83] Because of these observations, there is growing need for comprehensive studies that tackle how toxic heavy metal ions affect the structure, function and dynamics of $Ca^{2+}$-binding C2 domains.

Incidentally, there is an additional incentive to study C2 domains with the non-native metals. These studies have a tremendous potential to uncover the mechanistic determinants of C2-membrane interactions. Different thermodynamic, kinetic, and coordination properties of heavy metal ions can provide a way to selectively study certain factors that contribute to lipid-metal ion interactions while retaining the electrostatic makeup of the C2 domains intact. For instance, the coordination number (CN) of $Cd^{2+}$ in proteins is 4 or 6 as opposed to that of $Ca^{2+}$ and $Pb^{2+}$ is 6-8 and 9 respectively.[85-87] As a result, $Cd^{2+}$ cannot accommodate additional ligands into its coordination sphere and thus will likely serve as a poor bridge between C2 domains and lipids. This is manifested by the inability of $Cd^{2+}$ to support the membrane interactions of PKCα C2 domain.[82] Using $Cd^{2+}$ in lieu of $Ca^{2+}$ in the context of other C2 domains, one can therefore establish the importance of the lipid-mediated coordination of protein-bound metal ions towards C2-membrane interactions.

In conclusion, the usefulness of probing the interactions of non-native, xenobiotic metal ions with C2 domains is two-fold: 1. To discern the key determinants associated with C2-membrane interaction and, 2. To understand the molecular basic of the toxicity caused by $Ca^{2+}$ mimicking toxic metal ions such as $Pb^{2+}$ and $Cd^{2+}$. The subsequent chapters on C2 domains (Chapters IV, V, and VI) exhibit the direct application of these metal ions to understand the aforementioned factors.

## References

[1] Lemmon, M. A. (2008) Membrane recognition by phospholipid-binding domains, *Nat Rev Mol Cell Biol 9*, 99-111.

[2] Groves, J. T., and Kuriyan, J. (2010) Molecular mechanisms in signal transduction at the membrane, *Nat Struct Mol Biol 17*, 659-665.

[3] Scott, J. D., and Pawson, T. (2009) Cell signaling in space and time: where proteins come together and when they're apart, *Science 326*, 1220-1224.

[4] Sanders, C. R., and Myers, J. K. (2004) Disease-related misassembly of membrane proteins, *Annu Rev Biophys Biomol Struct 33*, 25-51.

[5] Takai, Y., Kishimoto, A., Inoue, M., and Nishizuka, Y. (1977) Studies on a cyclic nucleotide-independent protein kinase and its proenzyme in mammalian tissues. I. Purification and characterization of an active enzyme from bovine cerebellum, *J Biol Chem 252*, 7603-7609.

[6] Garg, R., Benedetti, L. G., Abera, M. B., Wang, H., Abba, M., and Kazanietz, M. G. (2014) Protein kinase C and cancer: what we know and what we do not, *Oncogene 33*, 5225-5237.

[7] Steinberg, S. F. (2008) Structural basis of protein kinase C isoform function, *Physiol Rev 88*, 1341-1378.

[8] Newton, A. C. (1995) Protein kinase C: structure, function, and regulation, *J Biol Chem 270*, 28495-28498.

[9] Boutwell, R. K. (1974) The function and mechanism of promoters of carcinogenesis, *CRC Crit Rev Toxicol 2*, 419-443.

[10] Castagna, M., Takai, Y., Kaibuchi, K., Sano, K., Kikkawa, U., and Nishizuka, Y. (1982) Direct activation of calcium-activated, phospholipid-dependent protein kinase by tumor-promoting phorbol esters, *J Biol Chem 257*, 7847-7851.

[11] Blumberg, P. M. (1988) Protein kinase C as the receptor for the phorbol ester tumor promoters: sixth Rhoads memorial award lecture, *Cancer Res 48*, 1-8.

[12] Newton, A. C. (1997) Regulation of protein kinase C, *Curr Opin Cell Biol 9*, 161-167.

[13] Perin, M. S., Brose, N., Jahn, R., and Sudhof, T. C. (1991) Domain structure of synaptotagmin (p65), *J Biol Chem 266*, 623-629.

[14] Maruyama, I. N., and Brenner, S. (1991) A phorbol ester/diacylglycerol-binding protein encoded by the unc-13 gene of Caenorhabditis elegans, *Proc Natl Acad Sci U S A 88*, 5729-5733.

[15] Hurley, J. H., Newton, A. C., Parker, P. J., Blumberg, P. M., and Nishizuka, Y. (1997) Taxonomy and function of C1 protein kinase C homology domains, *Protein Sci 6*, 477-480.

[16] Das, J., and Rahman, G. M. (2014) C1 domains: structure and ligand-binding properties, *Chem Rev 114*, 12108-12131.

[17] Eichmann, T. O., and Lass, A. (2015) DAG tales: the multiple faces of diacylglycerol--stereochemistry, metabolism, and signaling, *Cell Mol Life Sci 72*, 3931-3952.

[18] Zhang, G., Kazanietz, M. G., Blumberg, P. M., and Hurley, J. H. (1995) Crystal structure of the cys2 activator-binding domain of protein kinase C delta in complex with phorbol ester, *Cell 81*, 917-924.

[19] Hommel, U., Zurini, M., and Luyten, M. (1994) Solution structure of a cysteine rich domain of rat protein kinase C, *Nat Struct Biol 1*, 383-387.

[20] Blumberg, P. M., Kedei, N., Lewin, N. E., Yang, D., Czifra, G., Pu, Y., Peach, M. L., and Marquez, V. E. (2008) Wealth of opportunity - the C1 domain as a target for drug development, *Curr Drug Targets 9*, 641-652.

[21] Ichikawa, S., Hatanaka, H., Takeuchi, Y., Ohno, S., and Inagaki, F. (1995) Solution structure of cysteine-rich domain of protein kinase C alpha, *J Biochem 117*, 566-574.

[22] Dries, D. R., Gallegos, L. L., and Newton, A. C. (2007) A single residue in the C1 domain sensitizes novel protein kinase C isoforms to cellular diacylglycerol production, *J Biol Chem 282*, 826-830.

[23] Stewart, M. D., and Igumenova, T. I. (2017) Toggling of Diacylglycerol Affinity Correlates with Conformational Plasticity in C1 Domains, *Biochemistry 56*, 2637-2640.

[24] Wender, P. A., Hinkle, K. W., Koehler, M. F., and Lippa, B. (1999) The rational design of potential chemotherapeutic agents: synthesis of bryostatin analogues, *Med Res Rev 19*, 388-407.

[25] Wender, P. A., Baryza, J. L., Brenner, S. E., DeChristopher, B. A., Loy, B. A., Schrier, A. J., and Verma, V. A. (2011) Design, synthesis, and evaluation of potent bryostatin analogs that modulate PKC translocation selectivity, *Proc Natl Acad Sci U S A 108*, 6721-6726.

[26] Shen, N., Guryev, O., and Rizo, J. (2005) Intramolecular occlusion of the diacylglycerol-binding site in the C1 domain of munc13-1, *Biochemistry 44*, 1089-1096.

[27] Stahelin, R. V., Digman, M. A., Medkova, M., Ananthanarayanan, B., Rafter, J. D., Melowic, H. R., and Cho, W. (2004) Mechanism of diacylglycerol-induced membrane targeting and activation of protein kinase Cdelta, *J Biol Chem 279*, 29501-29512.

[28] Goni, F. M., and Alonso, A. (1999) Structure and functional properties of diacylglycerols in membranes, *Prog Lipid Res 38*, 1-48.

[29] Edidin, M. (1997) Lipid microdomains in cell surface membranes, *Curr Opin Struct Biol 7*, 528-532.

[30] Kortmansky, J., and Schwartz, G. K. (2003) Bryostatin-1: a novel PKC inhibitor in clinical development, *Cancer Invest 21*, 924-936.

[31] Mochly-Rosen, D., Das, K., and Grimes, K. V. (2012) Protein kinase C, an elusive therapeutic target?, *Nat Rev Drug Discov 11*, 937-957.

[32] Newton, A. C. (2018) Protein kinase C as a tumor suppressor, *Semin Cancer Biol 48*, 18-26.

[33] Antal, C. E., Hudson, A. M., Kang, E., Zanca, C., Wirth, C., Stephenson, N. L., Trotter, E. W., Gallegos, L. L., Miller, C. J., Furnari, F. B., Hunter, T., Brognard, J., and Newton, A. C. (2015) Cancer-associated protein kinase C mutations reveal kinase's role as tumor suppressor, *Cell 160*, 489-502.

[34] Newton, A. C., and Brognard, J. (2017) Reversing the Paradigm: Protein Kinase C as a Tumor Suppressor, *Trends Pharmacol Sci 38*, 438-447.

[35] Durr, U. H., Gildenberg, M., and Ramamoorthy, A. (2012) The magic of bicelles lights up membrane protein structure, *Chem Rev 112*, 6054-6074.

[36] Li, J., Ziemba, B. P., Falke, J. J., and Voth, G. A. (2014) Interactions of protein kinase C-alpha C1A and C1B domains with membranes: a combined computational and experimental study, *J Am Chem Soc 136*, 11757-11766.

[37] Ryckbosch, S. M., Wender, P. A., and Pande, V. S. (2017) Molecular dynamics simulations reveal ligand-controlled positioning of a peripheral protein complex in membranes, *Nat Commun 8*, 6.

[38] Coussens, L., Parker, P. J., Rhee, L., Yang-Feng, T. L., Chen, E., Waterfield, M. D., Francke, U., and Ullrich, A. (1986) Multiple, distinct forms of bovine and human protein kinase C suggest diversity in cellular signaling pathways, *Science 233*, 859-866.

[39] Knopf, J. L., Lee, M. H., Sultzman, L. A., Kriz, R. W., Loomis, C. R., Hewick, R. M., and Bell, R. M. (1986) Cloning and expression of multiple protein kinase C cDNAs, *Cell 46*, 491-502.

[40] Ono, Y., Kurokawa, T., Kawahara, K., Nishimura, O., Marumoto, R., Igarashi, K., Sugino, Y., Kikkawa, U., Ogita, K., and Nishizuka, Y. (1986) Cloning of rat brain protein kinase C complementary DNA, *FEBS Lett 203*, 111-115.

[41] Corbalan-Garcia, S., and Gomez-Fernandez, J. C. (2014) Signaling through C2 domains: more than one lipid target, *Biochim Biophys Acta 1838*, 1536-1547.

[42] Carafoli, E., and Krebs, J. (2016) Why Calcium? How Calcium Became the Best Communicator, *J Biol Chem 291*, 20849-20857.

[43] Pappa, H., Murray-Rust, J., Dekker, L. V., Parker, P. J., and McDonald, N. Q. (1998) Crystal structure of the C2 domain from protein kinase C-delta, *Structure 6*, 885-894.

[44] Sutton, R. B., Davletov, B. A., Berghuis, A. M., Sudhof, T. C., and Sprang, S. R. (1995) Structure of the first C2 domain of synaptotagmin I: a novel Ca2+/phospholipid-binding fold, *Cell 80*, 929-938.

[45] Brose, N., Petrenko, A. G., Sudhof, T. C., and Jahn, R. (1992) Synaptotagmin: a calcium sensor on the synaptic vesicle surface, *Science 256*, 1021-1025.

[46] Chapman, E. R. (2008) How does synaptotagmin trigger neurotransmitter release?, *Annu Rev Biochem 77*, 615-641.

[47] Fernandez, I., Arac, D., Ubach, J., Gerber, S. H., Shin, O., Gao, Y., Anderson, R. G., Sudhof, T. C., and Rizo, J. (2001) Three-dimensional structure of the synaptotagmin 1 C2B-domain: synaptotagmin 1 as a phospholipid binding machine, *Neuron 32*, 1057-1069.

[48] Shao, X., Davletov, B. A., Sutton, R. B., Sudhof, T. C., and Rizo, J. (1996) Bipartite Ca2+-binding motif in C2 domains of synaptotagmin and protein kinase C, *Science 273*, 248-251.

[49] Ubach, J., Zhang, X., Shao, X., Sudhof, T. C., and Rizo, J. (1998) Ca2+ binding to synaptotagmin: how many Ca2+ ions bind to the tip of a C2-domain?, *EMBO J 17*, 3921-3930.

[50] Verdaguer, N., Corbalan-Garcia, S., Ochoa, W. F., Fita, I., and Gomez-Fernandez, J. C. (1999) Ca(2+) bridges the C2 membrane-binding domain of protein kinase Calpha directly to phosphatidylserine, *EMBO J 18*, 6329-6338.

[51] Fernandez-Chacon, R., Konigstorfer, A., Gerber, S. H., Garcia, J., Matos, M. F., Stevens, C. F., Brose, N., Rizo, J., Rosenmund, C., and Sudhof, T. C. (2001) Synaptotagmin I functions as a calcium regulator of release probability, *Nature 410*, 41-49.

[52] Katti, S., Nyenhuis, S. B., Her, B., Srivastava, A. K., Taylor, A. B., Hart, P. J., Cafiso, D. S., and Igumenova, T. I. (2017) Non-Native Metal Ion Reveals the Role of Electrostatics in Synaptotagmin 1-Membrane Interactions, *Biochemistry 56*, 3283-3295.

[53] Evans, C. S., He, Z., Bai, H., Lou, X., Jeggle, P., Sutton, R. B., Edwardson, J. M., and Chapman, E. R. (2016) Functional analysis of the interface between the tandem C2 domains of synaptotagmin-1, *Mol Biol Cell 27*, 979-989.

[54] Zhang, X., Rizo, J., and Sudhof, T. C. (1998) Mechanism of phospholipid binding by the C2A-domain of synaptotagmin I, *Biochemistry 37*, 12395-12403.

[55] Shao, X., Fernandez, I., Sudhof, T. C., and Rizo, J. (1998) Solution structures of the Ca2+-free and Ca2+-bound C2A domain of synaptotagmin I: does Ca2+ induce a conformational change?, *Biochemistry 37*, 16106-16115.

[56] Cheng, Y., Sequeira, S. M., Malinina, L., Tereshko, V., Sollner, T. H., and Patel, D. J. (2004) Crystallographic identification of Ca2+ and Sr2+ coordination sites in synaptotagmin I C2B domain, *Protein Sci 13*, 2665-2672.

[57] Stein, A., Radhakrishnan, A., Riedel, D., Fasshauer, D., and Jahn, R. (2007) Synaptotagmin activates membrane fusion through a Ca2+-dependent trans interaction with phospholipids, *Nat Struct Mol Biol 14*, 904-911.

[58] Radhakrishnan, A., Stein, A., Jahn, R., and Fasshauer, D. (2009) The Ca2+ affinity of synaptotagmin 1 is markedly increased by a specific interaction of its C2B domain with phosphatidylinositol 4,5-bisphosphate, *J Biol Chem 284*, 25749-25760.

[59] Joung, M. J., Mohan, S. K., and Yu, C. (2012) Molecular level interaction of inositol hexaphosphate with the C2B domain of human synaptotagmin I, *Biochemistry 51*, 3675-3683.

[60] Kuo, W., Herrick, D. Z., Ellena, J. F., and Cafiso, D. S. (2009) The calcium-dependent and calcium-independent membrane binding of synaptotagmin 1: two modes of C2B binding, *J Mol Biol 387*, 284-294.

[61] Kuo, W., Herrick, D. Z., and Cafiso, D. S. (2011) Phosphatidylinositol 4,5-bisphosphate alters synaptotagmin 1 membrane docking and drives opposing bilayers closer together, *Biochemistry 50*, 2633-2641.

[62] Hirano, Y., Gao, Y. G., Stephenson, D. J., Vu, N. T., Malinina, L., Simanshu, D. K., Chalfant, C. E., Patel, D. J., and Brown, R. E. (2019) Structural basis of phosphatidylcholine recognition by the C2-domain of cytosolic phospholipase A2alpha, *Elife 8*.

[63] Honigmann, A., van den Bogaart, G., Iraheta, E., Risselada, H. J., Milovanovic, D., Mueller, V., Mullar, S., Diederichsen, U., Fasshauer, D., Grubmuller, H., Hell, S. W., Eggeling, C., Kuhnel, K., and Jahn, R. (2013) Phosphatidylinositol 4,5-bisphosphate clusters act as molecular beacons for vesicle recruitment, *Nat Struct Mol Biol 20*, 679-686.

[64] Guillen, J., Ferrer-Orta, C., Buxaderas, M., Perez-Sanchez, D., Guerrero-Valero, M., Luengo-Gil, G., Pous, J., Guerra, P., Gomez-Fernandez, J. C., Verdaguer, N., and Corbalan-Garcia, S. (2013) Structural insights into the Ca2+ and PI(4,5)P2 binding modes of the C2 domains of rabphilin 3A and synaptotagmin 1, *Proc Natl Acad Sci U S A 110*, 20503-20508.

[65] Czech, M. P. (2000) PIP2 and PIP3: complex roles at the cell surface, *Cell 100*, 603-606.

[66] Newton, A. C. (2018) Protein kinase C: perfectly balanced, *Crit Rev Biochem Mol Biol 53*, 208-230.

[67] Guerrero-Valero, M., Ferrer-Orta, C., Querol-Audi, J., Marin-Vicente, C., Fita, I., Gomez-Fernandez, J. C., Verdaguer, N., and Corbalan-Garcia, S. (2009) Structural

and mechanistic insights into the association of PKCalpha-C2 domain to PtdIns(4,5)P2, *Proc Natl Acad Sci U S A 106*, 6603-6607.

[68] van den Bogaart, G., Meyenberg, K., Diederichsen, U., and Jahn, R. (2012) Phosphatidylinositol 4,5-bisphosphate increases Ca2+ affinity of synaptotagmin-1 by 40-fold, *J Biol Chem 287*, 16447-16453.

[69] Morales, K. A., Lasagna, M., Gribenko, A. V., Yoon, Y., Reinhart, G. D., Lee, J. C., Cho, W., Li, P., and Igumenova, T. I. (2011) Pb2+ as modulator of protein-membrane interactions, *J Am Chem Soc 133*, 10599-10611.

[70] Ubach, J., Garcia, J., Nittler, M. P., Sudhof, T. C., and Rizo, J. (1999) Structure of the Janus-faced C2B domain of rabphilin, *Nat Cell Biol 1*, 106-112.

[71] Perisic, O., Fong, S., Lynch, D. E., Bycroft, M., and Williams, R. L. (1998) Crystal structure of a calcium-phospholipid binding domain from cytosolic phospholipase A2, *J Biol Chem 273*, 1596-1604.

[72] Arac, D., Chen, X., Khant, H. A., Ubach, J., Ludtke, S. J., Kikkawa, M., Johnson, A. E., Chiu, W., Sudhof, T. C., and Rizo, J. (2006) Close membrane-membrane proximity induced by Ca(2+)-dependent multivalent binding of synaptotagmin-1 to phospholipids, *Nat Struct Mol Biol 13*, 209-217.

[73] Seven, A. B., Brewer, K. D., Shi, L., Jiang, Q. X., and Rizo, J. (2013) Prevalent mechanism of membrane bridging by synaptotagmin-1, *Proc Natl Acad Sci U S A 110*, E3243-3252.

[74] Xue, M., Ma, C., Craig, T. K., Rosenmund, C., and Rizo, J. (2008) The Janus-faced nature of the C(2)B domain is fundamental for synaptotagmin-1 function, *Nat Struct Mol Biol 15*, 1160-1168.

[75] Zhou, Q., Lai, Y., Bacaj, T., Zhao, M., Lyubimov, A. Y., Uervirojnangkoorn, M., Zeldin, O. B., Brewster, A. S., Sauter, N. K., Cohen, A. E., Soltis, S. M., Alonso-Mori, R., Chollet, M., Lemke, H. T., Pfuetzner, R. A., Choi, U. B., Weis, W. I., Diao, J., Sudhof, T. C., and Brunger, A. T. (2015) Architecture of the synaptotagmin-SNARE machinery for neuronal exocytosis, *Nature 525*, 62-67.

[76] Ochoa, W. F., Garcia-Garcia, J., Fita, I., Corbalan-Garcia, S., Verdaguer, N., and Gomez-Fernandez, J. C. (2001) Structure of the C2 domain from novel protein kinase Cepsilon. A membrane binding model for Ca(2+)-independent C2 domains, *J Mol Biol 311*, 837-849.

[77] Murray, D., and Honig, B. (2002) Electrostatic control of the membrane targeting of C2 domains, *Mol Cell 9*, 145-154.

[78] Benes, C. H., Wu, N., Elia, A. E., Dharia, T., Cantley, L. C., and Soltoff, S. P. (2005) The C2 domain of PKCdelta is a phosphotyrosine binding domain, *Cell 121*, 271-280.

[79] Bhalla, A., Tucker, W. C., and Chapman, E. R. (2005) Synaptotagmin isoforms couple distinct ranges of Ca2+, Ba2+, and Sr2+ concentration to SNARE-mediated membrane fusion, *Mol Biol Cell 16*, 4755-4764.

[80] Shin, O. H., Rhee, J. S., Tang, J., Sugita, S., Rosenmund, C., and Sudhof, T. C. (2003) Sr2+ binding to the Ca2+ binding site of the synaptotagmin 1 C2B domain triggers fast exocytosis without stimulating SNARE interactions, *Neuron 37*, 99-108.

[81] Bouton, C. M., Frelin, L. P., Forde, C. E., Arnold Godwin, H., and Pevsner, J. (2001) Synaptotagmin I is a molecular target for lead, *J Neurochem 76*, 1724-1735.

[82] Morales, K. A., Yang, Y., Long, Z., Li, P., Taylor, A. B., Hart, P. J., and Igumenova, T. I. (2013) Cd2+ as a Ca2+ surrogate in protein-membrane interactions: isostructural but not isofunctional, *J Am Chem Soc 135*, 12980-12983.

[83] Katti, S., Her, B., Srivastava, A. K., Taylor, A. B., Lockless, S. W., and Igumenova, T. I. (2018) High affinity interactions of Pb(2+) with synaptotagmin I, *Metallomics 10*, 1211-1222.

[84] Jing, Z., Liu, C., Qi, R., and Ren, P. (2018) Many-body effect determines the selectivity for Ca(2+) and Mg(2+) in proteins, *Proc Natl Acad Sci U S A 115*, E7495-E7501.

[85] Katz, A. K., Glusker, J. P., Beebe, S. A., and Bock, C. W. (1996) Calcium Ion Coordination: A Comparison with That of Beryllium, Magnesium, and Zinc, *Journal of the American Chemical Society 118*, 5752-5763.

[86] Rulíšek, L. r., and Vondrášek, J. (1998) Coordination geometries of selected transition metal ions (Co2+, Ni2+, Cu2+, Zn2+, Cd2+, and Hg2+) in metalloproteins, *Journal of Inorganic Biochemistry 71*, 115-127.

[87] Kirberger, M., and Yang, J. J. (2008) Structural differences between Pb2+- and Ca2+-binding sites in proteins: implications with respect to toxicity, *J Inorg Biochem 102*, 1901-1909.

CHAPTER II DIFFERENTIAL DIACYLGLYCEROL SENSITIVITY AND NOVEL ANIONIC LIPID PREFERENCES OF PKCδ C1A DOMAIN REVEALED BY NMR

**Background**

Conventional PKC isoforms rely upon both C1 and C2 domains to achieve membrane localization and subsequent activation.[7] However, novel PKC isoforms like PKCδ do not possess the membrane-binding activity within their C2 domains, making C1 domains sole mediators of their membrane translocation.[88] PKCδ has two C1 domains arranged in tandem, C1A and C1B. The preliminary understanding of C1B-lipid and agonist interactions exists, but the properties of C1A with respect to these factors remain unclear.[16, 18, 27, 89] As far as the PKCδ activation is concerned, it is essential to understand the specific properties C1A domain might possess that can complement the C1B counterpart.

Unlike C1 domains of conventional PKC isoforms, C1A and C1B of PKCδ share the presence of Tryptophan (Trp, W) instead of Tyrosine (Tyr, Y) as the diacylglycerol toggle residue at their agonist/membrane-binding loops.[22] This residue is meant to enhance the diacylglycerol-sensitivity significantly.[22, 23, 89, 90] Whether such enhancement can actually be observed for C1A remains unclear. One report suggests based on ITC (Isothermal titration calorimetry) experiments that C1A shows high affinity towards diacylglycerol, while binding of C1B to the same was reported as not detectable.[27] However, the significant high affinity of C1B towards diacylglycerol reported by other

groups contradicts this ITC finding.[22, 89] It is therefore essential to revisit the diacylglycerol as well as phorbol ester dependence of C1A.

Finally, the differential arrangement of basic residues on C1A and C1B caught out attention (described in Chapter I). It is possible that the anionic lipid preferences of C1A might be different from other C1 domains, although no evidence to suggest that yet exists. This chapter describes our experimental work addressing some of these open questions associated with C1A domain of PKCδ.

## Experimental procedures

### Design of C1Aδ constructs for crystallization and NMR experiments

The DNA segment coding for the murine C1Aδ (residues 158-208) was cloned into the pET SUMO vector as a fusion partner to 6xHis-SUMO solubility tag. Four variations were prepared of this construct: 1. With additional non-native flanking sequences encoding N- and C-terminal β-strand extensions. This construct was used for crystallization purposes. 2. With additional native flanking sequences at N (residues 149-157) and C (residues 209-218) terminal to improve the solubility further. This construct referred to henceforth as "C1A71" was used for all NMR experiments, unless specified otherwise. 3. Inclusion of the native linker and C1B counterpart at the C-terminal (residues 209-285). This construct referred to as "C1A$_{short}$B" was used for NMR when applicable. 4. The inclusion of the remaining native linker and C1B counterpart to the C-terminal of C1A71 (residues 219-285). This construct referred to as "C1A71-C1B" was also used for NMR.

### Expression and purification of C1Aδ constructs

The constructs encoding the aforementioned C1Aδ variants were transformed into the *E. coli* BL21(DE3) cells. The cells were grown at 37 $^0$C under Kanamycin (Sigma-Aldrich) selection in LB until the optical density at 600 nm wavelength reached 0.6. For natural abundance preparations that do not require isotopic labelling (for crystallization), the cells were induced with 0.5 mM Isopropyl β-D-1-thiogalactopyranoside (Fisher Bioreagents) for 16 hrs at 18 $^0$C. The harvested cell pellets post-induction were stored at -20 $^0$C until lysis.

For isotopically labelled preparations, four cultures grown in LB (1 L each) were harvested, washed, and re-suspended into the 1L M9 minimal media supplemented with isotopic components: 1 g/L of ammonium chloride ($^{15}$N, 99%) (Cambridge Isotopes) and 2 g/L d-glucose ($^{13}$C, 99%) (Cambridge Isotopes) to achieve U-$^{13}$C,$^{15}$N labelling. For U-$^{15}$N labelling scheme, the glucose was natural abundance ($^{12}$C, 3 g/L). After equilibration for 1 hr at 18 $^0$C, the cells were induced with 0.5 mM Isopropyl β-D-1-thiogalactopyranoside (Fisher Bioreagents) for 16 hrs. The harvested cell pellets post-induction were stored at -20 $^0$C until lysis.

To purify these constructs, the cells were lysed using B-PER™ lysis reagent (Thermo-Scientific) and the clarified lysates were loaded onto the HisTrap HP Ni affinity column (GE Healthcare Life Sciences). The protein was eluted with Imidazole gradient, and cleaved with SUMO protease at room temperature for 2 hrs to remove the 6xHIS-SUMO tag. The cleaved protein was then collected as a flowthrough of HisTrap HP Ni affinity column, and concentrated. All constructs with the exception of the β-

extension C1A had no detectable impurities retained after these steps. This final purified

protein was exchanged into 20 mM [D-4]-Imidazole buffer at pH 6.5 (Cambridge

Isotopes), 150 mM KCl, 8% $D_2O$, 1 mM tris(2-carboxyethyl) phosphine (TCEP), and

0.02% $NaN_3$. This buffer was used for all NMR experiments described in this chapter.

Prior to crystallization setup of the natural abundance β-extension construct, additional

cation exchange step was performed (HiTrap SP HP) to further purify it. The eluted

protein was concentrated and used for crystallization.

<u>C1Aδ crystallization, structure determination and refinement</u>

Automated screening for crystallization was carried out using the sitting drop

vapour-diffusion method with an Art Robbins Instruments Phoenix system in the

UTHSCSA X-ray Crystallography Core Laboratory.  Initial crystals were obtained from

the Qiagen pHClear II Suite in 30% isopropanol and 0.1 M Tris, pH 8 at 22ºC followed

by optimization in 20% isopropanol, 10% ethylene glycol and 0.1 M Tris, pH 8.0 using

an Art Robbins Instruments Scorpion. Crystals were transferred to undersized cryo-loops

and manipulated to wick off excess mother liquor prior to flash-cooling in liquid

nitrogen.  X-ray diffraction data were acquired using a home source Rigaku MicroMax

007HF X-ray Generator equipped with VariMax HR confocal optics and RAXIS-HTC

image plate detectors.  Initial crystals diffracted to ~1.6 Å resolution but a molecular

replacement solution was not obtained as expected using search models available from

the Protein Data Bank. Therefore, highly redundant, high resolution data were collected

for an optimized crystal in three sweeps with adjustments to the detector *2θ* angle

between 0° and 18.5° with the intention of generating phase information from the zinc

and native sulfur atom positions. Data were integrated and scaled to 1.30 Å using XDS.[91] The structure of β-extension C1Aδ was determined with the single wavelength anomalous diffraction (SAD) method[92, 93] using the HKL2MAP graphical user interface for SHELX programs.[94]  Nine heavy atom sites were located and refined using direct methods in *SHELXD* [95] for positions later identified as six cysteine sulfur atoms, two zinc ions and a chloride ion.  SHELXE density modification and autotracing[96] produced a polypeptide backbone model used for completing the model sequence by addition of amino acid side chains with COOT.[97] Model coordinates were refined using PHENIX[98] including simulated annealing with torsion angle dynamics, anisotropic B-factor refinement and bulk solvent mask optimization.  Additional data were acquired to 0.85 Å resolution for an additional crystal at NE-CAT beamline 24-ID-C at the Advanced Photon Source (Argonne, IL). The SAD structure was further refined against the high-resolution data with hydrogens added in riding positions.  Data collection and refinement statistics for the 0.85 Å resolution structural model are shown in the **Table II.1**.

<u>Preparation of micelles</u>

$d_{38}$-Dodecylphosphocholine ($d_{38}$-DPC, Sigma-Aldrich) and 1,2-dihexanoyl-sn-glycero-3-phospho-L-serine (DPC, Avanti Polar lipids) were aliquoted from the chloroform stocks, dried extensively and mixed to achieve the molar ratio DPC:DPS 70:30 by resuspending into the NMR buffer mentioned above. The resulting mixture was rigorously vortexed to lead the formation of mixed micelles. The stocks prepared in such manner were stored at 4 $^0$C for less than 2 days. All C1A-micelle samples used for NMR experiments had total lipid concentration of 10 mM and C1A concentration of 100 μM.

Addition of DOG (di-octanoyl sn-1,2 glycerol, Avanti Polar lipids) and PDBu (phorbol 12,13-dibutyrate, Sigma-Aldrich) to micellar samples was done from their $d_6$-DMSO stocks.

<div align="center">NMR spectroscopy</div>

Unless specified otherwise, all NMR experiments were acquired at 298.15 K, calibrated using the deuterated Methanol. NMR data were processed with NMRPipe[99] and analyzed with Sparky.[100] Backbone amide assignments of C1A constructs were done by acquiring the 3D CBCA(CO)NH and HNCACB experiments on Bruker AVANCE III instrument operating at a $^1$H Larmor frequency of 600 MHz (equipped with cryogenically cooled probe) using samples of 0.5 mM concentration, U-$^{13}$C,$^{15}$N labelling scheme.

For agonist-binding experiments, U-$^{15}$N labelled C1A was mixed with micelles. For di-C4 PIP$_2$ binding experiments, the U-$^{13}$C,$^{15}$N labelled C1A was used with the exclusion of micelles. The $^{15}$N-$^1$H HSQC (Heteronuclear single quantum coherence) spectra were collected at each addition of micelles/agonists (Bruker AVANCE III instrument operating at a $^1$H Larmor frequency of 500 MHz, equipped with room-temperature probe) or diC4 PIP$_2$ (Bruker AVANCE Neo instrument operating at a $^1$H Larmor frequency of 600 MHz, equipped with cryogenically cooled probe). The combined chemical shift perturbations (CSPs, $\Delta$) were calculated using the expression:

$$\Delta = [\,\Delta\delta_H^2 + (0.152\Delta\delta_N)^2\,]^{1/2}$$

Where $\delta_H$ and $\delta_N$ are $^1H$ and $^{15}N$ chemical shift differences for a given resonance in the two spectra that are being compared.

The dissociation constant ($K_d$) value for C1A-di-C4 PIP$_2$ interaction was estimated using the expression for the single-site binding model:

$$\Delta = (\Delta_{max} / 2P_0)[(K_d + P_0 + L_0)$$
$$-((K_d + P_0 + L_0)^2 - 4P_0L_0)^{1/2}]$$

Where $\Delta_{max}$ is the maximum perturbation, and $P_0$ and $L_0$ are the total protein and di-C4-PIP$_2$ concentrations, respectively.

$^{15}N$-edited NOESY experiment on U-$^{13}C$,$^{15}N$ C1A71-C1B was acquired with Bruker AVANCE III instrument operating at a $^1H$ Larmor frequency of 600 MHz (equipped with cryogenically cooled probe) the mixing time of 150 ms.

The $^{15}N$ $R_2$ values (transverse relaxation rate constants) were measured on the Varian instrument operating at a $^1H$ Larmor frequency of 600 MHz (equipped with cryogenically cooled probe). U-$^{15}N$ labelled C1A with concentration of 0.3 mM was used. The site-specific $R_{2,CPMG}$ values [101] were extracted from fitting the $^{15}N$-$^1H_N$ cross-peak intensity changes at seven unique and three replicate relaxation points ranging from 8 to 200 ms. The free-precession $R_{2,HE}$ values [102] were measured with the Hahn-Echo delay set to 68 ms. The datasets were collected in the interleaved manner.

## Results and Discussion

Crystal structure of C1Aδ reveals occluded intra-loop region with limited solvent accessibility

In order to get structural insight into the agonist-binding loop region, we decided to obtain high-resolution crystal structure of C1Aδ. Limited success associated with crystallization of C1 domains posed a possible hindrance. To overcome that, we employed a strategy that involves the inclusion of stabilizing β-strand extensions to both N- and C-terminal ends of the domain (**Figure II.1A**). This strategy has been successful in crystallizing the non-identical twin of C1A, the C1B domain of PKCδ.[103] The speculation behind this approach was that the N- and C-terminal strands of a given protein molecule will converge to form a β-sheet, stabilizing the otherwise flexible ends.

We were successfully able to obtain a structure with excellent resolution of 0.85 Å (statistics shows in **Table II.1**). The structure showed a typical C1 domain architecture of the $Zn^{2+}$ finger but to our surprise, the N- and C-terminal β strands engineered to form a stabilizing anti-parallel interaction were instead observed in a domain swap (**Figure II.1B**). In this arrangement, one of the two $Zn^{2+}$ ions required for the fold were coordinated by 3 intra-domain ligands, and 1 inter-domain ligand (**Figure II.1B, inset**). Furthermore, each two-stranded anti-parallel β-sheet combined with a neighboring domain-swapped β sheet to form a stabilizing four-stranded, anti-parallel crystal packing contact.

**(A)** $\beta_{N-term}$   C1A$\delta$   $\beta_{C-term}$

SGS**RRASV**GS**NHEFIATFFGQPTFCSVCKEFVWGLNKQGYKCRQCNAAIHKKCIDKIIGRCEFIVT**D
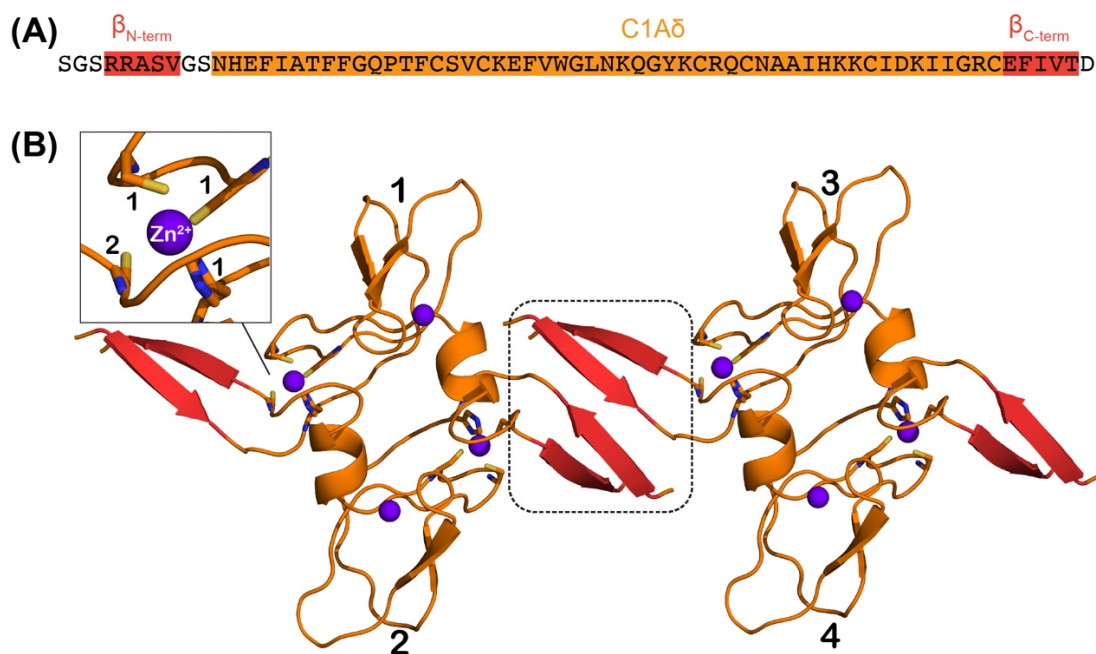
**Figure II.1 Crystal structure of C1A$\delta$ was successfully obtained using the engineered β-strand extensions**
(A) Primary sequence of the construct used for the crystallization trials (B) Packing contacts of the C1A structure that include domain-swapped arrangement within 4 units and β-sheet formation (dashed square). Inset: The coordination of one of the two structural $Zn^{2+}$ ions involves a Cys residue from the adjacent unit.

Using this structure in combination with the available NMR ensemble of the C1A domain (2YUU), we decided to take a closer look at the agonist-binding region (**Figure II.2**). The distinct "flipped in" orientation of the diacylglycerol (DAG) toggle residue W180 stood out (**Figure II.2A**). To our knowledge, in PKC C1 domains, this is the very first occurrence of the toggle residue sampling a stable orientation that occludes the agonist-binding cavity.[16] The only other case of this orientation is reported in the Munc13 C1 domain, which shows weaker DAG-dependence.[26] This comparison compelled us to revisit the DAG sensitivity of C1A domain, presented in later sections of this chapter.

49

**Table II.1 X-ray diffraction data collection and refinement statistics for C1Aδ**

| PDB Code | NA |
|---|---|
| **Data collection** | |
| X-ray source | Advanced Photon Source 24-ID-C |
| Space group | *P*2 |
| Cell dimensions | |
| *a, b, c* (Å) | 34.2, 23.8, 39.6 |
| α, β, γ, (°) | 90, 113.0, 80 |
| Wavelength (Å) | 0.72930 |
| Resolution (Å) | 36.44-0.85 |
| | (0.86-0.85) |
| $R_{meas}$ | 0.061 (2.08) |
| $R_{pim}$ | 0.023 (0.843) |
| Mean $I/\sigma I$ | 14.6 (0.8) |
| Completeness (%) | 99.0 (93.6) |
| Redundancy | 6.6 (5.8) |
| Wilson value (Å$^2$) | 9.10 |
| | |
| **Refinement** | |
| Resolution (Å) | 36.44-0.85 |
| No. reflections | 51,500 |
| $R_{work}/R_{free}$ | 0.127/0.140 |
| No. atoms | |
| Protein | 638 |
| Hetero atoms | 11 (2 Zn$^{2+}$, 1 Cl$^-$,1 isopropanol, 1 ethylene glycol) |
| Water | 81 |
| B-factors (Å$^2$) | |
| Protein | 13.2 |
| Hetero atoms | 19.6 |
| Water | 28.1 |
| R.m.s deviations | |
| Bond lengths (Å) | 0.007 |
| Bond angles (°) | 1.080 |
| Ramachandran Plot | |
| Favored (%) | 96.8 |
| Allowed (%) | 3.2 |
| Outliers (%) | 0.0 |

*Highest resolution shell is shown in parentheses.

Surface analysis of the intra-loop region further showed W180-P169 stack completely blocking the relatively hydrophilic portion of the pocket (**Figure II.2B**). The only pocket available for potential agonist interactions is therefore narrow and partially hindered by F165 from the opposite end. For the entire intra-loop region of C1A, the analysis of the first and second bonded-hydration layers revealed only a single water molecule, reflecting the limited solvent accessibility of this region (**Figure II.3A**). This finding was intriguing as the counterpart C1B domain has abundantly hydrated intra-loop region, with the solvent network that is believed to play important role in stabilizing the agonist interactions (**Figure II.3A**).[103] We posited based on this comparison that the ability of C1A to interact with agonists like DAG, that potentially require extensive H-bonding to stabilize,[36] might be compromised. On the other hand, significant solvation was observed outside the agonist-binding region of C1A indicating that these regions could serve as sites for putative agonist/ligand interactions (**Figure II.3B**).
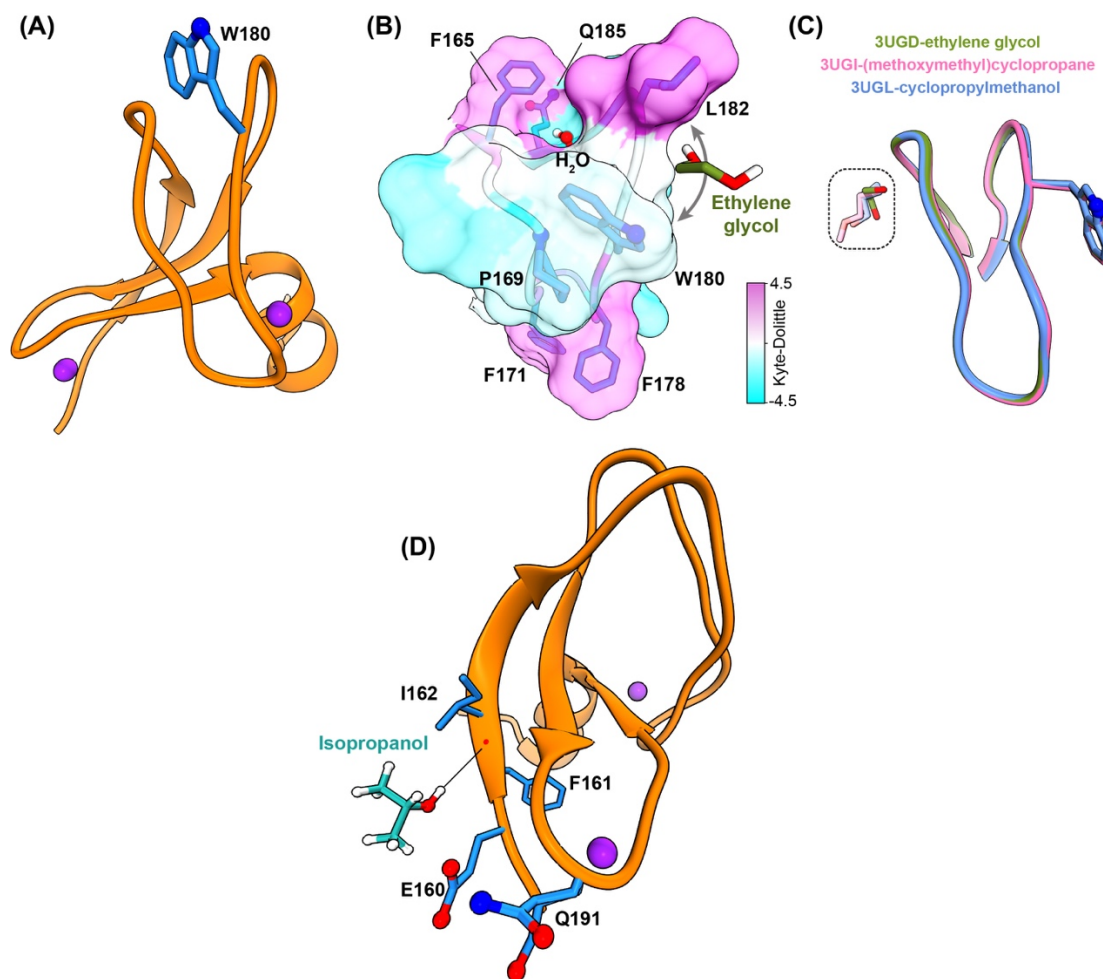
**Figure II.2 Distinct structural features of C1A**

(A) The occluding orientation of the toggle residue W180 is shown (B) The surface representation of the agonist-binding loop region colored using the Kyte-Dolittle scale. The intra-loop space is occluded by the W180-P169 stacking and F165. The resulting limited solvent accessibility of the region is evident by the presence of only 1 solvent molecule. The additive, ethylene glycol is seen stabilized against L182 and W180 (C) The anesthetic binding sites on C1B counterpart, shared by ethylene glycol are shown for comparison to indicate the possibility that ethylene glycol binding site on C1A (shown in B) can potentially bind anesthetics (D) The binding site of another additive, isopropanol at E160 supports the notion that this is a putative alcohol binding site. Solid line represents H-bond.

We also realized that the crystallization screen had two potentially informative additives: ethylene glycol and isopropanol. The former caught out attention as it seems to be interacting with C1A in our structure at the region flanked by W180 and L182 (**Figure II.2B**). It has been demonstrated that diol lipids like di-octanoyl ethylene glycol can activate PKC, but the mode by which this happens is unknown.[104] Given the general similarity in the structural features of diol lipids with DAG (which is a triol lipid), it is reasonable assumption that C1 domains might possess diol-sensitivity. We plan to explore this possibility in the future in the context of C1A, given the observation of C1A-ethylene glycol complex.

The ethylene glycol interaction site is further informative in the context of C1-anesthetic interactions. PKC is a putative target of general anesthetics and it is believed to occur via C1 domains.[103, 105] In case of C1B, ethylene glycol is seen to structurally occupy the same site as some of these anesthetic molecules (**Figure II.2C**).[103] Therefore, we speculate that the ethylene glycol interaction site seen on C1A could in fact be a putative anesthetic-binding site. We will explore this possibility in near future.

In addition to ethylene glycol, the interaction of the second crystallization screen additive, isopropanol was analyzed in the context of PKC-alcohol interactions. Alcohol, for instance ethanol, shows isoform-specific effects on PKC that link the altered kinase activation to alcohol consumption.[106, 107] The interaction sites of alcohols are identified on C1 domains of various PKCs. For C1A domain, although no structural information exists, it is reported that a site occurs in the vicinity of E160.[106] In our structure, we see an isopropanol (isopropyl alcohol) molecule interacting at this predicted site, potentially

providing direct structural evidence for the interaction (**Figure II.2D**). Whether such interaction with other alcohols persists in solution state will be explored in the future.
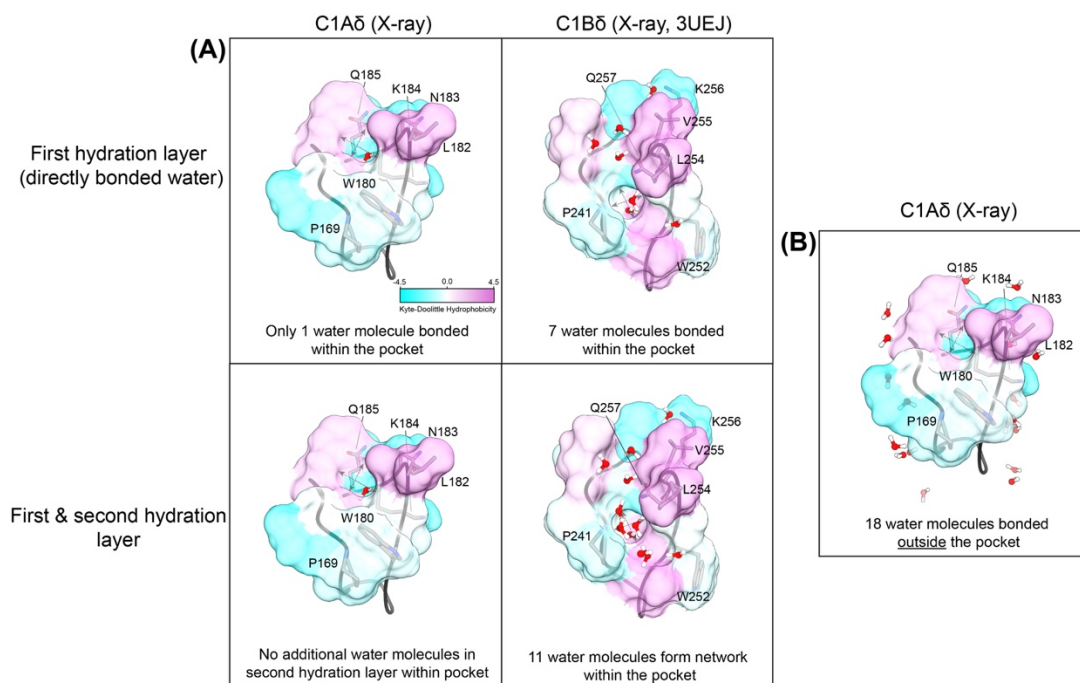


**Figure II.3 Agonist-binding region of C1Aδ shows limited solvent accessibility** (A) The first and second bonded-hydration layers of C1A and C1B are depicted (B) The region of C1A outside the agonist-binding loops is hydrated.

In conclusion, the structural analysis of C1A established that the agonist-binding region of this domain is significantly occluded due to the inward orientation of W180. Although such occlusion might limit solvent or agonist accessibility, it is in fact possible that the distinct orientation of the bulky indole ring of W180 might serve as a "pseudo-agonist", allowing the domain to interact with membranes in the absence of agonists. We also identified putative interaction sites for diol-lipids, anesthetics and alcohols on C1A, prompting further analysis.

## NMR studies on C1Aδ reveal agonist-independent micelle association

After obtaining structural information based on the crystallographic model, we decided next to see how C1A behaves in the solution state using NMR. First step towards that was to test if the domain can be optimized to achieve sufficient stability and solubility, a requisite for obtaining high-quality NMR data. We created two variants of C1A: first with the minimal folded core of 51 residues and the second one with the additional endogenous residues at both ends (**Figure II.4A**). During the initial tests, it was apparent that the later had substantially better solution state behavior. Subsequent NMR experiments were therefore conducted using this variant, henceforth referred to as C1Aδ71. A further inclusion of C1B counterpart at the C-terminal resulted in the two domain C1Aδ71-C1B tandem construct, which is also used for comparisons wherever relevant.

The $^{15}$N-$^1$H HSQC spectrum acquired on C1Aδ71 showed a well-dispersed distribution of resonances, ensuring the intact fold (**Figure II.4B**). Notably, the NMR experiments conducted to assign the residue identities to the detectable amide resonances revealed that all non-proline agonist-binding loop residues except V179 were detectable and showed single resonance per residue. This is in contrast with the C1B counterpart, where most loop region residues are broadened due to chemical exchange in the absence of agonists (discussed in the next chapter). This observation suggested that C1A agonist-binding region is comparatively less dynamic.

Next, we compared the $^{15}$N-$^1$H HSQC spectra of C1Aδ71-C1B and C1Aδ71 (**Figure II.4C**). The overlay shows near identical match between the relevant

resonances. This observation suggests that there are no interactions between C1A and C1B domains, and C1Aδ71 behaves in solution as an independent unit. We further conducted a $^{15}$N-edited NOESY experiment on C1Aδ71-C1B and looked at the strips relevant to the W180 (C1A) and W252 (C1B) side-chain resonances. Cross-peaks observed in this experiment (called NOEs) help identify nuclei that are spatially close to one another. In this case, the purpose was to check whether we could detect any NOEs for W180 side chain that would provide the evidence for its spatial proximity to the intra-loop region observed in our crystal structure (**Figure II.2A**). Indeed, we observed additional NOE cross-peaks for W180 that were consistent with the chemical shifts of the protons from P169 (**Figure II.4D**).[108] Such NOEs were not observed for W252 (C1B), indicating in C1B, the toggle residue does not stably sample the orientation similar to the one observed in our crystal structure for C1A (**Figure II.2A**).
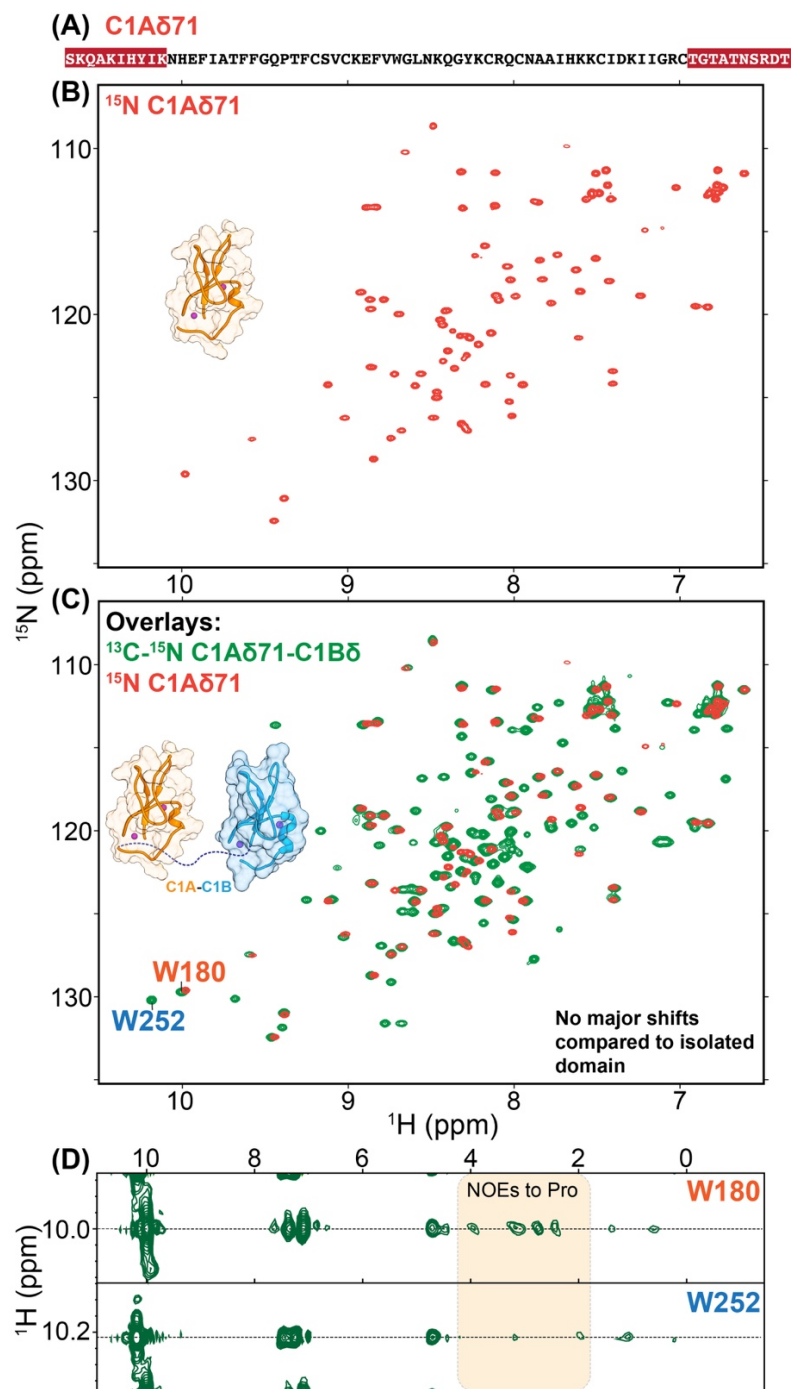
**Figure II.4 C1A is amenable to NMR studies**
(A) The $^{15}N$-$^{1}H$ HSQC spectrum of 0.3 mM C1A (U-$^{15}N$) is shown to demonstrated well-dispersed distribution of resonances, representative of the well-folded core (B) The $^{15}N$-$^{1}H$ HSQC spectral overlay of 0.3 mM C1A (U-$^{15}N$) and 0.3 mM C1A71-C1B (U-

$^{15}$N, $^{13}$C) (C) The $^{15}$N-edited NOESY strips of the toggle residues (W180, C1A and W252, C1B), showing NOEs consistent with their differential orientation.

After establishing that W180 can form stacking interaction with P169 in the solution state, we tested whether C1A can interact with mimics of lipidic environment in the absence of agonists.  We hypothesized that the distinct indole ring orientation (of W180) should allow the domain to insert into the membrane effectively, as Trp is capable of potent interactions with PtdCho head group (cation-π), phosphate region, glycerol backbone, as well as acyl chains.[109]  Consistent with our hypothesis, addition of micelles containing PtdCho/PtdSer-mimicking components (DPC:DPS 70:30) resulted in significant chemical shift perturbations (CSPs, Δ) suggesting interaction (**Figure II.5A**). The perturbations were dominant at the agonist-binding loops indicating insertion/peripheral association of this region with the micelles (**Figure II.5B**).  The poly-basic helix in conjunction with the adjacent β-strand were also perturbed, indicating putative electrostatic interactions of this region with the anionic DPS component.  Although these findings clearly support our hypothesis, future experiments will be conducted using bilayer-containing membrane mimetics such as bicelles and liposomes for additional verification.
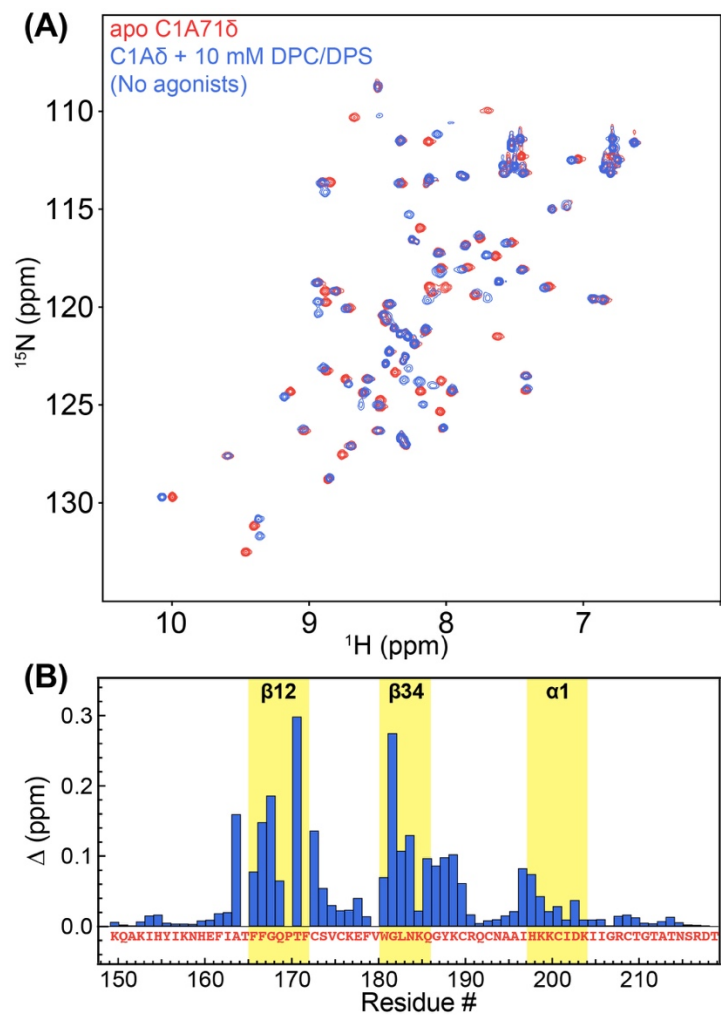
**Figure II.5 C1A can interact with micelles in the absence of agonists**
(A) The $^{15}$N-$^1$H HSQC spectral overlay of 0.1 mM C1A (U-$^{15}$N) with and without
DPC:DPS (70:30) micelles (B) The combined chemical shift perturbations (Δ) are
plotted as a function of primary sequence. The regions of interest with major
perturbations are highlighted.

## C1Aδ shows remarkably weak diacylglycerol dependence but sensitive to phorbol esters

In light of our findings that demonstrated agonist-free interactions of C1A with micelles, we explored the dependence of this interaction on the endogenous agonist diacylglycerol using the di-octanoyl sn-1,2 diacylglycerol (DOG). We acquired a series of $^{15}N$-$^1H$ HSQC spectra, with progressive increase in the concentration of DOG in the presence of DPC:DPS (70:30) micelles (**Figure II.6A**). The CSPs resulting from the DOG-dependent enhancement of C1A-micelle interactions (in the "fast" regime on chemical shift timescale) were plotted as a function of DOG concentration (**Figure II.6A, inset**). The apparent dissociation constant for this interaction was ~840 μM. In comparison, for the identical experiment, C1B counterpart shows the apparent dissociation constant of < 0.2 μM.[89] The CSPs were predominantly localized to the agonist-binding loops (**Figure II.6B**). The remarkably weak intrinsic DOG dependence of C1A was in fact consistent with our prediction based on the structural analysis. It can be attributed to the occlusion of the agonist-binding region by W180 and the limited solvent accessibility.

To our knowledge, such a weak DAG-dependence in typical (DAG/phorbol ester sensitive) C1 domains of PKC is unprecedented. The presence of Trp as the toggle residue is associated with the high DAG sensitivity.[22] We show here that it is in fact, the orientation of the toggle residue with respect to the agonist-binding region that further modulates DAG sensitivity. Given the fact that DAGs do not possess any headgroups, the interactions with C1 domains are believed to be mediated by the hydrogen bonds formed between glycerol backbone and the protein residues.[36] This makes readily

60

accessible agonist-binding region an essential factor.  Furthermore, it is likely that initial

"anchoring" of DAGs to the C1 domains is mediated by the ordered solvent molecules

of the intra-loop space. In case of C1A, since both of these factors are not fulfilled,

weaker intrinsic DAG dependence is observed.

We want to point out that the results reported above are probing DAGs strictly in

the context of directly interacting agonists. As discussed briefly in Chapter I, micro-

domains of concentrated DAG also induce membrane-altering effects including

distortions and formation of inverted hexagonal phases.[28]  These effects are DAG

concentration dependent and will not faithfully manifest (if at all) in non-bilayer forming

mimics of the lipidic environment such as micelles.  This factor is essential to consider

as these membrane distortions could allow the protein easier access to the hydrophobic

acyl chain region, enabling C1A to interact with membranes more effectively.  This

mechanistic model might be applicable to certain C1 domains like C1A that may not

possess intrinsic sensitivity towards DAGs as agonists.  For C1B on the other hand, this

model can serve as an additional contributory factor.  We will test this model in the

future in the context of C1A using bilayer membrane mimics, isotropically-tumbling

bicelles and liposomes.
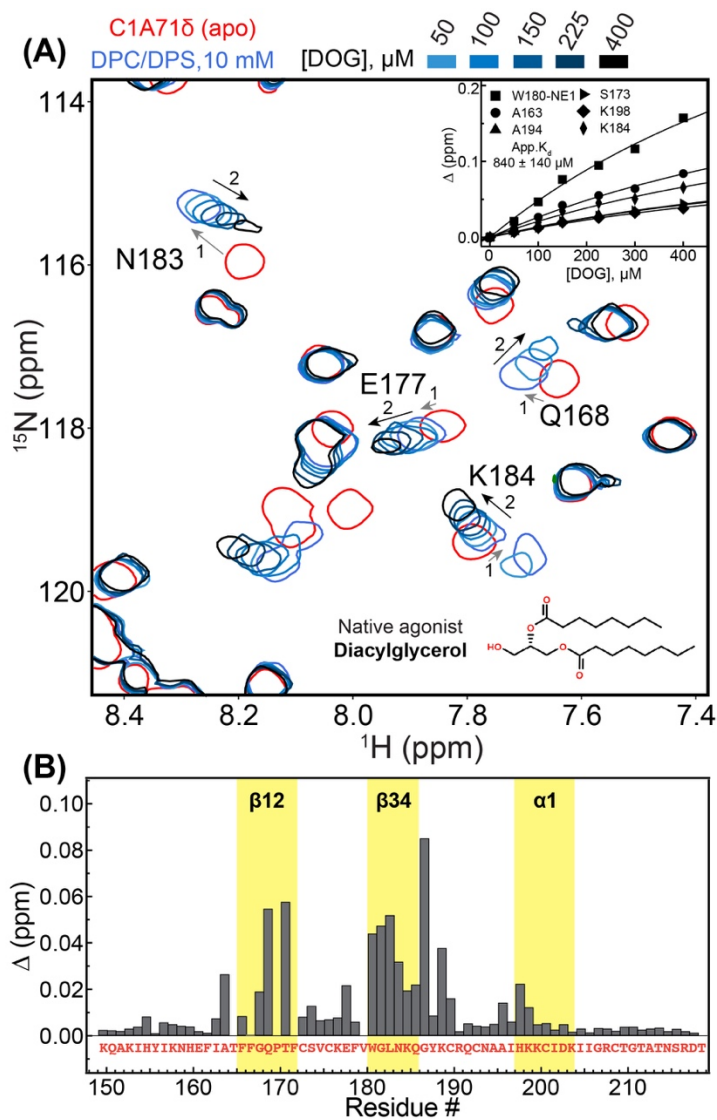
**Figure II.6 Weak diacylglycerol dependence is observed for C1A**
(A) The $^{15}N$-$^1H$ HSQC spectral overlay of 0.1 mM C1A (U-$^{15}N$), with DPC:DPS (70:30) micelles, at each successive concentration of DOG. Select residues in "fast" exchange are labelled. Inset: The binding curves for select residues. The global fit resulted in the estimated $K_d$ of 840 μM (B) The combined chemical shift perturbations (Δ) are plotted as a function of primary sequence. These represent the difference between C1A-DPC:DPS complex and C1A-DPC:DPS with stoichiometric DOG (0.l mM). The regions of interest with major perturbations are highlighted.

Although DAGs may not possess the ability to displace the blocking W180 side chain form the intra-loop space, there is a possibility that more bulky agonists with groups structurally comparable to Trp could achieve this. Phorbol esters, the tumor-promoting agents that bind to C1 domains have the phorbol groups that possess the hydroxyls capable of hydrogen-bonding with protein residues in addition to "ringed" framework akin to the Trp indole ring.[18] As a result, we hypothesized that phorbol esters might in fact be able to displace W180, and embed into the agonist-binding region. To test this hypothesis, we added half- and one-stoichiometric concentrations of phorbol 12,13-dibutyrate (PDBu) to C1A-DPC/DPS micelle complex and observed for the signatures of binding by acquiring $^{15}$N-$^{1}$H HSQC spectra (**Figure II.7**).

Consistent with our hypothesis, we observed clear CSPs upon PDBu addition that were in "slow" regime on the chemical shift timescale (**Figure II.7A**). At stoichiometric PDBu concentration, the resonances representing the PDBu-free state were nearly broadened beyond detection, suggesting population shift to the PDBu-saturated state (**Figure II.7B**). These apparent signatures of PDBu dependent C1A-micelle association suggest that bulky phorbol group is capable of displacing W180 from the occluding position in the agonist-binding region.

Taken together, these findings shed light on the agonist-preferences of C1A domain of PKCδ, and the underlying factors responsible for these preferences. We propose the conformational sampling of the toggle residues with respect to agonist-binding region as an additional layer of control over DAG sensitivity of C1 domains. We also suggest that the C1-effector function of DAG might involve its role as a directly

interacting agonist for certain C1 domains, while as a modulator of membrane properties

that indirectly enhances membrane interactions for domains like C1A.
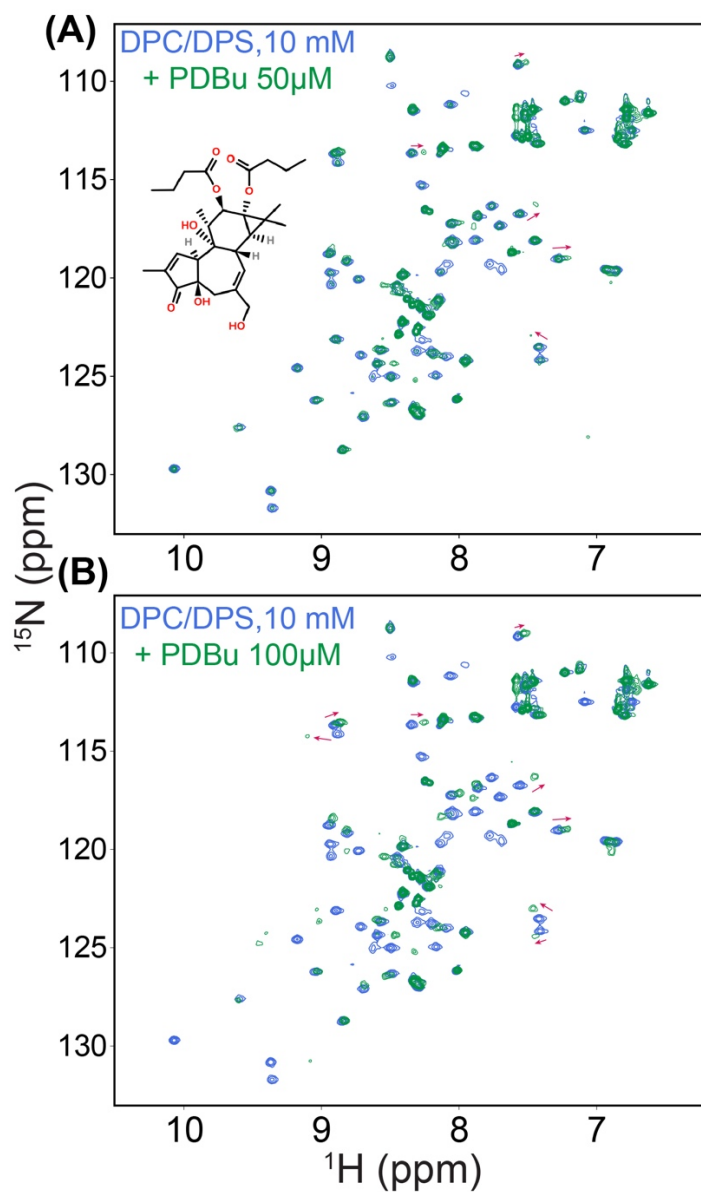


**Figure II.7 C1A can interact with phorbol esters**
(A) and (B) The $^{15}$N-$^1$H HSQC spectral overlay of 0.1 mM C1A (U-$^{15}$N) with DPC:DPS (70:30) micelles at half and one-stoichiometric concentration point of phorbol ester, PDBu respectively

## C1Aδ is capable of PtdIns(4,5)P$_2$ interactions

Our next objective was to determine whether C1A domain is capable of interactions with poly-anionic lipids such as PtdIns(4,5)P$_2$.  Nearly all C1 domains can bind PtdSer to a variable degree,[16] a key anionic lipid component of the membranes. However to our knowledge, none of the C1 domains are reported to bind PtdIns(4,5)P$_2$. This is likely because an uninterrupted, contiguous arrangement of basic residues is typically required for PtdIns(4,5)P$_2$ sensitivity.[64]  In other C1 domains, C1B for instance, the arrangement of basic residues around the PtdSer-binding region is not contiguous (**Figure I.3A**).[18]  However, for C1A the electrostatic surface potential is highly basic (positive) around the analogous region, attributed to spatially clustered arrangement of 5 Lys residues (**Figure I.3B**).  Such architecture is often seen in bonafide PtdIns(4,5)P$_2$-sensors like C2B domain of Synaptotagmin 1(**Figure I.9B**).[64] Furthermore, since the C2 domain of PKCδ is incapable of Ca$^{2+}$-dependent interactions with anionic membranes,[88] it is compelling to speculate that this activity is adopted by one of the C1 domains. Based on these arguments, we hypothesized that C1A domain might show intrinsic affinity for PtdIns(4,5)P$_2$, allowing the translocation of PKCδ to the plasma membranes where this second messenger is localized.

We tested this hypothesis by progressively adding diC4-PIP$_2$, a soluble analog of PtdIns(4,5)P$_2$ to C1A domain and observing the interaction by collecting a series of $^{15}$N-$^1$H HSQC spectra (**Figure II.8**).  The use of this soluble variant allowed us to probe the affinity of C1A towards PtdIns(4,5)P$_2$ exclusively, without the presence of membrane mimics.  Distinct chemical shift perturbations resulted from this addition (**Figure II.8A**).

The perturbations were within the "fast" regime on the chemical shift timescale (**Figure II.8B**), allowing us to plot the changes as a function of diC4-PIP$_2$ concentration (**Figure II.8C**).  The estimated affinity obtained for this interaction was 198 μM.  In comparison, Syt1 C2B domain, a canonical PtdIns(4,5)P$_2$ sensor showed the affinity of 215 μM during identical experiment (see chapter V).  Although these affinities might appear weak, note that these values are severe underestimates due to the absence of membranes.  At membranes, where PtdIns(4,5)P$_2$ can occur in concentrated micro-domains,[110, 111] the affinity will be much greater given the fact that C1A can intrinsically interact with lipidic moieties.

To obtain the idea of where this putative PtdIns(4,5)P$_2$ binding region is located, we plotted the perturbations as a function of primary sequence (**Figure II.8D**).  Although the residues with significant perturbations appear randomly distributed, mapping these changes on the lowest energy NMR conformer of C1Aδ71 revealed a distinct region (**Figure II.8E**).  To our surprise, in addition to the poly-basic region that we predicted on the folded core of C1A, significant perturbations were also observed in the N-terminal native extension (K152, I153).  Even though this region is typically not considered a part of the minimal folded core of C1A, the β-stand formed by this region appears to stabilize against the folded core in the NMR conformers.  It is possible that in the native full-length regulatory segment where C2-C1A-C1B are on same polypeptide chain, such interaction of C1A-N-terminal extension with the core persists, allowing further support for PtdIns(4,5)P$_2$ binding.
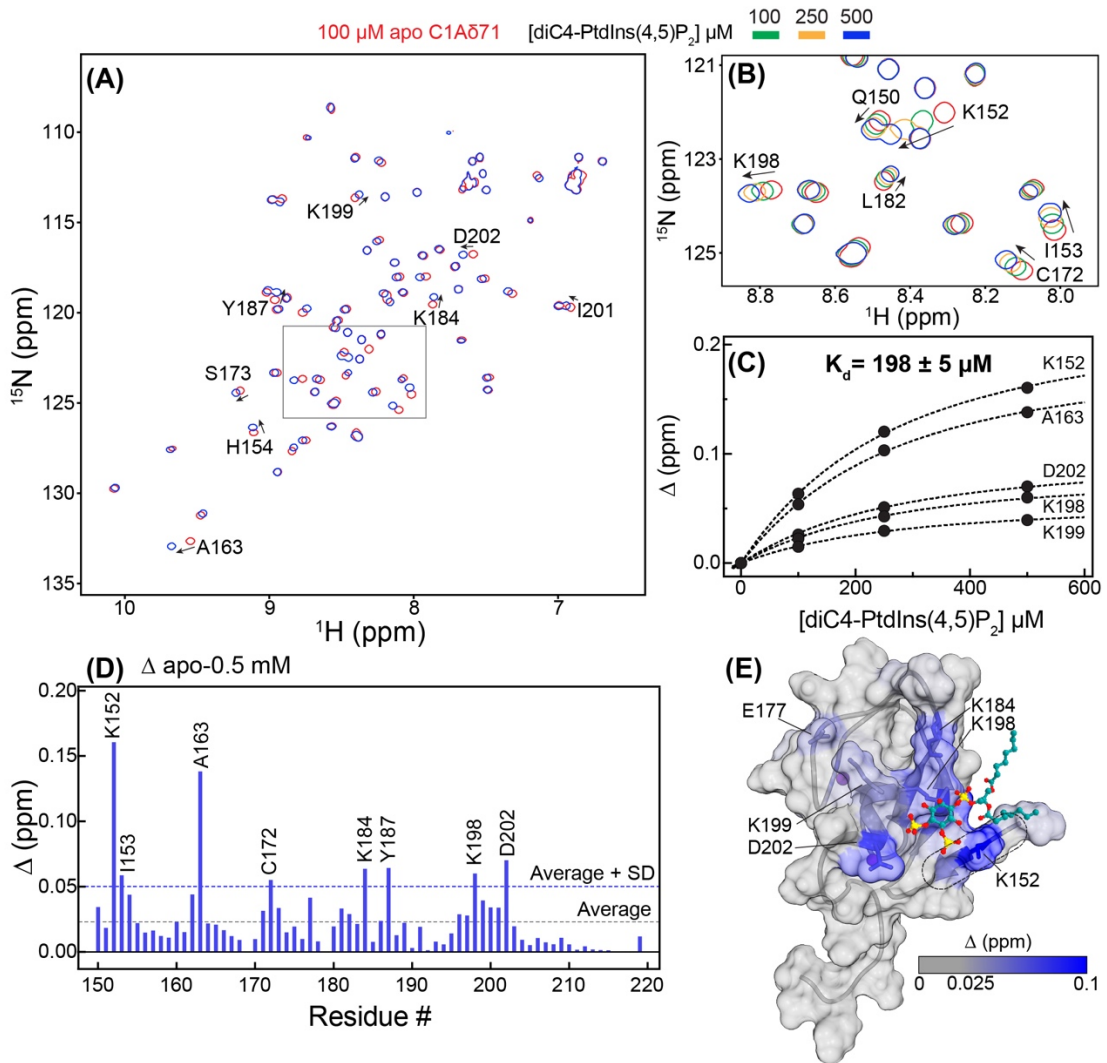
**Figure II.8 C1A is sensitive to PtdIns(4,5)P₂**

(A) The $^{15}N$-$^1H$ HSQC spectral overlay of 0.1 mM C1A (U-$^{15}N$,$^{13}C$), with 0.5 mM di-C4 PIP₂ (B) The expansion of the squared region from panel (A), depicting additional concentration points of di-C4 PIP₂ to demonstrate the "fast" exchange regime. (C) The binding curves for select residues. The global fit resulted in the estimated $K_d$ of 198 μM. (D) The combined chemical shift perturbations ($\Delta$) are plotted as a function of primary sequence. The residues of interest with major perturbations are labelled. (E) The perturbations shown in panel (D) are mapped onto the structure of C1A (2YUU, lowest energy conformer). The putative binding site of PtdIns(4,5)P₂ is depicted by the placement of the molecule.

To test this possibility, we first made a short tandem C1AB construct (referred to as C1A$_{short}$B), where instead of using the 71-residue variant, we used only the minimal folded core of C1A. The $^{15}$N-$^1$H HSQC spectrum of this construct revealed disperse distribution of resonances indicating well folded architecture (**Figure II.9A**). If the additional N-terminal extension of C1A does not interact with the folded core, then the prediction was that the resonances corresponding to the folded core of C1A71 would match well with those on the C1A$_{short}$B. Contrary to this, and consistent with our hypothesis, the overlay shows that the resonances do not match (**Figure II.9A**), suggesting that the N-terminal extension indeed interacts with the C1A core. Furthermore, the $^{15}$N-$^1$H HSQC spectrum acquired on the full-length regulatory segment of PKCδ shows excellent correlation with the C1A71 spectrum (**Figure II.9B**). Since in the full-length construct, the additional N-terminal sequence at C1A persists, this observation further implies that this region should be included as a structural and functional extension of C1A, at least in the context of PtdIns(4,5)P$_2$ interactions.

In summary, we demonstrated that C1A is inherently sensitive to PtdIns(4,5)P$_2$ and might mediate the translocation of PKCδ to plasma membranes as a result. Based on these findings, we predict a model of PKCδ membrane translocation via tandem C1 domains. C1A although not inherently sensitive to DAG, could in lieu of C2, work as a driving force to localize C1B at the regions rich in PtdIns(4,5)P$_2$. Since the hydrolysis product of PtdIns(4,5)P$_2$ (by phospholipase cβ) is diacylglycerol, such localization would put the C1B domain directly in the vicinity of this endogenous agonist. Our future work will focus on testing this mechanistic model.
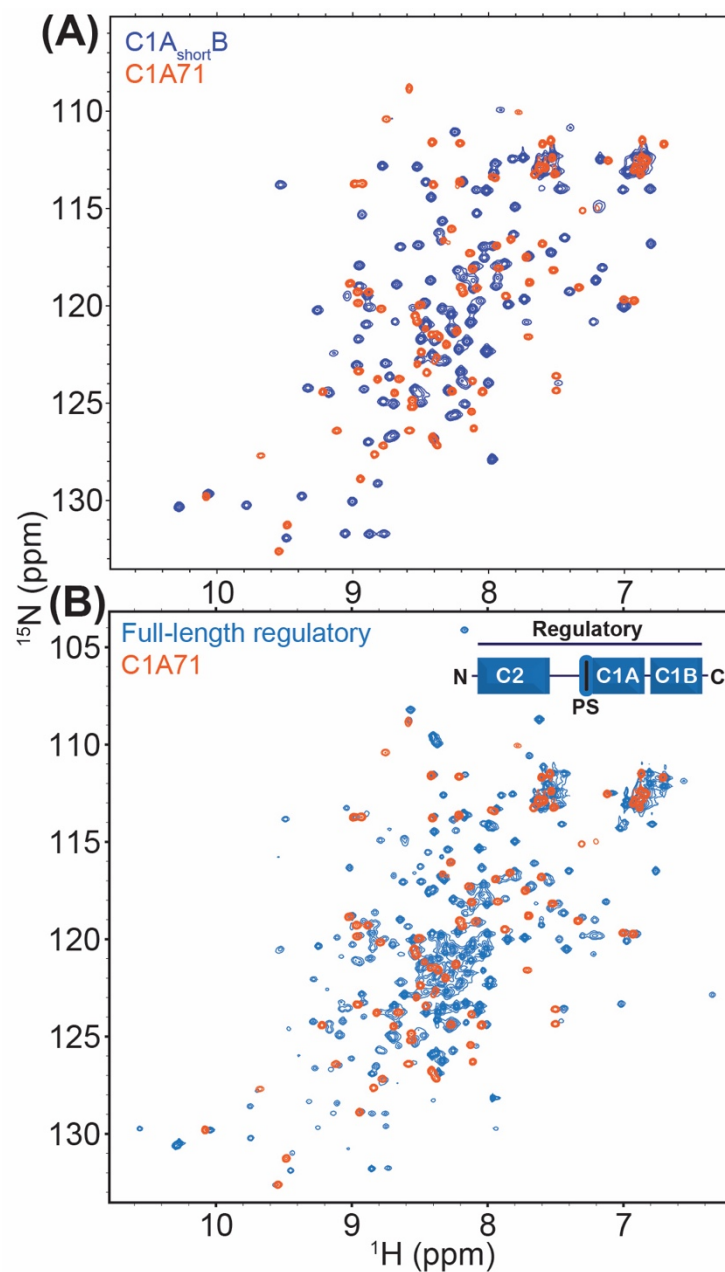
**Figure II.9 C1A is a functional 71-mer**
(A) The $^{15}$N-$^{1}$H HSQC spectral overlay of 0.1 mM C1A71 (U-$^{15}$N), with 0.3 mM C1A$_{short}$B (U-$^{15}$N,$^{13}$C). Both constructs show well-folded core but the common resonances differ in chemical shifts. (B) The $^{15}$N-$^{1}$H HSQC spectral overlay of 0.1 mM C1A71 (U-$^{15}$N) with full-length regulatory region of PKCδ (spectrum provided by Dr. Taylor R. Cole). The common resonances show comparable chemical shifts.

<u>Regions of C1A β34 loop and the helix show millisecond-microsecond timescale</u>

<u>dynamics</u>

Conformational exchange processes typically occur on the μs-to-ms timescale, categorized as "slow" dynamics.[112]  Motions of this regime are particularly relevant to ligand binding, catalysis, and allosteric effects.  To identify the regions on C1A domain that show such conformational dynamics, we acquired and looked at two NMR parameters, $R_{2,HE}$ and $R_{2,CPMG}$ for all spectrally resolved amides of the apo C1A backbone (**Figure II.10**).  $R_{2,HE}$ is a free-precession transverse relaxation rate constant, whose elevated values are indicative of ms-to-μs conformational exchange processes. $R_{2,CPMG}$ is a transverse relaxation rate constant whose elevated values reflect dynamics on timescales faster than 100 μs.  A comparison of the two rate constants would enable us to estimate, in a residue-specific manner, the timescale of motions that are present in C1A.

This analysis revealed a number of residues around β34 loop and α1 helix undergoing conformational exchange, evident by elevated $R_{2,HE}$.  These elevated values were marginally attenuated in $R_{2,CPMG}$ measurements indicating dominant contribution from relatively faster dynamics (>100 μs).  Notable among the β34 loop residues are W180, and Q185 backbone amides and W180 side-chain N-$H_{\varepsilon1}$.  Although the W180 backbone is dynamic, the side chain does not appear to be so. This is consistent with the stable staked orientation of the ring with P169.  The residue at the analogous position to Q185 in C1B domain i.e Q257 is involved in H-bonding interactions that "stitch" the

two agonist-binding loops together.[18]  The elevated dynamics of Q185 in C1A suggests that differential Trp orientation in C1A compared to C1B likely "uncouples" Q185 mediated H-bonding interactions.  Such uncoupling might be necessary to expand the intra-loop region in order to accommodate the indole ring of W180.

The elevated dynamics observed at the $\alpha$1 helix residues, I196 and H197 might be relevant to the anionic lipid sensitivity of C1A.  This elevation was not seen in C1B for the analogous residues.[23]  In particular, C1B H269 (analogous to H197) shows no dynamics within this timescale, consistent with the stable $\pi$-$\pi$ interactions it is involved with W252 (analogous to W180) indole ring.[18, 103]  In C1A, since this interaction is not present, the helix region likely becomes dynamic.  It will be interesting to see whether interactions of anionic lipids like PtdSer or PtdIns(4,5)$P_2$ are required to attenuate the dynamics of this region.  Such interaction could in principle also attenuate the loop region dynamics allosterically, a change that might be prerequisite for the effective agonist recognition by C1A.  In future, we will test these possibilities.
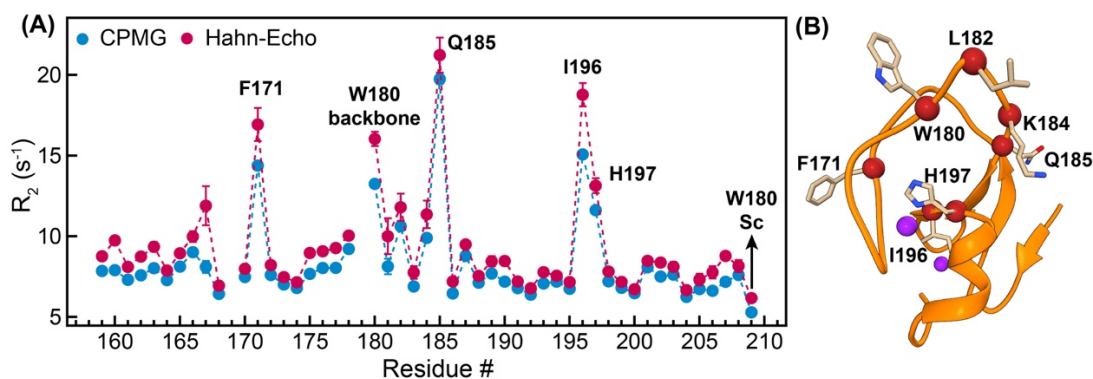
**Figure II.10 The agonist-binding loop region of C1A is dynamic on the microsecond timescale.**
(A) $R_{2,HE}$ and $R_{2,CPMG}$ values are plotted against the primary sequence of C1A. (B) Residues with elevated dynamics on this timescale are labelled and mapped onto the structure of C1A (2YUU, lowest energy NMR conformer).

## Conclusions

The contribution of C1A domain in the overall membrane interactions of PKCδ is unknown. The tandem arrangement of C1 domains does suggest that C1A must serve some function that can complement C1B, which is regarded as the dominant driving force for membrane translocation of this isozyme (PKCδ). In this work, using the combined use of crystallographic and solution state biophysical techniques, we provide valuable knowledge that sheds light on the role(s) C1A domain might serve.

We report that C1A domain can interact with lipidic mimics (micelles) even in the absence of agonists. Given the occluding orientation of the DAG toggle residue (W180) and the resulting solvent inaccessibility, we report that C1A shows weak dependence on DAG as a directly interacting agonist. However, bulky agonists like phorbol esters can in principle displace the indole ring of Trp and bind to C1A. We also demonstrate the inherent ability of C1A to bind PtdIns(4,5)P$_2$ that is yet unrecognized in

any other C1 domains.  In conclusion, C1A domain appears to neither fit the profile of "typical" C1 domains (that are sensitive to DAG/phorbol esters) nor the "atypical" ones (that are not sensitive to these agonists).  Further analysis of the exact ligand-binding preferences, including the possible sensitivity towards diol lipids could in principle reveal the existence of such "neo-typical" C1 domains, with C1A as a paradigm.

# References

[7] Steinberg, S. F. (2008) Structural basis of protein kinase C isoform function, *Physiol Rev 88*, 1341-1378.

[16] Das, J., and Rahman, G. M. (2014) C1 domains: structure and ligand-binding properties, *Chem Rev 114*, 12108-12131.

[18] Zhang, G., Kazanietz, M. G., Blumberg, P. M., and Hurley, J. H. (1995) Crystal structure of the cys2 activator-binding domain of protein kinase C delta in complex with phorbol ester, *Cell 81*, 917-924.

[22] Dries, D. R., Gallegos, L. L., and Newton, A. C. (2007) A single residue in the C1 domain sensitizes novel protein kinase C isoforms to cellular diacylglycerol production, *J Biol Chem 282*, 826-830.

[23] Stewart, M. D., and Igumenova, T. I. (2017) Toggling of Diacylglycerol Affinity Correlates with Conformational Plasticity in C1 Domains, *Biochemistry 56*, 2637-2640.

[26] Shen, N., Guryev, O., and Rizo, J. (2005) Intramolecular occlusion of the diacylglycerol-binding site in the C1 domain of munc13-1, *Biochemistry 44*, 1089-1096.

[27] Stahelin, R. V., Digman, M. A., Medkova, M., Ananthanarayanan, B., Rafter, J. D., Melowic, H. R., and Cho, W. (2004) Mechanism of diacylglycerol-induced membrane targeting and activation of protein kinase Cdelta, *J Biol Chem 279*, 29501-29512.

[28] Goni, F. M., and Alonso, A. (1999) Structure and functional properties of diacylglycerols in membranes, *Prog Lipid Res 38*, 1-48.

[36] Li, J., Ziemba, B. P., Falke, J. J., and Voth, G. A. (2014) Interactions of protein kinase C-alpha C1A and C1B domains with membranes: a combined computational and experimental study, *J Am Chem Soc 136*, 11757-11766.

[64] Guillen, J., Ferrer-Orta, C., Buxaderas, M., Perez-Sanchez, D., Guerrero-Valero, M., Luengo-Gil, G., Pous, J., Guerra, P., Gomez-Fernandez, J. C., Verdaguer, N., and Corbalan-Garcia, S. (2013) Structural insights into the Ca2+ and PI(4,5)P2 binding modes of the C2 domains of rabphilin 3A and synaptotagmin 1, *Proc Natl Acad Sci U S A 110*, 20503-20508.

[88] Giorgione, J. R., Lin, J. H., McCammon, J. A., and Newton, A. C. (2006) Increased membrane affinity of the C1 domain of protein kinase Cdelta compensates for the lack of involvement of its C2 domain in membrane recruitment, *J Biol Chem 281*, 1660-1669.

[89] Stewart, M. D., Cole, T. R., and Igumenova, T. I. (2014) Interfacial partitioning of a loop hinge residue contributes to diacylglycerol affinity of conserved region 1 domains, *J Biol Chem 289*, 27653-27664.

[90] Stewart, M. D., Morgan, B., Massi, F., and Igumenova, T. I. (2011) Probing the determinants of diacylglycerol binding affinity in the C1B domain of protein kinase Calpha, *J Mol Biol 408*, 949-970.

[91] Kabsch, W. (2010) Xds, *Acta Crystallogr D Biol Crystallogr 66*, 125-132.

[92] Hendrickson, W. A., and Teeter, M. M. (1981) Structure of the hydrophobic protein crambin determined directly from the anomalous scattering of sulphur, *Nature 290*, 107-113.

[93] Rose, J. P., Wang, B. C., and Weiss, M. S. (2015) Native SAD is maturing, *IUCrJ 2*, 431-440.

[94] Pape, T., and Schneider, T. R. (2004) HKL2MAP: a graphical user interface for macromolecular phasing with SHELX programs, *Journal of Applied Crystallography 37*, 843-844.

[95] Schneider, T. R., and Sheldrick, G. M. (2002) Substructure solution with SHELXD, *Acta Crystallogr D Biol Crystallogr 58*, 1772-1779.

[96] Sheldrick, G. M. (2002) Macromolecular phasing with SHELXE, *217*, 644.

[97] Emsley, P., Lohkamp, B., Scott, W. G., and Cowtan, K. (2010) Features and development of Coot, *Acta Crystallogr D Biol Crystallogr 66*, 486-501.

[98] Adams, P. D., Afonine, P. V., Bunkoczi, G., Chen, V. B., Davis, I. W., Echols, N., Headd, J. J., Hung, L. W., Kapral, G. J., Grosse-Kunstleve, R. W., McCoy, A. J., Moriarty, N. W., Oeffner, R., Read, R. J., Richardson, D. C., Richardson, J. S., Terwilliger, T. C., and Zwart, P. H. (2010) PHENIX: a comprehensive Python-based system for macromolecular structure solution, *Acta Crystallogr D Biol Crystallogr 66*, 213-221.

[99] Delaglio, F., Grzesiek, S., Vuister, G. W., Zhu, G., Pfeifer, J., and Bax, A. (1995) NMRPipe: a multidimensional spectral processing system based on UNIX pipes, *J Biomol NMR 6*, 277-293.

[100] Lee, W., Tonelli, M., and Markley, J. L. (2015) NMRFAM-SPARKY: enhanced software for biomolecular NMR spectroscopy, *Bioinformatics 31*, 1325-1327.

[101] Farrow, N. A., Muhandiram, R., Singer, A. U., Pascal, S. M., Kay, C. M., Gish, G., Shoelson, S. E., Pawson, T., Forman-Kay, J. D., and Kay, L. E. (1994) Backbone dynamics of a free and phosphopeptide-complexed Src homology 2 domain studied by $^{15}$N NMR relaxation, *Biochemistry 33*, 5984-6003.

[102] Wang, L., Pang, Y., Holder, T., Brender, J. R., Kurochkin, A. V., and Zuiderweg, E. R. (2001) Functional dynamics in the active site of the ribonuclease binase, *Proc. Natl. Acad. Sci. U.S.A. 98*, 7684-7689.

[103] Shanmugasundararaj, S., Das, J., Sandberg, W. S., Zhou, X., Wang, D., Messing, R. O., Bruzik, K. S., Stehle, T., and Miller, K. W. (2012) Structural and functional characterization of an anesthetic binding site in the second cysteine-rich domain of protein kinase Cdelta*, *Biophys J 103*, 2331-2340.

[104] Severin, S. E., Jr., Tovmasyan, E. K., Shvets, V. I., Molotkovsky, J. G., and Bergelson, L. D. (1988) Diol lipids are activators of protein kinase C, *FEBS Lett 232*, 286-288.

[105] Das, J., Addona, G. H., Sandberg, W. S., Husain, S. S., Stehle, T., and Miller, K. W. (2004) Identification of a general anesthetic binding site in the diacylglycerol-binding domain of protein kinase Cdelta, *J Biol Chem 279*, 37964-37972.

[106] Das, J., Zhou, X., and Miller, K. W. (2006) Identification of an alcohol binding site in the first cysteine-rich domain of protein kinase Cdelta, *Protein Sci 15*, 2107-2119.

[107] Pany, S., and Das, J. (2015) Alcohol binding in the C1 (C1A+C1B) domain of protein kinase C epsilon, *Biochim Biophys Acta 1850*, 2368-2376.

[108] Ziemba, B. P., Booth, J. C., and Jones, D. N. (2011) 1H, 13C and 15N NMR assignments of the C1A and C1B subdomains of PKC-delta, *Biomol NMR Assign 5*, 125-129.

[109] Newport, T. D., Sansom, M. S P., and Stansfeld, P. J. (2018) The MemProtMD database: a resource for membrane-embedded protein structures and their lipid interactions, *Nucleic Acids Research 47*, D390-D397.

[110] Wang, J., and Richards, D. A. (2012) Segregation of PIP2 and PIP3 into distinct nanoscale regions within the plasma membrane, *Biol Open 1*, 857-862.

[111] van den Bogaart, G., Meyenberg, K., Risselada, H. J., Amin, H., Willig, K. I., Hubrich, B. E., Dier, M., Hell, S. W., Grubmuller, H., Diederichsen, U., and Jahn, R. (2011) Membrane protein sequestering by ionic protein-lipid interactions, *Nature 479*, 552-555.

[112] Kleckner, I. R., and Foster, M. P. (2011) An introduction to NMR-based approaches for measuring protein dynamics, *Biochim Biophys Acta 1814*, 942-968.

CHAPTER III MEMBRANE INSERTION OF PKCδ C1B DOMAIN PROBED BY

PARAMAGNETIC NMR

**Background**

The C1B domain of PKCδ is the very first C1 domain for which the phorbol ester-complexed structure was solved.[18] Several studies were since conducted on this domain, revealing its preference towards diacylglycerol, phorbol esters, alcohols, anesthetics, and therapeutic C1-targeted drug candidates.[16] Therefore, it is astonishing to fathom the fact that no atomic-resolution structural model yet exists that can describe the membrane interactions of C1B mediated by either of these agonists. Furthermore, C1B represents one of the fascinating examples where the potency its agonists is studied extensively in living cells,[27, 113-117] yet how these agents actually interact with the domain is unknown (with the exception of phorbol ester). These issues are not limited to C1B in particular, but also extend to other C1 domains.

Any biophysical approach aimed to solve this problem will likely be stonewalled by the challenging nature of this system. C1 domains and their agonist-binding loop regions can be inherently dynamic, making crystallization challenging. Furthermore, C1 agonists are highly lipophilic in nature, making their complexes nearly impossible to solubilize without proper membrane mimics. Obtaining structural information of the membrane-bound complexes of C1-agonists is an achievable goal in theory using bicelles, detergents and lipid cubic phases, but hasn't been attempted or reported to our knowledge.

Solution-state NMR (Nuclear magnetic resonance) is a technique uniquely suited to study dynamic systems such as C1 domains. It has been successfully applied to C1B previously.[89] In this chapter, we take this application a step further by proposing a comprehensive approach that can be used to obtain reliable experimental information on C1B-membrane and C1B-agonist-membrane complexes. This information is atomic-resolution and can potentially be used further as "restraints" to informatively drive the molecular dynamics simulations on this system. The final structural models prepared in this manner can then be extrapolated to ascertain the observations in the living cells, and drive the field of C1-targeted drug design.

## Experimental procedures

### Expression and purification of isotopically labelled C1Bδ

The DNA construct coding for the murine C1Bδ (residues 229-281) as a cleavable fusion partner of the solubility tag 6xHis-SUMO was transformed into the *E. coli* BL21(DE3) cells. The cells were grown at 37 $^0$C under Kanamycin (Sigma-Aldrich) selection in LB until the optical density at 600 nm wavelength reached 0.6. Four such cultures (1 L each) were harvested, washed, and re-suspended into the 1L M9 minimal media supplemented with isotopic components: 1 g/L of ammonium chloride ($^{15}$N, 99%) (Cambridge Isotopes) and 2 g/L d-glucose ($^{13}$C, 99%) (Cambridge Isotopes) to achieve U-$^{13}$C,$^{15}$N labelling. Alternatively, to obtain U-$^{13}$C,$^{15}$N, ~75%-D labelling, the media was prepared in 80% D$_2$O (deuterium oxide, Cambridge Isotopes) supplemented with 0.25 g/L of U-$^{13}$C,$^{15}$N, 97-99%-D ISOGRO® (Sigma-Aldrich). After equilibration for 1 hr at 18 $^0$C, the cells were induced with 0.5 mM Isopropyl β-D-1-thiogalactopyranoside (Fisher Bioreagents) for 16 hrs. The harvested cell pellets post-induction were stored at -20 $^0$C until lysis.

The cells were lysed using B-PER™ lysis reagent (Thermo-Scientific) and the clarified lysate was loaded onto the HisTrap HP Ni affinity column (GE Healthcare Life Sciences). The column-immobilized protein was eluted with Imidazole gradient, and cleaved with SUMO protease at room temperature for 24 hrs to remove the 6xHIS-SUMO tag. The cleaved protein was then collected as a flowthrough of HisTrap HP Ni affinity column, concentrated and further purified using size-exclusion column. The final purified fractions were concentrated and exchanged into 20 mM [D-4]-Imidazole buffer

at pH 6.5 (Cambridge Isotopes), 50 mM KCl, 8% $D_2O$, 0.1 mM tris(2-carboxyethyl) phosphine (TCEP), and 0.02% $NaN_3$. This buffer was used for all NMR experiments described in this chapter.

<div align="center">Preparation of isotropically-tumbling bicelles</div>

All lipid components were acquired from Avanti Polar lipid unless specified otherwise. To prepare isotropically tumbling bicelles, chloroform solutions of DMPC (1,2-dimyristoyl-sn-glycero-3-phosphocholine) and DHPC (1,2-dihexanoyl-sn-glycero-3-phosphocholine) were aliquoted, dried under vacuum extensively and resuspended in the aforementioned NMR buffer. DMPC preparation was hydrated, vortexed and subjected to 3 rapid freeze-thaw cycles to create homogeneous slurry. Clear DHPC solution was then added to this slurry to achieve two-fold molar excess to DMPC (q=0.5). The resulting mixture was briefly vortexed and subjected to 4 rapid freeze-thaw cycles, resulting in clear homogeneous bicelle stock. Total lipid concentration was verified using phosphate determination assay. Additional long-chain lipid components, such as DMPS (1,2-dimyristoyl-sn-glycero-3-phospho-L-serine), 5/14-doxyl PC (1-pamitoyl-2-stearoyl-(5/14-doxyl)- sn-glycero-3-phosphocholine) were dried and added during the bicelle preparation wherever applicable. DMPS was added to achieve DMPC:DMPS molar ratio of 85:15. 5/14-doxyl PC components were added to achieve average 1 molecule per leaflet. The bicelle stock solutions were flash frozen and stored at -20 ºC. Before use, the frozen stocks were thawed at 42 ºC, followed by incubation at room temperature.

Di-octanoyl sn-1,2 diacylglycerol (DOG) was incorporated to desired concentration by directly resuspending the oil into the bicelle solution, followed by incubation at 42 ºC and gentle vortexing until the solution becomes clear. Other agonists like phorbol 12,13 di-butyrate (PDBu), Prostratin, and Bryostatin-1 were added extraneously into the C1B-bicelle mixture. With the exception of DOG, all other agonists were acquired from Sigma-Aldrich.

<div align="center">NMR spectroscopy</div>

Unless specified otherwise, all NMR experiments were acquired at 298.15 K, calibrated using the deuterated Methanol. NMR data were processed with NMRPipe[99] and analyzed with Sparky.[100] Isotopically enriched C1B was mixed with bicelles, in proportions and concentration described in the main text. The $^{15}$N-$^1$H TROSY (Transverse relaxation-optimized spectroscopy) spectra were collected on Bruker AVANCE III instrument operating at a $^1$H Larmor frequency of 800 MHz (equipped with cryogenically cooled probe) at each subsequent addition of agonist or upon change in lipid composition of the bicelles. The combined chemical shift perturbations (CSPs, $\Delta$) were calculated using the expression:

$$\Delta = [\,\Delta\delta_H^2 + (0.152\Delta\delta_N)^2\,]^{1/2}$$

Where $\delta_H$ and $\delta_N$ are $^1$H and $^{15}$N chemical shift differences for a given resonance in the two spectra that are being compared.

The $^{13}C$-$^1H$ HSQC (Heteronuclear single quantum coherence) spectra were also collected with Bruker AVANCE Neo instrument operating at a $^1H$ Larmor frequency of 600 MHz (equipped with cryogenically cooled probe) for select samples to inspect methyl/aromatic regions using U-$^{13}C$,$^{15}N$ labelled C1B and bicelles prepared using deuterated lipid components.

$^{15}N$-edited NOESY experiments were acquired with Bruker AVANCE III instrument operating at a $^1H$ Larmor frequency of 600 MHz (equipped with cryogenically cooled probe) using U-$^{13}C$,$^{15}N$, ~75%-D C1B and protonated bicelles and the mixing time of 120 ms. These experiments were acquired in the presence of DOG (dioctanoyl sn-1,2 diacylglycerol) as well as in the absence.

The distance-dependent $^1H_N$ PRE (Paramagnetic relaxation enhancement, $\Gamma_2$) measurements were done with Bruker AVANCE III instrument operating at a $^1H$ Larmor frequency of 800 MHz (equipped with cryogenically cooled probe) using the TROSY-based pulse sequence implementing two-point acquisition scheme.[118] The $^1H_N$ $R_2$ (transverse relaxation rate constants) obtained using these experiments for diamagnetic ($R_{2,dia}$:without 5/14-doxyl PC) and paramagnetic bicelle ($R_{2,para}$:with 5/14-doxyl PC) samples provide the residue-specific PREs by following expression:

$$\Gamma_2 = R_{2,para} - R_{2,dia}$$

**Results and Discussion**

Design and application of the NMR-based approach to characterize the membrane-

bound complexes of C1Bδ

The lack of experimentally derived, atomic-resolution information of how C1 domains interact with the membranes in the absence and presence of various agonists limits our understanding of them. This prompted us to devise a strategy that is presented in this section using the C1B as a paradigm. This strategy combines the benefits of solution-state NMR with the bilayer-forming membrane mimics, bicelles to look at the C1B-agonist-membrane ternary complexes (**Figure I.6, III.1**).

All three components involved in the successful implementation of this approach have inherent variabilities that can lead to wealth of information. For instance, the different labelling schemes ($^{15}$N, $^{13}$C, aromatic-$^{19}$F) one can implement with the protein component can lead to NMR-detected readouts on the amides, methyl side-chains, and the DAG toggle residues involved in the membrane/agonist interactions. On the other hand, the lipid composition of the isotropically tumbling bicelles can be easily modified. One can include various specialized components like anionic (PtdSer, PtdIns(4,5)P$_2$), and paramagnetic lipids (5/14-doxyl PtdCho) that can shed light on the lipid preferences and membrane insertion parameters of the domain respectively (**Figure III.1A**). Finally, the third agonist component can vary from the endogenous DAGs, tumor promoting agents (phorbol esters) to therapeutic compounds like Prostratin and Bryostatin 1(**Figure III.1B**). Multitude of variations of each of the components used in this solution-state strategy provide it the edge over other biophysical approaches.

84

**(A)** C1B-agonist-bicelle ternary complex

Agonist

C1 domain

PRE effect ~ $r^{-6}$
Paramagnetic nitroxide labels

**(B)** C1Bδ-agonists

| Native agonist | Tumor promoter | Drug candidate | Drug candidate |
|---|---|---|---|
| **Diacylglycerol** | **PDBu** | **Prostratin** | **Bryostatin-1** |
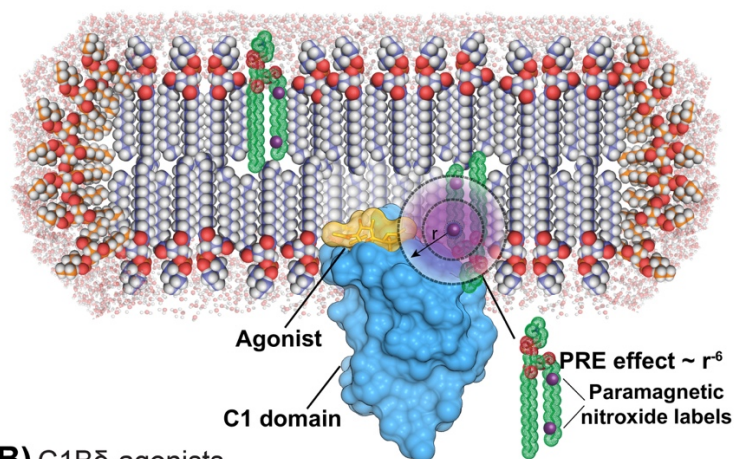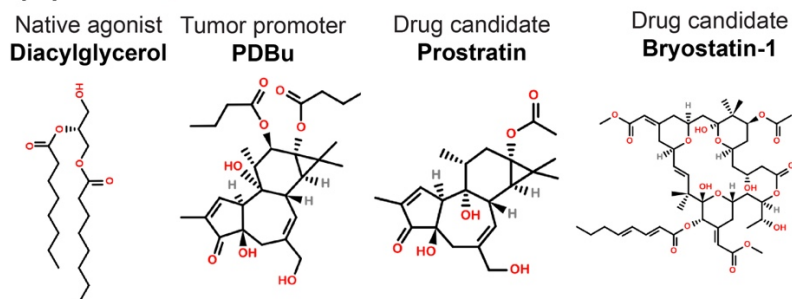
**Figure III.1 NMR-based experimental strategy to obtain information of C1-agonist-membrane ternary complexes**

(A) General schematic depicting the use of isotropically tumbling bicelles as membrane mimics to probe C1-agonist-membrane interactions. The cross-section of the discoid bicelles, shows bilayer core (made of long-chain DMPC) that can be compositionally modified to include specific lipids. The inclusion of paramagnetic lipids to get distance-dependent information on the membrane insertion of the C1 domain regions is schematically depicted as an example. The exposed edges of the bilayer are shielded by the short -chain DHPC. The ratio of DMPC:DHPC used is 1:2 for this work, that leads to formation of isotropically tumbling bicelles amenable to NMR studies. (B) The chemical architecture of the C1B agonists used in this work is shown.

<u>C1Bδ interacts with bicelles made of zwitterionic and anionic lipids in the agonist-</u>

<u>independent manner</u>

Before we started implementing the aforementioned approach to the C1B ternary complexes (C1B-membrane-agonist), we decided to test the applicability by probing the formation of C1B-membrane binary complexes. Experiments conducted with micelles indicate that C1B, similar to C1A, can interact with these lipid mimics in the absence of agonists.[89] To test whether we can replicate these findings using the bicelles, we prepared NMR samples of C1B with (U-$^{15}$N,$^{13}$C)-labelling and ~75% deuteration. Due to suppression of spin diffusion and reduction of the relaxation rates of $^{13}$C/$^{15}$N spins, the deuteration enables greater signal-to-noise in the NMR spectra, especially useful when the protein binds to large entities like bicelles.[119] To the protein, we added bicelles that were made of DMPC:DHPC (1:2) supplemented with DMPS component (to achieve molar ratio of ~15% in the bilayer region), referred to henceforth as PCPS bicelles. Small bicelles of such composition are well-characterized and amenable to NMR studies.[35, 120-126] In this composition, the long-chain DMPC (14:0 PtdCho) and DMPS (14:0 PtdSer) form a bilayer disk with the exposed edges covered by the layer of short-chain DHPC (6:0 PtdCho). The protein to bicelle ratio was kept at ~1:1.
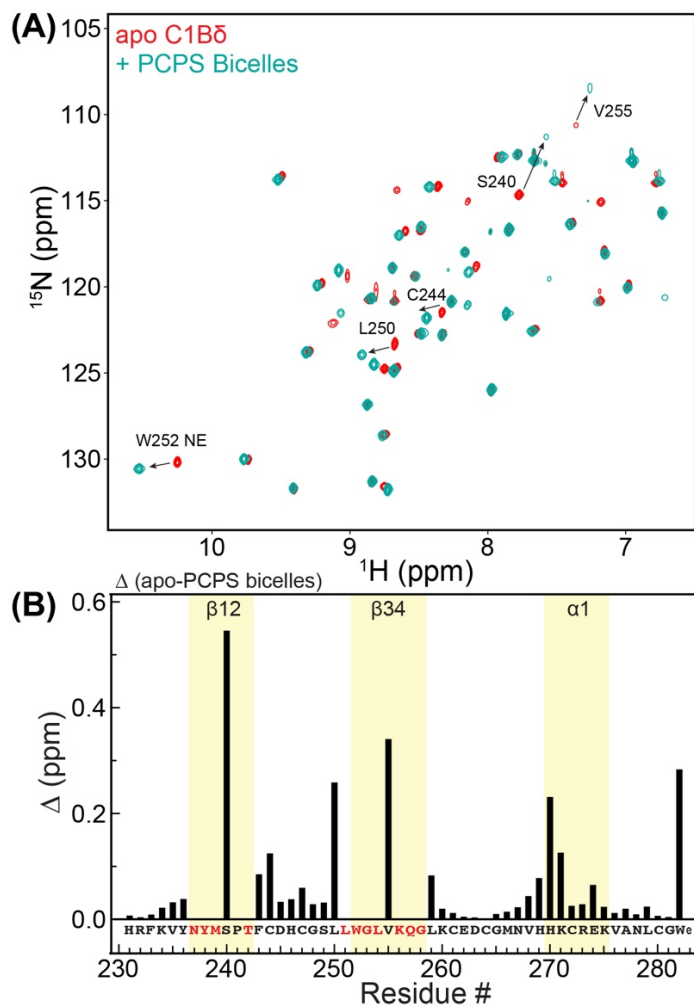
**Figure III.2 C1Bδ can interact with anionic bicelles in agonist-independent manner**
(A) $^{15}N$-$^{1}H$ TROSY-HSQC spectral overlay of apo C1B (0.4 mM), with PCPS bicelles (also 0.4 mM, 100mM total lipids). Select residues with distinct chemical shift perturbations (CSPs) are labelled. (B) Combined CSPs are plotted as a function of primary sequence to identify the most affected regions. Regions of interest with significant perturbations are highlighted. The residues that are exchange broadened and therefore could not be detected are marked red within the primary sequence. Perturbation of the W252 side-chain is plotted at the end, and denoted as "$W_e$".

Several agonist-binding loop region residues were exchange broadened, evident by their absence in the $^{15}$N-$^{1}$H TROSY spectrum of apo C1B (no bicelles). Addition of PCPS bicelles resulted in distinct chemical shift perturbations (CSPs) in select residues (**Figure III.2A**). Plotting these changes as a function of C1B sequence revealed that they were primarily manifested by the detectable loop resonances along with the α1 helix (**Figure III.2B**). These observations show that C1B can indeed interact with the PCPS bicelles in the absence of any agonists. The perturbations observed at the relatively basic α1 helix indicate that this region likely participates in the electrostatic interactions with the anionic lipid component, DMPS.

To determine whether the ability of C1B to partition into the membranes is exclusively due to the electrostatic interaction with anionic lipids, we compared the $^{15}$N-$^{1}$H TROSY spectra of C1B in the presence of PC-only bicelles vs the PCPS bicelles (**Figure III.3A**). With the exception of few resonances, the chemical shifts match well, indicating the persistent membrane partitioning. The residue-specific chemical shift differences between these spectra distinctly identify the α1 helix as the most affected region (**Figure III.3B**). In combination, these findings indicate that the agonist-independent C1B membrane association is not exclusively electrostatic in nature and likely involves direct interactions between the hydrophobic loop region residues with the lipid moieties.
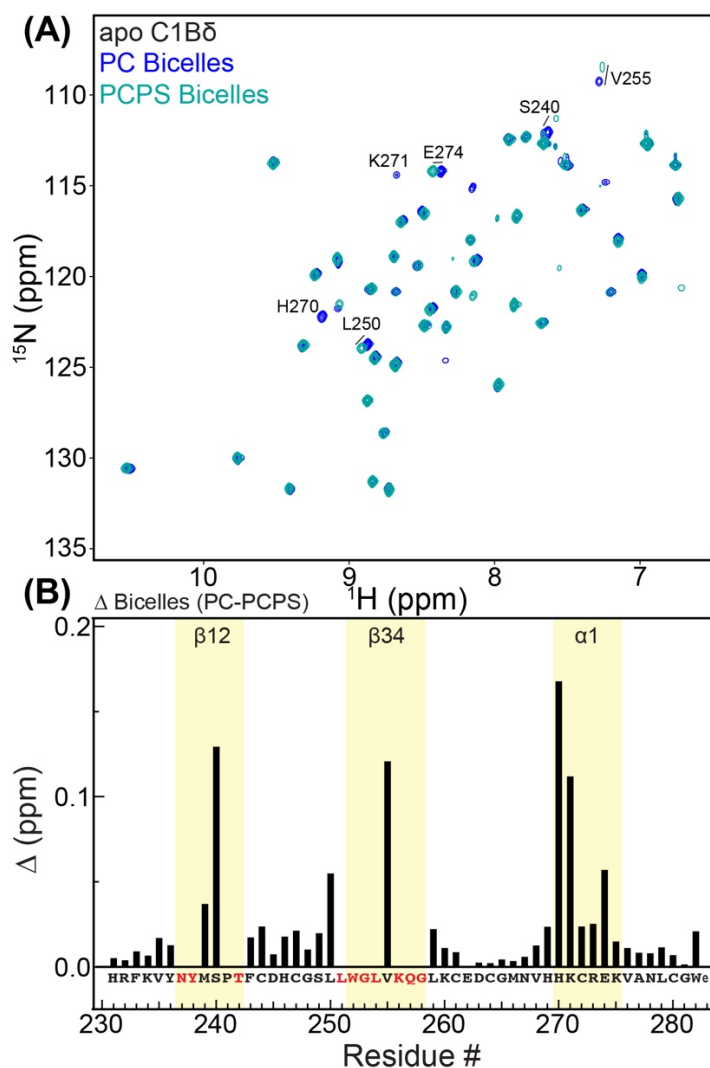
**Figure III.3 The presence of anionic lipids is not obligatory for agonist-free bicelle interactions of C1Bδ**

(A) $^{15}N$-$^{1}H$ TROSY-HSQC spectral overlay of C1B with PCPS bicelles (both 0.4 mM, 100mM total lipids) and PC-only bicelles. Select residues with different chemical shifts are labelled. (B) Differences in the chemical shifts of resonances between the spectra depicted in (A) are plotted as a function of primary sequence. Regions of interest with perturbations are highlighted. The residues that are exchange broadened and therefore could not be detected are marked red within the primary sequence. Perturbation of the W252 side-chain is plotted at the end, and denoted as "$W_e$". Significant perturbations are seen for the positively charged helix region ($\alpha$1).

Notably in these backbone amide-detected experiments, most loop region residues remain exchange broadened despite C1B interaction with bicelles in the absence of agonists. Therefore, to get better understanding of how loop residues are affected by these interactions, we acquired $^{13}$C-$^{1}$H HSQCs on (U-$^{13}$C,$^{15}$N)-labelled protein (not deuterated). Given the abundance of methyl containing side-chains in the loop region residues, we specifically looked at the methyl region of $^{13}$C HSQCs in presence and absence of PCPS bicelles (**Figure III.4A**). Significant perturbations were detected for residues M239, L250, L251, L254, and V255 (**Figure III.4A,C**), indicating these side chains are likely involved in the membrane interactions.

Furthermore, to directly look at the toggle residue W252, we acquired $^{13}$C aromatic HSQC and $^{15}$N-edited NOESY experiments in the presence and absence of PCPS bicelles. The former clearly shows perturbations within the indole ring of W252 in the presence of bicelles (**Figure III.4B,C**). The later shows appearance of additional NOE peaks that suggest the spatial proximity of W252 side-chain N-Hε to P241 (**Figure III.4B inset**).[108] These NOEs are not observed in the absence of bicelles (data not shown). These NOEs could only appear if the W252 side chain rotates towards the intra-loop space and stacks against the P241 present on the opposite loop, β12 (**Figure III.4C**). Comparison of this with the analogous position of C1A toggle residue (W180), described in the previous chapter, indicates that the indole ring can indeed serve as a "pseudo-agonist" in the absence of agonist and assist the membrane association process.
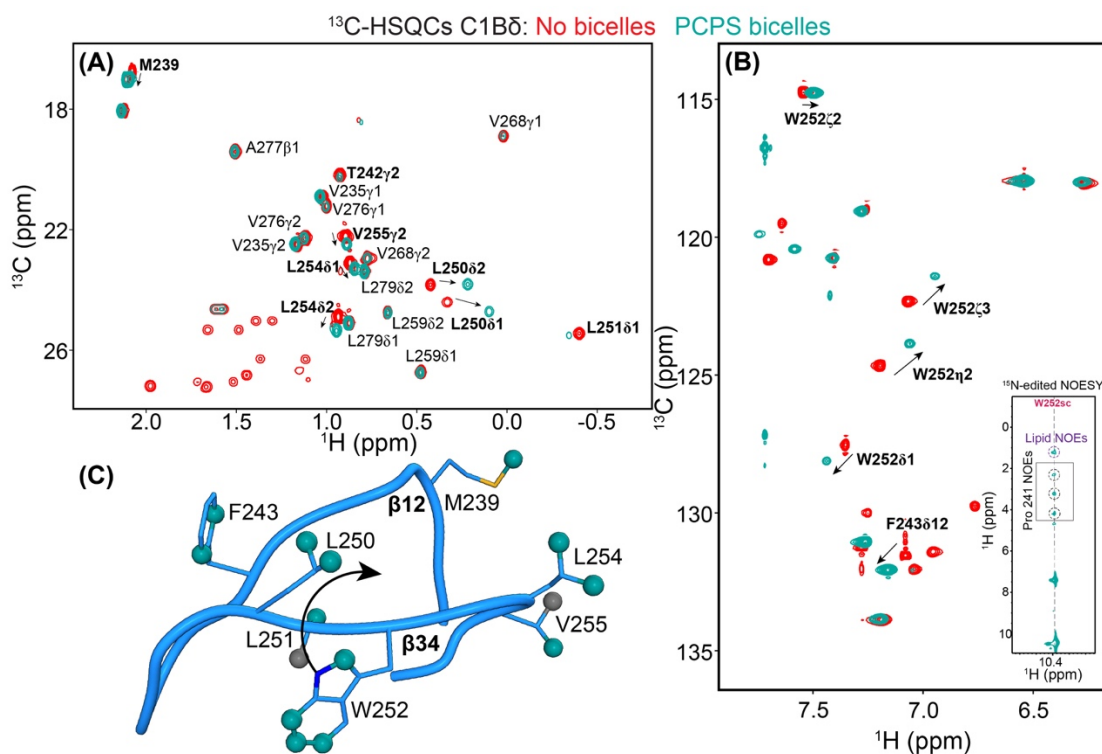
**Figure III.4 Agonist-independent C1Bδ bicelle interactions involve the methyl-containing hydrophobic residues of the loops and toggle-residue rearrangement**
(A) $^{13}$C-$^{1}$H HSQC spectral overlay of apo C1B, with PCPS bicelles (both 0.3 mM, 80mM total lipids, deuterated), showing the methyl region. The hydrophobic loop region residues with methyl containing side chains show perturbations in presence of bicelles (B) aromatic-$^{13}$C-$^{1}$H HSQC spectral overlay showing perturbations in the indole ring of W252. Inset: The $^{15}$N-edited NOESY strip of W252 side-chain Hε proton, with appearance of NOE peaks consistent with the chemical shifts of P241 protons in presence of bicelles. This indicates rearrangement of the side chain towards the intra-loop region. (C) The side-chains that show CSPs in (A) and (B) are mapped on the loop region of the C1B (1PTQ). The NOEs suggest the relocation of W252 side chain from the orientation observed in this structure towards the intra-loop space.

Finally, to conclusively establish that the agonist-binding loops partition into the bicelles, we included a paramagnetic lipid component: 5-doxyl PC. The lone pair of electrons on the stable nitroxide radical of the doxyl group, localized at the 5$^{th}$ carbon of the PtdCho acyl chain, can allow distance-dependent readout on the protein partitioning into the lipidic environment (**Figure III.1A**).[127] The phenomenon, referred to as paramagnetic relaxation enhancement (PRE) causes elevation in the transverse-relaxation rate constants (R$_2$) for the spins (in this case, amide protons) that are within 35 Å from the paramagnetic center (in this case, the 5-doxyl).[128] The distance-dependence of the PREs is very steep (r$^{-6}$), and will lead to the broadening of spins that are contacting the acyl-chain region. If the C1B loops partition into the membrane, then we expected to see elevated values of PREs for amide protons ($^1$H Γ2) of interacting residues.

Consistent with our prediction, the presence of 5-doxyl PC in the bicelles (1 molecule per leaflet of the bilayer) caused PRE-induced broadening of detectable loop region residues, including the N-Hε of the W252 side chain (**Figure III.5**). These observations were persistent regardless of the presence of PtdSer in the bicelles (**Figure III.5A and B**), indicating loop region residues do partition into the bilayer. On the contrary, the α1 helix residues did not show any PREs, suggesting that this region likely interacts only peripherally with the anionic lipid headgroups.

Taken together, these results show that C1B interacts with membranes in the absence of agonists. This interaction likely involves transient shift of the toggle residue orientation (W252) towards the intra-loop region and direct partitioning of the loop

residues into the bilayer. The electrostatic component exists for this interaction, via the

relatively basis helix region of the protein. However, this component is not obligatory.
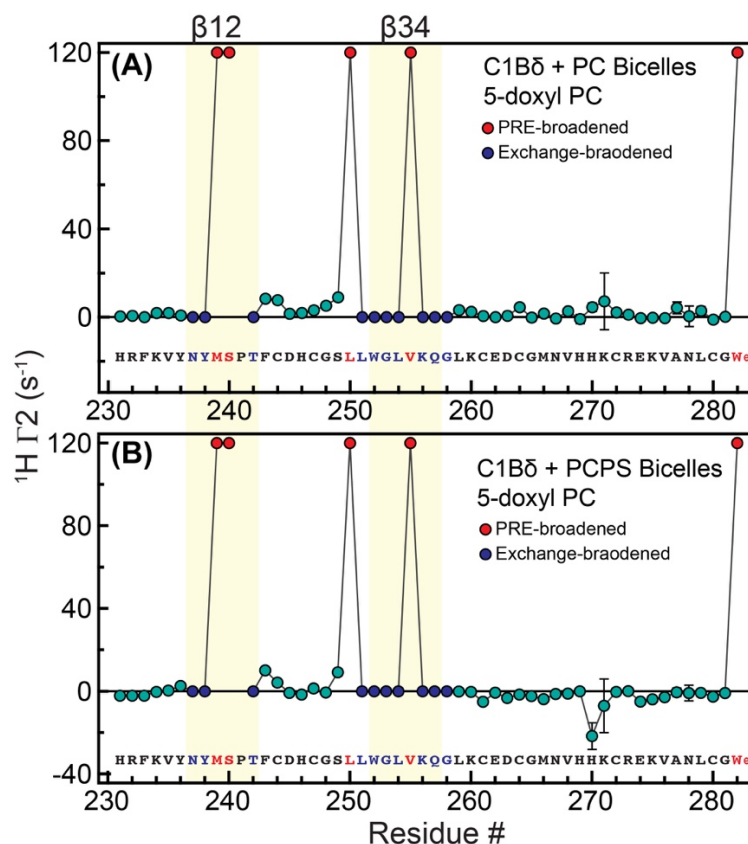


**Figure III.5 Loop regions partition into the membrane upon agonist-independent association of C1Bδ with bicelles**

(A) and (B) $^1H_N$ PREs ($^1H_N$-$\Gamma_2$) obtained by subtracting the residue specific $^1H_N$ $R_2$ (transverse relaxation rate constants) of paramagnetic (5-doxyl PC containing bicelles) samples from those of diamagnetic samples (no paramagnetic lipids). The residues completely broadened beyond detection due to PRE effect were given arbitrary value of 120 s$^{-1}$ (marked red). These residues are most proximal to the membrane embedded paramagnetic probe. The residues that were exchange broadened and thus undetectable in both diamagnetic and paramagnetic samples are marked blue. The PRE pattern on protein appears identical for both PC (A) and PCPS (B) containing bicelles.

## C1Bδ-bicelle interactions are stabilized by the presence of endogenous agonist diacylglycerol

To determine the effects of endogenous agonist diacylglycerol (DAG) on the C1B-bicelle binary complex, we conducted similar experiments in the presence of di-octanoyl sn-1,2 diacylglycerol (DOG). The $^{15}N$-$^{1}H$ TROSY experiments acquired in the presence of PC and PCPS bicelles show distinct CSPs upon inclusion of 8-fold molar excess of DOG (**Figure III.6A and 7A**). In addition to these perturbations, all previously exchange-broadened loop region residues are detectable in the spectra (**Figure III.6B and 7B**). These findings clearly indicate the formation of C1B-DOG-bicelle ternary complex. In this complex, the agonist binding region is significantly stabilized, leading to appearance of the resonances.

To get better understanding of the regions affected by presence of DOG, the CSPs were plotted as a function of primary sequence. With PC bicelles, the changes are located at the two agonist-binding loops, but marginal changes were observed at the basic α1 helix (**Figure III.6C**). On the other hand, with PCPS bicelles, in addition to the loops, the helix shows perturbations (**Figure III.7C**). Since the DOG and PtdSer binding regions are distinct (loops and helix respectively), this comparison suggests that DOG induced re-arrangement of C1B-bicelle interaction also indirectly affects this electrostatic component.
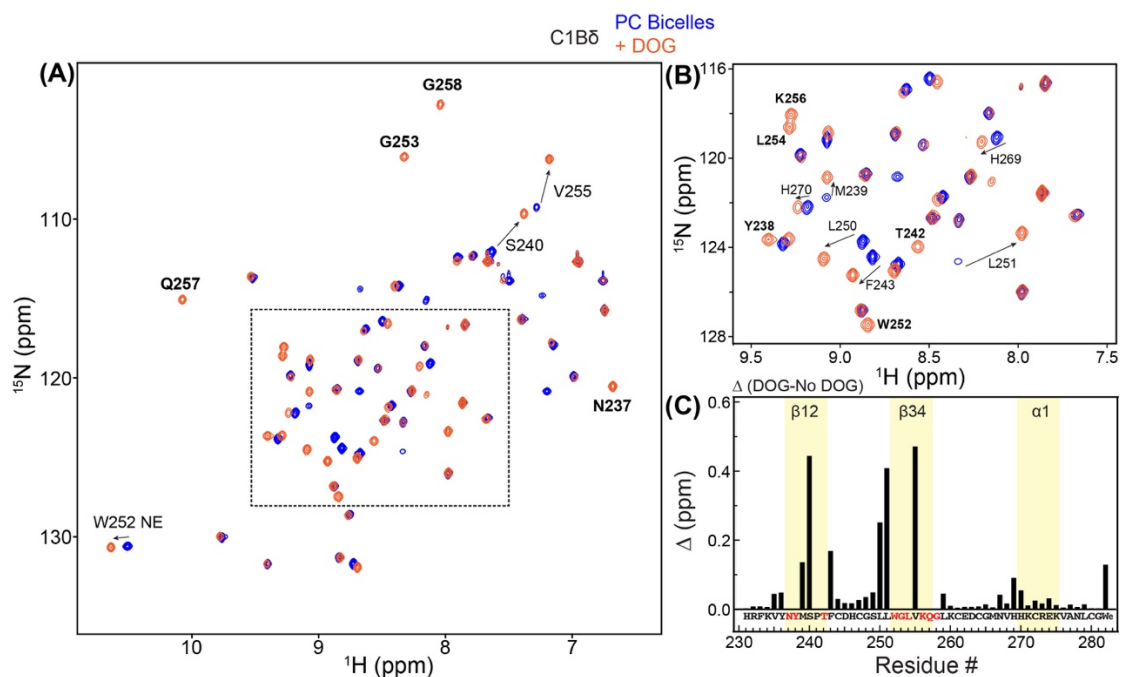
**Figure III.6 Interactions of C1Bδ-bicelle complex with DOG stabilize the loop region**

(A) $^{15}$N-$^{1}$H TROSY-HSQC spectral overlay of C1B-PC bicelles (0.4 mM each, 100mM total lipids) without and with the inclusion of DOG (3.2 mM, 8x to protein). Select residues with distinct chemical shift perturbations (CSPs) are labelled. Labels marked in bold appear in presence of DOG but were exchange broadened and undetectable in protein-bicelle sample. (B) The expansion of the boxed region shown in (A). (C) Combined CSPs resulting from the inclusion of DOG in the bicelles are plotted as a function of primary sequence to identify the most affected regions. Regions of interest are highlighted. The residues that are exchange broadened in C1B-bicelle complex and therefore could not be used for the perturbation analysis are marked red within the primary sequence. Perturbation of the W252 side-chain is plotted at the end, and denoted as "W$_e$".

**Figure III.7 Interactions of C1Bδ-bicelle complex with DOG in presence of anionic lipids perturb the α1 helix**

(A) $^{15}$N-$^1$H TROSY-HSQC spectral overlay of C1B-PCPS bicelles (0.4 mM each, 100mM total lipids) without and with the inclusion of DOG (3.2 mM, 8x to protein). Select residues with distinct chemical shift perturbations (CSPs) are labelled. Labels marked in bold appear in presence of DOG but were exchange broadened and undetectable in protein-bicelle sample. (B) The expansion of the boxed region shown in (A). (C) Combined CSPs resulting from the inclusion of DOG in the bicelles are plotted as a function of primary sequence to identify the most affected regions. Regions of interest are highlighted. The residues that are exchange broadened in C1B-bicelle complex and therefore could not be used for the perturbation analysis are marked red within the primary sequence. Perturbation of the W252 side-chain is plotted at the end, and denoted as "W$_e$". Perturbations in the helix region (α1) particularly with K271 are seen.

Formation of the membrane-embedded C1Bδ-DAG complex involves differential

contribution from the agonist-binding loops

Next, we wanted to determine which regions of C1B are directly embedded into the membrane in presence of DOG. To achieve this, we used the PRE-based approach reported earlier. In this case, since the amides of all the non-proline residues are detectable due to DOG-induced stabilization, we expected to obtain the full picture of C1B-membrane association with each residue effectively acting as the "pixel".

To deconvolute the contribution of PtdSer from this picture, we decided to conduct the experiment first with PC-only bicelles. Two different variants of the paramagnetic lipid were used: 5- and 14-doxyl PC, one at a time. The additional dataset with a deeper probe position (14th carbon on acyl chain) essentially creates a virtual "ruler" of depth,[127, 129] allowing us to estimate the extent of membrane insertion for the affected regions. In presence of 5-doxyl PC, we observed PREs for both DOG-binding loops (**Figure III.8A)**. However, several residues of β34 loop were PRE-broadened beyond detection, including the N-Hε of W252 side-chain. This observation suggests that β34 loop, when viewed as a spatiotemporal average of this dynamic system, is closer to the paramagnetic probe compared to β12 loop. This finding although unexpected, could be logically attributed to the differential composition of the residues on these loops. β34 loop contains several consecutive residues that are hydrophobic and have methyl-containing side chains. Furthermore, the toggle residue W252 is located on this loop. Typically, these residues tend to show higher contact frequencies with the lipidic moieties leading to their better partitioning into the hydrophobic core of the

membranes.[109] We believe, it is because of this, β34 loop is uniquely tuned to interact effectively with the acyl chains compared to β12 and likely drives the process of "fishing" for the agonist within the plane of the membrane.

In presence of 14- instead of 5-doxyl PC variant with PC-only bicelles, the PREs for the loop regions retained the same pattern, yet somewhat attenuated (**Figure III.8B**). Particularly the attenuation of V255 and W252 N-Hε PREs indicates that these residues are on average closer to $5^{th}$ acyl chain carbon than the $14^{th}$. This comparison conclusively places the affected residues of β34 loop within the acyl chain core of the bilayer. In presence of PCPS bicelles, we looked at the PREs obtained using only 14-doxyl PC variant (**Figure III.8C**). Essentially, the differential pattern observed for the loops persisted, but in comparison with PC-only bicelles, we observed significantly prominent effect on β34 loop residues. Particularly, with the exception of L251 and W252 N-Hε, all the residues on this loop were PRE-broadened beyond detection indicating deeper partitioning. On the other hand, with the exception of S240, β12 loop residues had attenuated PREs compared to PC only bicelles (**Figure III.8B and C**). It is likely that PtdSer interactions with the α1 helix (which is spatially proximal to β34) augment the better partitioning of this loop. This possibility will be explored further in the future.
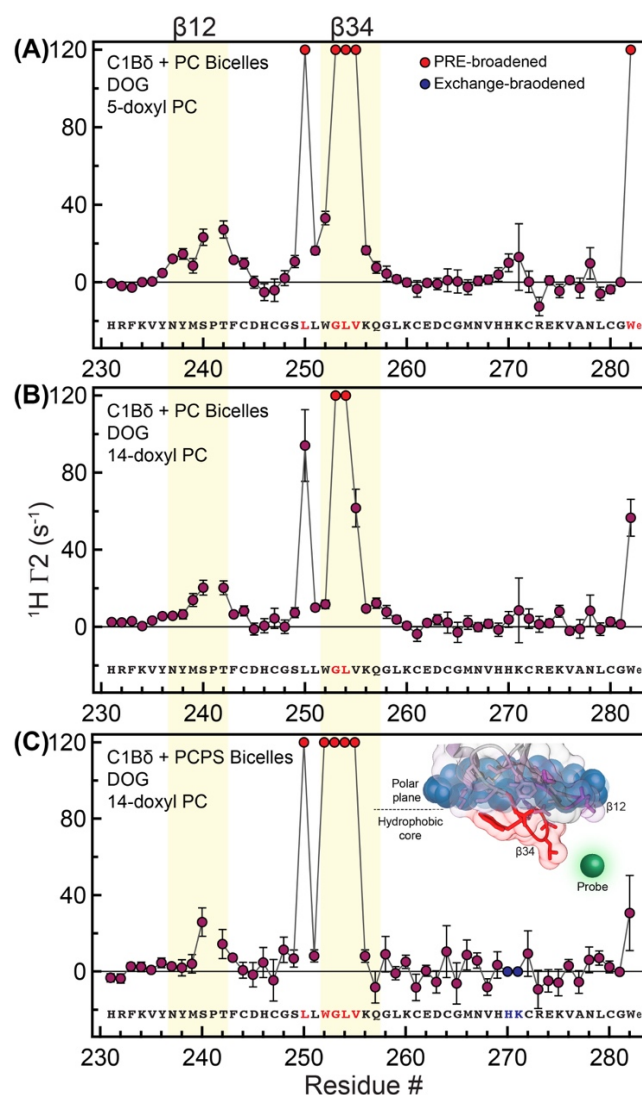
**Figure III.8 β34 loop of C1Bδ partitions more effectively into the membrane compared to β12 loop in presence of DOG**

Residue-specific $^1H_N$ PREs ($^1H_N$-$\Gamma_2$) obtained by incorporating 5-doxyl PC (A) and 14-doxyl PC (B) into PC bicelles in presence of DOG (3.2 mM, 8x to protein) are plotted. With PCPS bicelles, only 14-doxyl PC variant is used (C)The residues completely broadened beyond detection due to PRE effect were given arbitrary value of 120 s$^{-1}$ (marked red). These residues are most proximal to the membrane embedded paramagnetic probe. The residues that were exchange broadened and thus undetectable in both diamagnetic and paramagnetic samples are marked blue. The model to visually guide the membrane insertion pattern is depicted as inset in panel (C).

To further verify our findings obtained using the PRE data, we looked at $^{15}$N-edited NOESY strips of the loop region residues (**Figure III.9**). For the residues of β12 loop, we observed the NOEs that were consistent with proton-chemical shifts of head-group region and the adjacent part of the acyl chain region.[124] On the other hand, for β34 loop residues, we observed NOEs that were consistent with the acyl chain proton chemical shifts,[124] including the terminal methyl located at the end. These observations suggest that although both loops do partition in the membrane environment, β34 loop is nearest to the hydrophobic core.

Finally, the analysis of the methyl region from the $^{13}$C HSQC showed that these side chains were also significantly perturbed in the presence of DOG (**Figure III.10**). The perturbations observed for residues L250, L251, L254, and V255 of β34 loop as well as T242 from β12 loop report on their interactions with lipid moieties or DOG itself. By combining all the NMR readouts reported in this section, we conclude that C1B-DOG complex formation induces the membrane-embedded state of the protein that is dominantly anchored by the better lipid-contacts of β34 loop residues (**Figure III.8C inset model)**.

**Figure III.9 C1B loop region residues show proximity to lipidic moieties likely due to DOG-induced deeper partitioning**

Strips from the ^{15}N-edited 3D-NOESY experiment are depicted for residues of both loops. The relevant NOEs consistent with the proton chemical shifts of the lipidic moieties are color coded.
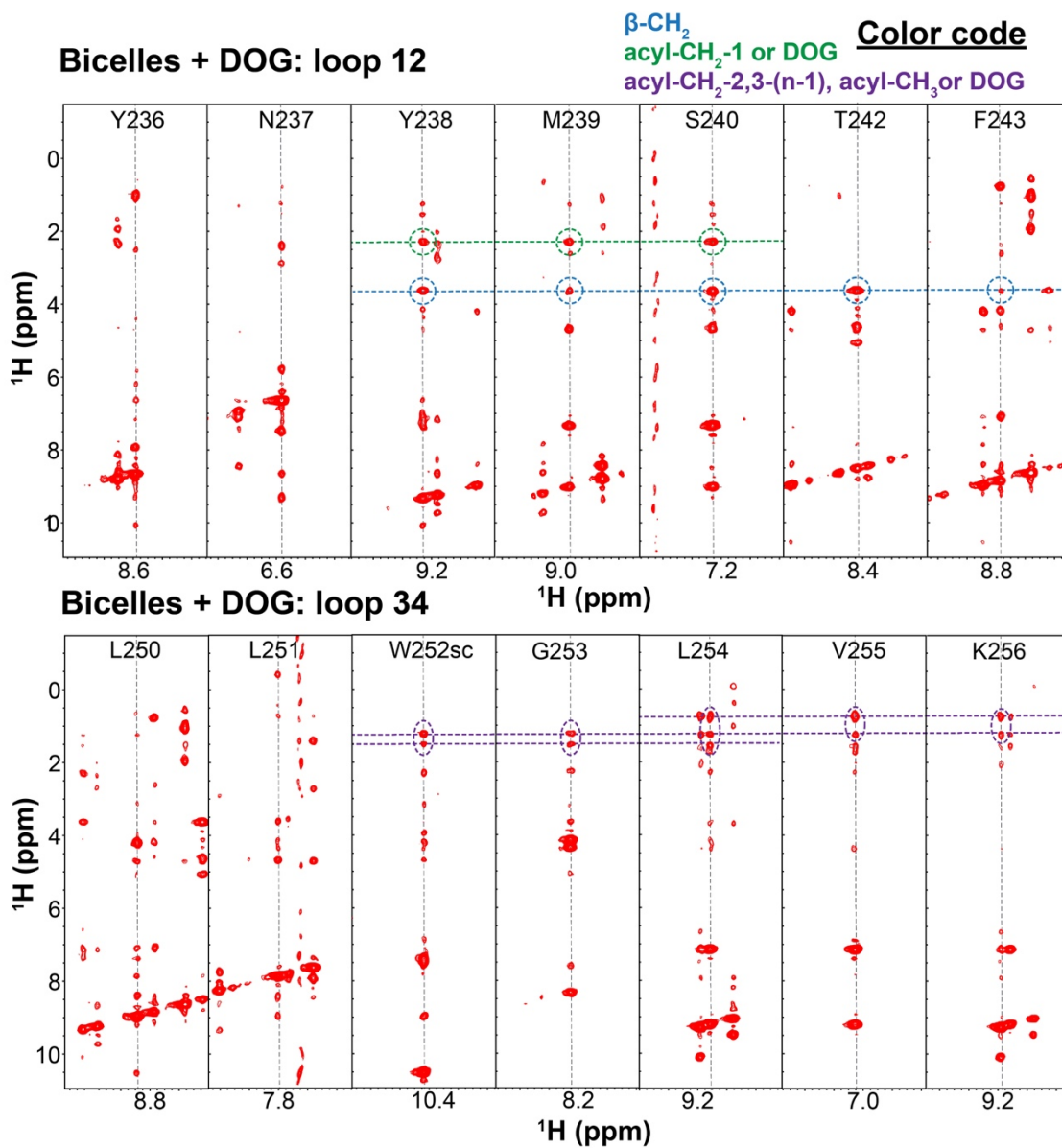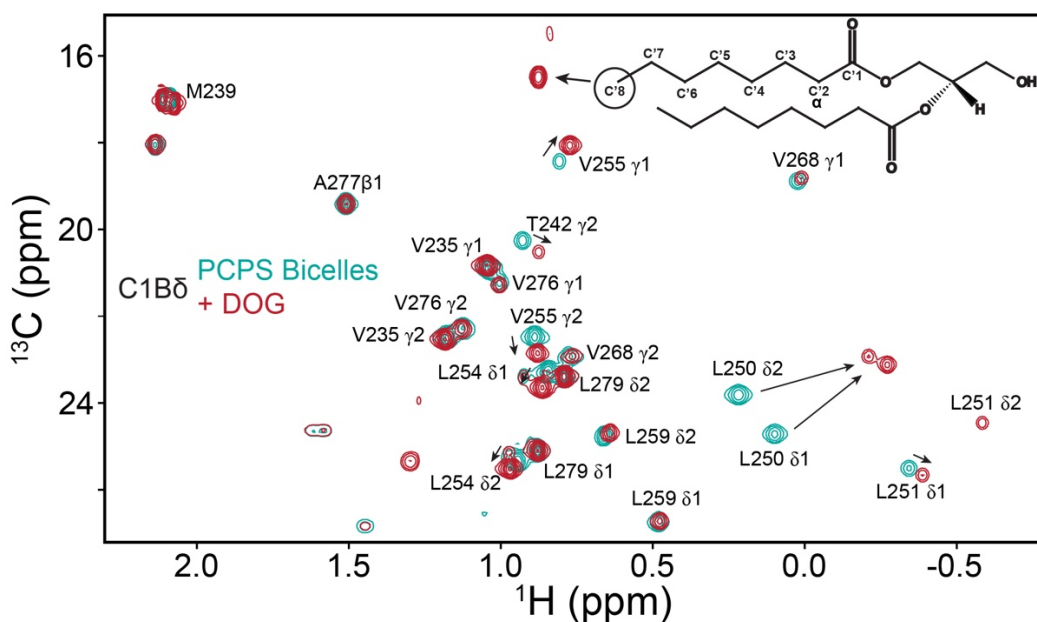
**Figure III.10 Methyl-containing hydrophobic residues of the loops are perturbed by DOG interactions**
$^{13}$C-$^1$H HSQC spectral overlay of C1B-PCPS bicelles (both 0.3 mM, 80mM total lipids, deuterated) without and with DOG, showing the methyl region.

<u>Diacylglycerol recognition by C1Bδ is linked to the solvent network of the loop region</u>

In order to get better grasp on why C1B can interact with diacylglycerol but C1A cannot (discussed in the previous chapter), we took closer look at the agonist-binding region of C1B. Using the crystal structure of C1B and CASTp,[130] we analyzed the solvent accessible area and volume of the agonist-binding pocket (**Figure III.11A**). Flanked by the hydrophobic residues, we were able to detect a polar region that is likely involved in the agonist interactions. The analogous region in the C1A counterpart is completely occluded by the indole ring of Trp (W180). This observation supports our prediction that presence and the modulation of the agonist-binding pocket might play significant role in DAG recognition.

To test this hypothesis, molecular dynamics simulations were conducted with PCPS bilayer, C1B and DAG (DOG) tri-partite system. We propose a mechanistic model of DAG recognition by C1B, using the results of this simulation for demonstration purposes. We suggest that the solvent network that is bonded to the loop region creates a polar layer within the pocket of C1B (**Figure III.11B**). During the agonist-independent interactions of C1B with membrane, the hydration layer is conserved as this region likely remains at the polar-apolar boundary of the membrane. In this state, the relatively hydrophobic residues with methyl-containing side chains of the β34 loop, in conjunction with the toggle residue W252 insert into the hydrophobic core of the membrane and "fish" for the agonists like DAG. Once encountered, the initial anchoring of DAG glycerol backbone with the C1B occurs as these moieties form H-bonds with the hydration layer of the intra-loop space (**Figure III.11B**). Such interaction further augments the hydrophobic contacts between protein (primarily β34 loop residues) and the acyl chains of DAG and/or surrounding lipids, prompting deeper insertion of the protein. Once the pocket is partitioned into the hydrophobic core, it might be energetically expensive to maintain the hydration layer. In such circumstances, the DAG molecule displaces the solvent network to the region of the protein which might still be at the polar-apolar boundary of the membrane (**Figure III.11B**). Such displacement allows DAG to directly interact with the protein residues, while the displaced solvent can interact with additional DAG molecules. We do not anticipate this process to occur linearly as described above but the sequence of events could change

103

depending upon factors such as lipid composition, depth of the protein within membrane at a given time, concentration of the DAG, and the resulting membrane altering effects.

To our knowledge, no mechanistic information about the C1-DAG recognition exists that can comprehensively explain this endogenous interaction. The model suggested here, once tested further with solution state and crystallographic approaches, can provide valuable insight that narrows this gap in our knowledge of C1 domains.
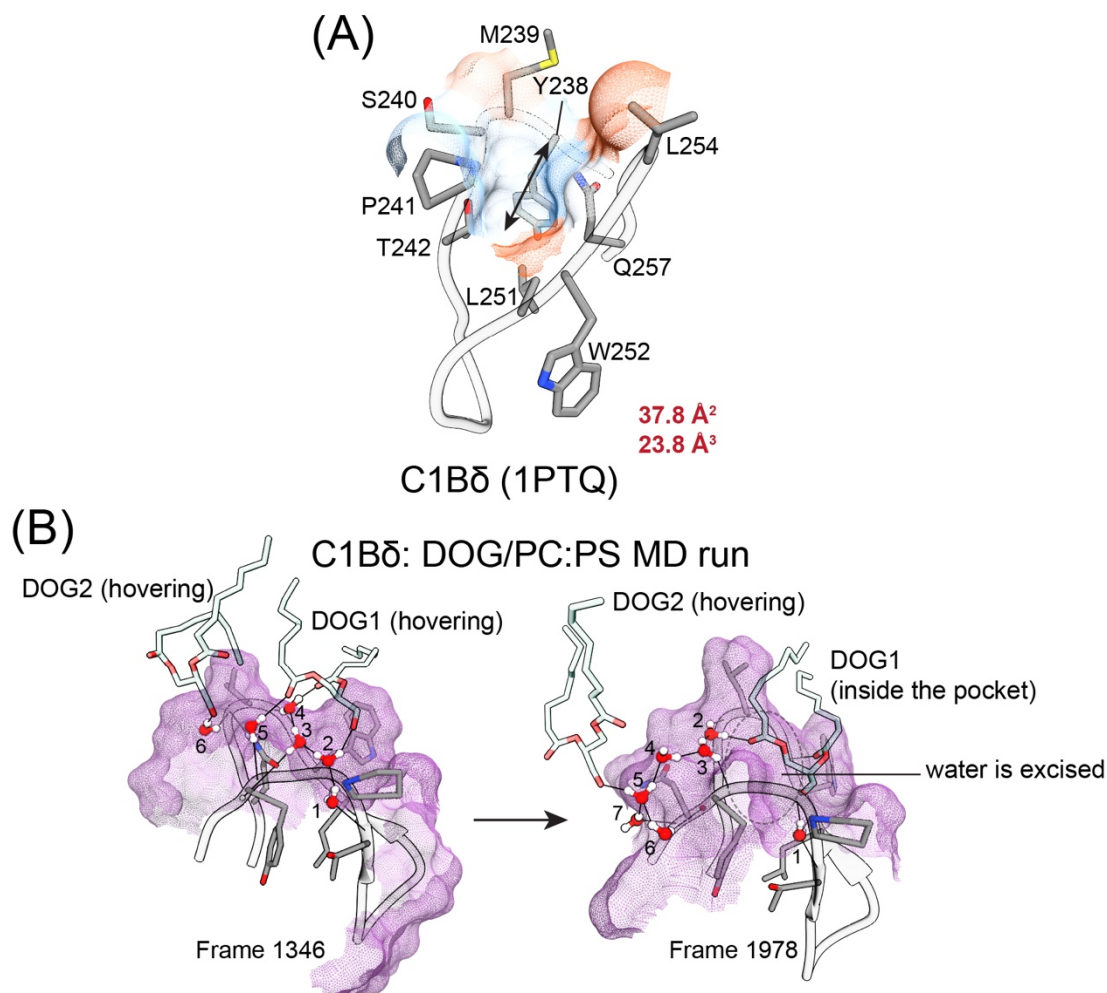
**Figure III.11 DOG recognition by C1Bδ is linked to the solvent accessibility of the agonist-binding pocket**

(A) The solvent accessible surface area and volume of the C1B agonist-binding pocket is determined by CASTp[130] analysis. The surface is colored by the Kyte-Dolittle hydrophobicity scale (-4.5, orange to +4.5, blue). (B) shows two different states encountered in the molecular dynamics simulation conducted on C1B-DOG-PCPS membrane system. The steps involved in DOG recognition could transition from the initial recruitment via solvent network (left) to complete occupation of the agonist-binding pocket (by DOG) and excision of solvent (right). Stabilizing H-bonds are depicted as solid lines. The PDB files representing these states from the simulation were provided by Dr. T.I. Igumenova.

## Phorbol ester induces virtually identical membrane insertion pattern of the agonist-binding loops of C1Bδ

After applying our NMR-based approach to the C1B-DAG system, we decided to explore whether we can apply it to non-endogenous agonists. Phorbol esters have been identified as the C1 modulators, as they induce the aberrant membrane translocation of these domains.[10, 131, 132] This DAG-mimicking property of phorbol esters is intriguing and to understand how it works, one needs to compare the membrane binding mode of phorbol ester-complexed C1 domains with that of DAG. To achieve this, we conducted NMR experiments on C1B domain in presence of phorbol esters and PC bicelles. Given the observation that phorbol esters can also translocate PKCδ to internal membranes,[131] we decided to omit anionic lipid component in this initial test.

First, we collected $^{15}$N-$^{1}$H TROSY spectra of C1B-PC bicelle complex in the presence of a short chain phorbol 12,13 di-butyrate (PDBu) and a long chain phorbol 12-myristate 13-acetate (PMA), both 1.2-fold to protein. Significant perturbations were observed upon addition of PDBu (**Figure III.12A**), primarily within the agonist-binding loop region. Same acquisition with relatively more lipophilic PMA showed no difference compared to PDBu (**Figure III.12B**). This finding indicates that the perturbations primarily report on the interaction of C1B with phorbol group and subsequent modulation of the membrane associated state. For subsequent experiments, only PDBu is used.
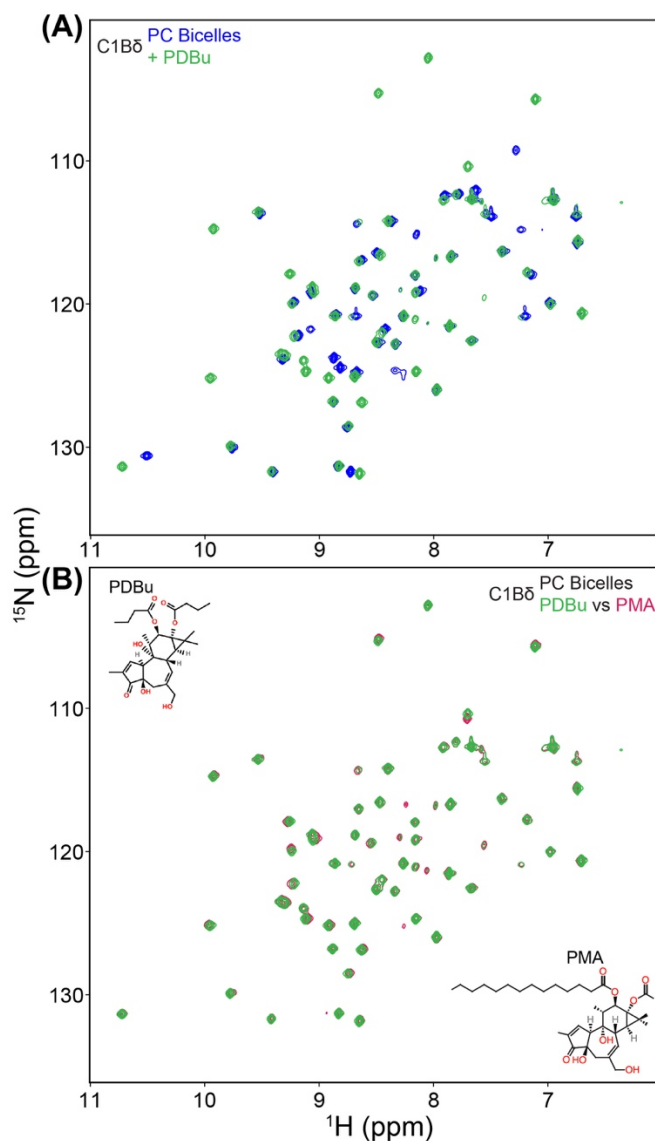
**Figure III.12 Phorbol esters stabilize the C1Bδ loop region in a manner similar to DOG**

(A) $^{15}N$-$^1H$ TROSY-HSQC spectral overlay of C1B-PC bicelles (both 0.4 mM, 100 mM total lipids) with and without PDBu. (B) Spectra with either PDBu or PMA are indistinguishable, indicating the length of the acyl chain anchor does not show major influence under these conditions.

Next, we employed the PRE-based approach using the addition of paramagnetic lipid component to the bicelles, in order to determine the pattern of membrane insertion (**Figure III.13**). In presence of 5-doxyl PC, we observed a pattern that is virtually similar to that of DOG (**Figure III.13A and 8A**). However nearly all the residues of β12 loop show systematically higher PREs with PDBu compared to DOG. On the other hand, V255 of β34 is not completely PRE broadened in presence of PDBu. These results indicate that although the overall differential contribution of the loop segments remains persistent for these agonists, β12 loop region gets inserted relatively deeper into the membrane in the presence of PDBu. To further verify this conclusion, we acquired the identical experiment in presence of 14-doxyl PC (**Figure III.13B**). Comparison with DOG data clearly supports our conclusion and provides further suggestion that β12 loop might be partitioned deeper with PDBu (**Figure III.13B and 8B, inset**).

Finally, when we used PCPS bicelles along with 14-doxyl PC, we observed the consistent pattern of attenuation in the β12 loop PREs that we saw for DOG (**Figure III.13C and 8C**). However, the PRE pattern for the β34 loop residues clearly suggests that this region partitions shallower with PDBu. In conclusion, we propose that the potency of phorbol esters to induce the activation of PKC stems from their ability to replicate the DAG-mediated membrane insertion pattern of C1 domains. The differences in the protein-interacting regions of these two agonists however likely factor into the relative insertion depth the protein can achieve.
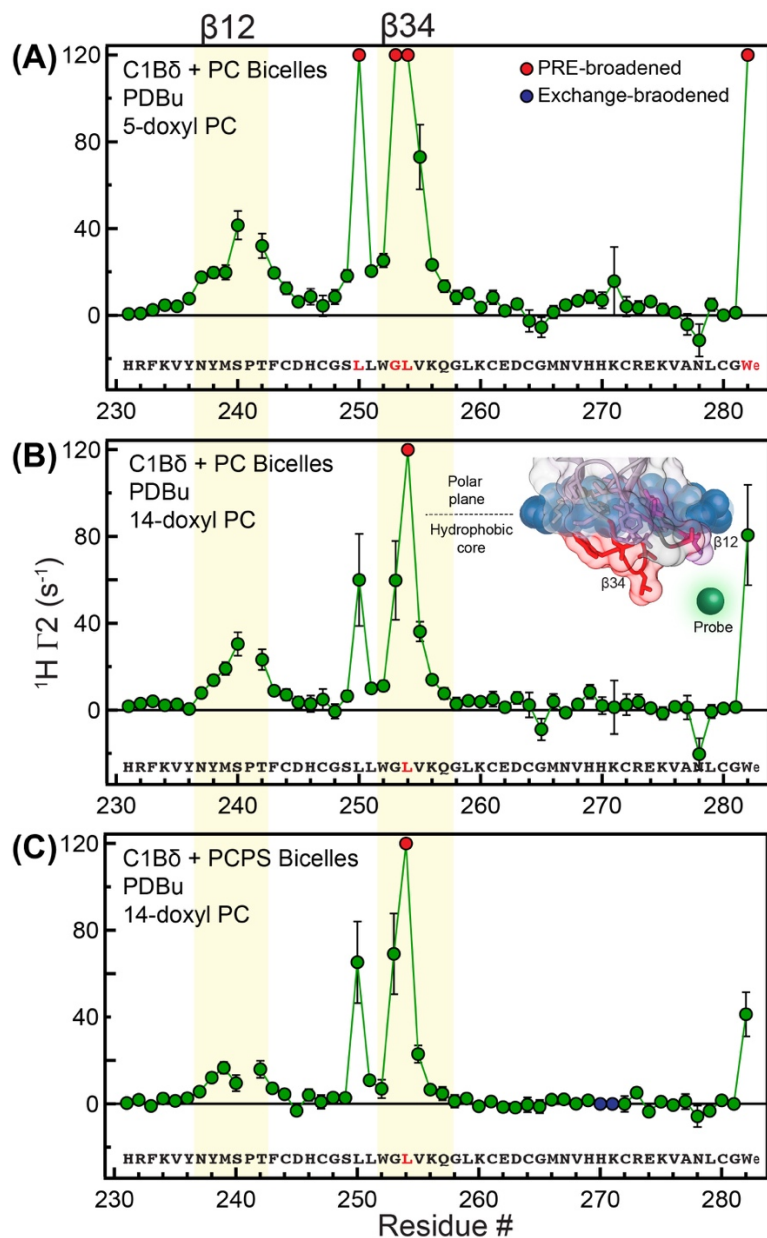
**Figure III.13 Differential PRE pattern for the agonist-binding loops of C1B is also observed with PDBu**

Residue-specific $^1H_N$ PREs ($^1H_N$-$\Gamma_2$) obtained by incorporating 5-doxyl PC (A) and 14-doxyl PC (B) into PC bicelles in presence of PDBu (0.48 mM, 1.2x to protein) are plotted. With PCPS bicelles, only 14-doxyl PC variant is used (C). The residues completely broadened beyond detection due to PRE effect were given arbitrary value of 120 s$^{-1}$ (marked red). These residues are most proximal to the membrane embedded paramagnetic probe. The residues that were exchange broadened and thus undetectable

in both diamagnetic and paramagnetic samples are marked blue. The model to visually guide the membrane insertion pattern with PDBu is depicted as inset in panel (B).

<u>Agonists with therapeutic properties exhibit substantial differences in the membrane insertion of C1Bδ</u>

After exploring the membrane-binding modes of C1B in presence of DOG and PDBu, we decided to extent the application of our approach to the other C1 agonists that show protective, rather than disruptive effects on PKC function. Two specific agonists, Prostratin and Bryostatin 1 are considered particularly promising in this regard.[24, 25, 30, 133-137] Exposure to these agents modulates the PKC activity yet does not lead to tumor formation (unlike phorbol esters).[115, 138] Bryostatin 1 (Bryo-1) in particular is peculiar in this regard as it leads to bi-phasic downregulation response from PKC,[139] a phenomenon that is typically not seen with other agonists. The underlying molecular mechanisms explaining the protective properties of these agonists are unknown. Given our comparative analysis of the C1B membrane association with DAG and phorbol esters, we propose that the agonist-specific differences likely reside in inducing differential membrane insertion of specific C1 regions.

In order to test this hypothesis, we conducted similar series of experiments mentioned before. $^{15}N$-$^{1}H$ TROSY spectra of C1B-PC bicelle complex in presence of Prostratin and Bryo-1 show significant CSPs that were distinctly different and specific to each agonist (**Figure III.14A and B**).  This was expected due to the structurally diverse nature of these agonists, and their potentially different partitioning into the membranes.

110

Prostratin architecture is highly similar to phorbol ester (PDBu), but it lacks the fatty-acyl chains and therefore likely less lipophilic. Due to the identical phorbol group, we compared the C1B-PC bicelle spectra with either PDBu or Prostratin bound state (**Figure III.14C**). The two spectra expectedly matched well, with the exceptions of residues S240 of β12 loop and L250, L254, V255 and the toggle residue W252 of β34 loop. This observation indicates that absence of one of the fatty acyl chains on Prostratin alters either the interactions of these residues with the phorbol group or it alters the depth of phorbol group that is partitioned into the membrane, leading to the residues experiencing slightly altered chemical environment. For Bryo-1, W252 and G253 amides remained exchange broadened indicating that these residues are not being stabilized by interactions with Bryo-1 or they are not partitioned deeper into the membrane.

To further shed light on membrane partitioning of the protein in response to these agonists, we conducted the PRE experiments (**Figure III.15**). Compared to DOG and PDBu, C1B β12 loop residues show systematically attenuated PRE values for both Prostratin and Bryo-1(**Figure III.15, 8A, and 13A**). A distinct exception to this general observation however was the residue S240 in presence of Prostratin. This residue shows much elevated PRE value. Between PDBu and Prostratin, this residue showed different chemical shifts (**Figure III.14C**), therefore it is likely that specific interactions of S240 with Prostratin lead to its deeper membrane insertion. For Bryo-1, the PREs observed for all the residues of the β12 loop were significantly lower compared to other agonists indicating that this region is either partitioned shallower or dynamic.
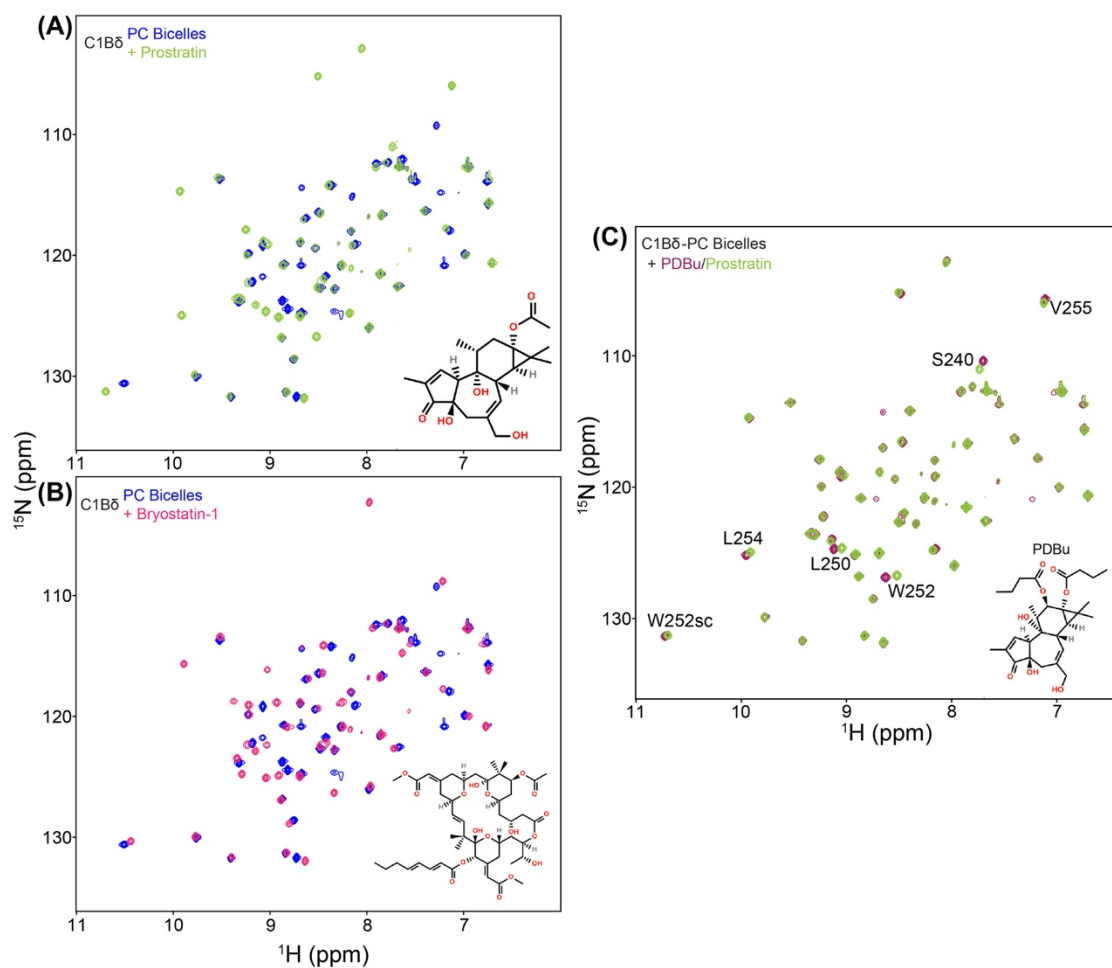
**Figure III.14 Prostratin and Bryostatin-1 induce distinctly different patterns of chemical shift perturbations upon binding to C1B-bicelle complexes**
(A) $^{15}$N-$^{1}$H TROSY-HSQC spectral overlay of C1B-PC bicelles (both 0.4 mM, 100 mM total lipids) with and without Prostratin (0.48 mM, 1.2x to protein) (B) $^{15}$N-$^{1}$H TROSY-HSQC spectral overlay of C1B-PC bicelles (both 0.3 mM, 80 mM total lipids) with and without Bryostatin-1 (0.45 mM, 1.5x to protein). (C) $^{15}$N-$^{1}$H TROSY-HSQC spectral overlay of C1B-PC bicelles (both 0.4 mM, 100 mM total lipids) with PDBu/Prostratin (both 0.48 mM, 1.2x to protein).

PREs for β34 loop residues were comparable between PDBu and Prostratin (**Figure III.15A, 13A-B**). On the other hand, for Bryo-1, with the exception of L250 and L254, all other residues showed systematically lower PREs while G253 and W252 (backbone amides) remained exchange broadened (**Figure III.15B**). These findings suggest that Bryo-1 does not induce deeper membrane insertion of either of the agonist-binding loops and the protein likely retains shallower state. This is likely related to the bulkier nature of this agonist which might result in its shallower (compared to other agonists) partitioning into the membranes.

Although these agonists are highly potent in modulating C1B-membrane interactions, they show distinct differences in the regions of the protein that partition into the membrane in response. This could be attributed to the differences in the lipophilicity of these agonists. Therefore, it is also essential to determine how the binary complexes of membrane-agonists are formed, in addition to studying the protein-membrane and protein-agonist-membrane complexes. Towards that, in the future we will use isotopically labelled agonists to obtain direct readouts of their membrane partitioning in conjunction with the in-silico approaches. Putting together the pieces of this tri-partite puzzle will eventually reveal the complete picture of C1-membrane association in response to endogenous, tumorigenic, and therapeutic agonists.
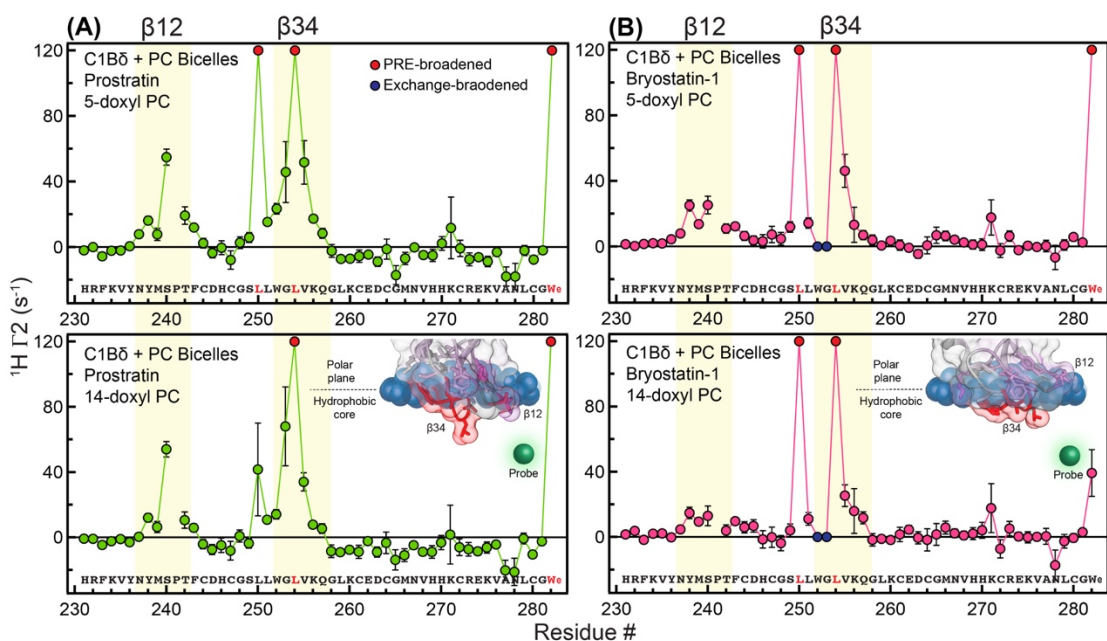
**Figure III.15 Membrane-bound states of C1B with Prostratin and Bryostatin-1 show specific differences from other agonists**

Residue-specific $^1H_N$ PREs ($^1H_N$-$\Gamma_2$) obtained by incorporating 5/14-doxyl PC with Prostratin (A) and 5/14-doxyl PC with Bryostatin-1 (B) into PC bicelles are plotted. The residues completely broadened beyond detection due to PRE effect were given arbitrary value of 120 s$^{-1}$ (marked red). These residues are most proximal to the membrane embedded paramagnetic probe. The residues that were exchange broadened and thus undetectable in both diamagnetic and paramagnetic samples are marked blue. The models to visually guide the membrane insertion patterns with these agonists are depicted as insets.

## Conclusions

The tandem arrangement of C1 domains on conventional and novel PKC isoforms indicates that they act synergistically to achieve the membrane translocation of the kinase. In PKCδ, C1B domain is believed to serve as the dominant effector of the membrane translocation in response to the agonists. The goal of this chapter was two-fold: First to determine how C1B, as opposed to C1A discussed in previous chapter, behaves in the presence of endogenous and exogenous agonists, and second to devise an experimental approach that can be applied universally to all C1 domains to understand their membrane interactions.

We demonstrate that the NMR based approach presented in this chapter can be applied successfully to probe the formation of C1-membrane and C1-agonist-membrane complexes. When applied to the C1B domain, we were able to detect the distinct membrane binding modes in presence of various agonists, at atomic resolution. The solution state nature is uniquely suited to factor in the inherent dynamics of the C1B, the fluidity of the membrane mimics, and the membrane-altering effects of the agonists (DAG specifically). In future, we will apply this approach to other C1 domains, starting with C1A of PKCδ. In addition, we will complement the experimental findings with the *in-silico* methods, not only to get better understanding of the interactions, but also to identify the current limitations associated with simulating these complex systems. The findings could guide the development of C1-specific modulatory therapeutic agents to treat disease states with underlying PKC disruption.

# References

[10] Castagna, M., Takai, Y., Kaibuchi, K., Sano, K., Kikkawa, U., and Nishizuka, Y. (1982) Direct activation of calcium-activated, phospholipid-dependent protein kinase by tumor-promoting phorbol esters, *J Biol Chem 257*, 7847-7851.

[16] Das, J., and Rahman, G. M. (2014) C1 domains: structure and ligand-binding properties, *Chem Rev 114*, 12108-12131.

[18] Zhang, G., Kazanietz, M. G., Blumberg, P. M., and Hurley, J. H. (1995) Crystal structure of the cys2 activator-binding domain of protein kinase C delta in complex with phorbol ester, *Cell 81*, 917-924.

[24] Wender, P. A., Hinkle, K. W., Koehler, M. F., and Lippa, B. (1999) The rational design of potential chemotherapeutic agents: synthesis of bryostatin analogues, *Med Res Rev 19*, 388-407.

[25] Wender, P. A., Baryza, J. L., Brenner, S. E., DeChristopher, B. A., Loy, B. A., Schrier, A. J., and Verma, V. A. (2011) Design, synthesis, and evaluation of potent bryostatin analogs that modulate PKC translocation selectivity, *Proc Natl Acad Sci U S A 108*, 6721-6726.

[27] Stahelin, R. V., Digman, M. A., Medkova, M., Ananthanarayanan, B., Rafter, J. D., Melowic, H. R., and Cho, W. (2004) Mechanism of diacylglycerol-induced membrane targeting and activation of protein kinase Cdelta, *J Biol Chem 279*, 29501-29512.

[30] Kortmansky, J., and Schwartz, G. K. (2003) Bryostatin-1: a novel PKC inhibitor in clinical development, *Cancer Invest 21*, 924-936.

[35] Durr, U. H., Gildenberg, M., and Ramamoorthy, A. (2012) The magic of bicelles lights up membrane protein structure, *Chem Rev 112*, 6054-6074.

[89] Stewart, M. D., Cole, T. R., and Igumenova, T. I. (2014) Interfacial partitioning of a loop hinge residue contributes to diacylglycerol affinity of conserved region 1 domains, *J Biol Chem 289*, 27653-27664.

[99] Delaglio, F., Grzesiek, S., Vuister, G. W., Zhu, G., Pfeifer, J., and Bax, A. (1995) NMRPipe: a multidimensional spectral processing system based on UNIX pipes, *J Biomol NMR 6*, 277-293.

[100] Lee, W., Tonelli, M., and Markley, J. L. (2015) NMRFAM-SPARKY: enhanced software for biomolecular NMR spectroscopy, *Bioinformatics 31*, 1325-1327.

[108] Ziemba, B. P., Booth, J. C., and Jones, D. N. (2011) 1H, 13C and 15N NMR assignments of the C1A and C1B subdomains of PKC-delta, *Biomol NMR Assign 5*, 125-129.

[109] Newport, T. D., Sansom, M. S P., and Stansfeld, P. J. (2018) The MemProtMD database: a resource for membrane-embedded protein structures and their lipid interactions, *Nucleic Acids Research 47*, D390-D397.

[113] Leach, K. L., and Blumberg, P. M. (1985) Modulation of protein kinase C activity and [3H]phorbol 12,13-dibutyrate binding by various tumor promoters in mouse brain cytosol, *Cancer Res 45*, 1958-1963.

[114] Pasti, G., Lacal, J. C., Warren, B. S., Aaronson, S. A., and Blumberg, P. M. (1986) Loss of mouse fibroblast cell response to phorbol esters restored by microinjected protein kinase C, *Nature 324*, 375-377.

[115] Hennings, H., Blumberg, P. M., Pettit, G. R., Herald, C. L., Shores, R., and Yuspa, S. H. (1987) Bryostatin 1, an activator of protein kinase C, inhibits tumor promotion by phorbol esters in SENCAR mouse skin, *Carcinogenesis 8*, 1343-1346.

[116] Lee, J., Marquez, V. E., Blumberg, P. M., Krausz, K. W., and Kazanietz, M. G. (1993) Conformationally constrained analogues of diacylglycerol (DAG)--II. Differential interaction of delta-lactones and gamma-lactones with protein kinase C (PK-C), *Bioorg Med Chem 1*, 119-123.

[117] Choi, S. H., Hyman, T., and Blumberg, P. M. (2006) Differential effect of bryostatin 1 and phorbol 12-myristate 13-acetate on HOP-92 cell proliferation is mediated by down-regulation of protein kinase Cdelta, *Cancer Res 66*, 7261-7269.

[118] Iwahara, J., Schwieters, C. D., and Clore, G. M. (2004) Ensemble approach for NMR structure refinement against (1)H paramagnetic relaxation enhancement data arising from a flexible paramagnetic group attached to a macromolecule, *J Am Chem Soc 126*, 5879-5896.

[119] Sattler, M., and Fesik, S. W. (1996) Use of deuterium labeling in NMR: overcoming a sizeable problem, *Structure 4*, 1245-1249.

[120] Vold, R. R., Prosser, R. S., and Deese, A. J. (1997) Isotropic solutions of phospholipid bicelles: a new membrane mimetic for high-resolution NMR studies of polypeptides, *J Biomol NMR 9*, 329-335.

[121] Glover, K. J., Whiles, J. A., Wu, G., Yu, N., Deems, R., Struppe, J. O., Stark, R. E., Komives, E. A., and Vold, R. R. (2001) Structural evaluation of phospholipid bicelles for solution-state studies of membrane-associated biomolecules, *Biophys J 81*, 2163-2171.

[122] Luchette, P. A., Vetman, T. N., Prosser, R. S., Hancock, R. E., Nieh, M. P., Glinka, C. J., Krueger, S., and Katsaras, J. (2001) Morphology of fast-tumbling bicelles: a small angle neutron scattering and NMR study, *Biochim Biophys Acta 1513*, 83-94.

[123] Lee, D., Walter, K. F., Bruckner, A. K., Hilty, C., Becker, S., and Griesinger, C. (2008) Bilayer in small bicelles revealed by lipid-protein interactions using NMR spectroscopy, *J Am Chem Soc 130*, 13822-13823.

[124] Bjorneras, J., Nilsson, M., and Maler, L. (2015) Analysing DHPC/DMPC bicelles by diffusion NMR and multivariate decomposition, *Biochim Biophys Acta 1848*, 2910-2917.

[125] Vestergaard, M., Kraft, J. F., Vosegaard, T., Thogersen, L., and Schiott, B. (2015) Bicelles and Other Membrane Mimics: Comparison of Structure, Properties, and Dynamics from MD Simulations, *J Phys Chem B 119*, 15831-15843.

[126] Mineev, K. S., Nadezhdin, K. D., Goncharuk, S. A., and Arseniev, A. S. (2016) Characterization of Small Isotropic Bicelles with Various Compositions, *Langmuir 32*, 6624-6637.

[127] Dancea, F., Kami, K., and Overduin, M. (2008) Lipid interaction networks of peripheral membrane proteins revealed by data-driven micelle docking, *Biophys J 94*, 515-524.

[128] Clore, G. M., and Iwahara, J. (2009) Theory, practice, and applications of paramagnetic relaxation enhancement for the characterization of transient low-population states of biological macromolecules and their complexes, *Chem Rev 109*, 4108-4139.

[129] Koppisetti, R. K., Fulcher, Y. G., Jurkevich, A., Prior, S. H., Xu, J., Lenoir, M., Overduin, M., and Van Doren, S. R. (2014) Ambidextrous binding of cell and membrane bilayers by soluble matrix metalloproteinase-12, *Nat Commun 5*, 5552.

[130] Binkowski, T. A., Naghibzadeh, S., and Liang, J. (2003) CASTp: Computed Atlas of Surface Topography of proteins, *Nucleic Acids Res 31*, 3352-3355.

[131] Wang, Q. J., Bhattacharyya, D., Garfield, S., Nacro, K., Marquez, V. E., and Blumberg, P. M. (1999) Differential localization of protein kinase C delta by phorbol esters and related compounds using a fusion protein with green fluorescent protein, *J Biol Chem 274*, 37233-37239.

[132] Wang, Q. J., Fang, T. W., Fenick, D., Garfield, S., Bienfait, B., Marquez, V. E., and Blumberg, P. M. (2000) The lipophilicity of phorbol esters as a critical factor in determining the pattern of translocation of protein kinase C delta fused to green fluorescent protein, *J Biol Chem 275*, 12136-12146.

[133] Szallasi, Z., and Blumberg, P. M. (1991) Prostratin, a nonpromoting phorbol ester, inhibits induction by phorbol 12-myristate 13-acetate of ornithine decarboxylase, edema, and hyperplasia in CD-1 mouse skin, *Cancer Res 51*, 5355-5360.

[134] Miana, G. A., Riaz, M., Shahzad-ul-Hussan, S., Paracha, R. Z., and Paracha, U. Z. (2015) Prostratin: An Overview, *Mini Rev Med Chem 15*, 1122-1130.

[135] Shen, X., Xiong, G. L., Jing, Y., Xiao, H., Cui, Y., Zhang, Y. F., Shan, Y. J., Xing, S., Yang, M., Liu, X. L., Dong, B., Wang, L. S., Luo, Q. L., Yu, Z. Y., and Cong, Y. W. (2015) The protein kinase C agonist prostratin induces differentiation of human myeloid leukemia cells and enhances cellular differentiation by chemotherapeutic agents, *Cancer Lett 356*, 686-696.

[136] Alotaibi, D., Amara, S., Johnson, T. L., and Tiriveedhi, V. (2018) Potential anticancer effect of prostratin through SIK3 inhibition, *Oncol Lett 15*, 3252-3258.

[137] Desimio, M. G., Giuliani, E., Ferraro, A. S., Adorno, G., and Doria, M. (2018) In Vitro Exposure to Prostratin but Not Bryostatin-1 Improves Natural Killer Cell Functions Including Killing of CD4(+) T Cells Harboring Reactivated Human Immunodeficiency Virus, *Front Immunol 9*, 1514.

[138] Szallasi, Z., Denning, M. F., Smith, C. B., Dlugosz, A. A., Yuspa, S. H., Pettit, G. R., and Blumberg, P. M. (1994) Bryostatin 1 protects protein kinase C-delta from down-regulation in mouse keratinocytes in parallel with its inhibition of phorbol ester-induced differentiation, *Mol Pharmacol 46*, 840-850.

[139] Lorenzo, P. S., Bogi, K., Hughes, K. M., Beheshti, M., Bhattacharyya, D., Garfield, S. H., Pettit, G. R., and Blumberg, P. M. (1999) Differential roles of the tandem C1 domains of protein kinase C delta in the biphasic down-regulation induced by bryostatin 1, *Cancer Res 59*, 6137-6144.

CHAPTER IV NON-NATIVE METAL ION REVEALS THE ROLE OF

ELECTROSTATICS IN SYNAPTOTAGMIN 1 C2-MEMBRANE INTERACTIONS[*]

**Background**

Ca$^{2+}$-dependent phospholipid-binding C2 domains[41, 140] are integral structural

elements of the proteins involved in signal transduction and membrane trafficking.[12, 141-]

[143] The regulation of numerous cellular activities such as neurotransmitter release,

cellular growth, and transcription depends on the interaction of these effector proteins

with membranes via C2 domains.[8, 144] Therefore, understanding the mechanism of how

C2 domains interact with lipid membranes is a crucial step towards elucidating their

molecular role in cellular signal transduction. In this work, we used the C2A and C2B

domains of Synaptotagmin 1 (Syt1), a major Ca$^{2+}$ sensor of evoked neurotransmission,[45]

to gain insight into the determinants of C2-membrane interactions.

The core of C2A/B domains has a characteristic β-sandwich fold that consists of

8 antiparallel β-strands, connected by loop regions (**Figure IV.1A** and **2A**).[44, 47] The

Ca$^{2+}$-sensing function of Syt1 resides on the aspartate-rich loops at the tips of C2A/B

domains that can bind up to 3 (C2A) and 2 (C2B) Ca$^{2+}$ ions.[48, 49] Ca$^{2+}$ binding triggers

the peripheral interaction of the C2 domains with membranes containing anionic

phospholipids, such as phosphatidylserine (PtdSer),[145-148] but has a negligible effect on

the average conformation of the protein backbone.[47, 55, 149, 150]  Rather, interactions with

metal ions attenuate the dynamics of the loop regions that have considerable flexibility

in the apo forms of C2 domains.[151, 152]

Calcium has been proposed to promote C2-membrane association by two

different mechanisms.  First, $Ca^{2+}$ binding makes the C2 domain more electropositive,

by neutralizing the negatively charged loop region.[55, 77]  Second, $Ca^{2+}$ acts to bridge the

C2 domain to membranes by directly coordinating negatively charged lipid head

groups.[50, 54, 63]  In the former $Ca^{2+}$ acts as a general "electrostatic switch" to promote

long-range Coulombic interactions with negatively charged membranes.  In the latter

$Ca^{2+}$ plays a specific role that involves the rearrangement of its coordination sphere.  In

addition to electrostatics, hydrophobic interactions mediated by residues surrounding the

loop regions contribute to the C2-membrane interaction.[153, 154]

Although the dominant role of electrostatics in the C2-membrane interactions is

well established, the contributions made by these general and specific roles of $Ca^{2+}$

remain unclear.  For instance, mutations that disrupt $Ca^{2+}$ binding to the C2A domain of

Syt1 implicate the $Ca^{2+}$-induced change in the electrostatic surface potential as a major

factor.[155]  Alternatively, the finding that charge-reversal mutations mimicking $Ca^{2+}$

binding cannot support membrane interaction of the C2 domain in PKCβII points

towards the importance of direct metal-lipid bridging.[156]  In this context, $Ca^{2+}$ surrogates

in the form of non-native divalent metal ions can be used as valuable tools to gain

insight into the contribution of long-range Coulombic interactions and metal ion-lipid

bridging to membrane binding.

We previously demonstrated that toxic heavy metal ions, $Cd^{2+}$ and $Pb^{2+}$, bind to the C2 domain of PKCα with higher affinity than $Ca^{2+}$.[69, 82] Both metal ions bind to the loop region of the C2 domain with the same stoichiometry as $Ca^{2+}$. However, the functional consequences are strikingly different: $Pb^{2+}$ supports the C2-membrane interactions, whereas $Cd^{2+}$ does not. We attributed this behavior to the differences in Lewis acidity and coordination preferences of $Cd^{2+}$ and $Pb^{2+}/Ca^{2+}$.[82] We speculated that the preference for low coordination numbers[86] and soft ligands[157] impairs the ability of $Cd^{2+}$ to directly coordinate the oxygens of lipid head-groups. The implication of these findings is that the long-range Coulombic interactions alone are not sufficient to drive membrane association of the PKC C2 domain.

In the present work, we examined the two C2 domains of Syt1 to determine whether the behavior of the PKC C2 domain could be generalized to other $Ca^{2+}$-dependent C2 domains. The C2A and C2B domains share 38% sequence identity and occur in tandem in the cytosolic part of Syt1 where they are separated by an 8-residue linker. We demonstrate that $Cd^{2+}$ serves as a good structural surrogate for $Ca^{2+}$ in the individual C2A and C2B domains, but can support their membrane association only in the context of full-length Syt1. Our results illustrate the significance of both, long-range Coulombic interactions and high effective local lipid concentrations in the native protein environment, for the membrane association of C2 domains.

## Experimental procedures

### Materials

1-palmitoyl-2-oleoyl-sn-glycero-3-phosphocholine (POPC), 1-palmitoyl-2-oleoyl-sn-glycero-3-phospho-L-serine (POPS), 1-palmitoyl-2-oleoyl-sn-glycero-3-phospho-(1'-rac-glycerol) (POPG), dimethyldioctadecylammonium (DDAB), and 1,2-dioleoyl-sn-glycero-3-phosphoethanolamine-N-(5-dimethylamino-1-naphthalenesulfonyl) (dansyl-PE) were obtained from Avanti Polar Lipids Inc. (Alabaster, AL). Residual divalent metal ions were removed from all buffers with the ion-chelating resin, Chelex 100 (Sigma-Aldrich). The stock solutions of metal ions were prepared using the following salts: Tb(III) chloride hexahydrate (Acros Organics), Cd(II) nitrate tetrahydrate (Sigma-Aldrich), and standardized 1 M solution of Ca (II) chloride (Fluka Analytical). Sigmacote® and IgG from human serum (both from Sigma-Aldrich) were used to coat quartz cuvettes for $Tb^{3+}$ luminescence and protein-to-membrane Förster resonance energy transfer (FRET) experiments, respectively. The cDNA of murine Syt1 was purchased from Open Biosystems (GE Life Sciences).

### Protein expression and purification

The following Syt1 domains: C2A (residues 137-265), C2B (residues 271-421), and C2AB (residues 137-421) were cloned into a pET-SUMO vector (Novagen, Madison, WI). To improve the SUMO protease cleavage efficiency of the C2A-containing constructs, a serine residue was added at the N-terminus using the QuikChange mutagenesis kit (Stratagene, La Jolla, CA). The sole cysteine residue of C2B at position 277 was replaced with a serine to eliminate the need for reducing agents

124

that are known to form complexes with metal ions. The C277S variant of C2B was used for all experiments with the exception of crystallographic studies. For the EPR and vesicle sedimentation experiments, the cytosolic Syt1 constructs included: C2A (residues 96-265), C2B (residues 249-421) and C2AB (residues 136-421), which were modified, expressed and purified as described previously.[61] The full-length Syt1 from *R. norvegicus* (1-421) was previously cloned into a pET-28a vector with an N-terminal 6xHis tag.[158] Native cysteines (C73A, C74A, C76A, C78A, C82S, and C277S) were mutated using the QuickChange site-directed mutagenesis kit, and single cysteine point mutations were introduced into the cysteine-free construct using the same method at positions M173C or V304C. DNA sequences for all mutations were verified by DNA sequencing (Genewiz, South Plainfield, NJ).

Fusion proteins comprising the 6xHis-tagged SUMO and Syt1 domains were expressed in BL21(DE3) (C2A and C2AB) and Rosetta(DE3) (C2B) cells. For the preparation of [U-$^{15}$N] and [U-$^{15}$N,$^{13}$C]-enriched NMR samples, the proteins were expressed in M9 medium containing either [U-$^{15}$N] NH$_4$Cl or [U-$^{15}$N] NH$_4$Cl/[U-$^{13}$C] D-glucose (Cambridge Isotope Laboratories). The induction of protein expression was initiated by adding 0.5 mM isopropyl β-D-1-thiogalactopyranoside (IPTG) to the medium and carried out for 16-18 hours at 15 °C.

The cells were harvested, re-suspended in ice-cold lysis buffer composed of 50 mM Tris-HCl at pH 7.5, 100 mM NaCl, 100 μM CaCl$_2$, and 1 mM DTT, and lysed with sonication. The lysate was loaded onto 2 x 5 mL HisTrap HP columns (pre-equilibrated with buffer solution containing 20 mM Tris pH 7.5, 500 mM NaCl, and 5 mM

Imidazole), from which the fusion protein was eluted with a 5-500 mM imidazole gradient.  Fractions containing fusion protein were exchanged into a SUMO protease buffer (50 mM Tris-HCl at pH 8.0, 150 mM NaCl, 1 mM TCEP) on a HiPrep 26/10 desalting column.  The cleavage reaction was initiated by adding SUMO protease to a final concentration of 10-12 μg/mL and allowed to proceed for 3 hours at 25 (30) °C to attain >90 % cleavage efficiency for C2B (C2A and C2AB).  The 6xHis-tagged SUMO was removed on a 2 x 5 mL HisTrap HP column.

Anion-exchange chromatography was used to further purify C2A and C2AB. The protein-containing fractions were exchanged into a buffer containing 100 μM EDTA and 20-50 mM Tris-HCl at pH 8.5 (C2A) or 7.2 (C2AB).  The proteins were loaded onto a 2 x 5 ml HiTrap Q HP column (GE Healthcare) and eluted with NaCl gradient.  C2B was purified in a similar manner, but using cation-exchange chromatography on a 2 x 5 ml HiTrap SP HP column (GE Healthcare) in a buffer containing 50 mM Tris-HCl at pH 7.0 and 100 μM EDTA.

EDTA was removed using four consecutive steps of 15-fold dilution and subsequent concentration with Vivaspin® concentrators (Sartorius) with a molecular mass cutoff of 5,000.  As an alternative method of EDTA removal, protein solutions were passed four times through the desalting PD MidiTrap G-25 columns.  The proteins were subsequently concentrated and exchanged into decalcified experiment-specific buffer (*vide infra*).  The molecular masses of all proteins were verified by MALDI-TOF mass spectrometry.

For EPR and sedimentation experiments carried out in D.S.C.'s laboratory, the expression and purification of the cytosolic constructs (C2A, C2B, C2AB) followed previously described protocols[147, 148, 159] with the following modifications. First, BL21(DE3) rather than BL21(DE3)pLysS cells were used for transformation to increase protein expression, and maximal cleavage of the GST tag was obtained by treating with thrombin on column at room temperature rather than at 4 °C. In addition, a HiTrap SP column (GE Healthcare) was used for ion exchange purification of the C2AB construct (residues 136-421) and higher initial salt concentrations (150 mM) were employed for the C2B and C2AB ion exchange procedure to prevent protein precipitation. Buffers used to purify C2AB using ion exchange were: SPA: 50 mM MOPS, 1 mM $CaCl_2$, 150 mM NaCl, pH 7.2; and SPB: 50 mM MOPS, 1 mM $CaCl_2$, 800 mM NaCl, pH 7.2. For EPR spectroscopy, the isolated domains were labeled as described previously.[159]

For the full-length Syt1, BL21(DE3)-RIL cells (Invitrogen, Waltham, MA) were transformed, and 50 mL precultures of TB medium containing 50 μg/L Kanamycin were grown for approximately 12-15 hours at 37 °C before addition of the preculture to 950 mL of TB medium and 50 μg/L Kanamycin in a 2.8 L Fernbach flask. This culture was then grown for approximately 2 h at 37 °C until an $OD_{600}$ of 0.8−1 was reached. Protein expression was induced with 0.5 mM IPTG after adding 50 μg/L chloramphenicol to the cell culture. The cells were grown for 15-18 h at 22 °C with 200 rpm shaking before pelleting by centrifugation at 12,000 rpm for 12 min at 4 °C. The pellet was first resuspended in extraction buffer 1 (20 mM HEPES, 500 mM NaCl, 8 mM imidazole, pH 7.4), and then an equal volume of extraction buffer 2 was added (20 mM HEPES, 500

mM NaCl, 8 mM imidazole, 10% Na-Cholate, pH 7.4).  Protease inhibitors (2 μL/mL

leupeptin, 5 μL/mL aproptinin, and 10 μL/mL AEBSF) and 750U Benzonase nuclease

were added to the cell suspension and the cells lysed using a French press. Cell debris

was pelleted by ultracentrifgation at 18,000 rpm for 35 min at 4 °C.  The supernatant

was added to a pre-equilibrated Ni-NTA column and allowed to bind to the resin

overnight at 4 °C with shaking.  The lysate was then allowed to flow through the column

and the resin was washed with 3 column volumes of wash buffer (20 mM HEPES, 300

mM NaCl, 40 mM Imidazole, 1% CHAPS, pH 7.4).  For spin labeling, the column was

left in a small volume of wash buffer and ~1 mg of MTSL (in ethanol) was added to the

column which was left in the dark at 4 degrees C overnight with shaking.  The resin was

then washed again with 3 column volumes of wash buffer, and subsequently eluted in

excess elution buffer (20 mM Tris, 300 mM NaCl, 400 mM Imidazole, 1% CHAPS, pH

7.4) until no protein absorbance at 280 nm was detected in the flow through.  Lysate,

flow through, wash, and elutions were run on a 12% SDS-Page gel to check for protein

purity.  Clean fractions were collected and concentrated in 30 K MWT cut-off

concentrator.  5 mg thrombin per L of protein grown was added and then allowed to

dialyze (20 mM HEPES, 300 mM NaCl, 1 mM EDTA, 1% CHAPS, pH 7.4) overnight

at 4 °C.

To ensure the complete removal of any nucleic acid contamination, the protein

was further purified by FPLC using an AKTA Prime chromatography system

(Amersham Biosciences, Piscataway NJ).  A HiTrap SP column (GE Healthcare) was

run using Akta A (20 mM HEPES, 1% CHAPS, pH 7.4) and Akta B (20 mM HEPES,

1000 mM NaCl, 1% Chaps, pH 7.4) buffers to create a 0-1 M salt gradient. Protein

fractions were analyzed using SDS-PAGE (12% gel) and the 260/280 nm absorption

ratios. Clean protein fractions were collected and concentrated in 30 K MWT Amicon

concentrators. Protein concentration was determined using a Bradford assay (Pierce,

Rockford, IL).

The reconstitution of full-length Syt1 followed a procedure previously described

(Kessling et al., 2013). The full-length Syt1 was reconstituted into either:

POPC:Cholesterol (Chol) (80:20), POPC:POPS (85:15), or POPC:POPS:DDAB

(70:15:15) liposomes. The appropriate lipid mixture was combined in chloroform and

methanol and evaporated under $N_2$ gas with stirring. The lipids were then put under

vacuum overnight and the lipid films subsequently dissolved in reconstitution buffer (20

mM HEPES, 150 mM KCL, 1% CHAPS, pH 7.4). The protein solution was added to

produce a 1:250 protein-to-lipid ratio. The mixture was left to incubate for 1.5 hours at

room temp with occasional stirring. The mixture was then diluted below the critical

micellar concentration by the addition of metal free buffer (20 mM HEPES, 150 KCl,

pH 7.4), and the protein was then dialyzed into metal free buffer to remove detergent.

### Crystallization, structure determination and refinement

The crystallization samples contained: (i) 17 mg/mL C2A and 7 mM Cd(II)

nitrate in a 20 mM MES buffer at pH 6.0; and (ii) 21 mg/mL C2B, 5 mM Cd(II) nitrate,

and 0.8 mM TCEP in a 10 mM HEPES buffer at pH 7.0. Automated screening for

crystallization was carried out using the sitting drop vapour-diffusion method with an

Art Robbins Instruments Phoenix system in the *X-ray Crystallography Core Laboratory*

at UTHSCSA.  Crystals for $Cd^{2+}$-bound C2A were obtained from Qiagen PEGs II Suite condition #80 (0.1 M tri-sodium citrate, 16% polyethylene glycol 6000) at 4 °C. Crystals for $Cd^{2+}$-bound C2B were obtained from Rigaku Precipitant Synergy condition #116 (13.4% polyethylene glycol 400, 10.05% polyethylene glycol 1000, 0.15 M potassium phosphate dibasic/sodium phosphate monobasic pH 6.5) at 22 °C.

Data collection and refinement statistics are given in **Table IV.1** below. Difference Fourier map analysis of both structures showed that the modeled $Cd^{2+}$ are indeed heavy atoms when compared to the anomalous signal observed for sulfur atoms in the proteins.  Anomalous difference Fourier peaks were observed at 23.3 and 21.4 r.m.s.d. for C2A-$Cd^{2+}$ and C2B-$Cd^{2+}$, respectively.  The coordinates of the $Cd^{2+}$ complexes were deposited in the Protein Data Bank under accession codes 5T0R (C2A) and 5T0S (C2B).

**Table IV.1 X-ray diffraction data collection and refinement statistics for the Cd²⁺ complexes of C2A and C2B**

|  | C2A Cd$^{2+}$ | C2B Cd$^{2+}$ |
|---|---|---|
| **Data collection** | | |
| Space group | $P2_12_12_1$ | $P2_12_12_1$ |
| Cell dimensions | | |
| $\quad a, b, c$ (Å) | 28.1, 63.3, 76.1 | 41.0, 42.0, 80.7 |
| $\quad \alpha, \beta, \gamma$ (°) | 90, 90, 90 | 90, 90, 90 |
| | | |
| Wavelength (Å) | 1.54178 | 1.54178 |
| Resolution (Å) | 38.07 - 1.95 (2.06 - 1.95) | 41.95 - 1.42 (1.49 - 1.42) |
| $R_{sym}$ | 0.107 (0.373) | 0.051 (0.544) |
| $R_{pim}$ | 0.057 (0.221) | 0.027 (0.302) |
| Mean ($I/\sigma I$) | 13.0 (3.2) | 18.7 (2.6) |
| Completeness (%) | 96.9 (85.0) | 99.0 (94.3) |
| Redundancy | 4.2 (3.5) | 4.4 (4.0) |
| Wilson B-factor (Å$^2$) | 24.2 | 12.1 |
| | | |
| **Refinement** | | |
| Resolution (Å) | 38.07 - 1.95 | 36.54 - 1.42 |
| No. Unique Reflections | 10,031 | 26,889 |
| $R_{work}$ / $R_{free}$ | 0.186/0.229 | 0.159/0.198 |
| No. Atoms | | |
| $\quad$ Protein | 1,017 | 1,285 |
| $\quad$ Ligand | 1 (Cd$^{2+}$) | 2 (Cd$^{2+}$, Na$^+$) |
| $\quad$ Solvent | 128 | 212 |
| $B$-factors (Å$^2$) | | |
| $\quad$ Protein | 31.2 | 17.1 |
| $\quad$ Ligand | 22.8 | 17.5 |
| $\quad$ Solvent | 35.8 | 31.0 |
| R.m.s. deviations | | |
| $\quad$ Bond lengths (Å) | 0.008 | 0.006 |
| $\quad$ Bond angles (°) | 1.134 | 1.037 |
| Ramachandran Plot | | |
| $\quad$ Favored (%) | 98.4 | 96.2 |
| $\quad$ Allowed (%) | 1.6 | 3.8 |
| $\quad$ Outliers (%) | 0.0 | 0.0 |

[*]The numbers in parentheses correspond to the highest resolution bin.

<center>Tb$^{3+}$ luminescence experiments</center>

Purified recombinant C2A and C2B were buffer-exchanged into a decalcified

solution of 10 mM Bis-tris at pH 7.0 and 100 mM KCl, using PD-10 desalting columns.

The luminescence measurements were carried out on a PC1 photon counting

spectrofluorometer (ISS, Champaign, IL) at 25 °C with an excitation wavelength of 280

nm, and 1 (2) nm slit widths on the excitation (emission) channels.  A 370 nm cut-on

filter was used on the emission channel to attenuate the Trp emission and water Raman

peak.  The Tb$^{3+}$ luminescence spectrum consists of several peaks, with the highest-

intensity peak having a maximum at 545 nm.  Tb$^{3+}$ binding experiments were carried out

by adding the aliquots of Tb$^{3+}$ stock solution (buffer) to the sample (reference) cuvettes

containing 2 ml of 15 μM C2A or C2B domains.  The sample dilution at the end of the

experiments never exceeded 10%.  The intensity of Tb$^{3+}$ luminescence was monitored at

the maxima of its most intense emission peak, 545 nm, with averaging over 60

measurements.  The post-acquisition processing included the correction of all intensities

for dilution and subtraction of the sample and reference signals.  The standard deviation

of three independent replicates was used as an estimate of experimental error.  To obtain

the apparent binding affinity of Tb$^{3+}$ to the C2B domain, the data were fitted with the

following equation:

**Equation 1**

$$I = (I_{max} / 2P_0)\left[(K_d + P_0 + L_0) - ((K_d + P_0 + L_0)^2 - 4P_0L_0)^{1/2}\right]$$

where I is the intensity of $Tb^{3+}$ luminescence at 545 nm; $I_{max}$ is the intensity reached upon full C2B saturation; and $P_0$ and $L_0$ are the total C2B and $Tb^{3+}$ concentrations, respectively.  For the metal ion displacement experiments, $Tb^{3+}$-bound proteins were prepared by adding 240 μM $Tb^{3+}$ to 15 μM C2A and 65 μM $Tb^{3+}$ to 15 μM C2B.  The $Tb^{3+}$ luminescence intensity at 545 nm was monitored as a function of increasing $[M^{2+}]$, where M=Ca, Cd.

## Nuclear Magnetic Resonance (NMR) spectroscopy

All binding experiments were conducted at 25 ºC on a Bruker AVANCE III NMR instrument, operating at $^1H$ Larmor frequency of 500 MHz and equipped with a room temperature probe.  The binding of $M^{2+}$ (M=Ca,Cd) to [U-$^{15}N$] enriched C2A and C2B was monitored using $^1H$-$^{15}N$ HSQC or SOFAST-HMQC[160] spectra.  The protein concentration was 100 μM in a buffer solution containing 20 mM MES at pH 6.0, 150 mM KCl, 0.02% $NaN_3$, and 8% $D_2O$.  The spectra were acquired at $Ca^{2+}$ concentrations ranging from 25 μM to 40 mM, and $Cd^{2+}$ concentrations ranging from 25 μM to 20 mM (C2A) and 40 mM (C2B).  The spectra were processed using NMRPipe[99] and analyzed using Sparky.[100]  The cross-peaks assignments were obtained from BMRB entries #4039 (apo C2A), #4041 ($Ca^{2+}$-bound C2A), and #5194 ($Ca^{2+}$-bound C2B).  In addition, 3D HNCACB and CBCACONH spectra[161] acquired on a VNMRS NMR instrument operating at $^1H$ Larmor frequency of 600 MHz were used to verify the assignments of apo C2A.  The spectra at intermediate $Ca^{2+}$ and $Cd^{2+}$ concentrations were assigned by monitoring the trajectory of the cross-peaks in the NMR spectra at different

concentrations of $M^{2+}$.  The chemical shift perturbation (CSP) due to $M^{2+}$ binding, $\Delta$,

was calculated using the following equation:

**Equation 2**

$$\Delta = \left[ \Delta\delta_H^2 + (0.152\Delta\delta_N)^2 \right]^{1/2}$$

where $\Delta\delta_H$ and $\Delta\delta_N$ are residue-specific $^1H$ and $^{15}N$ chemical shift differences

between the apo and metal ion-bound states of the proteins.  $Cd^{2+}$ binding curves were

constructed by plotting $\Delta$ as a function of total $Cd^{2+}$ concentration.  The binding curves

were globally fitted with a single-site binding model described by Eq. (1) (*vide supra*),

except that combined chemical shift differences were used instead of fluorescence

intensities.

<u>Protein-to-membrane FRET experiments</u>

Membrane interactions of C2A, C2B and C2AB in the presence of $Ca^{2+}$ and $Cd^{2+}$

were monitored by FRET between the native tryptophan residues and vesicle-embedded

dansyl-PE fluorophores, as previously described.[149, 162]  The lipid composition of the 100

nm large unilamellar vesicles (LUVs) was POPC:POPS:dansyl-PE=73:20:7.  The buffer

solution comprising 10 mM Bis-tris at pH 7.0 and 100 mM KCl was supplemented with

1 mM TCEP in the case of C2AB to maintain the reducing environment.

The C2A experiments were carried out in the metal-ion titration mode, where the

aliquots of metal ion stock solutions were added to 0.5 µM C2A pre-incubated with 150

µM total lipids.  The C2B and C2AB experiments were carried out in the LUV titration

mode, where the aliquots of the LUV stock solution were added stepwise to 0.5 µM proteins pre-incubated with 0.5 mM $Ca^{2+}$ or $Cd^{2+}$. Because C2B has a propensity to cluster LUVs, which in turn significantly increases the intensity of light scattering, the total lipid concentration was kept below 70 µM.

The change in dansyl fluorescence was monitored at 495 nm using single-wavelength intensity scans with averaging over 60 measurements. Protein-to-membrane FRET efficiency, $\Delta F$, was calculated by subtracting the signals from sample and reference cuvettes, with the reference cuvette containing all components except protein. The experimental error in $\Delta F$ was estimated as the standard deviation in the average dansyl fluorescence of three replicate samples. The data were plotted as $\Delta F$ versus total metal ion or protein-accessible POPS concentrations. The C2A data, for which the plateau region $\Delta F_{max}$ could be obtained experimentally, were fitted with the following equation:

**Equation 3**

$$\Delta F = \Delta F_{max}\left(\frac{[M^{2+}]^n}{[M^{2+}]^n + [M^{2+}]^n_{1/2}}\right)$$

where $[M^{2+}]$ is the concentration of metal ion and n is the Hill coefficient.

<u>Vesicle co-sedimentation and dynamic light scattering (DLS) experiments</u>

Vesicle co-sedimentation assays were conducted independently by two laboratories (T.I.I. and D.S.C.), as described below:

*T.I.I.'s laboratory:* 5 μM C2A/C2B/C2AB in 10 mM Bis-tris pH 7.0 and 100 mM KCl was incubated with sucrose-loaded 100 nm-diameter LUVs containing 1.5 mM total lipids (POPC:POPS=80:20) for 30 min at room temperature, followed by addition of $M^{2+}$ (M=Ca,Cd) to the final concentration of 0.5 or 1 mM. Control samples contained all components except the divalent metal ions. After an additional 1-hour incubation, the LUVs were pelleted using a tabletop ultracentrifuge (Optima$^{TM}$ MAX-XP, Beckman Coulter) for 30 min at 150,000 g and 25 °C. Bicinchoninic acid (BCA) assay (Thermo Scientific) was used to determine the amount of protein in the supernatant. The fraction of protein bound to the vesicles, $f_{bound}$, was calculated as:

**Equation 4**

$$f_{bound} = \frac{P_0 - P}{P_0}$$

where $P_0$ is the total amount of protein and $P$ is the amount of protein in the supernatant. The experimental errors were estimated as standard deviations of 6 $f_{bound}$ values (two independent samples, each sample measured with BCA assay in triplicate).

*D.S.C.'s laboratory:* An ultracentrifugation assay described previously was used to measure the equilibrium membrane affinity of the cytosolic Syt1 domains (C2A, C2B) to LUVs of different lipid composition, under varied salt and metal ion conditions.[60, 163] Large unilamellar vesicles (LUVs) were prepared as described previously using 100 nm

pore diameter polycarbonate filters.[148, 159]  The lipid mixtures included POPC:POPS

(80:20), POPC:POPS (85:15), or POPC:POPS:DDAB (70:15:15), which were

resuspended in Sucrose buffer (20 mM HEPES, 256 mM sucrose, pH 7).  The sucrose

concentration was adjusted to balance the osmotic pressure of the final external salt

concentration.  Final lipid concentrations for all samples were determined using a

modified Barlett phosphate assay.[164, 165]  The domains were at a total concentration of 2

µM.  The free protein concentration in the upper supernatant was determined using

intrinsic tryptophan fluorescence.  Data for the fraction of bound protein as a function of

the accessible lipid concentration [L] was fit to the expression:

**Equation 5**

$$f_B = \frac{K[L]}{1 + K[L]}$$

where $f_B$ is the fraction of bound protein and K is the reciprocal molar partition

coefficient.

DLS experiments were carried out at 25 °C using a Malvern Zetasizer™ Nano S

instrument equipped with a 633 nm He-Ne laser source.  The samples contained a

mixture of 0.5 µM C2B, 100 nm-diameter LUVs (100 µM total lipids,

POPC:POPS=80:20), and 1-2 mM of $M^{2+}$ (M=Ca, Cd) in a 10 mM Bis-tris pH at 7.0 and

100 mM KCl.  Prior to measurements, the samples were incubated for 30 min at 25 °C or

12 hours at 4 °C.

## Electron Paramagnetic Resonance (EPR) measurements

For EPR measurements, LUVs were formed from POPC:POPS=80:20 in a $Ca^{2+}$ free buffer (20 mM HEPES, 150 mM KCl, pH 7.4) and either 1 mM $Ca^{2+}$ or $Cd^{2+}$ was added as needed. EPR spectra were recorded using a Bruker X-Band EMX spectrometer (Bruker Biospin, Billerica, MA) equipped with an ER 4123D dielectric resonator. All EPR spectra were recorded using a 100 G magnetic field sweep, 1 G modulation, and 2.0-milliwatt incident microwave power at a temperature of 298 K. The measurements were performed on 10-µl samples in glass capillary tubes (0.60 mm inner diameter × 0.84 mm outer diameter round capillary; VitroCom, Mountain Lakes, NJ). The protein concentrations used were approximately 75 µM. The phasing, normalization, and subtraction of EPR spectra were performed using LabVIEW software provided by Dr. Christian Altenbach (UCLA, Los Angeles, CA). Progressive power saturation of the EPR spectrum was used to determine nitroxide membrane depth and was performed as previously described.[61, 166] In this case, samples were placed into TPX-2 capillaries, and the values of $\Delta P_{1/2}$ obtained in air and in the presence of Ni(II)EDDA were used to calculate a depth parameter, $\Phi$.[147] The spin label depth was then estimated using the empirical expression:

**Equation 6**

$$\Phi = 3.4\tanh(0.11(x - 8.56)) + 1.1$$

where x is the distance of the spin label from the phospholipid phosphate plane in the bilayer.[159]

## Results

### Structural analysis of $Cd^{2+}$-complexed C2A and C2B domains

The C2A and C2B domains of Syt1 bind $Ca^{2+}$ ions at loop regions located at the tip of the domains.[47, 49] The coordinating atoms are all-oxygen, with the majority of ligands provided by the sidechains of aspartic acids in both mono- and bidentate coordination modes. Our first objective was to identify $Cd^{2+}$ binding sites on C2A and C2B domains, determine their coordination geometry, and evaluate the conformation of the loop regions. We were able to crystallize both domains in the $Cd^{2+}$-complexed states and obtain their high-resolution structures using X-ray crystallography. The crystallization was carried out with protein samples pre-incubated with concentrated solutions of Cd(II) nitrate. In both structures, there was a single $Cd^{2+}$ ion bound to Syt1 domains.

The backbone superposition of the $Cd^{2+}$-complexed C2A with other available C2A structures produced r.m.s.d. values ranging from 0.9 to 1.2 Å (**Figure IV.1A** and **Table IV.2**). The largest deviation in backbone conformation was observed for loop 1, which is tilted away from the metal ion-binding site in the ultra-high resolution structure of the apo C2A. The reason for these conformational differences is evident from the expansion of the loop region (**Figure IV.1B**): Asp172 is rotated "out" of the metal-ion binding site in the apo form, while in the $Cd^{2+}$-bound form Asp172 is "in", forming a coordination bond between its sidechain oxygen and $Cd^{2+}$.
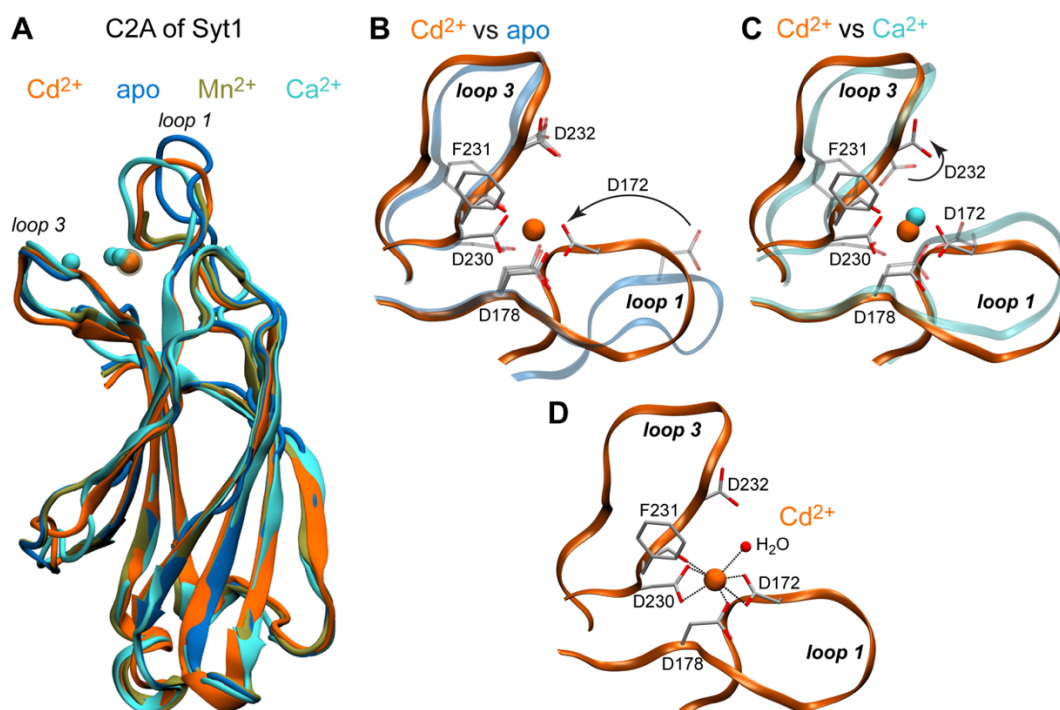
**Figure IV.1 Structural analysis of Cd$^{2+}$-complexed C2A**
(A) Backbone superposition of four C2A structures: Cd$^{2+}$-complexed (this work, 5T0R, orange), apo (4WEE, blue), Ca$^{2+}$-complexed (1BYN/NMR,[55] cyan), and Mn$^{2+}$-complexed (3F05, tan). (B, C) Pairwise comparison of loop regions of Cd$^{2+}$-complexed C2A with those of the apo and Ca$^{2+}$-complexed C2A (shown with transparent representation) highlights the differences between the conformation of loops and coordinating residues. In the ultra-high resolution structure of apo C2A, D178 and D232 are modeled as two conformations. In (C), only one Ca$^{2+}$ ion and protein ligands of Cd$^{2+}$ are shown for clarity. (D) Coordination geometry of the Cd$^{2+}$ site. Cd$^{2+}$ has 7 oxygens ligands in its first coordination sphere, 6 contributed by C2A and 1 by a water molecule.

**Table IV.2 C2A r.m.s.d. values calculated for the backbone Cα carbons**

| C2A (pdb ID) | Apo (4wee) | Ca$^{2+}$ (1byn) | Mn$^{2+}$ (3f05) | Cd$^{2+}$ (5t0r) |
|---|---|---|---|---|
| Apo (4wee) | 0 | 1.45 | 0.73 | 1.20 |
| Ca$^{2+}$ (1byn) | | 0 | 1.17 | 1.02 |
| Mn$^{2+}$ (3f05) | | | 0 | 0.87 |
| Cd$^{2+}$ (5t0r) | | | | 0 |

With respect to the metal ion position, $Cd^{2+}$ binds to what was previously

identified as the Ca1 site in the first NMR structure of C2A that contains 3 $Ca^{2+}$ ions

(**Figure IV.1A**);[55] only one $Ca^{2+}$ populating Ca1 site is shown for clarity in **Figure**

**IV.1C**. The major difference is the conformation of the Asp232 sidechain that

coordinates the first (and second) $Ca^{2+}$ ions but not $Cd^{2+}$. In the $Cd^{2+}$-bound structure,

the Asp232 sidechain is rotated "out", with its place taken by a water molecule (**Figure**

**IV.1D**). Altogether, $Cd^{2+}$ has seven oxygen ligands in its first coordination sphere.

Asp230 and Asp172 sidechains show bidentate coordination, contributing 2 ligands

each. The other three are the backbone oxygen of Phe231, one of the Asp178 sidechain

oxygens, and the water molecule (**Table IV.3**).

**Table IV.3 Metal-oxygen distances in the crystal structures of C2A of Syt1**

| Ligand | $Cd^{2+}$ (5t0r) | $Mn^{2+}$ (3f05) |
|---|---|---|
| Asp172 Od1 | 2.92 | |
| Asp172 Od2 | 2.42 | 2.00 |
| Asp178 Od2 | 2.40 | 2.31 |
| Asp230 Od1 | 2.44 | 2.34 |
| Asp230 Od2 | 2.61 | |
| Phe231 O | 2.52 | 2.38 |
| Asp232 Od2 | | 2.16 |
| HOH | #403, 2.57 | #81, 2.81 |
| Total number of ligands | **7 (6 protein, 1 water)** | 6 (5 protein, 1 water) |

Inspection of the $Cd^{2+}$-complexed C2B structure revealed that $Cd^{2+}$ binding alters

the conformation of loop 3. This is evident from the backbone superposition of C2B

structures (**Figure IV.2A and Table IV.4**) and the expansion of loop regions (**Figure**

**IV.2B** and **C**). Similar to C2A, $Cd^{2+}$ binds to the Ca1 site of C2B and has a coordination

number of 7 (**Figure IV.2D**). Asp303 and Asp363 serve as bidentate ligands,

contributing 4 oxygens total to the coordination sphere. Asp309 and Tyr364 contribute one sidechain and one carbonyl oxygen, respectively. The 7th ligand is the water molecule, which takes the place of the Asp365 sidechain in the $Ca^{2+}$-complexed C2B (**Table IV.5**).

In summary, under crystallization conditions we observed a single hepta-coordinated $Cd^{2+}$ ion bound to the Ca1 site of the C2A and C2B domains. $Cd^{2+}$ binding slightly alters the loop conformation of the domains in the crystalline state.
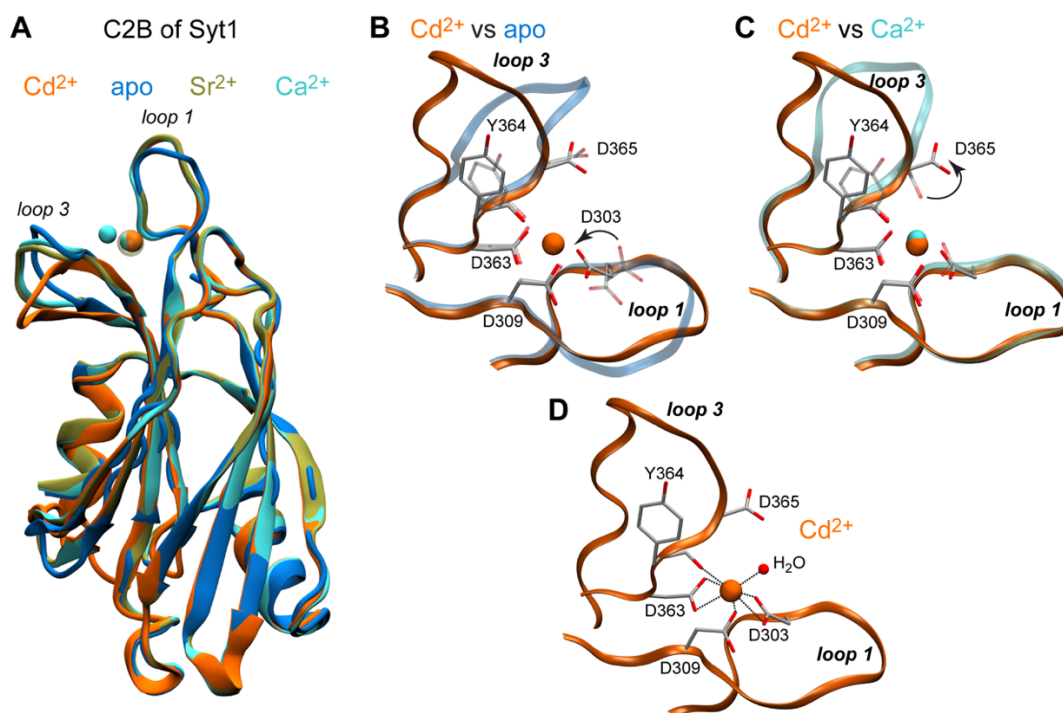


**Figure IV.2 Structural analysis of $Cd^{2+}$-complexed C2B**
(A) Backbone superposition of four C2B structures: $Cd^{2+}$-complexed (this work, 5T0S, orange), apo penta-mutant (5CCJ,[75] blue), $Ca^{2+}$-complexed (1TJX,[56] cyan), and $Sr^{2+}$-complexed (1TJM,[56] tan). (B, C) Pairwise comparison of loop regions of $Cd^{2+}$-complexed C2B with those of the apo and $Ca^{2+}$-complexed C2B highlights the differences between the conformation of loops and coordinating residues. The structural elements of apo and $Ca^{2+}$-complexed C2B are shown with transparent representation. Only one $Ca^{2+}$ ion and

protein ligands of $Cd^{2+}$ are shown for clarity in (C). (D) Coordination geometry of the $Cd^{2+}$ site. $Cd^{2+}$ has 7 oxygens ligands in its first coordination sphere, 6 contributed by C2B and 1 by a water molecule.

**Table IV.4 C2B r.m.s.d. values calculated for the backbone Cα carbons**

| C2B (pdb ID) | Apo (5ccj) | Ca²⁺ (1tjx) | Sr²⁺ (1tjm) | Cd²⁺ (5t0s) |
|---|---|---|---|---|
| Apo (5ccj) | 0 | 0.6542 | 0.7102 | 1.1376 |
| Ca²⁺ (1tjx) | | 0 | 0.1768 | 0.9937 |
| Sr²⁺ (1tjm) | | | 0 | 0.9683 |
| **Cd²⁺ (5t0s)** | | | | 0 |

**Table IV.5 Metal-oxygen distances in the crystal structures of C2B of Syt1**

| Ligand | 1ˢᵗ Ca²⁺ (1tjx) | 2ⁿᵈ Ca²⁺ (1tjx) | Sr²⁺ (1tjm) | Cd²⁺ (5t0s) |
|---|---|---|---|---|
| Met302 O | | 2.48 | | |
| Asp303 Od1 | 2.51 | 2.45 | 2.52 | 2.76 |
| Asp303 Od2 | 2.56 | | | 2.72 |
| Asp309 Od1 | 2.50 | | 2.45 | |
| Asp309 Od2 | | | | 2.67 |
| Asp363 Od1 | | 2.43 | 2.68 | 2.48 |
| Asp363 Od2 | 2.48 | | 2.43 | 2.75 |
| Tyr364 O | 2.41 | | 2.49 | 2.56 |
| Asp365 Od1 | 2.49 | 2.75 | | |
| Asp365 Od2 | | 2.61 | | |
| HOH | #109, 2.41 | #37, 2.47 | #231, 2.26 | #203, 2.26 |
| Total number of ligands | 7 (6 protein, 1 water) | 7 (5 protein, 1 water | 6 (5 protein, 1 water) | **7 (6 protein, 1 water)** |

<u>C2A and C2B bind $Cd^{2+}$ with higher affinity than $Ca^{2+}$</u>

FRET between native Trp residues and protein-bound $Tb^{3+}$ is a sensitive probe of metal ion binding sites in proteins.[167, 168]  We used the displacement of $Tb^{3+}$ by $Ca^{2+}$ and $Cd^{2+}$ to evaluate the relative affinities of these metal ions for the C2A and C2B domains. The C2A-$Tb^{3+}$ binding curve (inset of **Figure IV.3A**) shows a linear increase in $Tb^{3+}$ luminescence at high total $Tb^{3+}$ concentrations.  This non-saturatable behavior occurs because FRET efficiency in $Tb^{3+}$-complexed C2A domain is low and comparable to the luminescence of unbound aqueous $Tb^{3+}$ whose concentration builds up once the protein is saturated.  Since the stoichiometry of $Tb^{3+}$ binding to C2A is not known a priori, it is difficult to obtain a reliable apparent $K_{d,Tb}$ from these data.  We therefore used this curve to guide our choice of $Tb^{3+}$ concentration needed for displacement experiments.

Displacement of $Tb^{3+}$ from C2A by divalent metal ions manifests itself as a steady decrease of $Tb^{3+}$ luminescence (**Figure IV.3A**).  At high concentrations of $Cd^{2+}$, the luminescence reaches the level of aqueous $Tb^{3+}$, indicating full displacement.  $Ca^{2+}$ can displace some, but not all $Tb^{3+}$ from C2A.  This is evident from the plateau-like region at high calcium concentrations; the intensity of this region exceeds that of aqueous $Tb^{3+}$.  Overall, it takes ~8 times more $Ca^{2+}$ than $Cd^{2+}$ to decrease the luminescence of $Tb^{3+}$-saturated C2A by 50%, indicating that $Cd^{2+}$ has higher affinity to C2A than $Ca^{2+}$.

In the C2B domain, the FRET efficiency significantly exceeded the luminescence of aqueous $Tb^{3+}$.  This resulted in a binding curve with apparent saturatable behavior that could be fit well with a single-site binding model (inset of **Figure IV.3B**).  We obtained

a $Tb^{3+}$ dissociation constant of 4.3±0.2 μM and used it to conduct a Scatchard-type analysis[169] of the $Tb^{3+}$/$Cd^{2+}$ displacement data. The analysis assumes a 1:1 metal ion replacement without additional binding events, and is therefore inapplicable to $Ca^{2+}$ because it has 2 binding sites on C2B. The Scatchard-type analysis produced the dissociation constant of the C2B-$Cd^{2+}$ complex, 16.3±0.2 μM, which is considerably lower than the corresponding $Ca^{2+}$ values of 300-600 μM.[47] In summary, $Tb^{3+}$ displacement experiments demonstrate that C2A and C2B domains bind $Cd^{2+}$ with higher affinity than $Ca^{2+}$.
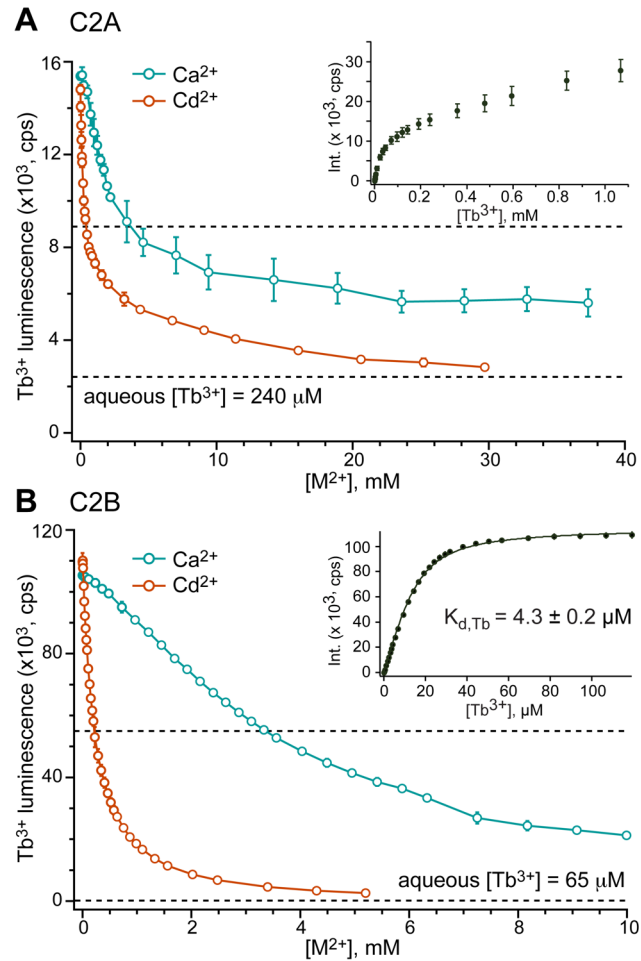
**Figure IV.3 C2A and C2B domains of Syt1 bind $Cd^{2+}$ with higher affinity than $Ca^{2+}$**
(A) Displacement of bound $Tb^{3+}$ from C2A by $Ca^{2+}$ and $Cd^{2+}$. C2A and $Tb^{3+}$ concentrations are 15 and 240 µM, respectively. Inset: C2A-$Tb^{3+}$ binding curve that has non-saturable behavior due to comparable contributions of FRET and luminescence of free $Tb^{3+}$ to the observed signal. (B) Displacement of bound $Tb^{3+}$ from C2B by $Ca^{2+}$ and $Cd^{2+}$. C2B and $Tb^{3+}$ concentrations are 15 and 65 µM, respectively. Inset: C2B-$Tb^{3+}$ binding curve that shows saturable behavior and produces $K_{d,Tb}$ of 4.3±0.2 µM when fitted with a single-site binding model.

146

<u>Solution NMR experiments report on the stoichiometry and affinity of $Cd^{2+}$ binding</u>

To evaluate the residue-specific response of C2A/B to $Cd^{2+}$ binding, we collected $^{1}H$-$^{15}N$ HSQC NMR spectra of [U-$^{15}N$] domains in the presence of varying metal ion concentrations. Binding of divalent metal ions to C2 domains alters the electronic environment of the $^{1}H$ and $^{15}N$ nuclei in the loop regions, resulting in chemical shift changes. When binding kinetics falls in the fast exchange regime on the NMR chemical shift timescale, the dependence of the chemical shift on total ligand concentration can be used to construct binding curves and obtain the dissociation constants.

We found that $Cd^{2+}$ binding kinetics is either fast or intermediate-to-fast for the majority of metal-ion responsive residues in C2B and C2A. This is illustrated by the expansions of the $^{15}N$-$^{1}H$ HSQC spectra of the C2A (**Figure IV.4A**) and C2B (**Figure IV.5A**), where several cross-peaks follow a smooth trajectory in response to increasing $Cd^{2+}$ concentration. For both domains, one can clearly discern the presence of two types of $Cd^{2+}$ binding events: one that occurs in the "low" $Cd^{2+}$ concentration regime ($\leq$ 1 mM, color-coded as a blue-red gradient); and the other one that occurs in the "high" concentration regime (1-40 mM, color-coded gray). For both binding studies, we used 100 $\mu$M C2A/B.
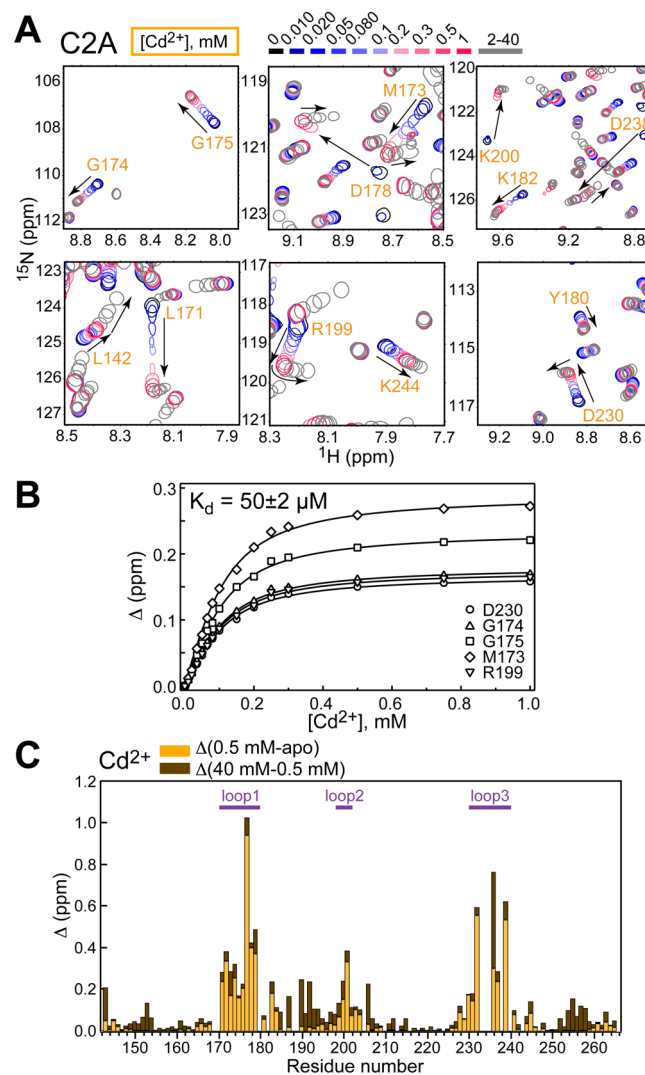
**Figure IV.4 Cd$^{2+}$ populates two types of sites on C2A with drastically different affinities**

(A) Expansions of $^{15}$N-$^{1}$H HSQC C2A spectra for the Cd$^{2+}$ concentration range of 0-40 mM. C2A residues of the loop region respond to either one (e.g., G175, Y180, K200) or both (e.g., L142, D178, R199) binding events. Peak displacement due to the first and second binding events is shown as a blue-red gradient and monochromatic gray, respectively. (B) Representative NMR-detected binding curves constructed for the high-affinity Cd$^{2+}$ sites(s). Solid lines represent the global fit of 14 residues for the high-affinity site with a K$_d$ of 50±2μM. (C) Chemical shift perturbation plot for the low- and high-concentration regimes of Cd$^{2+}$.

C2A has three $Ca^{2+}$ binding sites with affinities of 54-75 µM, 530 µM, and ~20 mM at pH 7.4/100 mM NaCl.[49, 51] Under our experimental conditions (pH 6.0/150 mM KCl), the dissociation constants of $Ca^{2+}$ decreased ~4-5 fold due to competition with protons, to 230±11 µM and 1.59±0.05 mM for the first and second sites, respectively (section S5). $Cd^{2+}$ binding curves constructed for the C2A domain in the low-concentration regime could be fitted well with a single-site binding model, producing the $K_d$ of 50±2 µM (**Figure IV.4B**). This represents a ~5-fold increase in affinity to site 1 compared to $Ca^{2+}$. At >1 mM $Cd^{2+}$, we observed chemical shift changes for a number of residues indicating the presence of low-affinity $Cd^{2+}$ interactions with C2A (**Figure IV.4A**). This is illustrated in the N-H chemical shift perturbation plot that separates out low and high $Cd^{2+}$ concentration regimes (**Figure IV.4C**). The low-affinity binding data cannot be fitted reliably due to the absence of a plateau region. Therefore, we can only provide an estimate of >10 mM for the $K_d$. This represents a >6-fold decrease in affinity of $Cd^{2+}$ to site 2 compared to $Ca^{2+}$.

C2B has two $Ca^{2+}$ sites whose affinities were estimated to be 300-400 and 500-600 µM at pH 6.3/150 mM NaCl,[47] and 600-700 and 700-800 µM at pH 6.0/150 mM KCl. In our $Cd^{2+}$ binding experiments, we were able to discern two distinct binding events (**Figure IV.5A**). The first event occurred in the micromolar-low millimolar range of $Cd^{2+}$. The binding curves showed clear saturatable behavior and could be globally fitted with a single-site binding model that produced a dissociation constant of 30±1 µM (**Figure IV.5B**), in good agreement with the $K_d$ value obtained from $Tb^{3+}$ displacement experiments. This exceeds >20-fold the affinity of $Ca^{2+}$ to C2B. The second binding

event occurred at high mM concentrations of $Cd^{2+}$. Several loop residues, including Met302, Ile367, and Gly368 (see **Figure IV. 5A**), showed titratable behavior at high mM $Cd^{2+}$ with an estimated $K_d$ of ~50 mM. This represents a >60-fold decrease in affinity of $Cd^{2+}$ to site 2 compared to $Ca^{2+}$. Qualitatively, this behavior produced the same chemical shift perturbation pattern as in C2A, with both high- and low-affinity events affecting mostly the loop region (**Figure IV.5C**).

In summary, two $Cd^{2+}$ ions per domain bind to the loop regions of C2AB in solution, with two of those sites (one in C2A, the other one in C2B) being higher-affinity, and the other two sites being lower-affinity than $Ca^{2+}$. We then asked if $Cd^{2+}$ could act as a functional surrogate of $Ca^{2+}$ and mediate the interactions of Syt1 domains with anionic membranes.
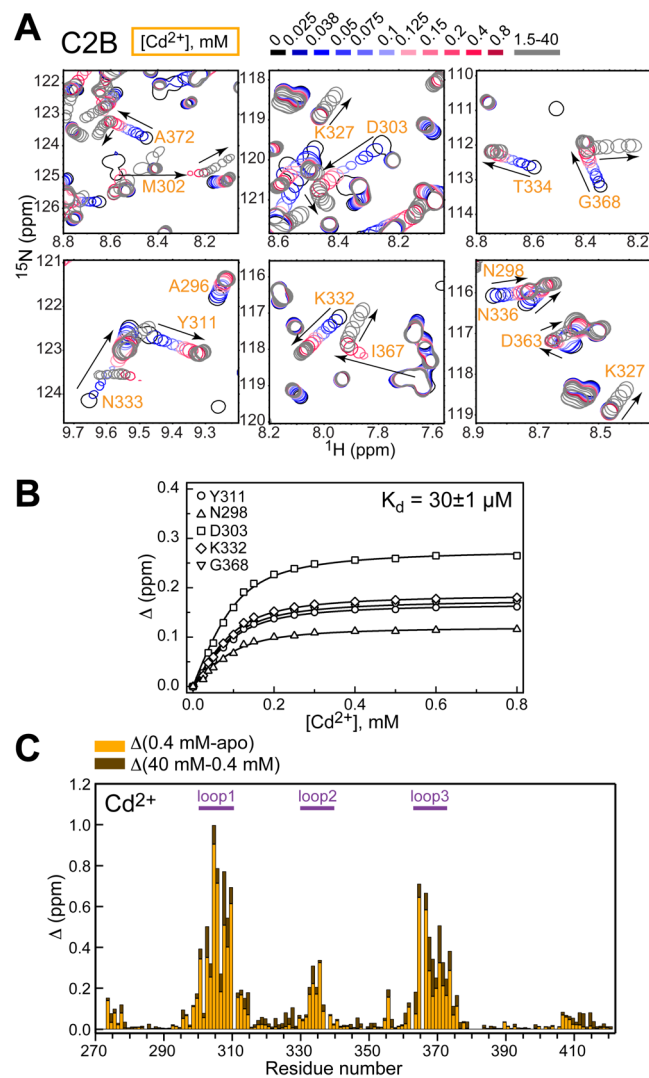
**Figure IV.5 Cd²⁺ populates two sites on C2B with drastically different affinities**
(A) Expansions of $^{15}N$-$^1H$ HSQC C2B spectra for the Cd²⁺ concentration range of 0-40 mM. C2B residues of the loop region respond to either one (e.g., Y311, K327, T334) or both (e.g., M302, I367, G368) binding events. Peak displacement due to the first and second binding events is shown as a blue-red gradient and monochromatic gray, respectively. (B) Representative NMR-detected binding curves constructed for the high-affinity Cd²⁺ sites(s). Solid lines represent the global fit of 30 residues for the high-affinity site with a $K_d$ of 30±1μM. (C) Chemical shift perturbation plot for the low- and high-concentration regimes of Cd²⁺.

Isolated $Cd^{2+}$-complexed C2A does not associate with PtdSer-containing membranes

C2A-membrane interactions were probed using FRET between native Trp residues and the dansyl-labeled lipid incorporated into LUVs containing 15-20% (molar) PtdSer as an anionic lipid component. $Ca^{2+}$-driven association of C2A with membranes resulted in the increase of dansyl emission at 495 nm due to protein-membrane FRET (**Figure IV.6A**). Fitting the FRET binding curve with Hill equation produced $[Ca^{2+}]_{1/2} =$ $24\pm1$ $\mu$M (inset of **Figure IV.6A**). The n value, which reports on the cooperativity[170] of the C2A $Ca^{2+}$-binding sites in the presence of lipids, is $2.1 \pm 0.1$. In contrast, we observed no increase in dansyl fluorescence upon adding $Cd^{2+}$ to the C2A in the presence of LUVs (**Figure IV.6B**). This is further corroborated by the results of co-sedimentation experiments: while in the presence of saturating $Ca^{2+}$ C2A is fully membrane-bound, there is no measurable membrane association at 0.5 and 1 mM $Cd^{2+}$ (inset of **Figure IV.6B**).

The significance of electrostatics in C2A-membrane interactions is illustrated by the results of lipid-dependent co-sedimentation experiments. Increasing the salt concentration from 100 to 300 mM lowers the reciprocal molar membrane partition coefficient of the $Ca^{2+}$-complexed C2A domain (see Table S6) by 15 fold or 1.6 kcal/mole, and neutralizing the PtdSer negative charge by including equimolar positively charged DDAB into the LUVs completely abolishes any detectable binding (**Figure IV.6C**). As a result, one might expect that $Cd^{2+}$ binding would make C2A more electropositive and promote interactions with PtdSer-containing membranes. However,

even 10 mM total lipid is not sufficient to drive the formation of the C2A-$Cd^{2+}$-LUV

complex (**Figure IV.6D**).



**Figure IV.6 $Cd^{2+}$-complexed C2A domain does not associate with PtdSer-containing LUVs**

(A) $Ca^{2+}$-dependent fluorescence emission spectra showing an increase in the intensity of the dansyl band due to protein-membrane FRET.  Inset: $Ca^{2+}$-dependent C2A lipid-binding curve constructed using FRET intensity at 495 nm.  (B) $Cd^{2+}$-dependent fluorescence emission spectra demonstrating that no increase in dansyl emission intensity in the C2A-LUV system is observed upon addition of $Cd^{2+}$.  Inset: the results of vesicle sedimentation experiments that were conducted at 5 μM C2A and 1.5 mM total lipids. (C, D) C2A-lipid binding curves obtained using vesicle co-sedimentation experiments.  The increase in ionic strength and neutralization of the negative charge by DDAB significantly weakens the interaction between $Ca^{2+}$-complexed C2A and membranes (C).  No binding of $Cd^{2+}$-complexed C2A to PtdSer-containing vesicles is observed (D).  In both (C) and (D), $Ca^{2+}$ and $Cd^{2+}$ are added to a concentration of 1 mM.

153

We then tested whether or not $Cd^{2+}$ is able to compete $Ca^{2+}$ off C2A in the presence of LUVs. We prepared a ternary C2A-$Ca^{2+}$-LUV complex by combining LUVs, C2A, and saturating $Ca^{2+}$. Upon addition of $Cd^{2+}$ to this sample, FRET progressively decreased, reaching zero at $Cd^{2+}$ to $Ca^{2+}$ concentration ratio of 5 (**Figure IV.7A** and black trace of **Figure IV.7B**). We conclude that $Cd^{2+}$ displaces $Ca^{2+}$ through high-affinity interactions with a small population of $Ca^{2+}$-complexed C2A that is not membrane-bound and thereby shifts the equilibrium towards a $Cd^{2+}$-complexed form that is unable to interact with membranes. The reverse is not true: $Ca^{2+}$ cannot readily displace $Cd^{2+}$ from site 1 of C2A even at 8-fold molar excess. This is manifested in a negligible increase of FRET upon $Ca^{2+}$ titration into the C2A-$Cd^{2+}$ complex in the presence of LUVs (blue trace of **Figure IV.7B**). These data are consistent with two possible scenarios: (i) the binding of $Cd^{2+}$ to site 1 reduces the affinity of $Ca^{2+}$ to sites 2/3 and thereby prevents the formation of mixed $Cd^{2+}/Ca^{2+}$ C2A species that could potentially associate with membranes; or (ii) the mixed $Cd^{2+}/Ca^{2+}$ species are formed in solution but their affinity to membranes is low because $Cd^{2+}(1)$ cannot effectively coordinate the lipids.

154
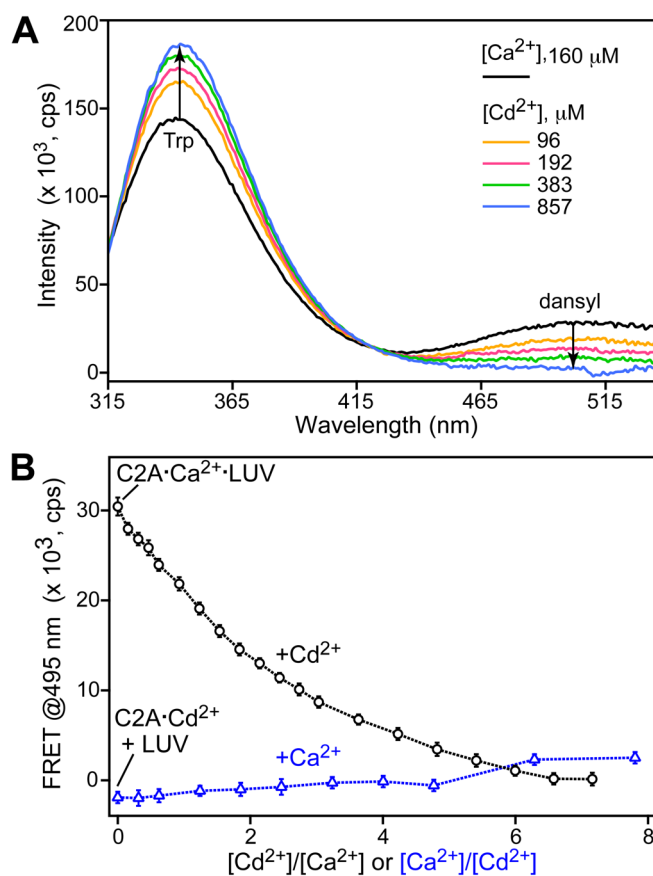
**Figure IV.7 Cd²⁺ competes Ca²⁺ off C2A, resulting in protein dissociation from the membrane**

(A) Fluorescence emission spectra of C2A (0.5 μM) in the presence of LUVs (150 μM) and saturating [Ca²⁺] (160 μM) collected at increasing [Cd²⁺]. The intensity of the dansyl band decreases, with the concomitant increase of the intensity of the Trp emission band, indicating C2A displacement from the membrane. (B) FRET-monitored competition experiments between Ca²⁺ and Cd²⁺ in the presence of LUVs. The intensity of dansyl emission band plotted as a function of Cd²⁺/Ca²⁺ (black trace; [Ca²⁺]=160 μM) and Ca²⁺/Cd²⁺ concentration ratios (blue trace; [Cd²⁺]=160 μM). While Cd²⁺ displaces Ca²⁺ from the protein and results in membrane dissociation, Ca²⁺ cannot displace Cd²⁺ from C2A and support membrane association.

<u>Isolated Cd$^{2+}$-complexed C2B neither appreciably associates with PtdSer-containing</u>

<u>membranes nor bridges LUVs</u>

The next step was to determine if Cd$^{2+}$ has a similar effect on the membrane-binding function of C2B. FRET and co-sedimentation experiments carried out in the lipid-titration mode revealed the same pattern as seen for C2A: while Ca$^{2+}$ promotes C2B-membrane interactions (**Figure IV. 8A, C**), weak membrane binding is observed for the Cd$^{2+}$-complexed C2B (**Figure IV. 8B, C**). Similar to C2A, neutralizing the negative membrane charge with the DDAB membrane component abolished C2B binding to the membrane, indicating the dominant role of electrostatic interactions.

Ca$^{2+}$-complexed C2B has a well-known propensity to bridge LUVs in a manner that can be reversed by EDTA treatment.[72, 73] This behavior manifested itself in our FRET experiments through the increase in scattering intensity at high concentrations of lipids. Basic residues located at the bottom of the C2B domain (defined relative to the position of the loop regions) have been shown to play an important role in vesicle bridging.[72] Most likely, C2B interacts with two membranes simultaneously through the Ca$^{2+}$-binding loops at the top of the domain and the basic region at the bottom. Dynamic light scattering experiments showed that in contrast to Ca$^{2+}$, Cd$^{2+}$-complexed C2B did not alter the size distribution of LUVs (**Figure IV.8D**). We conclude that the interaction between the loop region of Cd$^{2+}$-complexed C2B and LUVs is too weak to result in appreciable membrane binding, which in turn hinders the ability of C2B to bridge the vesicles.

In summary, our FRET and sedimentation data clearly illustrate that despite high-affinity interaction of Syt1 C2A/B domains with $Cd^{2+}$ in solution, neither protein-metal ion complex is able to appreciably interact with PtdSer-containing membranes.
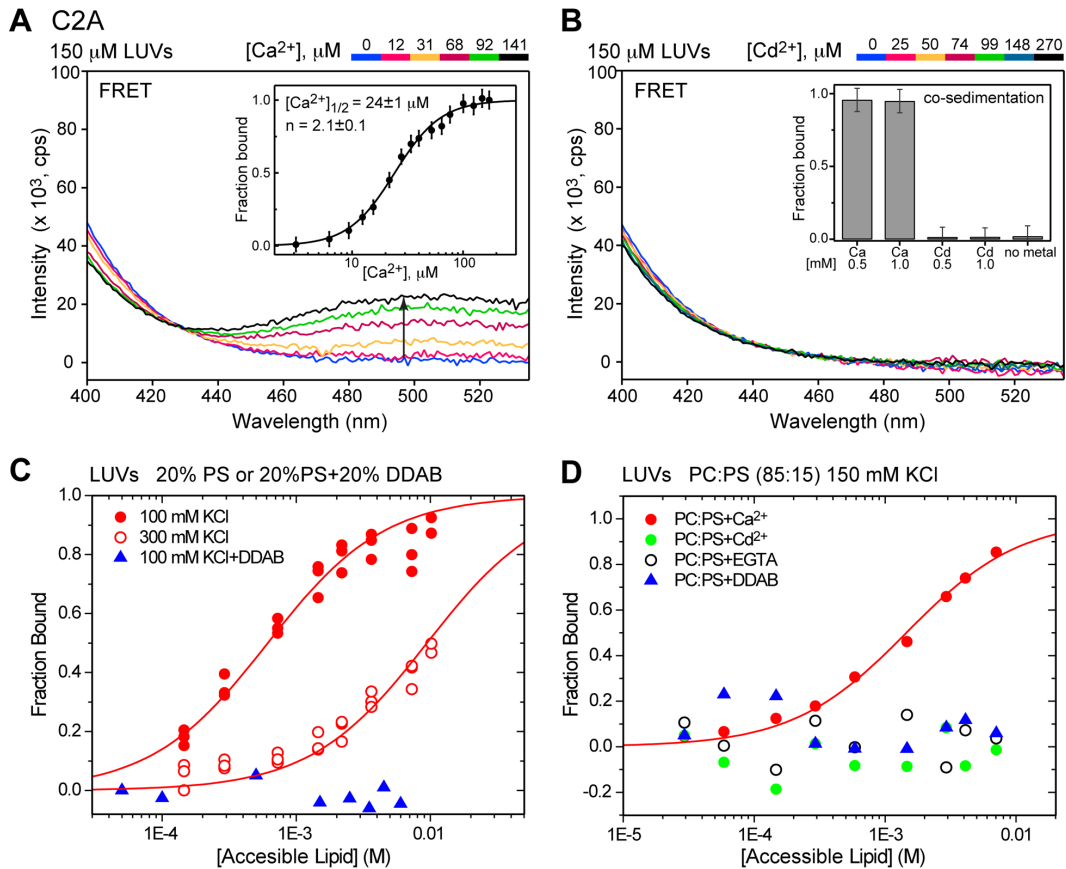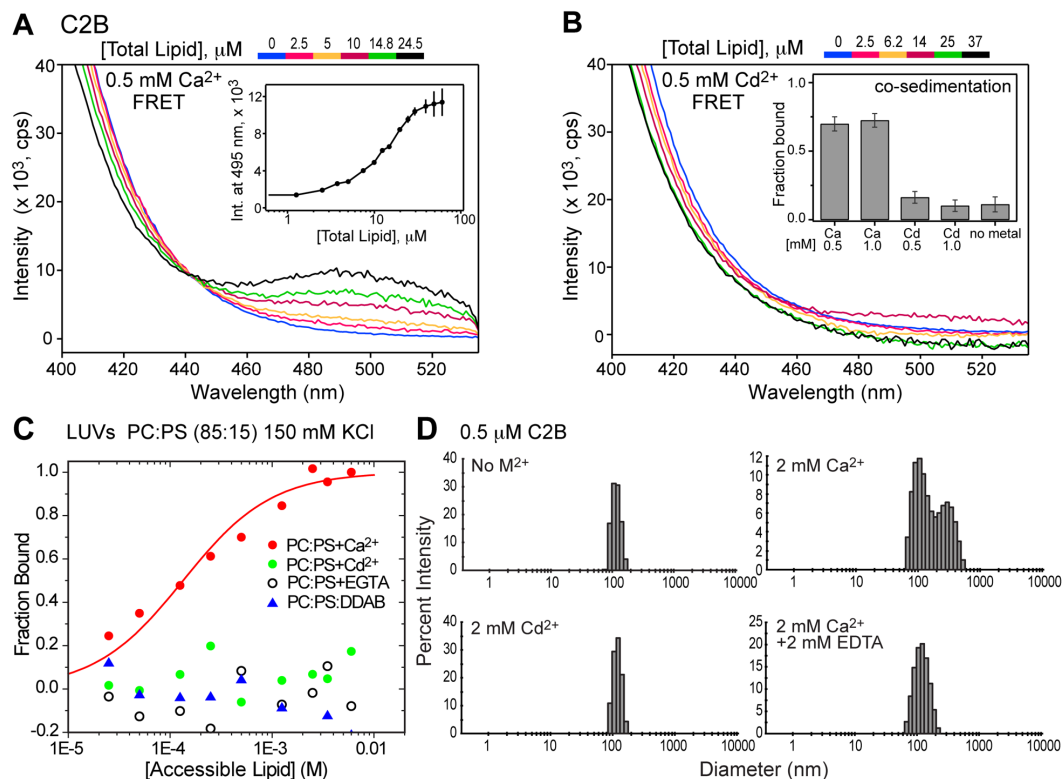


**Figure IV.8 $Cd^{2+}$-complexed C2B domain does not appreciably associate with PtdSer-containing LUVs**
(A) PtdSer-dependent fluorescence emission spectra showing an increase in the intensity of the dansyl band due to FRET between $Ca^{2+}$-complexed C2B and LUVs. Inset: PtdSer-dependent C2B lipid binding curve constructed using FRET intensity at 495 nm. (B) PtdSer-dependent fluorescence emission spectra demonstrating that no significant increase in dansyl emission intensity in the $Cd^{2+}$-C2B system is observed upon addition of LUVs. Inset: the results of vesicle sedimentation experiments conducted at 5 μM C2B and 1.5 mM total lipids. (C) C2B-lipid binding curves obtained using vesicle sedimentation experiments. The neutralization of the negative charge by DDAB abolishes the interactions between $Ca^{2+}$-complexed C2B and membranes. $Ca^{2+}$ and $Cd^{2+}$ are present at concentrations of 1 mM. (D) Dynamic light scattering data show that while $Ca^{2+}$-

complexed C2B can reversibly cluster 100 nm LUVs, the $Cd^{2+}$-complexed C2B cannot, due its inability to interact with the membranes through the loop regions.

<u>C2AB fragment and full-length Syt1 associate with membranes in the presence of $Cd^{2+}$</u>

In full-length Syt1, an 8-residue linker connects C2A and C2B. We used the two-domain fragment, C2AB, to determine how $Cd^{2+}$ binding to both domains affects its membrane-binding properties. We found that under conditions of our FRET experiments, C2AB associated with anionic membranes even in the absence of divalent metal ions (**Figure IV.9**). The membrane association was not due to residual $Ca^{2+}$, because FRET efficiency did not change upon the addition of EDTA to the sample. Addition of $Cd^{2+}$ resulted in moderate increase in FRET efficiency, indicating that although the interaction of $Cd^{2+}$-complexed individual domains with membranes is very weak, the avidity effect due to having two domains on the same polypeptide chain is significant.
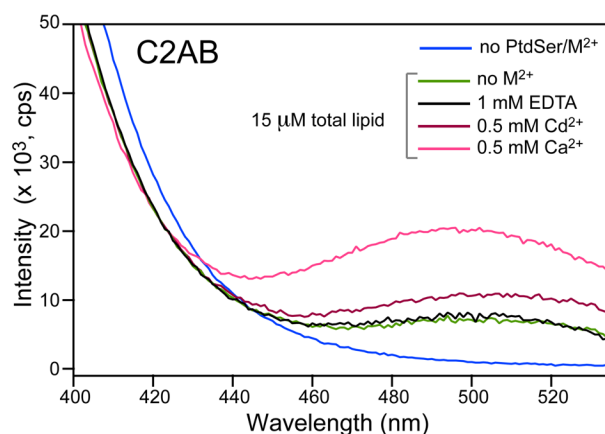
**Figure IV.9 Metal-ion free and Cd²⁺-complexed C2AB associates with PtdSer-containing LUVs**
Fluorescence emission spectra showing the C2AB-to-membrane FRET efficiency under different metal-ion conditions. The C2AB and total lipid concentrations are 0.5 μM and 15 μM, respectively. C2AB associates with PtdSer-containing membranes in a metal-ion independent manner. This interaction is slightly enhanced by Cd²⁺ based on the increase in FRET efficiency. Ca²⁺ data are shown for comparison.

To determine the conditions that support membrane insertion of the C2 domains in the full-length protein, the spin labeled side chain R1 (**Figure IV.10A**) was attached to one site in C2A (173R1) and a second site in C2B (304R1) that are known to penetrate negatively charged membranes in the presence of Ca²⁺ in the soluble C2AB fragment. For the isolated C2AB domain, these sites exhibit dramatic changes in EPR lineshape that are the result of membrane insertion (**Figure IV.10B**). This broadening of the EPR spectrum is due to slower motion of the R1 label that is likely due to interactions between R1 and the protein that take place in a membrane hydrocarbon environment.[171, 172]

For the full-length protein reconstituted into bilayers containing PtdSer, the EPR spectra in the Ca²⁺-free state resemble those for the aqueous C2AB fragment (**Figure**

159

**IV.10C**).  These EPR lineshapes are characteristic of those seen for the R1 side chain in loop regions of proteins.  In the presence of $Ca^{2+}$, the EPR lineshapes dramatically broaden, indicating that both C2A and C2B have inserted into the membrane (red traces).  The spectra for full-length protein in the presence of $Ca^{2+}$ and PtdSer are virtually identical to those seen at the same positions for the C2AB fragment.  No evidence for insertion of C2A and C2B is observed in the absence of $Ca^{2+}$ or in the absence of PtdSer.  However, membrane insertion does occur in the presence of $Ca^{2+}$ to charge neutralized membranes formed from PtdSer and DDAB (blue traces **Figure IV.10C**), and line-shape changes indicating insertion of the domains is seen in the presence of $Cd^{2+}$ to PtdSer containing bilayers (green traces, **Figure IV.10C**).

For the C2A site, both the charge neutralized and $Cd^{2+}$ bound lineshapes are similar (inset **Figure IV.10C**), but slightly more mobile than the $Ca^{2+}$/PtdSer case, suggesting that these conditions produce a slightly shallower membrane penetration than does $Ca^{2+}$.  For the C2B site, the spectra obtained for $Ca^{2+}$-dependent insertion into PtdSer or charged neutralized membranes is identical (red and blue traces, respectively), but the spectrum obtained for the $Cd^{2+}$/PtdSer state is more mobile, suggesting that first loop in C2B does not insert as deeply when bound to $Cd^{2+}$.

To confirm that these domains insert into the bilayer, and to determine whether the lineshape differences reflect differences in membrane depth, we used progressive power saturation of the EPR spectra and a collision-gradient approach (see Methods) to determine the membrane depth of 173R1 and 304R1.  Shown in **Table IV.6** are depth parameters and membrane depths under several conditions.  In the presence of $Ca^{2+}$ and

PtdSer, the spin label at 173 on C2A is positioned at an average position of approximately 9 Å into the bilayer below the level of the lipid phosphates and the label at 304 on C2B is positioned at about 3.5 Å.  For the $Cd^{2+}$-bound and charge-neutralized states, 173R1 assumes a shallower position, and it is displaced by as much as 10 Å towards the aqueous phase for the charge-neutralized membrane.  For 304R1, a similar position is seen for the $Ca^{2+}$-dependent insertion into the PtdSer and charge-neutralized membranes, but a more peripheral membrane association is seen for the $Cd^{2+}$/PtdSer case, where the label is displaced 6 to 7 Å towards the aqueous phase.  As seen by a comparing **Figure IV.10** and **Table IV.6**, motional averaging of the R1 side chain and the EPR spectra qualitatively follows the membrane depth of the label.
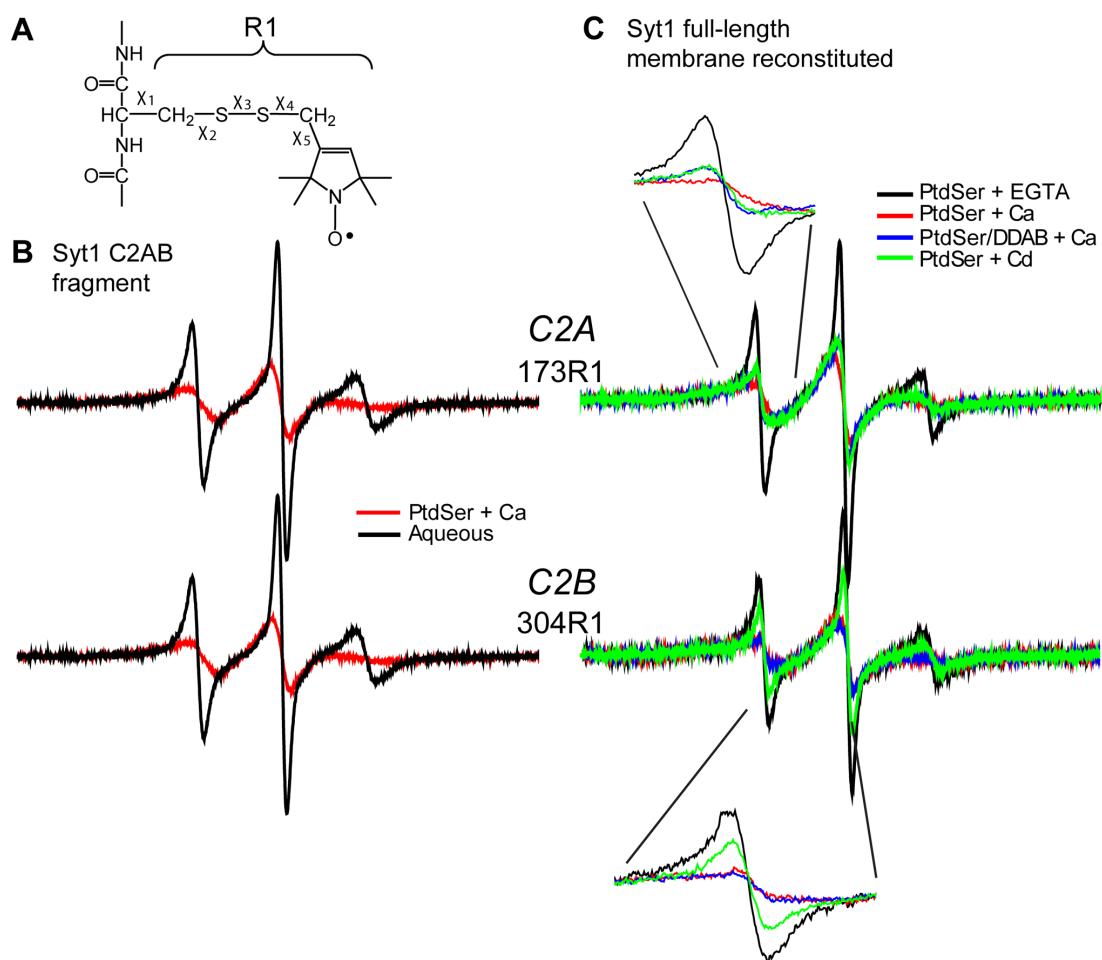
**Figure IV.10 EPR spectra reveal membrane contact and insertion of C2A and C2B**
(A) The spin labeled side chain R1 is attached to cysteines using a sulfhydryl specific MTS label. (B) EPR spectra for the Syt1 C2AB fragment with R1 at position 173 in C2A or position 304 in C2B in solution (black traces) or in the presence of $Ca^{2+}$ and PtdSer containing vesicles (red traces), (PC:PS=85:15). (C) EPR spectra from R1 at sites 173 and 304 in full-length Syt1 reconstituted into PtdSer in the absence of $Ca^{2+}$ (black trace), in the presence of 1 mM $Ca^{2+}$ (red trace), in the presence of 1 mM $Cd^{2+}$ (green trace) (PC:PS=85:15) or in the presence of 1 mM $Ca^{2+}$ when reconstituted into charge neutralized membranes of PtdSer and DDAB (blue trace) (PC:PS:DDAB=70:15:15). Shown in the insets are expansions of the low-field resonance.

162

**Table IV.6 Depth parameters for full-length membrane reconstituted Syt1**

| protein mutant | lipid conditions | metal added | depth parameter ($\Phi$) | Position from lipid phosphate (Å)[a] |
|---|---|---|---|---|
| FL SYT 173R1 | PC[b] | $Ca^{2+}$ | $-1.9 \pm 0.05$ | aqueous |
| | PC:PS(15%) | $Ca^{2+}$ | $1.03 \pm 0.05$ | 9.29 |
| | | $Cd^{2+}$ | $-0.57 \pm 0.1$ | 3.38 |
| | PC:PS:DDAB(15%) | $Ca^{2+}$ | $-1.44 \pm 0.2$ | -1.32 |
| FL SYT 304R1 | PC[b] | $Ca^{2+}$ | $-2.0 \pm 0.05$ | aqueous |
| | PC:PS(15%) | $Ca^{2+}$ | $-0.535 \pm 0.05$ | 3.53 |
| | | $Cd^{2+}$ | $-1.7 \pm 0.1$ | -3.32 |
| | PC:PS:DDAB(15%) | $Ca^{2+}$ | $-0.897 \pm 0.2$ | 1.85 |

[a]Negative depths are positioned on the aqueous side of the membrane phosphate plane; positive values are positioned towards the hydrocarbon interior. Depths were estimated using the calibration curve reported in Frazier et al.[147] Both $Ca^{2+}$ and $Cd^{2+}$ are added to 1 mM. [b]These depth parameters place the spin label on the C2A or C2B binding loops in the aqueous phase 5 Angstroms or further from the lipid phosphates. Full length Syt1 is present at approximately 75 μM concentration with a total lipid concentration of 15 mM to yield a protein:lipid ratio of approximately 200.

## Discussion

In this work, we explored the role of electrostatics in metal ion-mediated interactions of C2A/B domains of Syt1 with phosphatidylserine-containing membranes using a non-native metal ion, $Cd^{2+}$. The C2A and C2B crystal structures contain a single $Cd^{2+}$ ion bound to the first calcium site of the C2A/B domains (**Figures IV.1** and **2**). $Cd^{2+}$ has a near-identical coordination sphere to that of $Ca^{2+}$, and causes only moderate perturbation of the loop regions. Our solution NMR data support the 1:1 binding stoichiometry: for both domains, we observed only one high affinity $Cd^{2+}$ site (**Figures IV.4-5**) that would be populated under the conditions of our membrane-binding experiments. This is different from $Ca^{2+}$ that is expected to populate 2/3 and 2 sites in

the C2A and C2B domains, respectively.  The incomplete neutralization of the negatively charged loops of C2A/B by $Cd^{2+}$ is one possible reason why we detected no appreciable interactions between $Cd^{2+}$-complexed isolated domains and the anionic membranes in protein-membrane FRET and vesicle co-sedimentation experiments (**Figures IV.6** and **8**).  Another reason could be the inability of protein-bound $Cd^{2+}$ to coordinate lipid head-groups.  We previously demonstrated that the C2 domain of PKC$\alpha$, whose loop region binds a full complement of $Cd^{2+}$ ions, does not associate with PtdSer-containing membranes.[82]  We speculated that the preference for low coordination numbers[86] and soft ligands[157] prevents $Cd^{2+}$ from effectively coordinating the oxygen atoms of lipid headgroups.  When the C2A/B domains are present in tandem in the C2AB fragment, the combined binding free energy is sufficient to result in weak but measurable membrane association (**Figure IV.9**).  This is in general agreement with the previous finding that $Sr^{2+}$, which is known to bind C2B with 1:1 stoichiometry[56] (the C2A interactions were not investigated), can promote the interactions between the cytoplasmic domain of Syt1 and phosphatidylserine-containing vesicles.[79]

In contrast to the isolated soluble domains, in full-length Syt1, $Cd^{2+}$ does mediate insertion of the Syt1 C2 domains into PtdSer membranes, and $Ca^{2+}$ does mediate insertion into charge-neutralized membranes (**Figure IV.10**).  As shown above (**Figures IV.6** and **8**) these conditions do not support binding for the isolated C2 domains.  The simplest explanation for these apparently contradictory results is that both generalized electrostatics (a long-range Coulombic interaction) and metal ion coordination are important in promoting syt1 C2 domain membrane attachment.

In the full-length protein, the C2 domains of Syt1 are tethered to the membrane through a long juxta-membrane linker, and much of this linker is associated with the interface, which may limit how far the C2 domains extend from the membrane.[158] As a result, the C2 domains will experience a high local lipid concentration in the native protein. For example, if the C2 domains are tethered within 4 Å of the membrane interface, the effective lipid concentration presented to the domains will be near 1 M. By comparison, the highest lipid concentrations that can be reached in co-sedimentation experiments are almost two orders of magnitude lower. As a result, weak interactions (for example, interactions that would yield a membrane partition coefficient of 20 $M^{-1}$) would not be sufficient to observe membrane binding for the isolated domain, but would be sufficient for the domains to bind membranes in the context of the full-length protein. The substitution of $Cd^{2+}$ for $Ca^{2+}$ or the neutralization of the membrane surface potential should diminish the contributions made by lipid-metal ion coordination[54, 82] or long-range Coulombic interactions,[49, 77] respectively, to the binding of these domains. Neither of these interactions alone produces a strong interaction; however, since the free energy contributions are additive and partition coefficients multiply, both interactions together become significant. The slightly shallower penetration of the domains with $Cd^{2+}$ or with charge-neutralized membranes seen in the full-length protein is consistent with a significantly reduced binding energy. In addition, for C2B, $Cd^{2+}$ and PtdSer only allow for a peripheral association of this domain. This might be the result of a reduced electrostatic polarization of the C2B domain and reduced Coulombic attraction due to the fact that only one $Cd^{2+}$ ion binds with high affinity to this domain (**Figure IV.1**).

165

In conclusion, our results demonstrate that even if the loop region of C2A/B domains does not contain a full complement of divalent metal ions, long-range Coulombic interactions alone – enhanced by high effective local concentration of the domains – can drive the association of the cytoplasmic domain of Syt1 with anionic membranes. In view of this finding, the Syt1-membrane interaction may initially be driven only by $Ca^{2+}$ populating site 1 of C2A/B domains. The formation of $Ca^{2+}$-lipid coordination bonds and binding of additional $Ca^{2+}$ ions to the loop region may occur after the formation of the shallow "encounter" complex, as was proposed for the C2 domain from protein kinase C.[173]

# References

[8] Newton, A. C. (1995) Protein kinase C: structure, function, and regulation, *J Biol Chem 270*, 28495-28498.

[12] Newton, A. C. (1997) Regulation of protein kinase C, *Curr Opin Cell Biol 9*, 161-167.

[41] Corbalan-Garcia, S., and Gomez-Fernandez, J. C. (2014) Signaling through C2 domains: more than one lipid target, *Biochim Biophys Acta 1838*, 1536-1547.

[44] Sutton, R. B., Davletov, B. A., Berghuis, A. M., Sudhof, T. C., and Sprang, S. R. (1995) Structure of the first C2 domain of synaptotagmin I: a novel Ca2+/phospholipid-binding fold, *Cell 80*, 929-938.

[45] Brose, N., Petrenko, A. G., Sudhof, T. C., and Jahn, R. (1992) Synaptotagmin: a calcium sensor on the synaptic vesicle surface, *Science 256*, 1021-1025.

[47] Fernandez, I., Arac, D., Ubach, J., Gerber, S. H., Shin, O., Gao, Y., Anderson, R. G., Sudhof, T. C., and Rizo, J. (2001) Three-dimensional structure of the synaptotagmin 1 C2B-domain: synaptotagmin 1 as a phospholipid binding machine, *Neuron 32*, 1057-1069.

[48] Shao, X., Davletov, B. A., Sutton, R. B., Sudhof, T. C., and Rizo, J. (1996) Bipartite Ca2+-binding motif in C2 domains of synaptotagmin and protein kinase C, *Science 273*, 248-251.

[49] Ubach, J., Zhang, X., Shao, X., Sudhof, T. C., and Rizo, J. (1998) Ca2+ binding to synaptotagmin: how many Ca2+ ions bind to the tip of a C2-domain?, *EMBO J 17*, 3921-3930.

[50] Verdaguer, N., Corbalan-Garcia, S., Ochoa, W. F., Fita, I., and Gomez-Fernandez, J. C. (1999) Ca(2+) bridges the C2 membrane-binding domain of protein kinase Calpha directly to phosphatidylserine, *EMBO J 18*, 6329-6338.

[51] Fernandez-Chacon, R., Konigstorfer, A., Gerber, S. H., Garcia, J., Matos, M. F., Stevens, C. F., Brose, N., Rizo, J., Rosenmund, C., and Sudhof, T. C. (2001) Synaptotagmin I functions as a calcium regulator of release probability, *Nature 410*, 41-49.

[54] Zhang, X., Rizo, J., and Sudhof, T. C. (1998) Mechanism of phospholipid binding by the C2A-domain of synaptotagmin I, *Biochemistry 37*, 12395-12403.

[55] Shao, X., Fernandez, I., Sudhof, T. C., and Rizo, J. (1998) Solution structures of the Ca2+-free and Ca2+-bound C2A domain of synaptotagmin I: does Ca2+ induce a conformational change?, *Biochemistry 37*, 16106-16115.

[56] Cheng, Y., Sequeira, S. M., Malinina, L., Tereshko, V., Sollner, T. H., and Patel, D. J. (2004) Crystallographic identification of Ca2+ and Sr2+ coordination sites in synaptotagmin I C2B domain, *Protein Sci 13*, 2665-2672.

[60] Kuo, W., Herrick, D. Z., Ellena, J. F., and Cafiso, D. S. (2009) The calcium-dependent and calcium-independent membrane binding of synaptotagmin 1: two modes of C2B binding, *J Mol Biol 387*, 284-294.

[61] Kuo, W., Herrick, D. Z., and Cafiso, D. S. (2011) Phosphatidylinositol 4,5-bisphosphate alters synaptotagmin 1 membrane docking and drives opposing bilayers closer together, *Biochemistry 50*, 2633-2641.

[63] Honigmann, A., van den Bogaart, G., Iraheta, E., Risselada, H. J., Milovanovic, D., Mueller, V., Mullar, S., Diederichsen, U., Fasshauer, D., Grubmuller, H., Hell, S. W., Eggeling, C., Kuhnel, K., and Jahn, R. (2013) Phosphatidylinositol 4,5-bisphosphate clusters act as molecular beacons for vesicle recruitment, *Nat Struct Mol Biol 20*, 679-686.

[69] Morales, K. A., Lasagna, M., Gribenko, A. V., Yoon, Y., Reinhart, G. D., Lee, J. C., Cho, W., Li, P., and Igumenova, T. I. (2011) Pb2+ as modulator of protein-membrane interactions, *J Am Chem Soc 133*, 10599-10611.

[72] Arac, D., Chen, X., Khant, H. A., Ubach, J., Ludtke, S. J., Kikkawa, M., Johnson, A. E., Chiu, W., Sudhof, T. C., and Rizo, J. (2006) Close membrane-membrane proximity induced by Ca(2+)-dependent multivalent binding of synaptotagmin-1 to phospholipids, *Nat Struct Mol Biol 13*, 209-217.

[73] Seven, A. B., Brewer, K. D., Shi, L., Jiang, Q. X., and Rizo, J. (2013) Prevalent mechanism of membrane bridging by synaptotagmin-1, *Proc Natl Acad Sci U S A 110*, E3243-3252.

[75] Zhou, Q., Lai, Y., Bacaj, T., Zhao, M., Lyubimov, A. Y., Uervirojnangkoorn, M., Zeldin, O. B., Brewster, A. S., Sauter, N. K., Cohen, A. E., Soltis, S. M., Alonso-Mori, R., Chollet, M., Lemke, H. T., Pfuetzner, R. A., Choi, U. B., Weis, W. I., Diao, J., Sudhof, T. C., and Brunger, A. T. (2015) Architecture of the synaptotagmin-SNARE machinery for neuronal exocytosis, *Nature 525*, 62-67.

[77] Murray, D., and Honig, B. (2002) Electrostatic control of the membrane targeting of C2 domains, *Mol Cell 9*, 145-154.

[79] Bhalla, A., Tucker, W. C., and Chapman, E. R. (2005) Synaptotagmin isoforms couple distinct ranges of Ca2+, Ba2+, and Sr2+ concentration to SNARE-mediated membrane fusion, *Mol Biol Cell 16*, 4755-4764.

[82] Morales, K. A., Yang, Y., Long, Z., Li, P., Taylor, A. B., Hart, P. J., and Igumenova, T. I. (2013) Cd2+ as a Ca2+ surrogate in protein-membrane interactions: isostructural but not isofunctional, *J Am Chem Soc 135*, 12980-12983.

[86] Rulíšek, L. r., and Vondrášek, J. (1998) Coordination geometries of selected transition metal ions (Co2+, Ni2+, Cu2+, Zn2+, Cd2+, and Hg2+) in metalloproteins, *Journal of Inorganic Biochemistry 71*, 115-127.

[99] Delaglio, F., Grzesiek, S., Vuister, G. W., Zhu, G., Pfeifer, J., and Bax, A. (1995) NMRPipe: a multidimensional spectral processing system based on UNIX pipes, *J Biomol NMR 6*, 277-293.

[100] Lee, W., Tonelli, M., and Markley, J. L. (2015) NMRFAM-SPARKY: enhanced software for biomolecular NMR spectroscopy, *Bioinformatics 31*, 1325-1327.

[140] Nalefski, E. A., and Falke, J. J. (1996) The C2 domain calcium-binding motif: structural and functional diversity, *Protein Sci 5*, 2375-2390.

[141] Cho, W., and Stahelin, R. V. (2006) Membrane binding and subcellular targeting of C2 domains, *Biochim Biophys Acta 1761*, 838-849.

[142] Nishizuka, Y. (1988) The molecular heterogeneity of protein kinase C and its implications for cellular regulation, *Nature 334*, 661-665.

[143] Perin, M. S., Fried, V. A., Mignery, G. A., Jahn, R., and Sudhof, T. C. (1990) Phospholipid binding by a synaptic vesicle protein homologous to the regulatory region of protein kinase C, *Nature 345*, 260-263.

[144] Geppert, M., Goda, Y., Hammer, R. E., Li, C., Rosahl, T. W., Stevens, C. F., and Sudhof, T. C. (1994) Synaptotagmin I: a major Ca2+ sensor for transmitter release at a central synapse, *Cell 79*, 717-727.

[145] Chapman, E. R., and Jahn, R. (1994) Calcium-dependent interaction of the cytoplasmic region of synaptotagmin with membranes. Autonomous function of a single C2-homologous domain, *J Biol Chem 269*, 5735-5741.

[146] Chapman, E. R., and Davis, A. F. (1998) Direct interaction of a Ca2+-binding loop of synaptotagmin with lipid bilayers, *J Biol Chem 273*, 13995-14001.

[147] Frazier, A. A., Roller, C. R., Havelka, J. J., Hinderliter, A., and Cafiso, D. S. (2003) Membrane-bound orientation and position of the synaptotagmin I C2A domain by site-directed spin labeling, *Biochemistry 42*, 96-105.

[148] Rufener, E., Frazier, A. A., Wieser, C. M., Hinderliter, A., and Cafiso, D. S. (2005) Membrane-bound orientation and position of the synaptotagmin C2B domain determined by site-directed spin labeling, *Biochemistry 44*, 18-28.

[149] Morales, K. A., Lasagna, M., Gribenko, A. V., Yoon, Y., Reinhart, G. D., Lee, J. C., Cho, W., Li, P., and Igumenova, T. I. (2011) Pb2+ as Modulator of Protein–Membrane Interactions, *Journal of the American Chemical Society 133*, 10599-10611.

[150] Essen, L.-O., Perisic, O., Katan, M., Wu, Y., Roberts, M. F., and Williams, R. L. (1997) Structural Mapping of the Catalytic Mechanism for a Mammalian Phosphoinositide-Specific Phospholipase C†, *Biochemistry 36*, 1704-1718.

[151] Hsu, Y.-H., Burke, J. E., Stephens, D. L., Deems, R. A., Li, S., Asmus, K. M., Woods, V. L., and Dennis, E. A. (2008) Calcium binding rigidifies the C2 domain

and the intradomain interaction of GIVA phospholipase A2 as revealed by hydrogen/deuterium exchange mass spectrometry, *Journal of Biological Chemistry 283*, 9820-9827.

[152] Morales, K. A., Yang, Y., Cole, T. R., and Igumenova, T. I. (2016) Dynamic Response of the C2 Domain of Protein Kinase Cα to Ca 2+ Binding, *Biophysical Journal 111*, 1655-1667.

[153] Scott, A. M., Antal, C. E., and Newton, A. C. (2013) Electrostatic and hydrophobic interactions differentially tune membrane binding kinetics of the C2 domain of protein kinase Cα, *Journal of Biological Chemistry 288*, 16905-16915.

[154] Gerber, S. H., Rizo, J., and Sudhof, T. C. (2002) Role of electrostatic and hydrophobic interactions in Ca(2+)-dependent phospholipid binding by the C(2)A-domain from synaptotagmin I, *Diabetes 51 Suppl 1*, S12-18.

[155] Striegel, A. R., Biela, L. M., Evans, C. S., Wang, Z., Delehoy, J. B., Sutton, R. B., Chapman, E. R., and Reist, N. E. (2012) Calcium binding by synaptotagmin's C2A domain is an essential element of the electrostatic switch that triggers synchronous synaptic transmission, *J Neurosci 32*, 1253-1260.

[156] Edwards, A. S., and Newton, A. C. (1997) Regulation of Protein Kinase C βII by Its C2 Domain, *Biochemistry 36*, 15615-15623.

[157] Chakraborty, S., Kravitz, J. Y., Thulstrup, P. W., Hemmingsen, L., DeGrado, W. F., and Pecoraro, V. L. (2011) Design of a three-helix bundle capable of binding heavy metals in a triscysteine environment, *Angew Chem Int Ed Engl 50*, 2049-2053.

[158] Lu, B., Kiessling, V., Tamm, L. K., and Cafiso, D. S. (2014) The juxtamembrane linker of full-length synaptotagmin 1 controls oligomerization and calcium-dependent membrane binding, *J Biol Chem 289*, 22161-22171.

[159] Herrick, D. Z., Sterbling, S., Rasch, K. A., Hinderliter, A., and Cafiso, D. S. (2006) Position of synaptotagmin I at the membrane interface: cooperative interactions of tandem C2 domains, *Biochemistry 45*, 9668-9674.

[160] Schanda, P., and Brutscher, B. (2005) Very fast two-dimensional NMR spectroscopy for real-time investigation of dynamic events in proteins on the time scale of seconds, *J Am Chem Soc 127*, 8014-8015.

[161] Muhandiram, D. R., and Kay, L. E. (1994) Gradient-Enhanced Triple-Resonance Three-Dimensional NMR Experiments with Improved Sensitivity, *Journal of Magnetic Resonance, Series B 103*, 203-216.

[162] Morales, K. A., and Igumenova, T. I. (2012) Synergistic Effect of Pb2+ and Phosphatidylinositol 4, 5-Bisphosphate on C2 Domain–Membrane Interactions, *Biochemistry 51*, 3349-3360.

[163] Buser, C. A., and McLaughlin, S. (1998) Ultracentrifugation technique for measuring the binding of peptides and proteins to sucrose-loaded phospholipid vesicles, *Methods Mol Biol 84*, 267-281.

[164] Bartlett, G. R. (1959) Phosphorus assay in column chromatography, *J Biol Chem 234*, 466-468.

[165] Pokorny, A., Birkbeck, T. H., and Almeida, P. F. (2002) Mechanism and kinetics of delta-lysin interaction with phospholipid vesicles, *Biochemistry 41*, 11044-11056.

[166] Victor, K., and Cafiso, D. S. (1998) Structure and position of the N-terminal membrane-binding domain of pp60src at the membrane interface, *Biochemistry 37*, 3402-3410.

[167] Dehorrocks, W., and Collier, W. E. (1981) Lanthanide Ion Luminescence Probes - Measurement of Distance between Intrinsic Protein Fluorophores and Bound Metal-Ions - Quantitation of Energy-Transfer between Tryptophan and Terbium(Iii) or Europium(Iii) in the Calcium-Binding Protein Parvalbumin, *Journal of the American Chemical Society 103*, 2856-2862.

[168] Walters, J. D., and Johnson, J. D. (1990) Terbium as a luminescent probe of metal-binding sites in protein kinase C, *J Biol Chem 265*, 4223-4226.

[169] Yang, P., Ma, G. B., and Yang, B. S. (1989) Terbium (III) as fluorescence probe in the study of the interaction of rare earth and transition metal ions with concanavalin A, *Acta Chimica Sinica English Edition 7*, 443-449.

[170] Weiss, J. N. (1997) The Hill equation revisited: uses and misuses, *The FASEB Journal 11*, 835-841.

[171] Kroncke, B. M., Horanyi, P. S., and Columbus, L. (2010) Structural origins of nitroxide side chain dynamics on membrane protein alpha-helical sites, *Biochemistry 49*, 10045-10060.

[172] Freed, D. M., Khan, A. K., Horanyi, P. S., and Cafiso, D. S. (2011) Molecular origin of electron paramagnetic resonance line shapes on beta-barrel membrane proteins: the local solvation environment modulates spin-label configuration, *Biochemistry 50*, 8792-8803.

[173] Corbin, J. A., Evans, J. H., Landgraf, K. E., and Falke, J. J. (2007) Mechanism of specific membrane targeting by C2 domains: localized pools of target lipids enhance Ca2+ affinity, *Biochemistry 46*, 4322.

# CHAPTER V PARTIAL METAL-ION SATURATION OF C2 DOMAINS PRIMES SYNAPTOTAGMIN 1-MEMBRANE INTERACTIONS[*]

## Background

The process of neurotransmitter release is tightly coupled to the changes in neuronal $Ca^{2+}$ levels [174]. Synaptotagmin 1 (Syt1), an integral membrane protein that is anchored to synaptic vesicles through its N-terminal region, plays a major regulatory role in this process [13, 45, 144]. Together with its protein effectors, such as SNAREs (soluble N-ethylmaleimide sensitive factor attachment protein receptors) [175, 176] and complexin [177], Syt1 triggers the vesicle fusion in a $Ca^{2+}$-dependent manner [178]. This results in the opening of membrane fusion pore, through which neurotransmitters are released from the vesicles into the synaptic cleft [179, 180].

The $Ca^{2+}$-sensing function of Syt1 resides on its cytosolic, phospholipid-binding C-terminal region that comprises tandem C2A and C2B domains, connected by a 9-residue linker. These domains have five intrinsically weak $Ca^{2+}$-binding sites: three on C2A and two on C2B, formed by the apical aspartate-rich loops [47, 49]. In the absence of anionic lipids, the population of three sites of C2A by $Ca^{2+}$ occurs in a sequential, non-cooperative manner with the high-affinity Site 1 (shown in **Figure V.1A** in the context of $Pb^{2+}$-complexed C2 domains, *vide infra*) getting occupied first [51, 181]. In C2B, the

$Ca^{2+}$ affinities for two sites differ approximately 2-fold, with Site 1 having a higher affinity [47]. Anionic phospholipids, such as phosphatidylserine (PtdSer) and phosphatidylinositol-(4,5)-bisphosphate, impart positive cooperativity on $Ca^{2+}$ binding to the C2 domains [51, 58]. As a result, Syt1 is able to respond to $Ca^{2+}$ elevation in neurons and trigger the synaptic exocytosis.

Several models have been proposed to explain the membrane-binding modes of these C2 domains and their contributions to the overall $Ca^{2+}$ response [54, 61, 182, 183]. However, it remains unclear what the roles of individual metal ion sites are in driving the association of the C2 domains with anionic membranes. The challenge here lies in the overlapping $Ca^{2+}$ affinities [47, 49] and the resulting complex speciation of metal-ion bound C2 domains in solution. The role of Site 1 is of particular importance, as this site is predominantly populated at the initial stages of C2-membrane recruitment.

Our objective was to determine the role of metal ion binding event to Site 1 in C2-membrane interactions, which necessarily requires generating C2-metal ion complexes with well-defined stoichiometry. To overcome the challenge of overlapping $Ca^{2+}$ affinities, we made use of $Pb^{2+}$, a $Ca^{2+}$-mimicking divalent cation [184]. Heavy metal ions were shown to be useful tools to establish the C2 structure-function relationship [52, 69, 82, 185]. What sets $Pb^{2+}$ apart from other metal ions is two features. First, it supports the membrane interactions of C2 domains and is therefore isofunctional to $Ca^{2+}$ [69, 186, 187]. Second, although $Pb^{2+}$ populates the exact same C2 domain sites as $Ca^{2+}$ in solution, there are significant differences in its affinities to Site 1 and 2-3: the affinity of $Pb^{2+}$ to Site 1 is ~450-fold higher than that to Site 2 (**Figure V.1B**) [187]. These unique properties

of $Pb^{2+}$ with respect to its interactions with C2 domains enabled us to simultaneously achieve selective population of specific metal binding site, Site 1, with minimum perturbation of the membrane binding function of the proteins.

For both C2 domains of Syt1, we found that population of Site 1 by a divalent metal ion attenuates the conformational dynamics of their membrane-binding regions. Using isotropically tumbling bicelles and large unilamellar vesicles as membrane mimics, we characterized the membrane-binding properties of $Pb^{2+}$-complexed C2 domains: individual, in tandem, and in the context of full-length Syt1. Our work provides evidence that Syt1 can adopt a dynamic and partially membrane-bound state under conditions when there is only a single divalent metal ion per C2 domain. Formation of such "primed" state driven by a metal ion in Site 1 could be an essential step in eliciting the mutually cooperative $Ca^{2+}$ and membrane-binding response.

## Experimental procedures

### Materials

The murine Syt1 cDNA was purchased from Open Biosystems (GE Life Sciences). Concentrated stock solutions of $Pb^{2+}$ were prepared by dissolving Lead acetate tri-hydrate (Sigma-Aldrich) in HPLC-grade water or decalcified buffers. The necessary dilutions of this stock solution were freshly prepared prior to use to make working solutions. All the buffer solutions used in the experiments (MES/Bis-tris, Sigma-Aldrich) were treated with the ion-chelating resin Chelex-100 (Sigma-Aldrich) to remove trace divalent metals before use. Lipid components used in the phospholipid vesicle as well as bicelle preparations: 1-palmitoyl-2-oleoyl-sn-glycero-3-

176

phosphocholine (POPC), 1-palmitoyl-2-oleoyl-sn-glycero-3-phospho-L-serine (POPS), 1,2-dimyristoyl-sn-glycero-3-phosphocholine (DMPC), 1,2-diheptanoyl-sn-glycero-3-phosphocholine (DHPC), 1,2-dimyristoyl-sn-glycero-3-phospho-L-serine (DMPS), L-$\alpha$-phosphatidylinositol-4,5-bisphosphate (PtdIns(4,5)P$_2$) were obtained from Avanti Polar Lipids Inc. (Alabaster, AL).  The short-chain Phosphatidylinositol 4,5-bisphosphate (di-C4- PtdIns(4,5)P$_2$) was obtained from Echelon Biosciences.

<div align="center">Protein expression and purification</div>

The gene segments encoding Syt1 C2A (residues 137-265), C2B (residues 271-421), and C2AB (residues 137-421) were cloned into pET-SUMO vector (Novagen, Madison, WI) and expressed as 6xHis-tagged SUMO fusion proteins in the *E. coli* BL21(DE3) (C2A, C2AB) and Rosetta(DE3) (C2B) strains as described previously [52, 187]. The full length-Syt1 (FL-Syt1) (residues 1-421) with the native cysteines mutated as: C73A, C74A, C76A, C78A, C82S, and C277S was cloned into a pET-28a vector. For EPR measurements, additional cysteine mutation were introduced into the cysteine-free FL-Syt1 at either positions M173C or V304C and expressed as 6xHis-tagged proteins in the *E. coli* BL21(DE3)-RIL strain as described before [52, 188].  M173 and V304 are located on loop 1 of the C2A and C2B domains, respectively.  We chose loop 1 because we had used it in previous studies, and it yields clear differences between aqueous and membrane bound states [52, 188].  Loop 3 is also known to penetrate the bilayer, but we have no reason to think that adding more sites would change the conclusions.  All mutants were prepared using the QuickChange site-directed

mutagenesis kit (Stratagene, La Jolla, CA.) and verified by DNA sequencing (Genewiz, South Plainfield, NJ).

Expression and purification steps from the previously described protocols were followed [52, 187, 188]. Briefly, all SUMO fusion proteins were purified from cell lysates using HisTrap HP columns followed by removal of 6xHis-SUMO fusion tag using SUMO protease. The partially purified proteins were further refined using anion (HiTrap Q HP, C2A and C2AB) and cation (HiTrap SP HP, C2B)-exchange chromatography steps to remove any charged protein or nucleic acid impurities. The ion-exchange chromatography buffers were also supplemented with 100 μM EDTA to ensure that the purified Syt1 domains are free of metal contamination. Immediately prior to use, the protein stock solutions were concentrated and subjected to four successive passes through the desalting PD MidiTrap G-25 columns to attain complete buffer-exchange and removal of EDTA.

For the NMR measurements, individual C2 domains were uniformly enriched with $^{15}$N, as described previously [52, 187]. The C2AB fragment was additionally deuterated to a level of ~80%, by growing *E. coli* on the M9 medium supplemented with $D_2O$ and BioExpress® 1000 (10 ml/L; [U-$^2$H 98%, U-$^{15}$N 98%]). The isotopically enriched chemicals were purchased from Cambridge Isotope Laboratories, Inc. Unless specified otherwise, all isotopically enriched protein preparations were exchanged post-purification into an NMR buffer of the composition: 20 mM MES (pH 6.0), 100 mM KCl, 8% $D_2O$, and 0.02% $NaN_3$.

FL-Syt1 used for the EPR experiments was purified in CHAPS (3-[(3-Cholamidopropyl)dimethylammonio]-1 propanesulfonate) by affinity chromatography using Ni-NTA agarose resin (Qiagen). The protein was spin labeled overnight at 4 °C using the thiol-specific spin label, MTSL (1-oxy-2,2,5,5-tetramethylpyrrolinyl-3-methyl methanethiosulfonate) while bound to the Ni-NTA column. The labeled protein was eluted followed by removal of the 6xHis tag by thrombin cleavage and further purified by cation-exchange chromatography (HiTrap SP HP).

### Preparation of phospholipid vesicles and bicelles

Large unilamellar vesicles (LUVs) of desired compositions were prepared by aliquoting the chloroform solutions of the POPC/POPS lipids, followed by extensive vacuum drying and extrusion in NMR buffer (Mini-Extruder, Avanti Polar Lipids, Inc.). All LUV preparations were verified for the mean diameter of 100 nm by dynamic light scattering and used within 2 days of preparation. Phospholipid concentrations in LUV solutions were calibrated using the phosphate determination assay [189].

To prepare isotropically tumbling bicelles, chloroform solutions of DMPC and DHPC were aliquoted, extensively dried under vacuum and resuspended in NMR buffer. DMPC preparation was vortexed and subjected to 3 rapid freeze-thaw cycles to create homogeneous slurry. Clear DHPC solution was then added to achieve two-fold molar excess to DMPC (q=0.5). The resulting mixture was briefly vortexed and subjected to 4 rapid freeze-thaw cycles, resulting in clear homogeneous bicelle stock solutions. Total lipid concentration was verified using phosphate determination assay [189]. Additional long-chain lipid components, such as DMPS and PtdIns(4,5)P$_2$, were dried and added

179

during the bicelle preparation wherever applicable.  The bicelle stock solutions were

flash frozen and stored at -20 ºC.  Before use, the frozen stocks were thawed at 42 ºC,

followed by incubation at room temperature.

<div align="center">

Nuclear Magnetic Resonance (NMR) spectroscopy

</div>

All NMR experiments were conducted at 298.2 K, unless specified otherwise; the

temperature was calibrated using deuterated methanol.  NMR data were processed with

NMRPipe [99] and analyzed with Sparky [190].  Curvefit program (Arthur G. Palmer's

laboratory, Columbia University) was used to fit the relaxation data and extract

relaxation parameters.  The NMR observables, such as relaxation rate constants and

chemical shift perturbations, were measured for all spectrally resolved N-H groups and

plotted against the primary structure.

<div align="center">

Measurements of $^{15}N$ transverse relaxation rate constants, $R_2$

</div>

The $R_2$ values were measured on an NMR spectrometer (Avance III HD, Bruker

Biospin) operating at the $^1H$ Larmor frequency of 600 MHz (14.1 T) and equipped with

a cryogenically cooled probe.  NMR samples contained 300 µM [U-$^{15}N$]-enriched C2A

or C2B, each in the absence or presence of stoichiometric amounts of $Pb^{2+}$.  Additional

relaxation measurements were conducted on the $Pb^{2+}$-complexed C2A domain in the

presence of LUVs.  The site-specific $R_{2,CPMG}$ values [101] were extracted from fitting the

$^{15}N$-$^1H_N$ cross-peak intensity decays at seven unique and three duplicate relaxation time

points ranging from 8 to 140 ms.  The free-precession $R_{2,HE}$ values [102] were measured to

estimate the exchange contribution to the observed relaxation behavior and the timescale of exchange, both through direct comparison with the $R_{2,CPMG}$ values. The Hahn-Echo delay was set to 48.2 ms. All relaxation data were acquired in the interleaved manner.

### NMR-detected interactions between Syt1 domains and their ligands

*C2AB and Pb²⁺*. Binding of $Pb^{2+}$ to C2AB was monitored using $^{15}N$-$^{1}H$ TROSY-HSQC spectra collected on an NMR spectrometer (Avance III HD, Bruker Biospin) operating at the $^{1}H$ Larmor frequency of 800 MHz (18.8 T) and equipped with a cryogenically cooled probe. $Pb^{2+}$ was added to the NMR sample containing 100 µM [U-$^{15}N$, ~80%-$^{2}H$] C2AB at 1- and 2-fold stoichiometric excess. The chemical shift perturbations (CSPs, $\Delta$) due to $Pb^{2+}$ interactions with proteins were calculated using the following equation:

$$\Delta = [\, \Delta\delta_H^2 + (0.152\Delta\delta_N)^2 \,]^{1/2}$$

where $\Delta\delta_H$ and $\Delta\delta_N$ are residue-specific $^{1}H$ and $^{15}N$ chemical shift differences between metal-free and $Pb^{2+}$-complexed states of C2AB.

*Syt1 domains and bicelles*. Binding of isotropic anionic bicelles to metal-free and $Pb^{2+}$-complexed C2A, C2B and C2AB was conducted at 18.8 T and 300 K. A series of $^{1}H$-$^{15}N$ HSQC (TROSY-HSQC) spectra were acquired at each sample condition for the C2A/C2B (C2AB) domains. Protein concentration was kept at 150 µM. The bicelles were added to a total lipid concentration of 60 mM. The bilayer compositions of the

181

added bicelles were either DMPC:DMPS:PtdIns(4,5)P$_2$=84:14:2 or

DMPC:DMPS=85:15.  The chemical shift perturbations induced by bicelle interactions

were calculated using eq. (1).  The absolute resonance intensities for the bicelle-

containing samples were normalized to their respective bicelle-free reference

counterparts in order to estimate the signal attenuation.

*C2A and LUVs.*  The interaction of the C2A domain with LUVs composed of

either pure POPC or POPC:POPS=80:20 was monitored at 14.1 T using a 100 μM

sample of [U-$^{15}$N] C2A.  A series of $^{15}$N-$^1$H HSQC spectra were collected in the

presence of LUVs, with the total lipid concentration ranging from 0 to 2.0 mM.

Residue-specific intensity changes were distributed into linearly and exponentially

decaying patterns based on their behavior, and the respective fitting models were used to

extract the "decay" rates.

*C2B and di-C4-PtdIns(4,5)P$_2$.*  Interactions of C2B with di-C4-PtdIns(4,5)P$_2$

were monitored at 14.1 T, using 100 μM C2B in either apo- or Pb$^{2+}$-complexed forms.

The di-C4-PtdIns(4,5)P$_2$ concentrations were: 0, 10, 50, 100, 150, 300, and 550 μM for

the C2B·Pb1 sample; and 55, 100, 150, 250, 400, 600, 800, and 1000 μM for the apo

C2B sample.  Residue-specific chemical shift perturbation values Δ were calculated

using Eq. (1).  The binding curves were constructed by plotting Δ as a function of di-C4-

PtdIns(4,5)P$_2$ concentration.  To extract the dissociation constant $K_d$, the curves were

globally fitted (C2B·Pb1: 7 residues, apo C2B: 5 residues) with the single-site binding

model:

$$\Delta = (\Delta_{max} / 2P_0 )[(K_d + P_0 + L_0 )$$
$$-((K_d + P_0 + L_0 )^2 - 4P_0 L_0 )^{1/2} ]$$

where $\Delta_{max}$ is the maximum perturbation, and $P_0$ and $L_0$ are the total protein and di-C4-PtdIns(4,5)P$_2$ concentrations, respectively.

<u>Measurements of Electron Paramagnetic Resonance (EPR) spectra</u>

For EPR measurements, FL-Syt1 was reconstituted into POPC:POPS=85:15 at a 1:200 protein to lipid ratio and dialyzed into metal-free buffer (20 mM HEPES, 150 mM KCl, pH 7.4) in the presence of Bio-Beads (Bio-Rad Laboratories, Hercules, CA) [188]. $Pb^{2+}$ was then added to samples at either a 2:1 $Pb^{2+}$:FL-Syt1 ratio or in 12- to 50-fold excess. Measurements were taken as described previously, using a Bruker X-Band EMX spectrometer (Bruker Biospin, Billerica, MA) equipped with an ER 4123D dielectric resonator. Continuous wave spectra were taken with 100 G magnetic field sweep, 1 G modulation, and 2.0-milliwatt incident microwave power at room temperature. 10 μL samples of protein with concentrations varying between 15-75 μM depending on the desired $Pb^{2+}$:FL-Syt1 ratio were prepared in glass capillary tubes (0.60 mm inner diameter × 0.84 mm outer diameter round capillary; VitroCom, Mountain Lakes, NJ). The phasing, normalization, and subtraction of EPR spectra were performed using in-Lab software written by David Nyenhuis and LabVIEW software provided by Dr. Christian Altenbach [188]. Progressive power saturation of the EPR spectrum was used to determine nitroxide membrane depth and was performed as previously described [52, 188]. Samples were run in gas-permeable TPX-2 capillaries, and the values of $\Delta P_{1/2}$ obtained

in air and in the presence of Ni(II)EDDA were used to calculate a depth parameter, $\Phi$ [147]. The spin label depth was then estimated using the empirical expression:

$$\Phi = A \tanh[B(x-C)]+D$$

where $x$ is the distance of the spin label from the lipid phosphate plane (positive $x$ values are inside while the negative values are outside the bilayer) and $A$, $B$, $C$, and $D$ are empirically determined constants [52, 188].

## Results and discussion

### Electrostatic properties of C2 domains in different states of metal ligation

We previously obtained high-resolution crystal structures of individual $Pb^{2+}$-complexed Syt1 C2 domains, where $Pb^{2+}$ ions bind to Site 1 with two-orders of magnitude higher affinity than $Ca^{2+}$ [187] (**Figure V.1A,B**). To determine how metal ion binding to Site 1 alters the electrostatic profiles of these C2 domains, we calculated the surface electrostatic potential maps of the proteins in different states of metal ligation. The negatively charged metal ion-binding region is formed by the aspartate-rich loops (**Figure V.1C**). In the presence of a full complement of $Ca^{2+}$ ions, C2A undergoes a prominent electrostatic shift where the intra-loop potential changes from negative to positive (**Figure V.1D**). The effect of bound $Ca^{2+}$ on the same region in C2B is the neutralization of the negative charge (**Figure V.1D**). This is because C2A can accommodate 3 $Ca^{2+}$ ions within the intra-loop region, as compared to the C2B's maximum of 2. $Pb^{2+}$ binding to Site 1 partially neutralizes the intra-loop region in both

domains.  Due to the differences in the arrangement of basic residues, loop 2 of C2A

becomes more electropositive while loop 2 of C2B becomes neutral (**Figure V.1E**).  The

differences in electrostatic properties between the two C2 domains determine how the

single metal-ion bound states interact with anionic membranes (*vide infra*).
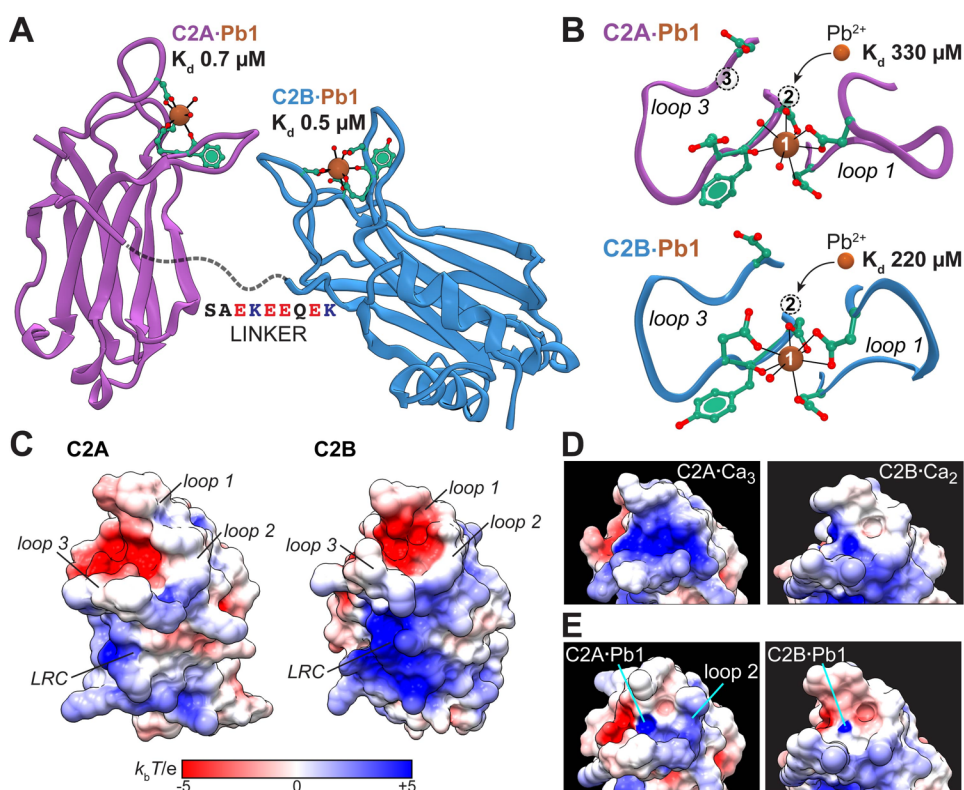


**Figure V.1 High-affinity Pb$^{2+}$-binding sites of Syt1**
(A) Cartoon representation of the Syt1 cytoplasmic region assembled from the Pb$^{2+}$-bound
crystal structures of isolated C2 domains, C2A (5VFE) and C2B (5VFG).  The Pb$^{2+}$
affinities to Site 1 exceed those of Ca$^{2+}$ by ~2 orders of magnitude. (B) Expansion of loop
regions in C2A·Pb1 and C2B·Pb1 showing the numbered metal-ion binding sites and the
low affinity of Pb$^{2+}$ to Site 2.  (C) Electrostatic potential maps of apo C2A and C2B.  (D,E)
Electrostatic potential maps of loop regions with full complement of metal ions (D) and
with Site 1 selectively populated by Pb$^{2+}$ (E).  The maps were generated using Adaptive
Poisson- Boltzmann Solver (APBS) plugin of UCSF Chimera.  The PDB IDs of structures
used: 4WEE (C2A apo), 1BYN (C2A·Ca$_3$), 5CCJ (C2B apo), and 1TJX (C2B·Ca$_2$).

Population of Site 1 by a metal ion alters conformational plasticity of the membrane-binding regions

In addition to electrostatics, the conformation and dynamics of the membrane-binding regions in the C2·Pb1 complexes can have profound influence on the membrane association. The average conformation of the domains, as it exists in the crystalline state, changes only moderately upon metal ion binding. The ms-to-μs, but not the sub-nanosecond backbone dynamics in a related C2 domain were previously shown to be responsive to the state of metal ligation [191]. We therefore investigated the ms-to-μs dynamics of the Syt1 C2 domains in apo and single-$Pb^{2+}$ states using solution NMR methods.

Two types of NMR parameters, $R_{2,HE}$ and $R_{2,CPMG}$, were measured for all spectrally resolved N-H groups of the C2 domain backbone. $R_{2,HE}$ is a free-precession transverse relaxation rate constant, whose elevated values are indicative of ms-to-μs conformational exchange processes. $R_{2,CPMG}$ is a transverse relaxation rate constant whose elevated values reflect dynamics on timescales faster than 100 μs. A comparison of the two transverse relaxation rate constants enables one to estimate, in a residue-specific manner, the timescale of motions present in macromolecules.

The NMR relaxation data for the apo C2 domains are presented in **Figure V.2**. Based on the elevated $R_{2,HE}$ values (**Figure V.2A**), the backbone of apo C2A has two highly dynamic regions: loop 3, which participates in both metal-ion coordination and binding to PtdSer-rich membranes; and the lysine-rich cluster (LRC). Surprisingly, there

is little dynamics in loop 1, which provides roughly half of the oxygen ligands when Site

1 gets populated by a divalent metal ion.
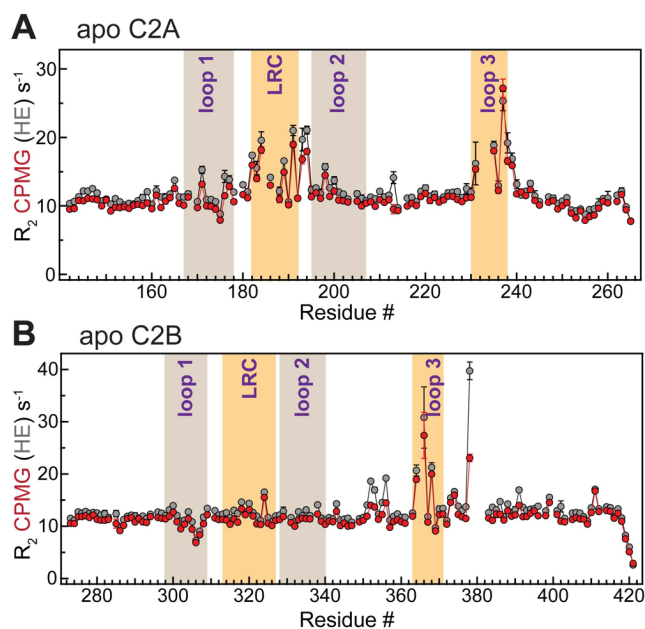


**Figure V.2 The membrane-binding regions of apo C2A and C2B are dynamic on the microsecond timescale**
$R_{2,HE}$ (gray) and $R_{2,CPMG}$ (red) are plotted against the amino acid sequence of C2A (A) and C2B (B).  The regions corresponding to metal-ion coordinating loops and lysine-rich clusters are highlighted.

The dynamics profile is different for C2B (**Figure V.2B**).  The most significant

difference between C2B and C2A is located in the LRC that shows no conformational

exchange in C2B but is highly dynamic in C2A.  The functional role of LRC in C2B

domains is to provide an additional docking site for the negatively charged signaling

lipids, such as PtdIns(4,5)P₂, and thereby increase the residence time at the membrane

[192].  Another noteworthy difference is that although in both domains loop 3 undergoes

conformational exchange, only in C2B the regions adjacent to loop 3 hinges are also

dynamic. To evaluate the timescale, we inspected the difference plots between the $R_{2,HE}$

and $R_{2,CPMG}$ values. In both domains, the attenuation of dynamics due to the application

of the CPMG pulse train is modest (**Figure V.S1A and S1B**). These data indicate that

the timescale of loop 3 and LRC (in C2A) motions is faster than 100 μs.
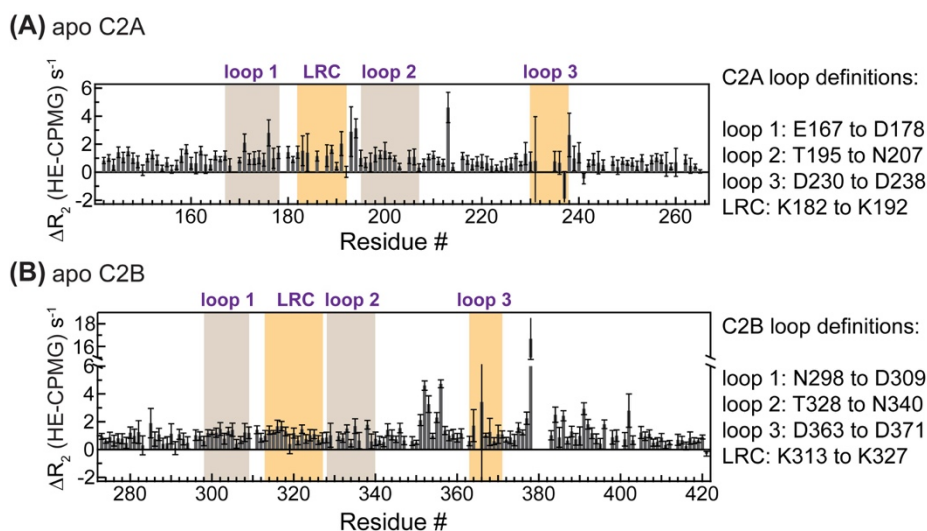


**Figure V.S1 Small differences between residue-specific $R_{2,HE}$ and $R_{2,CPMG}$ values indicate that the timescale of the membrane-binding region dynamics in apo C2A**
(A) and C2B (B) domains is faster than 100 μs. This figure represents difference plots of the data shown in Figure 2.

To determine how metal ion binding to Site 1 influences the backbone dynamics,

we prepared single-$Pb^{2+}$ complexes of the C2 domains and measured their $R_{2,HE}$ and

$R_{2,CPMG}$ values. Under 1:1 stoichiometric conditions of our sample, Site 1 is slightly

under-populated. Although the population of apo proteins is very low (~2-3 %), the

inter-conversion between apo and metal-ion bound species can lead to large chemical

exchange effects on the millisecond timescale, as was previously shown for the $Ca^{2+}$ ion

binding to the C2A variant [193]. Indeed, we observed a significant elevation of the $R_{2,HE}$ values in the loop regions of both domains. Fortunately, these processes occur on a timescale of ms and therefore can be efficiently suppressed by an application of the CPMG pulse train (**Figure V.S2**). Therefore, the $R_{2,CPMG}$ values in the C2·Pb1 complexes report almost exclusively on the intrinsic dynamics of the loops.
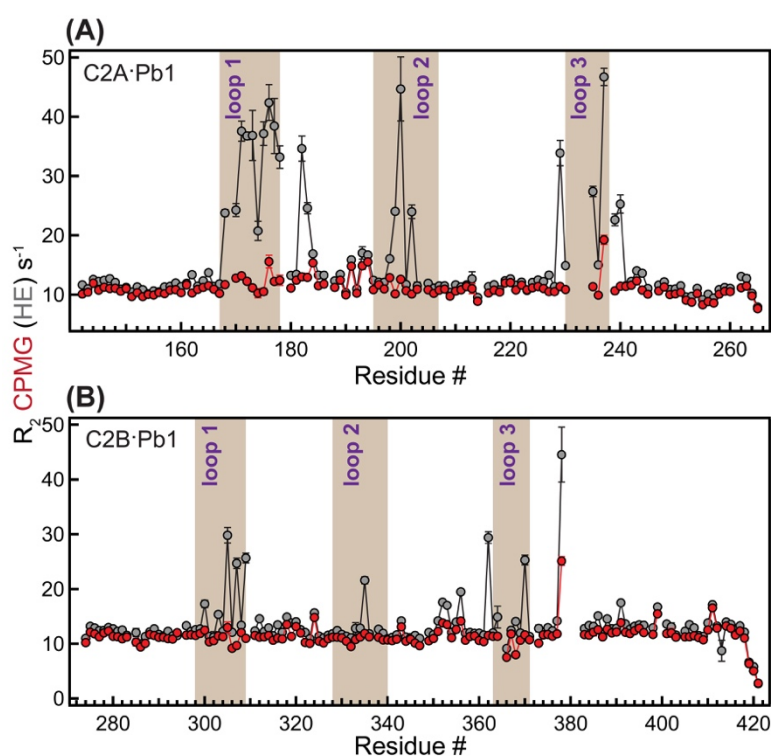


**Figure V.S2 Evidence for the millisecond (ms)-timescale dynamics associated with under-population of Site 1 by Pb$^{2+}$**
(A) C2A data and (B) C2B data. The conclusion regarding the timescale comes from the comparison of the residue-specific transverse relaxation rate constants $R_2$ obtained in the Hahn-Echo (HE, gray) and Carr-Purcell-Meiboom-Gill (CPMG, red) experiments. Application of the CPMG pulse train results in almost complete attenuation of chemical exchange contributions to the $R_{2,CPMG}$ values, which is an unambiguous evidence for the ms-timescale dynamics.
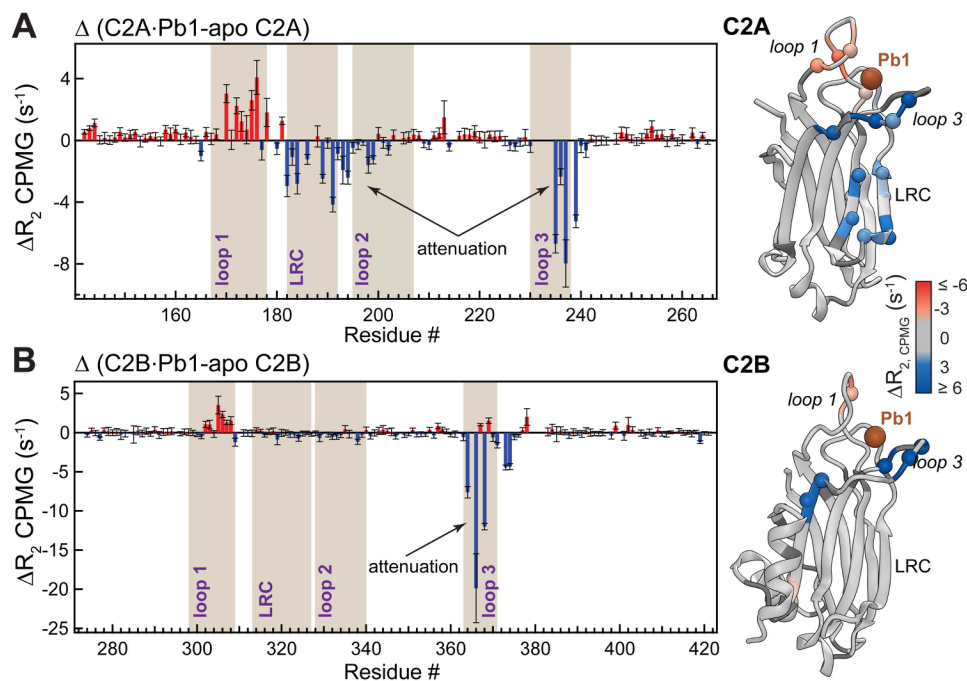
**Figure V.3 Binding of a single metal ion to C2 attenuates the µs-timescale dynamics of the membrane-binding regions**
Difference plots of the $R_{2,CPMG}$ values measured in apo and $Pb^{2+}$-complexed C2 domains are shown for the C2A (A) and C2B (B) domains. Negative values indicate the attenuation of dynamics. The $R_{2,CPMG}$ differences are color-coded and mapped onto the 3D structures of the $Pb^{2+}$-complexed C2 domains.

The $R_{2,CPMG}$ differences between the $Pb^{2+}$-complexed and apo proteins revealed that metal ion binding to Site 1 attenuates the dynamics of loop 3 (**Figure V.3**). This is manifested in large negative values of $\Delta R_{2,CPMG}$ in loop 3 for both domains. In addition, the entire positively charged LRC region of C2A loses its conformational plasticity (**Figure V.3A**). This indicates that the dynamic effect of metal ion binding to Site 1 propagates as far as ~15-25 Å throughout the C2A domain in what could be an allosteric communication between the metal ion binding sites and LRC. Loop 1, which is

191

immobile on the ms-to-μs timescales in the apo-states of C2A and C2B (**Figure V.2**), experiences a slight increase in $R_{2,CPMG}$ due to incomplete suppression of the ms-timescale chemical exchange due to metal ion binding (*vide supra*).

For the function of C2 domains, the implications of the attenuated dynamics are two-fold.  First, conformational restriction brought about by a metal ion in Site 1 may facilitate membrane interactions through imposing loop 3 orientation that is favorable for membrane insertion.  Second, the geometric restriction of the Asp ligands, some of which are shared by metal ions in Sites 1 and 2, will likely facilitate the subsequent metal-ion binding to Site 2.  In either case, the effect of populating Site 1 with a metal ion would "prime" the C2 domains of Syt1 for metal-ion dependent membrane interactions.

<u>C2A weakly associates with anionic membranes in a single metal-ion bound state</u>

We then asked if the population of Site 1 by a metal ion is sufficient to support the membrane interactions of the Syt1 C2 domains.  Starting with C2A, we prepared the [U-$^{15}$N]-enriched C2A·Pb1 complex and mixed it with the preparation of isotropically tumbling bicelles that mimic the membrane environment.  Two anionic phospholipids: phosphatidylserine (PtdSer) and phosphatidylinositol-4,5-bisphosphate (PtdIns(4,5)P$_2$) were incorporated into the bicelles at 14% and 2%, respectively, relative to the long-chain phospholipid.  The low fraction of PtdIns(4,5)P$_2$ brings about the question of its distribution in the bicelles.  This distribution is stochastic, and some heterogeneity in the bicelle population with respect to PtdIns(4,5)P$_2$ content is expected.  All NMR observables measured in bicelles represent the average over this bicelle ensemble.

Comparison of the [$^{15}$N-$^1$H] HSQC spectra with and without bicelles (**Figure V.4A**) revealed two spectroscopic signatures: chemical shift perturbations (CSPs, Δ) of the N-H cross-peaks and attenuation of their intensities. The CSPs affected loop regions 1, 2, and 3 of the C2A domain, but not the lysine-rich cluster (**Figure V.4B,D**). No chemical shift perturbations were observed when C2A domain in the absence of any metal ions was mixed with bicelles, indicating that CSPs report specifically on the metal-ion dependent interactions of the C2A domain with membranes. Lack of CSPs in the LRC indicates that this region does not directly interact with PtdSer and PtdIns(4,5)P$_2$. In the membrane-free system, a similar interaction pattern was observed between the Ca$^{2+}$-complexed C2A domain and inositol-1,4,5-triphosphate [192].

The intensity attenuation of the C2A·Pb1 N-H cross-peaks, expressed as the ratio of intensities in the bicelle-containing (I) and bicelle-free (I$_0$) samples varied across the primary structure (**Figure V.4C**). The regions with the most reduced intensities correspond to the protein loops and mirror the CSP pattern. This is a manifestation of a chemical exchange process whose kinetics is in the intermediate-to-fast regime on the NMR chemical shift timescale. It is well established that the PtdSer can coordinate the C2-bound metal ions while interacting simultaneously with the loop residues [63, 194]. We conclude that the chemical exchange process represents the binding of the binary C2A·Pb1 complex to the bicelles, with the formation of the ternary C2A·Pb1·PtdSer(bicelle) complex. This conclusion is further reinforced by the comparison of the residue-specific I/I$_0$ ratios between apo C2A and C2A·Pb1 in the presence of bicelles (**Figure V.4E**). The intensity ratios are systematically lower for the

C2A·Pb1 complex, and not just for the loop regions. The overall decrease in intensities is due to the increase in the apparent rotational correlation time of C2A·Pb1, because it partially associates with bicelles that are slow-tumbling high-molecular-mass entities. The population of the membrane-bound C2A·Pb1 complex is low, based on the relatively modest attenuation of cross-peak intensities corresponding to regions not subject to chemical exchange.

The C2A·Pb1 association with membranes also occurs in the absence of PtdIns(4,5)P$_2$, where the only anionic lipid component is PtdSer. We demonstrated this by conducting NMR-detected experiments of the C2A·Pb1 binding to large unilamellar vesicles (**Figure V.S3**). Consistent with our bicelle data, the population of membrane-bound state of C2A·Pb1 is low, evidenced by the moderate systematic attenuation of cross-peak intensities (**Figure V.S4,** purple bars). Adding more Pb$^{2+}$ to solution results in the population of Site 2 of the C2A domain. This increases the fraction of membrane-bound Pb$^{2+}$-complexed C2A, as manifested in the ~2-fold decrease in the N-H cross-peak intensities (**Figure V.S4,** green bars).

Taken together, our data indicate that population of Site 1 by a divalent metal ion is sufficient to drive weak association of the C2A domain with anionic membranes. The membrane-interacting regions primarily involve the metal-binding loops, as shown schematically for the C2·Pb1·bicelle complex in **Figure V.4E**.
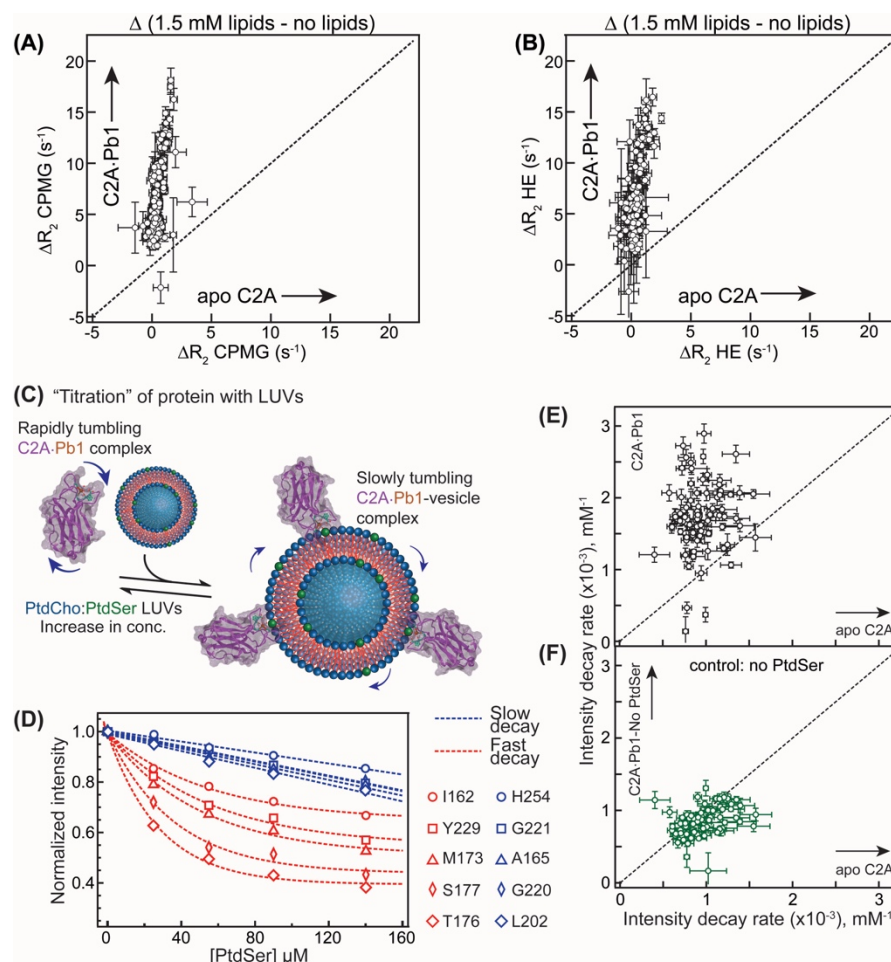
**Figure V.S3 Syt1 C2A·Pb1 complex binds to PtdSer-containing large unilamellar vesicles (LUVs)**

(A,B) Correlation plots of $\Delta R_{2,CPMG}$ (A) and $\Delta R_{2,HE}$ (B) values in the C2A·Pb1 complex and apo C2A. $\Delta R_{2,CPMG}$ and $\Delta R_{2,HE}$ are calculated as the differences in residue-specific $R_{2,CPMG}$ and $R_{2,HE}$ values, respectively, in the presence and absence of LUVs. While no significant changes are observed in apo C2A upon addition of LUVs, all $\Delta R_{2,CPMG}$ and $\Delta R_{2,HE}$ values are > 0 in the C2A·Pb1 complex. These data indicate that PtdSer as anionic lipid component is necessary and sufficient for C2A to interact with membrane mimics upon binding a single metal ion to Site 1. (C) Schematic representation of the experimental design to probe the interaction of C2A·Pb1 with LUVs. The experiments were carried out in the "titration" mode, where increasing concentrations of LUVs were added to the [U-$^{15}$N] enriched C2A·Pb1 complex. The $^{15}$N-$^1$H HSQC spectra of C2A·Pb1 were recorded at each LUV concentration point. (D) Normalized N-H cross-peak intensities of C2A·Pb1 show consistent decay upon increase of LUV concentration, plotted along the X-axis as accessible PtdSer. Two types of behavior were observed, depending on the chemical exchange regime of a given residue, slow (blue) and fast (red). (E,F)

Correlation plots of the intensity decay rates between C2A·Pb1 and apo C2A. In the presence of PtdSer-containing LUVs, the intensity decay rates of the C2A·Pb1 exceed those of apo C2A due to the interactions of the former with LUVs. This behavior is dependent on the presence of PtdSer in the membrane: omission of PtdSer results in comparable intensity decay rates that are mostly due to the increase in sample viscosity in both protein samples.
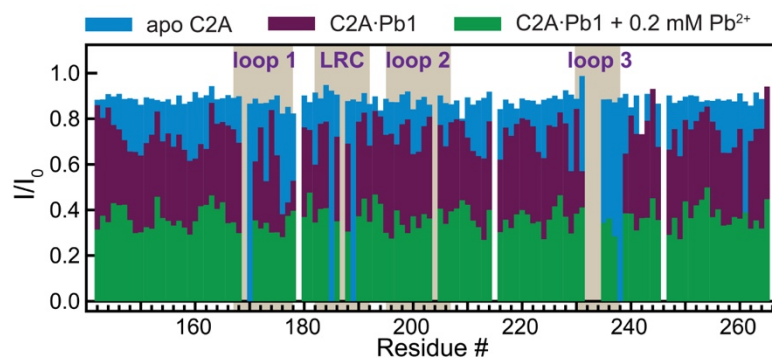


**Figure V.S4  Progressive population of metal ion binding sites by $Pb^{2+}$ in C2A drives the protein association with anionic membranes**

The ratio of the C2A N-H cross-peak intensities in the absence ($I_0$) and presence ($I$) of PtdSer-containing LUVs is plotted against the primary structure for three protein samples in different states of metal ligation. The composition of LUVs is PtdCho:PtdSer=80:20; the protein-to-lipid ratios are 1:20, 1:14, and 1:10 for the apo, C2A·Pb1, and (C2A·Pb1+0.2 mM $Pb^{2+}$) samples, respectively.
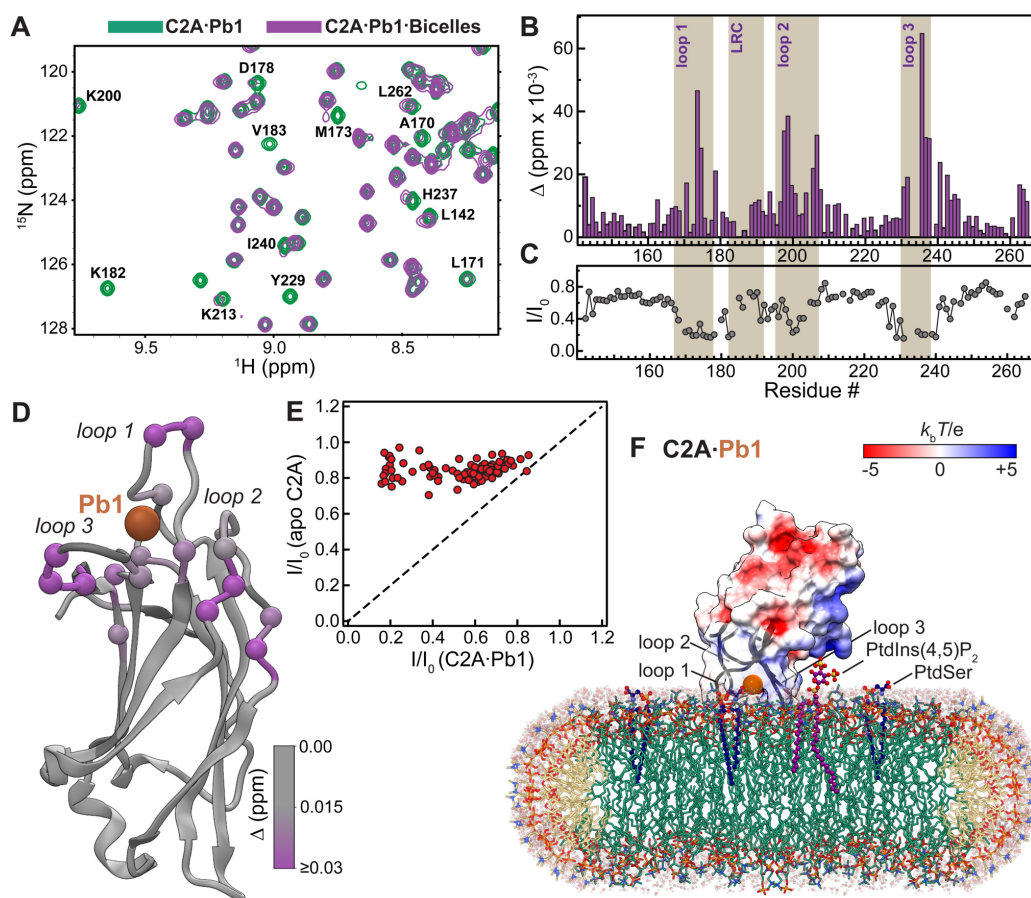
**Figure V.4 Syt1 C2A·Pb1 complex interacts with anionic bicelles**
(A) Overlay of the [$^{15}$N-$^{1}$H] HSQC spectral regions of C2A·Pb1 in the absence (green) and presence (purple) of anionic bicelles that illustrates CSPs experienced and broadening of protein resonances upon interactions with bicelles. (B) CSP plot showing that perturbations are localized primarily to the loop regions. (C) Attenuation of peak intensities in the C2A·Pb1 complex upon addition of anionic bicelles, expressed as residue-specific $I/I_0$ ratios, where I and $I_0$ are the peak intensities in the presence and absence of bicelles, respectively. Loop regions are preferentially broadened due to chemical exchange. (D) CSP values mapped on the C2A·Pb1 complex (PDB ID: 5VFE) illustrating the proximity of the affected regions to the metal ion binding Site 1. (E) Comparison of the residue-specific $I/I_0$ ratios in apo C2A and C2A·Pb1. The overall intensity attenuation is significant in the C2A·Pb1 sample, but negligible in the apo C2A sample, where it merely reflects an increase in solution viscosity due to bicelle addition. (F) Schematic representation of the C2A·Pb1-bicelle complex that is consistent with our experimental data.

<u>C2B interactions with anionic membranes are enhanced by metal ion binding to Site 1</u>

The C2B domain in Syt1 is distinct from C2A with respect to its electrostatic properties. The unique electrostatic makeup of the C2B surface provides additional complexity and control to the membrane interactions of Syt1 [47, 60, 183, 195]. The LRC of C2B has 6 basic residues while that of C2A has 4 basic residues that are flanked by two acidic ones. This makes the LRC of C2B significantly more electropositive (see **Figure V.1C**), turning it into an effective PtdIns(4,5)P$_2$ sensor [196]. Moreover, there are additional basic residues, Arg 398 and Arg 399, at the C2B end opposite to the loop region. These residues are implicated in the membrane-apposition process [182, 195]. In the presence of Ca$^{2+}$, the basic regions can create scaffolds by simultaneously interacting with various lipid and protein partners such as PtdSer, inositol polyphosphates, Ca$^{2+}$ channels, and SNAREs [58, 183, 197, 198]. In the absence of Ca$^{2+}$, the LRC of C2B is believed to pre-associate with the PtdIns(4,5)P$_2$-rich plasma membranes [199].

Using the same experimental strategy as for C2A, we prepared the [U-$^{15}$N]-enriched C2B·Pb1 and collected 2D [$^{15}$N-$^1$H] HSQC NMR spectra in the presence and absence of anionic bicelles (**Figure V.5A**). Extensive line broadening accompanied by significant chemical shift changes was observed for many N-H cross-peaks of C2B. The CSP pattern calculated for the bicelle-containing samples relative to bicelle-free C2B·Pb1 was clearly distinct from what we observed for the C2A·Pb1 complex in two aspects: (i) the CSPs for loop 3 of C2B were significantly larger than those for loop 1, suggesting a more prominent role of loop 3 in protein-membrane interactions; and (ii) there were very significant CSPs in the LRC-loop 2 region (compare **Figure V.4B** and

**5B**).  Mapping the CSP values onto the 3D structure of the $Pb^{2+}$-complexed C2B domain highlighted a contiguous surface likely to be involved in interactions with anionic membranes (**Figure V.5D**).  Another drastic difference between C2A·Pb1 and C2B·Pb1 was in the extent of signal attenuation upon addition of bicelles (compare **Figure V.4C** and **5C**).  The intensity drop for the C2B·Pb1 was uniform, with the exception of a few flexible C-terminal residues, and substantial: the mean $I/I_0$ value from the 5% trimmed data set was 0.14.  We conclude that the C2B·Pb1 complex, in contrast to C2A·Pb1, associates with anionic bicelles with high affinity.
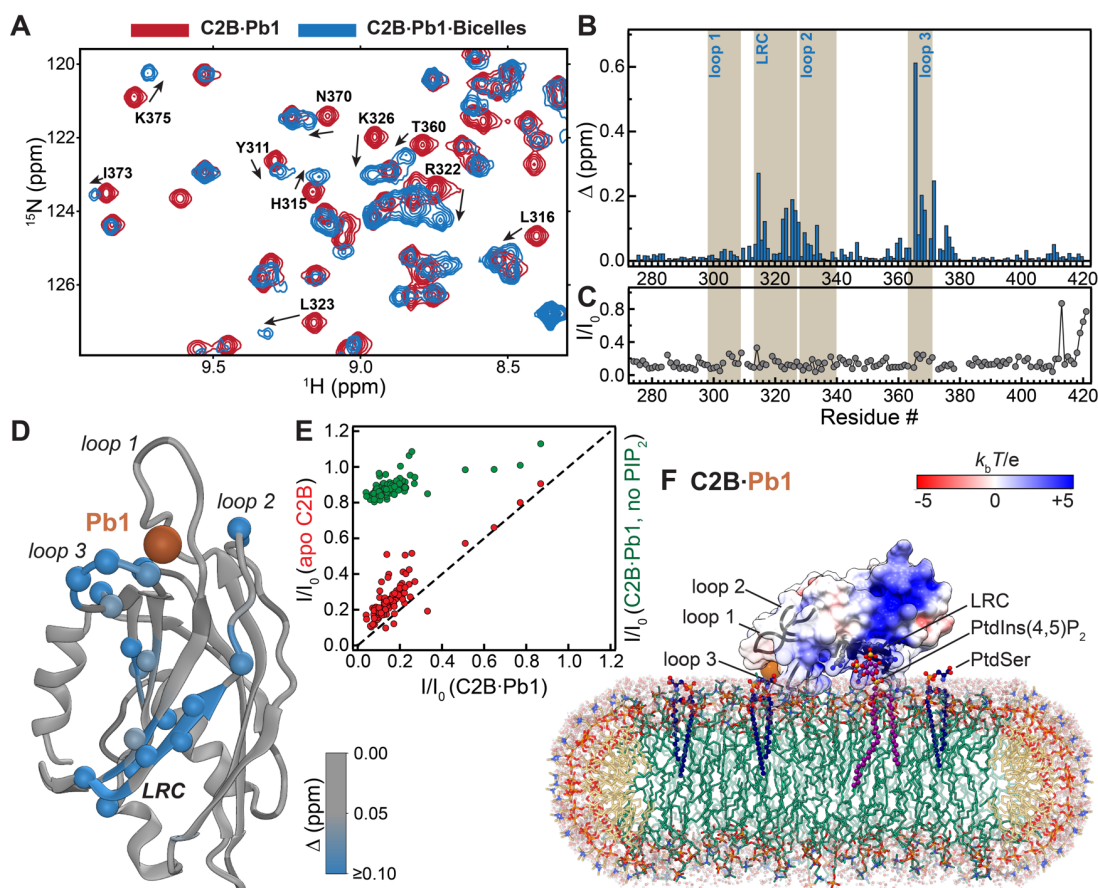
**Figure V.5 C2B·Pb1 binds to anionic bicelles with high affinity**

(A) Overlay of the $[^{15}N-^{1}H]$ HSQC spectral regions of C2B·Pb1 in the absence (red) and presence (blue) of anionic bicelles that illustrates CSPs and broadening of protein resonances upon interactions with bicelles. (B) CSP plot showing that perturbations are localized primarily to the LRC and loop 3 of the C2B domain. (C) Attenuation of peak intensities in the C2B·Pb1 complex upon addition of anionic bicelles, expressed as residue-specific $I/I_0$ ratios, where I and $I_0$ are the peak intensities in the presence and absence of bicelles, respectively. Significant uniform (with the exception of the flexible C-term residues) attenuation indicates high-affinity association of C2A·Pb1 with bicelles. (D) CSP values mapped on the C2B·Pb1 complex (PDB ID: 5VFG) cover a contiguous surface that includes primarily loop 3 and the LRC. (E) Correlation of residue-specific $I/I_0$ ratios in apo C2B and C2B·Pb1 in the presence of PtdIns(4,5)P$_2$ (red) indicates that metal ion binding to Site 1 contributes moderately to protein-bicelle interactions. Omitting PtdIns(4,5)P$_2$ abolishes the interactions of C2B·Pb1 with bicelles (green). (F) Schematic representation of the C2B·Pb1-bicelle complex that is consistent with our experimental data.

200

To establish the metal-ion dependence of this process, we conducted a control experiment in which the metal-ion free C2B domain (apo C2B) was mixed with anionic bicelles of the same composition. The observed CSP values were smaller than those for the C2B·Pb1 complex, especially for loop 3 (**Figure V.S5**). The correlation of $I/I_0$ intensity ratios between apo C2B and C2B·Pb1 showed systematically lower values for the latter, suggesting that the fractional population of the membrane-bound C2B·Pb1 species is higher than that of the apo species (**Figure V.5E**, red symbols). However, the overall effect is rather modest, suggesting that the presence of metal ion at Site 1 contributes moderately to the C2B-membrane interactions. The binding of C2B·Pb1 to bicelles is significantly enhanced by PtdIns(4,5)P$_2$: when we omitted PtdIns(4,5)P$_2$, the $I/I_0$ ratios increased to values of 0.8 and above (**Figure V.5E**, green symbols).
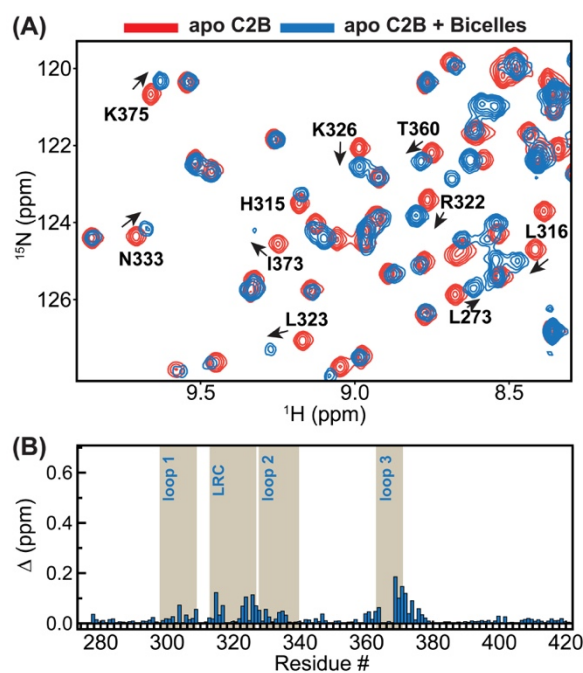
**Figure V.S5 Apo C2B binds to anionic bicelles that contain PtdIns(4,5)P$_2$ component**

(A) Overlay of the $^{15}$N-$^1$H HSQC spectral regions of apo C2B in the absence (red) and presence (blue) of anionic bicelles that illustrates CSPs experienced by the protein upon interactions with bicelles. The bicelle-containing spectrum is acquired with twice the number of scans compared to the bicelle-free one and depicted at the same contour threshold. (B) CSP plot calculated for the bicelle-containing C2B sample relative to the bicelle-free protein. The Y-axis scale is identical to that of the C2B·Pb1 plot shown in Fig 5B. The concentrations of protein and bicelle-lipids were 150 μM and 60 mM (~230 μM bicelles) respectively.

Our data are consistent with the orientation of C2B·Pb1 where the LRC and loop 3, but not loop 1, are in close membrane contact (**Figure V.5F**). In the previously reported model of the C2B-membrane complex under the saturating Ca$^{2+}$ conditions [61, 183], C2B has both loops 1 and 3 inserted into the membrane, while its LRC makes contact with PtdIns(4,5)P$_2$. The implication is that the metal-ion binding to Site 2 likely causes insertion of loop 1 into the headgroup region and "tilts" the C2B by reducing the angle between its long axis and the bilayer normal.

<u>The affinity of C2B to PtdIns(4,5)P$_2$ is enhanced by metal ion at Site 1</u>

Binding of a full complement of Ca$^{2+}$ ions enhances the affinity of C2 domains to PtdIns(4,5)P$_2$ [68, 186]. To evaluate the thermodynamic gain afforded exclusively by Site 1, we conducted NMR-detected binding experiments between C2B (apo and the C2B·Pb1 complex) and di-C4-PtdIns(4,5)P$_2$. The rationale behind using water-soluble di-C4-PtdIns(4,5)P$_2$, as compared to inositol 1,4,5-trisphosphate, is that it has the same electrostatic properties of the headgroup as the longer-chain PtdIns(4,5)P$_2$.

Both C2B species responded to increasing concentration of PtdIns(4,5)P$_2$ in a titratable manner (**Figure V.6A** and **Figure V.S6A**). The binding process is in the fast

exchange regime relative to the NMR chemical shift timescale. This is manifested in a smooth trajectory of the N-H cross-peaks as a function of increasing concentration of ligand in both apo C2B and C2B·Pb1 [$^{15}$N,$^{1}$H] HSQC spectra. The fast exchange behavior enabled us to construct the binding curves that represent the chemical shift changes experienced by the N-H cross-peaks, $\Delta$, as a function of total concentration of di-C4-PtdIns(4,5)P$_2$. Binding curves for well-resolved residues that showed a combined $\Delta$ of > 0.05 ppm were globally fitted to obtain the following dissociation constants: $K_d$ = 102 ± 3 μM (C2B·Pb1) and 215 ± 16 μM (apo C2B). We conclude that the presence of metal ion in Site 1 of the C2B domain alone is sufficient to cause 2-fold increase of affinity to PtdIns(4,5)P$_2$. A comparison of the CSP patterns (**Figure V.S6**) mapped onto the protein 3D structures (**Figure V.6**) shows that the same regions in apo C2B and the C2B·Pb1 are influenced by the PtdIns(4,5)P$_2$ interactions: the LRC and loop 3-adjacent β7 segment (**Figure V.6B**). These regions form a concave site that is typical for C2 domains with specificity towards phosphoinositides [196, 200].

The 2-fold increase in affinity represents the thermodynamic enhancement that is attributed solely to the interactions of the LRC residues with PtdIns(4,5)P$_2$. In neuronal membranes, an additional favorable contribution to the protein-membrane interactions would come from higher-abundance anionic phospholipids, such as PtdSer, which directly coordinates the metal ion bound to Site 1 of C2B [63].
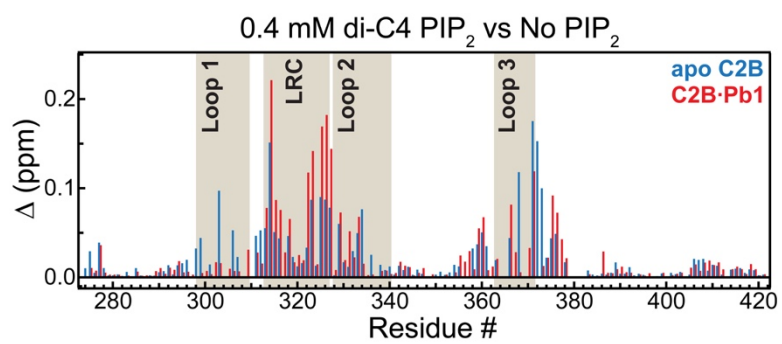
**Figure V.S6 Comparison of the chemical shift perturbations Δ due to di-C4-PtdIns(4,5)P₂ binding for apo C2B (blue) and the C2B.Pb1 complex (red)** [$^{15}$N-$^{1}$H] HSQC spectra shown in Fig. 6 of the main manuscript were used to calculate Δ values.
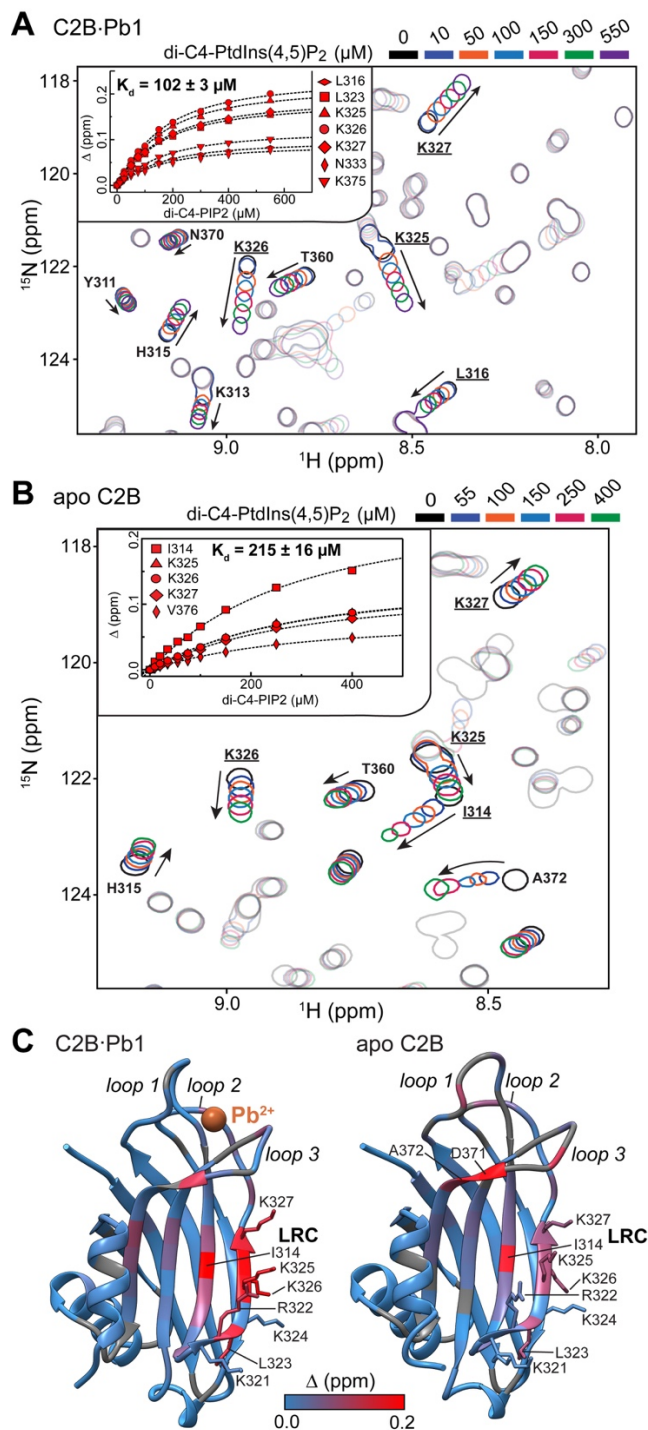
**Figure V.6 Binding of Pb²⁺ at Site 1 enhances the affinity of C2B towards PtdIns(4,5)P₂**

(A,B) Overlays of the [¹⁵N-¹H] HSQC spectral regions showing progressive chemical shift changes upon addition of di-C4-PtdIns(4,5)P₂ to the C2B·Pb1 complex (A) and

apo C2B (B). N-H cross-peaks that illustrate the binding of di-C4-PtdIns(4,5)P$_2$ to the canonical site in the LRC are labeled. Insets: NMR-detected binding curves for residues that either form or are in close proximity to the canonical binding site. The effective K$_d$ values extracted from the global fit of the curves are 102 μM (C2B·Pb1) and 215 μM (apo C2B). (C) Chemical shift perturbations Δ due to di-C4-PtdIns(4,5)P$_2$ binding (0-0.4 mM range) mapped onto the crystal structures the C2B·Pb1 complex (5VFG) and apo C2B (5CCJ). Positively charged residues that form LRC are shown in stick representation. Additionally, residues experiencing Δ larger than 0.15 ppm are labeled.

<u>The membrane interaction pattern of C2AB is similar to that of individual domains</u>

The tandem C2A and C2B domains (**Figure V.1A**) constitute the membrane-binding unit of Syt1 [47, 145]. Their distinct electrostatic properties and preferences towards binding partners govern the Syt1-mediated vesicle fusion [75, 183, 188]. The question of the C2AB conformational preferences has elicited some discussion in the literature. In crystalline state, C2AB can adopt a "closed" conformation with well-defined inter-domain interface [201]. In solution, the atomic force microscopy and intramolecular FRET measurements by Chapman and coworkers indicate that there exists an interaction between C2A and C2B [202] and that it is important for the Syt1 function [203]. However, NMR experiments conducted by Rizo's group argue against the presence of a well-defined inter-domain interface in solution [182]. What is evident is that there exists significant inter-domain conformational flexibility in the C2AB fragment. We sought to determine how this flexibility influences membrane interaction properties under limiting metal ion conditions.

Using the C2AB fragment, we first tested if Pb$^{2+}$ populates the same metal-ion binding sites as it does in the isolated domains. Due to the acidic nature of the 9-residue linker (there are 4 glutamate residues, **Figure V.1A**), there was a possibility that this

206

region could sequester added $Pb^{2+}$. [$^{15}N$-$^1H$] TROSY HSQC spectra of [U-$^{15}N$, ~80%-$^2H$] C2AB at 1:1 and 1:2 protein-to-$Pb^{2+}$ ratios (**Figure V.S7**) revealed the same chemical exchange regime, saturation behavior, and chemical shift perturbation patterns as for the isolated C2 domains [187]. These data indicate that $Pb^{2+}$ selectively populates Site 1 of the C2A and C2B domains in the context of the C2AB fragment and that the linker region is not involved in metal-ion binding. The state of C2AB with $Pb^{2+}$ bound to Site 1 in both domains is subsequently referred to as C2AB·Pb1.

Addition of anionic bicelles to the C2AB·Pb1 complex produced the following spectroscopic signatures in the [$^{15}N$-$^1H$] TROSY-HSQC spectra: decrease of the N-H cross-peak intensities and chemical shift perturbations, both of which are indicative of the protein-membrane binding process. The % intensity decrease was rather uniform within each domain, but the extent was different: 28% and 55% on average for the C2B and C2A domains, respectively. The pattern of chemical shift perturbations and their magnitude, small for the C2A domain loops and large for the LRC and loop 3 of the C2B domain (**Figure V.7A**), mirrored the data obtained for the individual domains (**Figure V.4B** and **5B**).
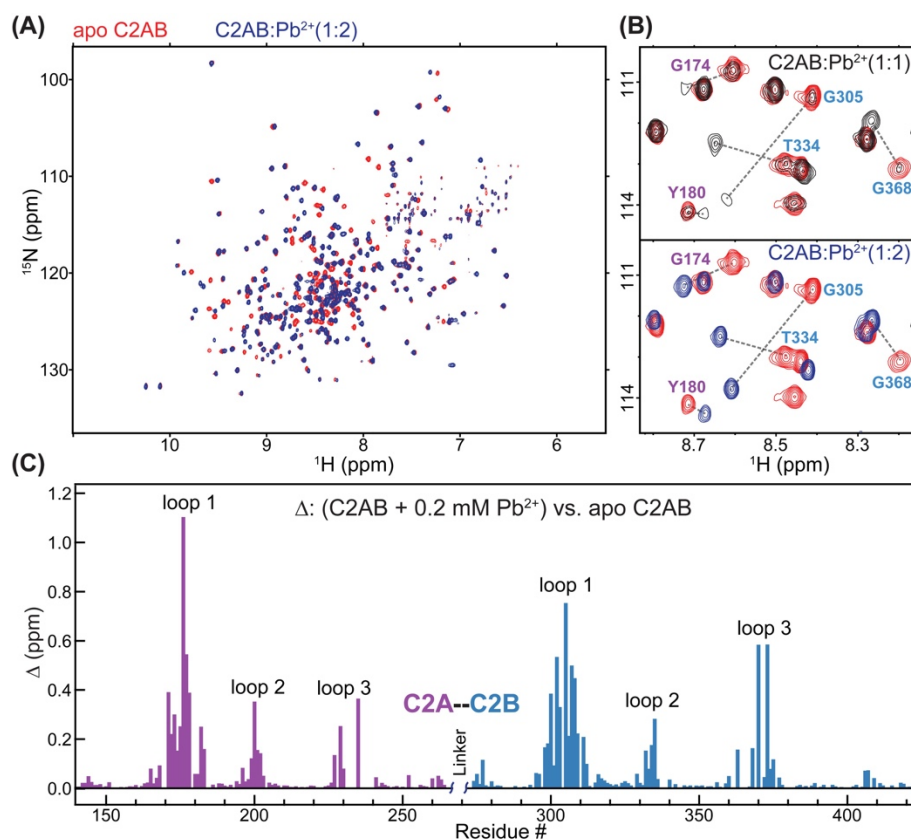
**Figure V.S7. Syt1 C2AB binds one $Pb^{2+}$ per C2 domain under $C2AB:Pb^{2+}$=1:2 conditions**

(A) Overlay of the $[^{15}N\text{-}^{1}H]$ TROSY-HSQC spectra of apo (red) and $Pb^{2+}$-complexed (blue) C2AB showing the chemical shift changes upon $Pb^{2+}$ binding to the C2AB domain. The concentrations of C2AB and $Pb^{2+}$ were 100 and 200 μM, respectively. (B) Expansion of the $[^{15}N\text{-}^{1}H]$ TROSY-HSQC spectra at protein:$Pb^{2+}$ =1:1 ratio (top) show that loop region residues are in slow exchange regime on the NMR chemical shift timescale. This is manifested in two sets of N-H cross-peaks: one set corresponding to the apo C2AB, and the other set corresponding to the $Pb^{2+}$-complexed C2AB; the peaks that belong to the same residue are connected with a dashed line. The N-H cross-peaks corresponding to the C2A and C2B residues are labeled in purple and blue, respectively. The spectrum of apo C2AB (red) is overlaid onto the spectrum of the $Pb^{2+}$-complexed C2AB for comparison. Addition of $Pb^{2+}$ to a final protein-to-$Pb^{2+}$ ratio of 1:2 results in complete redistribution of peak intensities towards the $Pb^{2+}$-complexed form (bottom). (C) Chemical shift perturbation plot showing that $Pb^{2+}$ binding affects the loop regions of both C2A and C2B. The pattern is consistent with that observed for the individual C2A and C2B domains with $Pb^{2+}$ bound to Site 1 (Katti, S., Her, B., Srivastava, A. K., Taylor, A. B., Lockless, S. W., and Igumenova, T. I. (2018) High affinity interactions of $Pb^{2+}$ with Synaptotagmin I. Metallomics 10, 1211-1222).

208

We used the paramagnetic relaxation enhancement (PRE) of NH groups to evaluate the extent of membrane contacts of C2 domains in the C2AB fragment. A lipid bearing a paramagnetic doxyl tag, 5- doxyl PC, was introduced into the bicelles to give ~3 molecules per leaflet (**Figure V.7B**). The unpaired electron of the doxyl group enhances the transverse relaxation rates of neighboring spins, resulting in broadening of the corresponding N-H cross-peaks and reduction in their intensities. The label position is such that N-H groups penetrating the headgroup region would experience the most broadening. If the protein-membrane binding process is in fast exchange on the NMR chemical shift timescale, which is the most likely scenario for the C2AB·Pb1 complex, the PRE effect is scaled by the population of paramagnetic species.

The residue-specific PRE values were calculated as the ratios of protein peak intensities in the C2AB·Pb1 samples containing diamagnetic and paramagnetic preparations of bicelles, $I_{dia}/I_{para}$ (**Figure V.7B**). Consistent with the chemical shift perturbation data of **Figure V.7A**, the C2A domain showed weak but readily discernable PRE effect in the loop regions. The PRE values were significantly larger for the C2B domain, with the residues of loop 3 (K366, I367, and G368) and LRC (L323 and K326) showing >15% intensity attenuation. Taken together, our data on the C2AB·Pb1 complex indicate that both domains make membrane contact when Site 1 on each domain is populated by a divalent metal ion. These results support the existence of a "primed" membrane-associated state under limiting metal ion conditions. In such a state, PtdIns(4,5)P$_2$-mediated membrane docking of C2B will be augmented by the metal ion at Site 1 and keep both domains anchored at the membrane interface. The membrane

binding of C2A will remain weak.  This will ensure a strict metal-ion concentration dependence of the membrane insertion process for the C2A that requires a full complement of metal ions to associate with PtdSer-containing membranes.
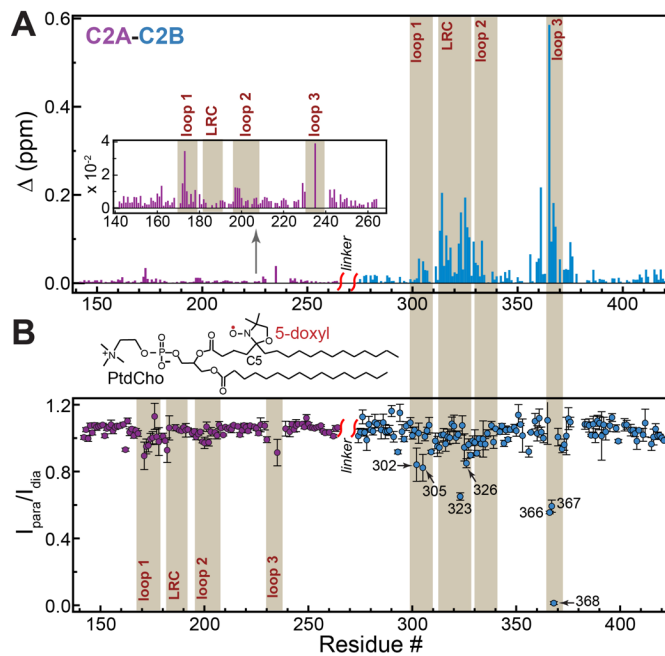
**Figure V.7 The C2AB·Pb1 complex binds to anionic bicelles with both domains contacting the membrane**
(A) Loop 3 and LRC of the C2B domain make a dominant contribution to the chemical shift perturbation experienced by the C2AB·Pb1 complex upon binding anionic bicelles. The C2A data are shown in the inset with the re-scaled Y-axis. The CSP patterns of the C2 domains in the context of the C2AB fragment-bicelle system are similar to those of the individual domains shown in Figs. 4B and 5B. The similarities refer to both the overall pattern and the magnitude. (B) Membrane contact of C2A and C2B is revealed through the attenuation of the C2AB·Pb1 peak intensities upon addition of anionic bicelles containing a paramagnetic lipid, 5-doxyl PtdCho, at ~3 molecules per leaflet. The attenuation is expressed as residue-specific $I_{para}/I_{dia}$ ratios, where $I_{para}$ and $I_{dia}$ are the peak intensities in the presence and absence of paramagnetic lipids, respectively.

Progressive saturation of metal ion binding sites in full-length Syt1 correlates with the

extent of membrane penetration

To determine how the occupancy of metal ion binding sites influences the

membrane insertion of the C2 domains in full-length Syt1, we conducted EPR

experiments on the protein reconstituted into anionic LUVs. Under the conditions of our

211

EPR experiments, both C2 domains of Syt1 bind in *cis* with respect to the transmembrane segment that anchors the protein to the LUVs [188]. The spin-labeled sidechain R1 (**Figure V.8**) was attached to either loop 1 site in C2A (173R1) or a loop 1 site in C2B (304R1). Both sites are known to penetrate negatively charged membranes under saturating $Ca^{2+}$ conditions. When no metal ions are present in solution, the R1 sidechain is in the aqueous phase and hence highly mobile, producing narrow EPR lineshapes for both C2 domains (**Figure V.8**, black traces). Addition of two-fold molar $Pb^{2+}$ excess with respect to protein selectively populates Site 1 in C2A and C2B. The EPR spectra under these conditions show significant broadening indicative of motional restriction due to partitioning of R1 into membranes (red trace in **Figure V.8**). There are two components: the broad component resembles that from a membrane bound state of the C2 domains and the more mobile component resembles that from an aqueous state. In these spectra, the membrane bound state dominates and represents 85% or more of the total protein. Addition of $Pb^{2+}$ at a molar ratio ($Pb^{2+}$:Syt1) of 20:1 eliminates the small aqueous population, further broadening the spectra and giving rise to a fully bound state (blue trace in **Figure V.8**). This occurs for both domains and suggests that with only partial binding of $Pb^{2+}$ to the domains, there is equilibrium between membrane inserted and aqueous populations that is eliminated with excess metal.

We used progressive power saturation of the EPR spectra and a collision-gradient approach to determine the membrane depth of 173R1 and 304R1. **Table V.1** gives the depth parameters and membrane depths under two $Pb^{2+}$ concentration conditions. When Site 1 is occupied by a metal ion, both 173R1 (C2A) and 304R1 (C2B) have apparent

positions on the aqueous side of the phosphate groups, with average distances of 0.8 Å

and 3.5 Å, respectively, above the level of lipid phosphates.  These depths likely reflect

contributions from both the membrane inserted and aqueous populations seen in the EPR

spectra.  Binding a full complement of $Pb^{2+}$ ions results in the stable insertion of R1 into

the membrane hydrocarbon region, with average distances of 3.6 Å (173R1, C2A) and

1.7 Å (304R1, C2B) below the phosphate level.
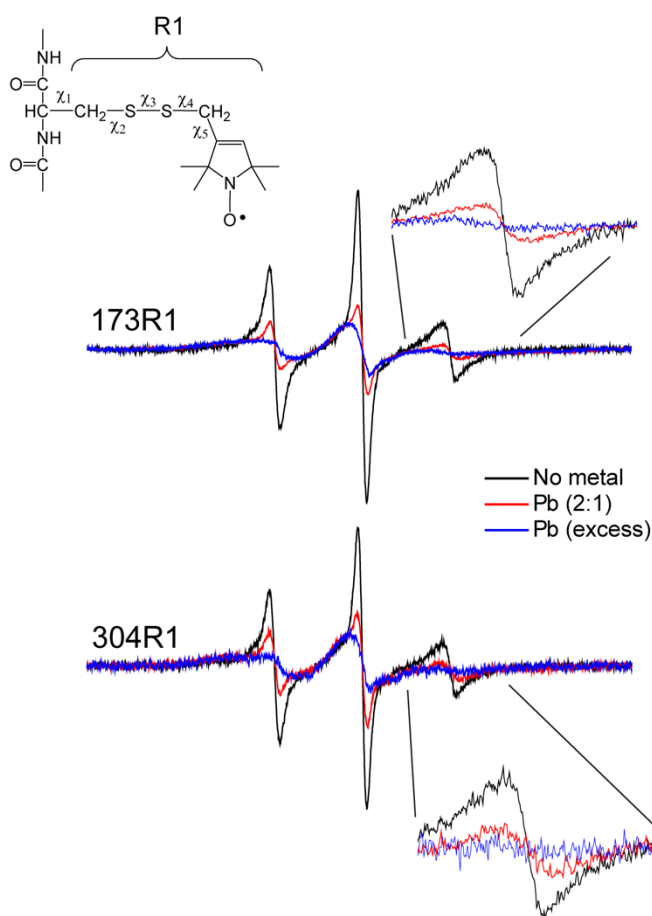


**Figure V.8 Membrane insertion of C2 domains in full-length Syt1 depends on the occupancy of metal-ion binding sites**
X-band EPR spectra of full-length membrane-reconstituted Syt1, where the first $Ca^{2+}$ binding loop of either the C2A domain (site 173) or the C2B domain (site 304) was labeled with MTSL to produce the R1 side-chain.  $Pb^{2+}$ binding to Syt1 promotes membrane insertion of the domains that is dependent upon the occupancy of the sites

in the binding loops.  The additional broadening in the EPR spectra with excess $Pb^{2+}$ ($Pb^{2+}$:Syt1, 20:1) suggests a deeper average membrane penetration of the domains in this state.  The ratio of $Pb^{2+}$:Syt1 was varied from 12:1 to 50:1 with no change in the EPR spectra.  The EPR spectra in the state labeled "No metal" were obtained after the addition of 4 mM EGTA, and these spectra were identical to spectra obtained prior to the addition of $Pb^{2+}$.

Both the EPR lineshapes and the membrane depth measurements support a more peripheral and dynamic membrane-bound state of Syt1 when the metal ion binding sites have low occupancy.  In the full-length protein the C2 domains are tethered to membranes via the N-terminal transmembrane region and this facilitates the formation of such a state by creating effectively high local lipid concentrations in the vicinity of the C2 domains.  Furthermore, it "primes" Syt1 to further metal ion events by placing its C2 domains in close proximity to the negatively charged membrane interface.

**Table V.1 Power saturation data for site 173R1 and 304R1when Syt1 is bound to membranes in the presence of $Pb^{2+}$**

| Label | lipid | metal ion added[§] | depth parameter ($\Phi$) | Position (Å)[†] |
|-------|-------|------|------|------|
| FL SYT 173R1 | PC/PS (15%) | $Pb^{2+}$ 2:1 ($Pb^{2+}$:Syt1) | $-1.56 \pm 0.1$ | -0.78 |
| | | $Pb^{2+}$ excess | $-0.72 \pm 0.05$ | 3.59 |
| FL SYT 304R1 | PC/PS (15%) | $Pb^{2+}$ 2:1 ($Pb^{2+}$:Syt1) | $-1.75 \pm 0.1$ | -3.53 |
| | | $Pb^{2+}$ excess | $-1.19 \pm 0.1$ | 1.73 |

[§]Data for the 2:1 $Pb^{2+}$ to FL-Syt1 ratio (1:1 lead to C2 domain) were taken to examine membrane penetration for a partially bound lead state, where only Site1 is populated [187]. In this state, there are two components in the EPR spectra, and the apparent depth has contributions from both these states.  Excess lead was then added to examine differences in membrane binding when both sites are populated in the C2 domains.

214

†The position indicates the average location of the nitroxide relative to the lipid phosphate plane. A negative value for the position indicates that the label is located on the aqueous side of the phosphate plane.

## Discussion

$Ca^{2+}$-dependent membrane binding of Syt1 plays a crucial role in the excitation-secretion coupling by enabling the SNAREs to initiate vesicle fusion [46, 177, 204]. Syt1-mediated evoked release has been detected at intracellular $Ca^{2+}$ concentrations as low as 25 μM [205]. Surprisingly, Syt1 is an intrinsically weak $Ca^{2+}$ sensor, with affinities ranging from 50 μM to >10 mM for the 5 $Ca^{2+}$-binding sites [47, 49, 51]. In the presence of anionic membranes, $Ca^{2+}$ binding to Syt1 becomes highly cooperative with an apparent affinity of ~3-4 μM, which corresponds to ~60-80 fold increase compared to the isolated C2AB fragment in absence of lipids [51, 68]. Conversely, $Ca^{2+}$ binding to the Syt1 C2 domains increases their affinity to anionic membranes [68]. The contribution of anionic phospholipids to this mutually cooperative response is attributed to: (i) masking of the positively charged surface patches of C2 (e.g., the LRC) through transient interactions; and (ii) direct coordination of the C2-bound divalent metal ions by the lipid headgroups [63, 194]. However, the role of individual $Ca^{2+}$-binding sites, specifically the high-affinity Site 1 of the C2 domains, in driving the membrane interactions remained unclear. $Pb^{2+}$, a high-affinity structural and functional surrogate of $Ca^{2+}$, enabled us to probe the properties of the C2 domains in which Site 1 is selectively populated by a divalent metal ion. We investigated the behavior of the isolated C2 domains, the C2AB fragment, and full-length Syt1.

215

Apart from the clear changes in electrostatics, population of Site 1 by $Pb^{2+}$ alters the dynamic behavior of the membrane-binding regions. Both C2 domains in the metal-free state have a highly dynamic loop 3 that undergoes conformational exchange on a timescale <100 µs (**Figure V.2**). The attenuation of loop 3 dynamics caused by a metal ion at Site 1 (**Figure V.3**) could facilitate the metal-ion dependent membrane-binding for the following three reasons: (i) loop 3 provides half of oxygen ligands of the metal ion at Site 1 and >60% of the coordinating ligands required for metal ion at Site 2; (ii) loop 3 harbors key positively charged residues (R233 in C2A; and K366 in C2B) that can potentially interact with anionic lipid headgroups upon partial or full neutralization of the intra-loop region [54, 206, 207]; and (iii) loop 3 has two hydrophobic residues (F231 and F234 for C2A; Y364 and I367 in C2B) that can potentially interact with the hydrophobic part of the bilayer [54, 146, 180]. In addition to loop 3, the LRC region in apo C2A, but not apo C2B, shows conformational dynamics that gets attenuated by metal ion binding to Site 1. The allosteric nature of this effect is surprising, as the LRC is positioned >10 Å away from Site 1. The functional significance of these changes in C2A dynamics remains to be investigated.

With respect to the membrane-binding properties, $Pb^{2+}$ in Site 1 enhances the membrane interactions of the C2 domains, individually and in the C2AB fragment (**Figures V. 4-7**). In C2A, it serves to promote weak association with anionic membranes containing PtdSer or both PtdSer and PtdIns(4,5)$P_2$. In C2B, $Pb^{2+}$ in Site 1 strengthens its metal-ion independent association with PtdIns(4,5)$P_2$ (**Figure V.6**). There was no obvious manifestation of avidity with respect to membrane binding of the

Pb$^{2+}$-complexed C2AB fragment (**Figure V.7**), suggesting that either the linker region connecting the two domains is sufficiently flexible for the domains to behave independently, or the C2 domains bind in "trans" mode relative to each other.

The experiments on full-length Syt1, where the protein is tethered to the membrane via the N-terminal helical segment, provided the clearest picture of the effect that sequential population of metal-ion binding sites has on the membrane interactions of the C2 domains. The EPR data (**Figure V.8** and **Table V.1**) show a clear correlation between the number of metal sites populated in the intra-loop region and the depth of membrane insertion. When only Site 1 in both domains is occupied, Syt1 adopts a membrane-bound state that is dynamic where the domains exchange between membrane associated and aqueous states. The domains become completely membrane inserted in the fully metal-ion loaded state.

We speculate that the formation of this dynamic membrane-bound state of Syt1 could occur during the initial stages of membrane recruitment, when cytosolic Ca$^{2+}$ predominantly populates high-affinity binding sites of the C2 domains prior to their binding to PtdSer. Both domains would make membrane contact: C2A through the loop regions, and C2B through its LRC region, with the latter interaction enhanced but not driven by the metal ion in Site 1 (**Figure V.9**). The attenuated conformational dynamics would serve to pre-organize the loops for subsequent metal-ion and membrane binding events. Given high local concentration of anionic lipids [208, 209] and Ca$^{2+}$ [210, 211] at the presynaptic membranes, the C2 domains would therefore be "primed" to bind a full

complement of $Ca^{2+}$ ions.  This will ensure a cooperative response that is necessary for Syt1 to respond to physiological $Ca^{2+}$ concentrations.

Attenuation of conformational dynamics and membrane recruitment through the involvement of the highest-affinity metal-ion binding site could be a feature shared by other $Ca^{2+}$-dependent C2 domains.  For example, stopped-flow kinetics measurements conducted by Falke's laboratory provided evidence for the membrane binding of the C2 domain from protein kinase C$\alpha$ that is complexed to a single $Ca^{2+}$ ion [212].  The conformational dynamics of this C2 domain upon population of Site 1 is attenuated in a manner similar to that of the Syt1 C2 domains [191].  Given that C2 domains are found in >100 proteins [1], the weak membrane recruitment step facilitated by a divalent metal ion at the highest affinity site could be part of the common mechanism employed by these proteins to fulfill their membrane-associated functions.
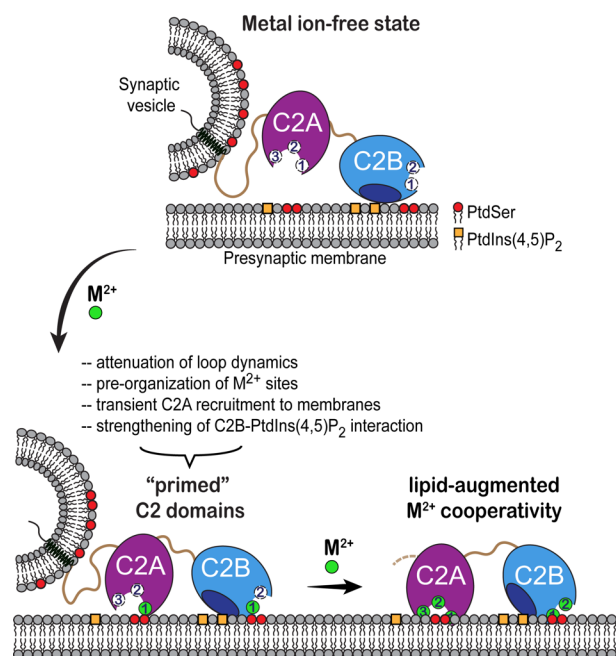
**Figure V.9 Contribution of Site 1 to Syt1-membrane interactions**

In the metal ion-free state, only the C2B domain is interacting with the PtdIns(4,5)P$_2$ component of the presynaptic membrane; there are no interactions with PtdSer through the loop regions of either C2 domain (SNAREs or interactions of C2B domain with SNAREs are not depicted for simplicity). Binding of metal ion to Site 1 is sufficient to drive weak association of C2A with the anionic lipids of the membrane and enhance the C2B-PtdIns(4,5)P$_2$ interactions. Both C2 domains would adopt a shallow membrane-bound state, in which the conformational flexibility of the loop regions (and the LRC region of C2A) is attenuated. The proximity of "primed" C2 domains to anionic phospholipids ensures mutually cooperative response, leading to the formation of fully metal-ion saturated C2 domains that undergo deep membrane insertion.

# References

[1] Lemmon, M. A. (2008) Membrane recognition by phospholipid-binding domains, *Nat Rev Mol Cell Biol 9*, 99-111.

[13] Perin, M. S., Brose, N., Jahn, R., and Sudhof, T. C. (1991) Domain structure of synaptotagmin (p65), *J Biol Chem 266*, 623-629.

[45] Brose, N., Petrenko, A. G., Sudhof, T. C., and Jahn, R. (1992) Synaptotagmin: a calcium sensor on the synaptic vesicle surface, *Science 256*, 1021-1025.

[46] Chapman, E. R. (2008) How does synaptotagmin trigger neurotransmitter release?, *Annu Rev Biochem 77*, 615-641.

[47] Fernandez, I., Arac, D., Ubach, J., Gerber, S. H., Shin, O., Gao, Y., Anderson, R. G., Sudhof, T. C., and Rizo, J. (2001) Three-dimensional structure of the synaptotagmin 1 C2B-domain: synaptotagmin 1 as a phospholipid binding machine, *Neuron 32*, 1057-1069.

[49] Ubach, J., Zhang, X., Shao, X., Sudhof, T. C., and Rizo, J. (1998) Ca2+ binding to synaptotagmin: how many Ca2+ ions bind to the tip of a C2-domain?, *EMBO J 17*, 3921-3930.

[51] Fernandez-Chacon, R., Konigstorfer, A., Gerber, S. H., Garcia, J., Matos, M. F., Stevens, C. F., Brose, N., Rizo, J., Rosenmund, C., and Sudhof, T. C. (2001) Synaptotagmin I functions as a calcium regulator of release probability, *Nature 410*, 41-49.

[52] Katti, S., Nyenhuis, S. B., Her, B., Srivastava, A. K., Taylor, A. B., Hart, P. J., Cafiso, D. S., and Igumenova, T. I. (2017) Non-Native Metal Ion Reveals the Role of Electrostatics in Synaptotagmin 1-Membrane Interactions, *Biochemistry 56*, 3283-3295.

[54] Zhang, X., Rizo, J., and Sudhof, T. C. (1998) Mechanism of phospholipid binding by the C2A-domain of synaptotagmin I, *Biochemistry 37*, 12395-12403.

[58] Radhakrishnan, A., Stein, A., Jahn, R., and Fasshauer, D. (2009) The Ca2+ affinity of synaptotagmin 1 is markedly increased by a specific interaction of its C2B domain with phosphatidylinositol 4,5-bisphosphate, *J Biol Chem 284*, 25749-25760.

[60] Kuo, W., Herrick, D. Z., Ellena, J. F., and Cafiso, D. S. (2009) The calcium-dependent and calcium-independent membrane binding of synaptotagmin 1: two modes of C2B binding, *J Mol Biol 387*, 284-294.

[61] Kuo, W., Herrick, D. Z., and Cafiso, D. S. (2011) Phosphatidylinositol 4,5-bisphosphate alters synaptotagmin 1 membrane docking and drives opposing bilayers closer together, *Biochemistry 50*, 2633-2641.

[63] Honigmann, A., van den Bogaart, G., Iraheta, E., Risselada, H. J., Milovanovic, D., Mueller, V., Mullar, S., Diederichsen, U., Fasshauer, D., Grubmuller, H., Hell, S. W., Eggeling, C., Kuhnel, K., and Jahn, R. (2013) Phosphatidylinositol 4,5-bisphosphate clusters act as molecular beacons for vesicle recruitment, *Nat Struct Mol Biol 20*, 679-686.

[68] van den Bogaart, G., Meyenberg, K., Diederichsen, U., and Jahn, R. (2012) Phosphatidylinositol 4,5-bisphosphate increases Ca2+ affinity of synaptotagmin-1 by 40-fold, *J Biol Chem 287*, 16447-16453.

[69] Morales, K. A., Lasagna, M., Gribenko, A. V., Yoon, Y., Reinhart, G. D., Lee, J. C., Cho, W., Li, P., and Igumenova, T. I. (2011) Pb2+ as modulator of protein-membrane interactions, *J Am Chem Soc 133*, 10599-10611.

[75] Zhou, Q., Lai, Y., Bacaj, T., Zhao, M., Lyubimov, A. Y., Uervirojnangkoorn, M., Zeldin, O. B., Brewster, A. S., Sauter, N. K., Cohen, A. E., Soltis, S. M., Alonso-Mori, R., Chollet, M., Lemke, H. T., Pfuetzner, R. A., Choi, U. B., Weis, W. I., Diao, J., Sudhof, T. C., and Brunger, A. T. (2015) Architecture of the synaptotagmin-SNARE machinery for neuronal exocytosis, *Nature 525*, 62-67.

[82] Morales, K. A., Yang, Y., Long, Z., Li, P., Taylor, A. B., Hart, P. J., and Igumenova, T. I. (2013) Cd2+ as a Ca2+ surrogate in protein-membrane interactions: isostructural but not isofunctional, *J Am Chem Soc 135*, 12980-12983.

[99] Delaglio, F., Grzesiek, S., Vuister, G. W., Zhu, G., Pfeifer, J., and Bax, A. (1995) NMRPipe: a multidimensional spectral processing system based on UNIX pipes, *J Biomol NMR 6*, 277-293.

[101] Farrow, N. A., Muhandiram, R., Singer, A. U., Pascal, S. M., Kay, C. M., Gish, G., Shoelson, S. E., Pawson, T., Forman-Kay, J. D., and Kay, L. E. (1994) Backbone dynamics of a free and phosphopeptide-complexed Src homology 2 domain studied by $^{15}$N NMR relaxation, *Biochemistry 33*, 5984-6003.

[102] Wang, L., Pang, Y., Holder, T., Brender, J. R., Kurochkin, A. V., and Zuiderweg, E. R. (2001) Functional dynamics in the active site of the ribonuclease binase, *Proc. Natl. Acad. Sci. U.S.A. 98*, 7684-7689.

[144] Geppert, M., Goda, Y., Hammer, R. E., Li, C., Rosahl, T. W., Stevens, C. F., and Sudhof, T. C. (1994) Synaptotagmin I: a major Ca2+ sensor for transmitter release at a central synapse, *Cell 79*, 717-727.

[145] Chapman, E. R., and Jahn, R. (1994) Calcium-dependent interaction of the cytoplasmic region of synaptotagmin with membranes. Autonomous function of a single C2-homologous domain, *J Biol Chem 269*, 5735-5741.

[146] Chapman, E. R., and Davis, A. F. (1998) Direct interaction of a Ca2+-binding loop of synaptotagmin with lipid bilayers, *J Biol Chem 273*, 13995-14001.

[147] Frazier, A. A., Roller, C. R., Havelka, J. J., Hinderliter, A., and Cafiso, D. S. (2003) Membrane-bound orientation and position of the synaptotagmin I C2A domain by site-directed spin labeling, *Biochemistry 42*, 96-105.

[174] Neher, E., and Sakaba, T. (2008) Multiple roles of calcium ions in the regulation of neurotransmitter release, *Neuron 59*, 861-872.

[175] Zhou, Q., Lai, Y., Bacaj, T., Zhao, M., Lyubimov, A. Y., Uervirojnangkoorn, M., Zeldin, O. B., Brewster, A. S., Sauter, N. K., and Cohen, A. E. (2015) Architecture of the synaptotagmin–SNARE machinery for neuronal exocytosis, *Nature 525*, 62.

[176] Brewer, K. D., Bacaj, T., Cavalli, A., Camilloni, C., Swarbrick, J. D., Liu, J., Zhou, A., Zhou, P., Barlow, N., and Xu, J. (2015) Dynamic binding mode of a Synaptotagmin-1–SNARE complex in solution, *Nat. Struct. Mol. Biol. 22*, 555.

[177] Zhou, Q., Zhou, P., Wang, A. L., Wu, D., Zhao, M., Südhof, T. C., and Brunger, A. T. (2017) The primed SNARE–complexin–synaptotagmin complex for neuronal exocytosis, *Nature 548*, 420.

[178] Sudhof, T. C. (2013) A molecular machine for neurotransmitter release: synaptotagmin and beyond, *Nat Med 19*, 1227-1231.

[179] Bai, J., Wang, C. T., Richards, D. A., Jackson, M. B., and Chapman, E. R. (2004) Fusion pore dynamics are regulated by synaptotagmin.t-SNARE interactions, *Neuron 41*, 929-942.

[180] Lynch, K. L., Gerona, R. R., Kielar, D. M., Martens, S., McMahon, H. T., and Martin, T. F. (2008) Synaptotagmin-1 utilizes membrane bending and SNARE binding to drive fusion pore expansion, *Mol. Biol. Cell 19*, 5093-5103.

[181] Fernandez-Chacon, R., Shin, O. H., Konigstorfer, A., Matos, M. F., Meyer, A. C., Garcia, J., Gerber, S. H., Rizo, J., Sudhof, T. C., and Rosenmund, C. (2002) Structure/function analysis of Ca2+ binding to the C2A domain of synaptotagmin 1, *J Neurosci 22*, 8438-8446.

[182] Arac, D., Chen, X., Khant, H. A., Ubach, J., Ludtke, S. J., Kikkawa, M., Johnson, A. E., Chiu, W., Sudhof, T. C., and Rizo, J. (2006) Close membrane-membrane proximity induced by $Ca^{2+}$-dependent multivalent binding of synaptotagmin-1 to phospholipids, *Nat. Struct. Mol. Biol. 13*, 209-217.

[183] Wang, S., Li, Y., and Ma, C. (2016) Synaptotagmin-1 C2B domain interacts simultaneously with SNAREs and membranes to promote membrane fusion, *Elife 5*.

[184] Gorkhali, R., Huang, K., Kirberger, M., and Yang, J. J. (2016) Defining potential roles of $Pb^{2+}$ in neurotoxicity from a calciomics approach, *Metallomics*.

[185] Rajalingam, D., Kumar, T. K., and Yu, C. (2005) The C2A domain of synaptotagmin exhibits a high binding affinity for copper: implications in the formation of the multiprotein FGF release complex, *Biochemistry 44*, 14431-14442.

[186] Morales, K. A., and Igumenova, T. I. (2012) Synergistic effect of $Pb^{2+}$ and phosphatidylinositol 4,5-bisphosphate on C2 domain-membrane interactions, *Biochemistry 51*, 3349-3360.

[187] Katti, S., Her, B., Srivastava, A. K., Taylor, A. B., Lockless, S. W., and Igumenova, T. I. (2018) High affinity interactions of $Pb^{2+}$ with synaptotagmin I, *Metallomics 10*, 1211-1222.

[188] Nyenhuis, S. B., Thapa, A., and Cafiso, D. S. (2019) Phosphatidylinositol 4,5 bisphosphate controls the cis and trans interactions of Synaptotagmin 1, *Biophys J 117*, 247-257.

[189] King, E. J. (1932) The colorimetric determination of phosphorus, *Biochem J 26*, 292-297.

[190] Lee, W., Tonelli, M., and Markley, J. L. (2015) NMRFAM-SPARKY: enhanced software for biomolecular NMR spectroscopy, *Bioinformatics 31*, 1325-1327.

[191] Morales, K. A., Yang, Y., Cole, T. R., and Igumenova, T. I. (2016) Dynamic Response of the C2 Domain of Protein Kinase Cα to $Ca^{2+}$ Binding, *Biophys. J. 111*, 1655-1667.

[192] Perez-Lara, A., Thapa, A., Nyenhuis, S. B., Nyenhuis, D. A., Halder, P., Tietzel, M., Tittmann, K., Cafiso, D. S., and Jahn, R. (2016) $PtdInsP_2$ and PtdSer cooperate to trap synaptotagmin-1 to the plasma membrane in the presence of calcium, *Elife 5*.

[193] Millet, O., Bernado, P., Garcia, J., Rizo, J., and Pons, M. (2002) NMR measurement of the off rate from the first calcium-binding site of the synaptotagmin I C2A domain, *FEBS Lett 516*, 93-96.

[194] Verdaguer, N., Corbalan-Garcia, S., Ochoa, W. F., Fita, I., and Gomez-Fernandez, J. C. (1999) $Ca^{2+}$ bridges the C2 membrane-binding domain of protein kinase Cα directly to phosphatidylserine, *EMBO J 18*, 6329-6338.

[195] Xue, M., Ma, C., Craig, T. K., Rosenmund, C., and Rizo, J. (2008) The Janus-faced nature of the $C_2B$ domain is fundamental for synaptotagmin-1 function, *Nat Struct Mol Biol 15*, 1160-1168.

[196] Guillen, J., Ferrer-Orta, C., Buxaderas, M., Perez-Sanchez, D., Guerrero-Valero, M., Luengo-Gil, G., Pous, J., Guerra, P., Gomez-Fernandez, J. C., Verdaguer, N., and Corbalan-Garcia, S. (2013) Structural insights into the $Ca^{2+}$ and $PI(4,5)P_2$ binding modes of the C2 domains of rabphilin 3A and synaptotagmin 1, *Proc. Natl. Acad. Sci. U.S.A. 110*, 20503-20508.

[197] Fukuda, M., Moreira, J. E., Lewis, F. M., Sugimori, M., Niinobe, M., Mikoshiba, K., and Llinas, R. (1995) Role of the C2B domain of synaptotagmin in vesicular release and recycling as determined by specific antibody injection into the squid giant synapse preterminal, *Proc. Natl. Acad. Sci. U.S.A. 92*, 10708-10712.

[198] Chapman, E. R., Desai, R. C., Davis, A. F., and Tornehl, C. K. (1998) Delineation of the oligomerization, AP-2 binding, and synprint binding region of the C2B domain of synaptotagmin, *J Biol Chem 273*, 32966-32972.

[199] Bai, J., Tucker, W. C., and Chapman, E. R. (2004) $PIP_2$ increases the speed of response of synaptotagmin and steers its membrane-penetration activity toward the plasma membrane, *Nat Struct Mol Biol 11*, 36-44.

[200] Guerrero-Valero, M., Ferrer-Orta, C., Querol-Audi, J., Marin-Vicente, C., Fita, I., Gomez-Fernandez, J. C., Verdaguer, N., and Corbalan-Garcia, S. (2009) Structural and mechanistic insights into the association of PKCα-C2 domain to $PtdIns(4,5)P_2$, *Proc. Natl. Acad. Sci. U.S.A. 106*, 6603-6607.

[201] Fuson, K. L., Montes, M., Robert, J. J., and Sutton, R. B. (2007) Structure of human synaptotagmin 1 C2AB in the absence of $Ca^{2+}$ reveals a novel domain association, *Biochemistry 46*, 13041-13048.

[202] Liu, H., Bai, H., Xue, R., Takahashi, H., Edwardson, J. M., and Chapman, E. R. (2014) Linker mutations reveal the complexity of synaptotagmin 1 action during synaptic transmission, *Nat Neurosci 17*, 670-677.

[203] Evans, C. S., He, Z., Bai, H., Lou, X., Jeggle, P., Sutton, R. B., Edwardson, J. M., and Chapman, E. R. (2016) Functional analysis of the interface between the tandem C2 domains of synaptotagmin-1, *Mol. Biol. Cell 27*, 979-989.

[204] Dai, H., Shen, N., Arac, D., and Rizo, J. (2007) A quaternary SNARE-synaptotagmin-$Ca^{2+}$-phospholipid complex in neurotransmitter release, *J Mol Biol 367*, 848-863.

[205] Schneggenburger, R., and Neher, E. (2000) Intracellular calcium dependence of transmitter release rates at a fast central synapse, *Nature 406*, 889-893.

[206] Wang, P., Wang, C. T., Bai, J., Jackson, M. B., and Chapman, E. R. (2003) Mutations in the effector binding loops in the C2A and C2B domains of synaptotagmin I disrupt exocytosis in a nonadditive manner, *J Biol Chem 278*, 47030-47037.

[207] Shao, X., Li, C., Fernandez, I., Zhang, X., Sudhof, T. C., and Rizo, J. (1997) Synaptotagmin-syntaxin interaction: the C2 domain as a $Ca^{2+}$-dependent electrostatic switch, *Neuron 18*, 133-142.

[208] James, D. J., Khodthong, C., Kowalchyk, J. A., and Martin, T. F. (2008) Phosphatidylinositol 4,5-bisphosphate regulates SNARE-dependent membrane fusion, *J Cell Biol 182*, 355-366.

[209] Lauwers, E., Goodchild, R., and Verstreken, P. (2016) Membrane lipids in presynaptic function and disease, *Neuron 90*, 11-25.

[210] Bornschein, G., and Schmidt, H. (2018) Synaptotagmin $Ca^{2+}$ sensors and their spatial coupling to presynaptic $Ca_v$ channels in central cortical synapses, *Front. Mol. Neurosci. 11*, 494.

[211] Bilkova, E., Pleskot, R., Rissanen, S., Sun, S., Czogalla, A., Cwiklik, L., Rog, T., Vattulainen, I., Cremer, P. S., Jungwirth, P., and Coskun, U. (2017) Calcium directly regulates phosphatidylinositol 4,5-bisphosphate headgroup conformation and recognition, *J Am Chem Soc 139*, 4019-4024.

[212] Corbin, J. A., Evans, J. H., Landgraf, K. E., and Falke, J. J. (2007) Mechanism of specific membrane targeting by C2 domains: localized pools of target lipids enhance Ca2+ affinity, *Biochemistry 46*, 4322-4336.

CHAPTER VI INTERFERENCE OF PH BUFFER WITH PB(II)-PERIPHERAL

DOMAIN INTERACTIONS: OBSTACLE OR OPPORTUNITY? [*]

**Background**

Lead ($Pb^{2+}$) is a xenobiotic heavy metal ion that shows acute as well as chronic

systemic toxicity in the human body.[213] No extent of $Pb^{2+}$ exposure is considered "safe",

and if undetected, can cause irreversible neurological damage in young children.[214, 215]

Among several proposed modes of $Pb^{2+}$ toxicity, the ability to mimic $Ca^{2+}$ is particularly

alarming, as it highlights the vulnerability of ubiquitous, multi-site $Ca^{2+}$-binding proteins

towards $Pb^{2+}$ attack.[216] Identification of physiologically relevant $Pb^{2+}$-binding sites on

these proteins is challenging because $Pb^{2+}$ interactions can be both specific as well as

opportunistic, and often exhibit affinities higher than those of native metal ions.[217]

Synaptotagmin 1 (Syt1), a key regulator of $Ca^{2+}$-evoked neurotransmitters release[144] and

putative molecular target of $Pb^{2+}$,[218] provides a remarkable example of this challenge. In

the non-chelating environment such as MES buffer, four out of total five $Ca^{2+}$-

coordinating sites on the tandem C2 domains of Syt1 (C2A and C2B, **Figure VI.1A**)

bind $Pb^{2+}$ with affinities higher than $Ca^{2+}$.[187] Site 1 on each domain exhibits sub-

micromolar $Pb^{2+}$ affinity, while Site 2 is substantially weaker in comparison (**Figure

VI.1A, table**).

---

Here, we demonstrate, using the C2 domains of Syt1 as a paradigm, an approach that uses a pH buffering agent and $Pb^{2+}$ chelator, Bis-Tris, to selectively probe high-affinity $Pb^{2+}$ sites and determine their specific functional roles.  Bis-Tris has five hydroxyl groups and one tertiary amine group (**Figure VI.1B**), all of which could potentially serve as ligands for a wide array of divalent metal ions.[219]  While the challenges of using chelating pH buffers for metal ion-binding studies are known,[220] Bis-Tris was our chelator of choice because, compared to other strong chelating agents such as EDTA, it forms weaker yet stable complexes with $Pb^{2+}$.[219]  In addition, Bis-Tris is a highly adaptable chelator in that the number of its functional groups engaged in metal-ion coordination can vary depending on the presence of competing ligands donated, e.g., by proteins, lipids, or other small molecules.  We reasoned that due to these properties, Bis-Tris would be a suitable mimic of a chelating physiological environment.  In this work, we show that not only the use of Bis-Tris enables discrimination between high- and low-affinity $Pb^{2+}$ sites, it also provides mechanistic information on the metal-ion dependent association of C2 domains with anionic membranes.  We therefore argue that a judicious use of chelating pH buffers in metal-binding studies could provide a valuable insight into the mechanisms of metallosensory proteins.
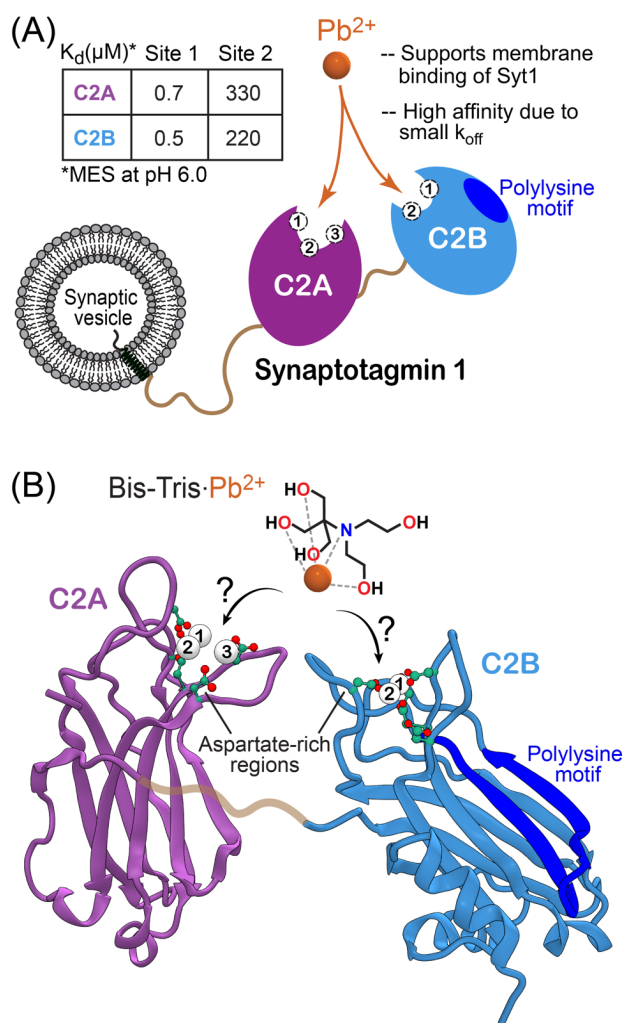
**Figure VI.1 C2 domains of Syt1 interact with Pb²⁺ ions through the aspartate-rich loop regions**

(A) Schematic representation of Syt1, a neuronal transmembrane protein and its cystosolic C2 domains, C2A and C2B. $Ca^{2+}$-binding sites are labeled individually in each C2 domain. The affinities of $Pb^{2+}$ to Sites 1 and 2 measured in MES buffer at pH $6.0$[187] are given in the table. $Pb^{2+}$ and $Ca^{2+}$ do not appreciably bind to Site 3 under these conditions. (B) 3D structures of C2A (1BYN) and C2B (1UOW) domains showing the location of the $Ca^{2+}$-binding aspartate-rich sites within the apical loop regions. Also shown is the schematic representation of the $Pb^{2+}$ complex with Bis-Tris. The exact coordination geometry of $Pb^{2+}$ in the Bis-Tris complex is unknown.

## Results and discussion

To determine which of the five metal-binding sites of Syt1 are populated by $Pb^{2+}$ in Bis-Tris, we conducted NMR-detected $Pb^{2+}$-binding experiments on the individual C2 domains, C2A and C2B.  Solution NMR spectroscopy is best suited for this purpose because it enables clear identification of metal-ion binding sites with a wide range of affinities, as demonstrated previously for the C2 domains of Syt1 and protein kinase C (PKC).[187, 221]  The information about protein-metal ion interactions is obtained by collecting 2D $^{15}N$-$^{1}H$ hetero-nuclear single-quantum coherence (HSQC) spectra of the uniformly $^{15}N$-enriched ([U-$^{15}N$]) C2 domains, in the presence of different concentrations of metal ions.  Binding of a metal ion alters the electronic environment of the backbone amide N-$H_N$ groups that are proximal to the binding site, which results in chemical shift changes of the $^{1}H_N$ and $^{15}N$ nuclei.  Given the tendency of certain buffering agents to interact with proteins,[222] prior to $Pb^{2+}$ addition, we compared the metal-free NMR spectra of the C2 domains in Bis-Tris and MES buffers.  For C2A, the spectra in MES and Bis-Tris were identical (**Figure VI.S1A**).  For C2B, a subset of N-$H_N$ resonances showed small variations in their chemical shifts as well as intensities (**Figure VI.S1B**), indicating possible weak interactions with one of these buffering agents.  Because of the highly basic nature of C2B and its propensity to interact with polyanionic molecules,[223] the weakly interacting buffer is likely to be MES.

**Figure VI.S1 C2A and C2B do not specifically interact with buffering agents**
Overlays of the [$^{15}$N-$^1$H] HSQC spectra of the metal-free forms of the Syt1 C2A **(A)** and C2B **(B)** domains. The C2A spectra are completely superimposable **(A)**. A subset of resonances in **(B)** shows small differences and intensity changes between the two buffers. Because of the highly basic nature of C2B and its propensity to interact with polyan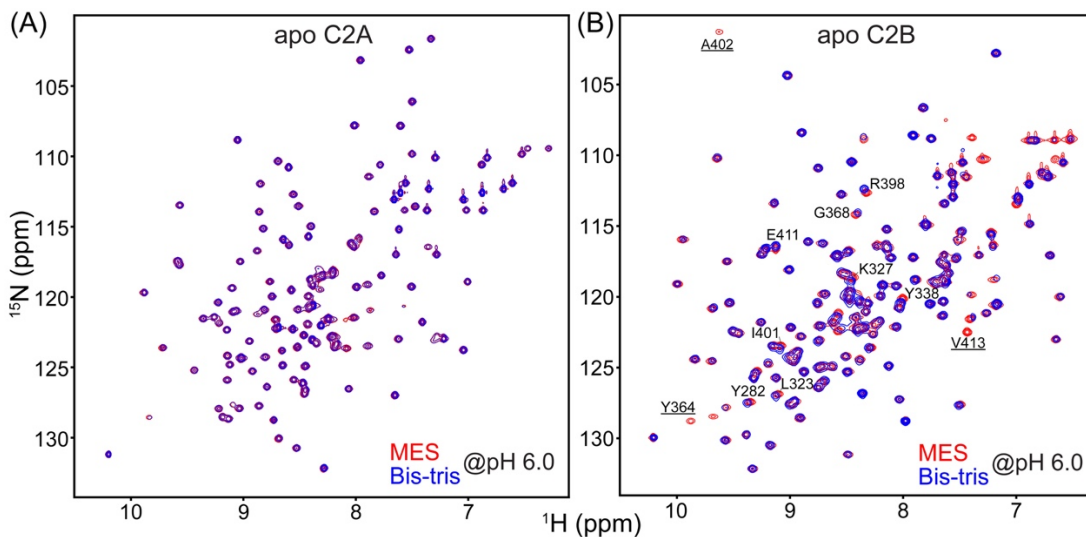ionic molecules, the interacting buffer is likely to be MES. The spectra were collected at 25 °C on the Avance III NMR instruments (Bruker Biospin) operating at the magnetic field of 14.1 T/equipped with a cryoprobe (C2A); and 11.7 T/equipped with the room-temperature probe (C2B). Protein concentration in the NMR samples was 100 μM. The buffer conditions were: 20 mM MES or Bis-Tris at pH 6.0, and 150 mM KCl.

Upon addition of Pb$^{2+}$ to the C2A domain at a molar ratio of 2:1 (C2A:Pb$^{2+}$), we observed an appearance of a subset of N-H$_N$ cross-peaks that belong to the Pb$^{2+}$-complexed protein species (top inset of **Figure VI.2A**, cyan). Adding more Pb$^{2+}$ to achieve a 1:1 molar ratio results in the formation of a single protein species, the C2A·Pb1 complex (**Figure VI.2A** and top inset, blue), where Pb$^{2+}$ is bound to Site 1. This behavior is identical to that in the non-chelating MES buffer,[187] suggesting that Bis-

Tris does not interfere with $Pb^{2+}$ binding to Site 1 of the C2A domain and full saturation of this site can be achieved at a stoichiometric ratio of protein to $Pb^{2+}$.

We found however that addition of more $Pb^{2+}$, with the objective to saturate Site 2 of the C2A domain, did not produce a drastic change in the $N-H_N$ cross-peak chemical shifts (**Figure VI.2B**) that we previously observed in MES.[187] The Pb2 binding event is in the "fast" exchange regime on the NMR chemical shift timescale, where a single population-weighted cross-peak for a given residue shows a smooth trajectory in response to increasing $Pb^{2+}$ concentration. This behavior enabled us to construct a binding curve by plotting the chemical shift perturbation $\Delta$ versus $Pb^{2+}$ concentration. The curve is linear, with no indication of reaching the cusp region even at 60-fold excess of $Pb^{2+}$ to protein (**Figure VI.2C**). For comparison, in MES, $Pb^{2+}$ was able to saturate Site 2 of the C2A domain at ~25-fold excess to produce a $K_d$ of 330 μM (see **Figure VI.1A**, table).[187] We observed the exact same pattern of $Pb^{2+}$ interactions with C2B in Bis-Tris: complete population of Site 1 at the stoichiometric protein-to-$Pb^{2+}$ ratio, and extremely weak binding to Site 2 (**Figure VI.S2**). We conclude that Bis-Tris does not affect $Pb^{2+}$ binding to the high-affinity Site 1 but inhibits the interactions of $Pb^{2+}$ with Site 2 of both C2 domains of Syt1. This is in agreement with the reported affinity of $Pb^{2+}$ to Bis-Tris (log Ka=4.3)[219] that exceeds the its affinity to Site 2 of the C2A domain. The affinity of $Pb^{2+}$ to Site 3 of the C2A domain is too weak to be appreciably populated in either buffer.
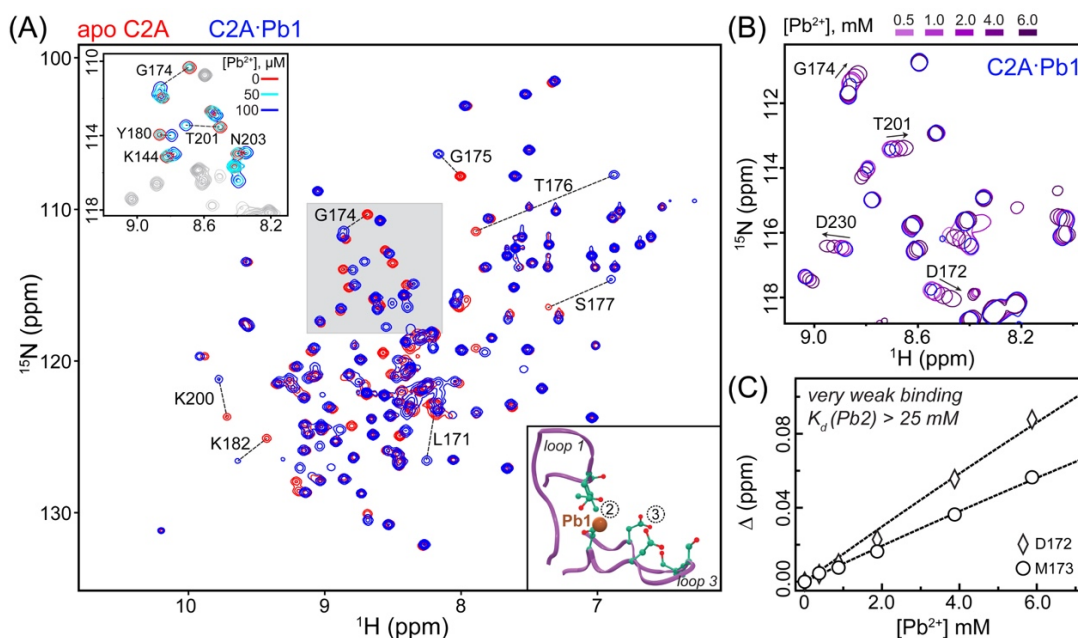
**Figure VI.2 Bis-Tris inhibits Pb$^{2+}$ binding to Site 2 but not Site 1 of the C2A domain**

(A) Overlay of the [$^{15}$N-$^{1}$H] HSQC spectra in the absence (apo) and presence of stoichiometric Pb$^{2+}$ (C2A:Pb$^{2+}$ 1:1, 100 μM each) in 20 mM Bis-Tris buffer at pH 6.0. Residues showing response to population of Site 1 by Pb$^{2+}$ are labeled. The spectra were collected at 25 °C on the Avance III NMR instrument (Bruker Biospin) operating at the magnetic field of 14.1 T and equipped with a cryogenically cooled probe. Top inset: expansion of the shaded spectral region with an additional Pb$^{2+}$ concentration point (50 μM, C2A:Pb$^{2+}$ 2:1, cyan) to illustrate the distinct chemical shifts of apo C2A and the C2A·Pb1 complex. Bottom inset: loop regions of the C2A domain showing the positions of Sites 1-3. (B) Overlay of the [$^{15}$N-$^{1}$H] HSQC expansions showing the chemical shift perturbations of several residues in the C2A·Pb1 complex due to Pb$^{2+}$ binding to Site 2. (C) Chemical shift perturbations Δ (calculated as described in ref. 8) of two representative residues plotted as a function of Pb$^{2+}$ concentration. The linear, non-saturable profiles indicate that binding is extremely weak with a K$_d$ of >25 mM. The lines are to guide the eye.
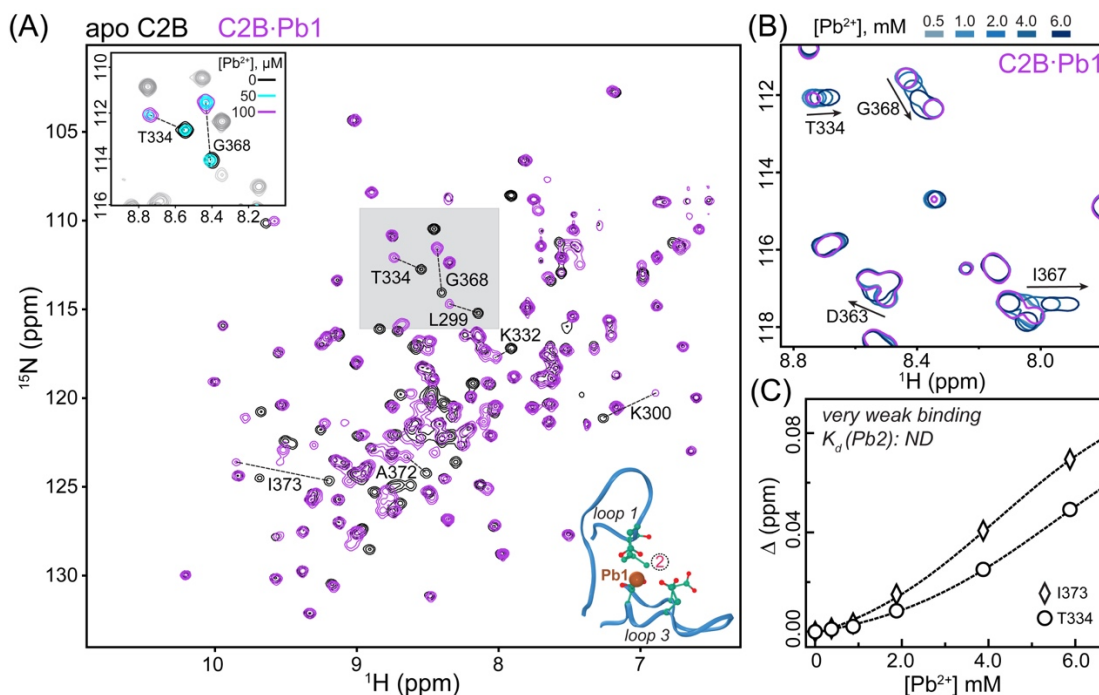
**Figure VI.S2 Bis-Tris inhibits Pb$^{2+}$ binding to Site 2 but not Site 1 of the C2B domain**

(A) Overlay of the [$^{15}$N-$^{1}$H] HSQC spectra in the absence (apo) and presence of stoichiometric Pb$^{2+}$ (C2B:Pb$^{2+}$ 1:1, 100 μM each) in 20 mM Bis-Tris buffer at pH 6.0. Residues showing response to population of Site 1 by Pb$^{2+}$ are labeled. The spectra were collected at 25 °C on the Avance III NMR instrument (Bruker Biospin) operating at the magnetic field of 14.1 T and equipped with a cryogenically cooled probe. Top inset: expansion of the shaded spectral region with an additional Pb$^{2+}$ concentration point (50 μM, C2B:Pb$^{2+}$ 2:1, cyan) to illustrate the distinct chemical shifts of apo C2B and the C2B·Pb1 complex. Bottom inset: loop regions of the C2B domain showing the positions of Sites 1 and 2. (B) Overlay of the [$^{15}$N-$^{1}$H] HSQC expansions showing the chemical shift perturbations of several residues in the C2B·Pb1 complex due to Pb$^{2+}$ binding to Site 2. (C) Chemical shift perturbations Δ (calculated as described in ref. 8 of the main text) of two representative residues plotted as a function of Pb$^{2+}$ concentration. The non-saturable profiles indicate that binding is extremely weak. The lines are to guide the eye.

We then asked if the Pb$^{2+}$ dependent membrane-binding function of the C2 domains is influenced by Bis-Tris. When Pb$^{2+}$ populates high- as well as low-affinity sites, as is the case in the MES buffer, both C2 domains interact readily with anionic

membranes.[187]  However, when we conducted the C2A-vesicle co-sedimentation experiments in Bis-Tris, we found that $Pb^{2+}$ was unable to support the membrane-binding function of the C2A domain.  The fraction of the $Pb^{2+}$-complexed protein bound to PtdSer-containing large unilamellar vesicles (LUVs) does not exceed 5%, even under conditions of the 40-fold molar excess of $Pb^{2+}$ over C2A (**Figure VI.3A**).  A control experiment with the native metal ion, $Ca^{2+}$, produced a fractional population of the membrane-bound species comparable to that observed in MES.[187]  Clearly, the effect of Bis-Tris is specific to the $Pb^{2+}$-C2A-anionic membrane system.  To ascertain that this finding is not technique-dependent, we conducted FRET-detected protein-to-membrane binding experiments shown schematically in **Figure VI.3B**.  In the presence of $Ca^{2+}$, the FRET curve of the C2A domain represents a typical membrane binding response reported for the C2 domains (**Figure VI.3C**).[51, 221]  In contrast, we observed no $Pb^{2+}$-driven interactions of C2A with membranes in Bis-Tris, which is fully consistent with the co-sedimentation data of **Figure VI.3A**.  We therefore conclude that Bis-Tris interferes with the membrane-binding function of the $Pb^{2+}$-complexed C2A domain.

To understand the underlying cause of this behaviour, we considered two factors that are essential for driving the C2A-membrane interactions:[54] (1) the general "electrostatic shift" due to metal-ion binding, which alters the charge of the intra-loop region from negative to positive; and (2) the specific interactions of anionic phospholipid headgroups with the C2-complexed metal ions (and potentially the basic residues of C2A surrounding the loop region).  Our data indicate that inhibition of $Pb^{2+}$ interactions with Site 2 by Bis-Tris locks the C2A domain in the single $Pb^{2+}$-bound state,

and that the resulting electrostatic shift is insufficient for the C2A to engage in high-affinity interactions with anionic membranes.
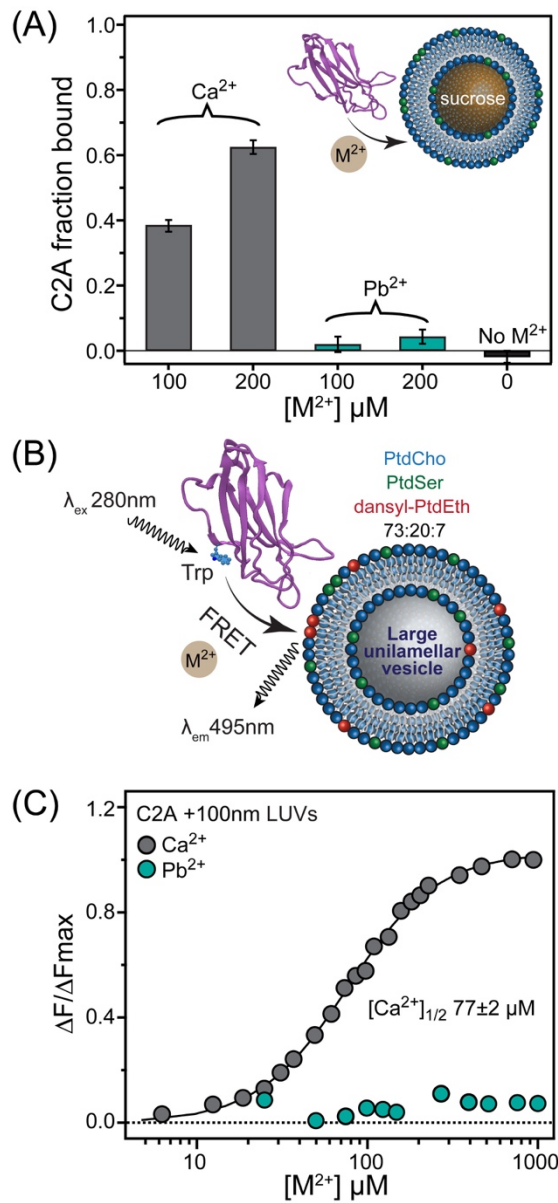
**Figure VI.3 Pb²⁺-dependent membrane binding of C2A is abolished in the presence of Bis-Tris**

(A) Fraction of C2A bound to sucrose-loaded LUVs in the presence of $Ca^{2+}$ and $Pb^{2+}$. The co-sedimentation experiments were conducted in 20 mM Bis-Tris at pH 7.0 and 150 mM KCl. The LUVs were 100 nm in diameter and consisted of PtdCho:PtdSer=80:20 (%, molar). The C2A concentration was 5 μM. (B) Schematic representation of FRET-detected C2-membrane binding experiments. The resonance energy transfer takes place between native Trp residues and dansyl-PE fluorophore embedded into LUVs. (C) FRET-detected C2A-membrane binding curves plotted as a function of increasing $M^{2+}$ (M=Ca, Pb) concentrations. The change in fluorescence

intensity at 495 nm, $\Delta F$, was normalized to the maximum change observed in $Ca^{2+}$-dependent experiments, $\Delta F_{max}$. Same buffer as for co-sedimentation experiments was used. The C2A concentration was 0.5 $\mu M$.

We next sought to investigate if specific interactions of the $Pb^{2+}$-complexed C2A domain with PtdSer are influenced by Bis-Tris. PtdSer is the most abundant anionic lipid component of the eukaryotic plasma membranes. It recruits metal ion-complexed C2 domains to membranes by engaging in electrostatic interactions with the protein and forming specific coordination bonds(s) with the protein-bound metal ion(s). In MES, the C2A·Pb1 complex prepared by mixing stoichiometric amounts of C2A and $Pb^{2+}$ associates weakly with PtdSer-containing bicelles.[224] The chemical exchange process between the C2A·Pb1-PtdSer ternary complex and the C2A·Pb1 binary complexes occurs on the "fast-to-intermediate" NMR chemical shift timescale. This produces a specific pattern of resonance intensity decrease in the NMR spectra that predominantly affects the loop regions of the C2A domain. Here, we used a short-chain PtdSer analogue, 1,2-dihexanoyl-sn-glycero-3-[phospho-L-serine] (DPS) to determine how Bis-Tris influences the interactions of the C2A·Pb1 complex with PtdSer. In MES, addition of 5 mM DPS to 100 $\mu M$ [U-$^{15}N$ enriched] C2A·Pb1 complex resulted in attenuation of the cross-peak intensities. The attenuation was quantified as the ratio of the N-$H_N$ cross-peak intensities in the absence ($I_0$) and presence ($I$) of DPS. Consistent with previous data obtained using PtdSer containing bicelles,[224] residues that belong to the loop regions showed significant decrease in $I/I_0$ values, along with several residues in the polylysine region between loops 1 and 2 (**Figure VI.4A**). In contrast, the C2A·Pb1 complex in

Bis-Tris showed little attenuation of signals that belong to the loop regions (**Figure VI.4B**).  This is especially evident in the difference $I/I_0$ plot (**Figure VI.4C**) that was constructed by subtracting the data in (**B**) from the data in (**A**).  We conclude that specific interactions of the C2A·Pb1 complex with PtdSer, while clearly present in the non-chelating MES buffer, are absent in the chelating Bis-Tris buffer.  How does Bis-Tris inhibit the interactions of the C2A·Pb1 complex with PtdSer?  There are examples of crystal structures of protein-metal ion complexes where Bis-Tris provides additional ligands to the protein-bound metal ions.[225-227]  It is therefore plausible that Bis-Tris directly coordinates Pb1 and thereby prevents $Pb^{2+}$ to form coordination bonds with the oxygens of PtdSer.  This scenario is schematically shown in **Figure VI.4D**.

In conclusion, Bis-Tris eliminates two factors that contribute to metal ion-driven C2A-membrane interactions: the effect of general electrostatics, by inhibiting $Pb^{2+}$ binding to Site 2; and the effect of C2A·Pb1-PtdSer interactions, likely by completing the coordination sphere of C2A-bound Pb1.  These findings provide the following insight into the metal-ion dependent membrane binding function of the C2 domains.  C2 domains with partially occupied metal-ion binding sites, through weak association with anionic membranes, are brought close to the polar membrane region.[212, 224]  It is believed that the resulting proximity to anionic lipid moieties elicits cooperative metal-ion binding to the remaining weaker sites by enhancing their affinities.  This mutual cooperativity enables the domain to perform its function at physiological concentrations of $Ca^{2+}$.[51]  Our results support this mechanistic model: by interfering with the PtdSer interactions of the C2A·Pb1 complex, Bis-Tris also precludes the cooperative

enhancement of Site 2 affinity towards $Pb^{2+}$.  As a result, the domain stays locked in Pb1-bound state, unable to achieve complete electrostatic shift required for membrane association.

When viewed from the perspective of $Pb^{2+}$ toxicity, our data indicate that in the cellular environment where Bis-Tris-like chelators and metabolites are abundant,[228] the membrane interactions of the C2A·Pb1 complex are unlikely to occur.  Combined with our previous finding that the presence of $Pb^{2+}$ in Site 1 of C2 domains desensitizes them to further $Ca^{2+}$ binding,[187, 221] the ability of $Pb^{2+}$-complexed C2A domain to interact with membranes is unlikely to be restored or rescued at physiological $Ca^{2+}$ concentrations.

The next step was to determine how $Pb^{2+}$-complexed C2B interacts with anionic membranes in Bis-Tris.  The C2B domain is significantly more basic than C2A due to the presence of a distinct polylysine motif (see **Figure VI.1B**), and additional positively charged residues, Arg 398 and Arg 399, at the end opposite to the loop regions. Although the polylysine region is located several Ångstroms away from the metal-ion binding loops, it plays a critical role in the membrane association process.[192, 229, 230]  In particular, its interaction with the second messenger $PtdIns(4,5)P_2$ dramatically increases the $Ca^{2+}$ affinity to C2B, lowering the $Ca^{2+}$ concentration threshold required for the membrane association of this domain.[231]  The underlying basis of this cooperative effect is the change of the electrostatic potential of C2B, caused by the interactions of its basic regions with anionic phospholipids.  The cooperativity between anionic phospholipids and divalent metal ions is mutual: binding of metal ions to the loop regions enhances the interactions of C2B with phospholipids.
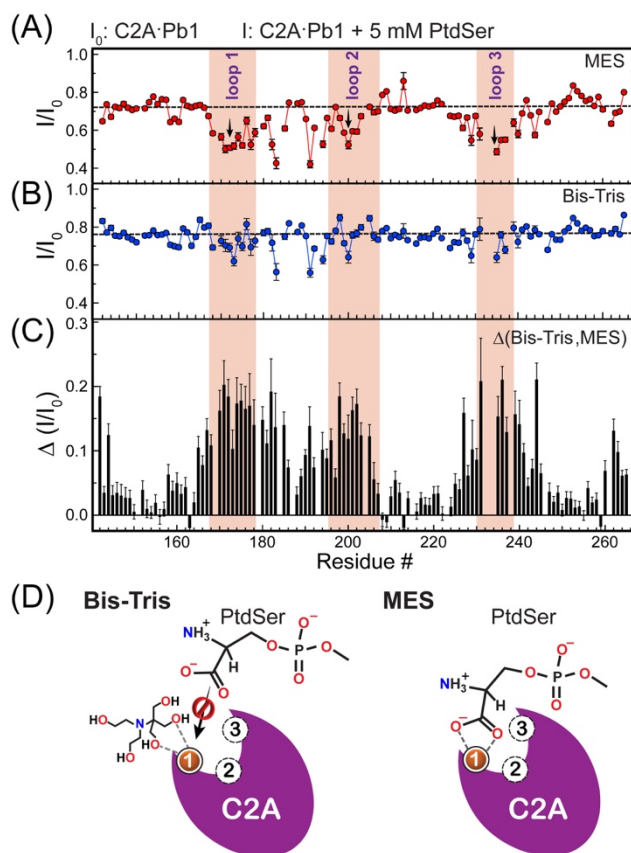
**Figure VI.4 Pb²⁺-complexed C2A domain does not appreciably interact with PtdSer in the presence of Bis-Tris**

Attenuation of peak intensities in the C2A·Pb1 complex upon addition of 5 mM DPS, expressed as residue-specific $I/I_0$ ratios, where $I$ and $I_0$ are the peak intensities in the presence and absence of PtdSer, respectively. The data were collected at pH 6.0 in 20 mM **(A)** MES and **(B)** Bis-Tris buffers. The errors in the intensity ratios were estimated using the r.m.s.d. of the base-plane noise in each of the collected spectrum. **(C)** The difference between $I/I_0$ ratios, demonstrating that the specific interaction of the C2A·Pb1 loops with PtdSer is present in the MES but not in the Bis-Tris buffers. **(D)** Schematic model showing how Bis-Tris can potentially interfere with C2A·Pb1-PtdSer interactions.

In stark contrast to C2A, Pb²⁺-complexed C2B associates with LUVs in Bis-Tris

(**Figure VI.5A,** compare with **Figure VI.3A**), with fractional population of the

membrane-bound protein species comparable to that observed in presence of Ca²⁺. The

FRET experiments were carried out by titrating the PtdSer-containing LUVs into a

solution containing C2B and excess $Pb^{2+}$, to minimize C2B-induced LUV clustering and associated increase in scattering.[52]  The FRET results mirrored those of the co-sedimentation experiments.  $Pb^{2+}$ was almost as effective as $Ca^{2+}$ in driving protein-membrane association, producing $[PtdSer]_{1/2}$ values of 3.4 μM compared to 2.8 μM, respectively (**Figure VI.5B**).  The two plausible explanations for this behaviour are: (1) the inherently basic nature of the C2B surface that enables membrane interactions in single $Pb^{2+}$-bound state; and (2) the allosteric enhancement of C2B affinity to $Pb^{2+}$ upon interactions of PtdSer with basic regions of the protein.

To assess the relative contribution of these factors, we added DPS to the $[U-^{15}N]$ C2B·Pb1 complex (prepared by mixing stoichiometric amount of C2B and $Pb^{2+}$) and compared the chemical shifts of the backbone amide groups between the NMR spectra of DPS-free and DPS-containing samples of C2B·Pb1.  We observed modest changes in the chemical shifts of the C2B·Pb1 resonances that are located predominantly near the polylysine motif and the adjacent "bottom" part of C2B (**Figure VI.5C**), suggesting that these regions are the primary PtdSer interaction sites.  The nature of the C2B·Pb1-DPS interactions is electrostatic and is therefore expected to produce large chemical shift changes if the protein is fully DPS-bound.  The small values of chemical shift perturbations suggest that the fractional population of the DPS-bound C2B·Pb1 species is small.  Therefore, the inherently basic nature of C2B alone cannot explain the affinity of $Pb^{2+}$-complexed C2B species to anionic membranes in Bis-Tris.

Next, we tested if the presence of PtdSer in solution enhances the affinity of C2B towards $Pb^{2+}$ to the extent that the domain acquires an ability to compete with Bis-Tris

243

and bind the second $Pb^{2+}$ ion. Upon addition of 5-fold molar excess of $Pb^{2+}$ to the C2B·Pb1 in the presence of 5 mM DPS, a new subset of cross-peaks appeared in the NMR spectrum (**Figure VI.5D**, red spectrum). This indicates the formation of new $Pb^{2+}$-bound species of the C2B domain that are in slow exchange on the NMR chemical shift timescale with the C2B·Pb1 complex. The only possible $Pb^{2+}$ interaction site with the C2B domain is Site 2. Indeed, residues whose cross-peaks are typically exchange-broadened in the C2B·Pb1 complex but only appear upon population of Site 2, G305 and D365, are detectable in the sample containing $Pb^{2+}$ excess. For several residues, more than two sets of resonances could be seen, reflecting the complex speciation of $Pb^{2+}$-bound C2B in the presence of DPS. In the absence of PtdSer, the population of Site 2 in C2B by $Pb^{2+}$ is negligible even at 60-fold molar $Pb^{2+}$ excess (**Figure VI.S2**). Therefore, we conclude that neutralization of the polylysine region via interactions with PtdSer and, to generalize, anionic phospholipids, is the dominant factor that enables the weaker Site 2 of C2B to successfully compete with Bis-Tris for $Pb^{2+}$. The resulting acquisition of a full complement of $Pb^{2+}$ ions by the C2B domain, and the mutual cooperativity between the polylysine motif and metal-ion binding loop regions drives the membrane association of C2B. This scenario is schematically illustrated in **Figure VI.5E**. In contrast to C2B, C2A showed barely any response to the addition of excess $Pb^{2+}$ in the presence of 5 mM DPS (**Figure VI.S3**).
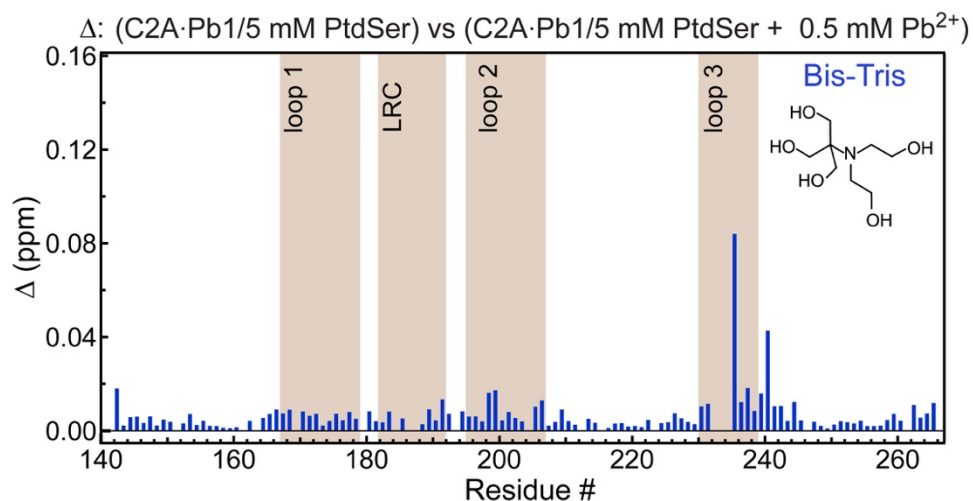
**Figure VI.S3 PtdSer does not appreciably enhance the affinity of $Pb^{2+}$ to Site 2 of the C2A domain**

The C2A·Pb1 complex was prepared by mixing stoichiometric amounts of [U-$^{15}$N] C2A and $Pb^{2+}$ in the presence of 5 mM DPS (1,2-dihexanoyl-sn-glycero-3-phospho-L-serine, 06:0 PS). The total protein concentration was 100 μM. Addition of 0.5 mM $Pb^{2+}$ caused very weak chemical shift perturbations in the [$^{15}$N, $^1$H] HSQC spectra of the C2B·Pb1 complex, as shown by the plot of chemical shift perturbation Δ versus primary structure. Small perturbations around loop 3 (compared to previously reported data for $Pb^{2+}$ to Site 2, Katti et al *Metallomics*, 2018, 10, 1211-1222) indicate that $Pb^{2+}$ interactions with Site 2 remain very weak.
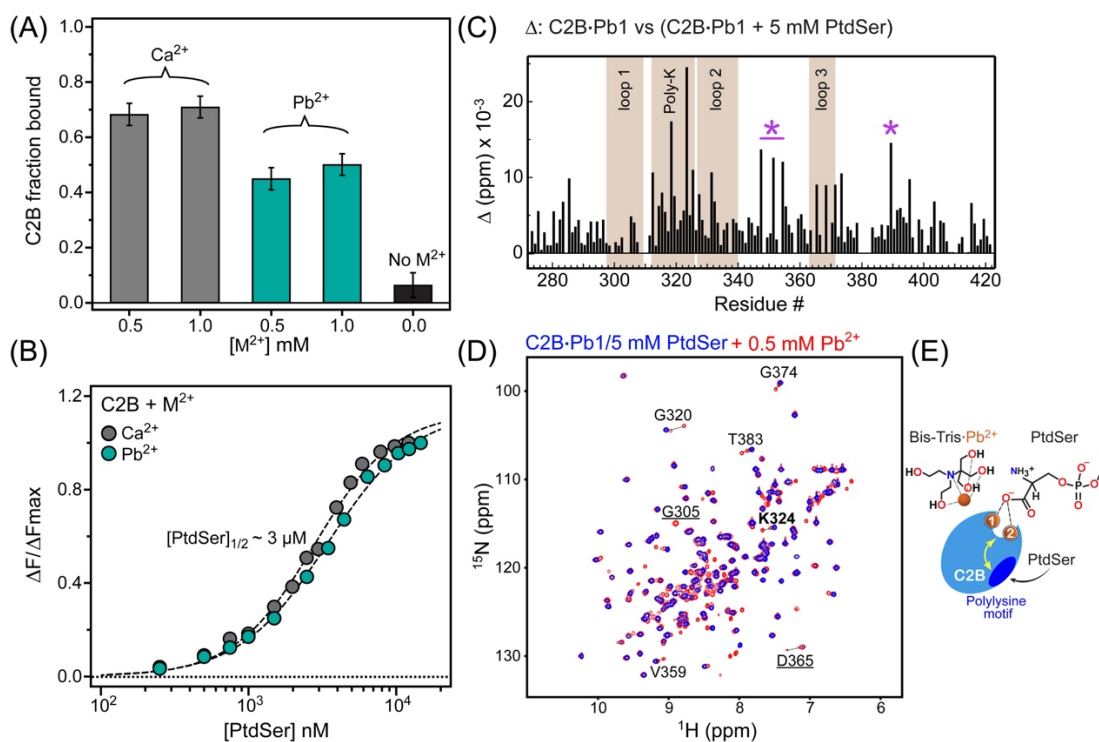
**Figure VI.5 Pb²⁺-dependent membrane binding of C2B persists in the presence of Bis-Tris**

(A) Vesicle co-sedimentation experiments conducted in 20 mM Bis-Tris and 150 mM KCl at pH 7.0 show that in contrast to C2A, Pb²⁺-complexed C2B associates with anionic membranes. The C2B concentration is 5 μM. (B) C2B-to-membrane binding curves plotted as normalized FRET efficiency versus accessible PtdSer concentration in LUVs. The concentrations of C2B and M²⁺ are 0.5 μM and 500 μM, respectively. Pb²⁺ is almost as effective as Ca²⁺ in driving membrane interactions. (C) Chemical shift perturbations Δ caused by addition of DPS (cmc ~ 12 mM) to the C2B·Pb1 complex are plotted as a function of primary structure. The polylysine motif and residues at the "bottom" of C2B, marked by asterisks, are the likely interaction sites based on the chemical shift data. (D) Overlay of the [¹⁵N-¹H] HSQC spectra showing an additional set of cross-peaks that appears upon addition of 0.5 mM Pb²⁺ to the C2B·Pb1 complex in the presence of 5 mM DPS. The newly formed Pb²⁺-bound C2B species are in slow exchange with the C2B·Pb1 species, as illustrated for residues G320, G374, T383, D365, and V359. The underlined residues G305 (loop 1) and D365 (loop 3) are broadened beyond detection in C2B·Pb1 but re-appear in the spectra upon Site 2 population by Pb²⁺. K324, shown in boldface, is a residue that belongs to the polylysine motif. (E) A model that schematically illustrates how interactions of anionic phospholipids with the polylysine motif of C2B could cause cooperative enhancement in Pb²⁺ affinities for the metal-ion binding sites of the C2B domain. This effect would enable C2B to effectively compete with Bis-Tris for Pb²⁺ and acquire a full complement of Pb²⁺ ions needed for membrane interactions.

In full-length Syt1, the C2A and C2B domains are connected by a flexible 9-residue linker and together form the full $Ca^{2+}$-sensing unit (**Figure VI.1B**).[232] To determine how $Pb^{2+}$-driven interactions of the C2AB fragment depend on the chelating properties of the environment, we conducted FRET-detected protein-to-membrane binding experiments in MES and Bis-Tris (**Figure VI.6A**). Due to the multivalent membrane binding mode of C2B[233] and the ability of the tandem C2 domains to interact with LUVs in "trans" mode with respect to each other,[234] the C2AB fragment shows significant clustering of LUVs. The clustering thresholds are marked in red (**Figure VI.6A**), and correspond to the accessible PtdSer concentration upon exceeding which visible precipitation of LUVs and concomitant decrease of FRET signal occur.

The most drastic difference between the binding curves of **Figure VI.6A** is the overall decrease of FRET efficiency in the Bis-Tris buffer: at 2.5 µM accessible PtdSer, the FRET efficiency is ~3-fold lower than that in MES. This suggests that C2AB-membrane interactions are significantly weakened in the presence of Bis-Tris. Based on the properties of individual domains in Bis-Tris (**Figure VI.3** and **5**), this behaviour is likely caused by the impairment of the C2A membrane-binding function. This conclusion is further supported by the observation that the clustering threshold in Bis-Tris requires more than twice the accessible PtdSer, 5.7 µM, than that in MES.

In addition to providing mechanistic information about the determinants of C2-membrane association, our data on the isolated domains and the C2AB fragment in Bis-Tris led us to propose a model of how $Pb^{2+}$ would interact with Syt1 under the chelating

247

conditions of the cellular milieu (**Figure VI.6B**). Due to the competition with the physiological chelators such as glutathione and metallothionein,[228, 235] only high-affinity $Pb^{2+}$ binding sites of Syt1 will be populated, i.e. Site 1 of each C2 domain. Upon population of Site 1 by $Pb^{2+}$, C2B domain will interact with anionic lipids of the presynaptic membranes, PtdIns(4,5)P$_2$ and PtdSer,[224] via the polylysine motif; due to the positive cooperativity, the affinity of C2B to divalent metal ions will be enhanced. As we demonstrated previously,[187, 221] $Ca^{2+}$ is unable to share ligands with Pb1 and occupy the remaining vacant metal ion sites. The reason is high electronegativity of $Pb^{2+}$[236] that results in protein-bound Pb1 depleting the electron density of the oxygen ligands[237] shared by Sites 1 and 2. It is therefore feasible that instead of $Ca^{2+}$, C2B·Pb1 will preferentially acquire $Pb^{2+}$ at Site 2, and that will drive the membrane association of Syt1 via the C2B domain. Our results suggest that contribution of C2A to membrane binding in the chelating environment will be significantly attenuated, because the C2A·Pb1 complex will neither engage with anionic membranes nor bind $Pb^{2+}$ at Site 2. Impaired membrane binding of the $Ca^{2+}$-sensing region of Syt1 could be a potential mechanism through which $Pb^{2+}$ interferes with the regulation of Syt1 function by $Ca^{2+}$ and disrupts the evoked release of neurotransmitters.[238-245] By the same token, $Pb^{2+}$-driven partial membrane association of Syt1 could explain how $Pb^{2+}$ induces sporadic release of certain neurotransmitters.[242]
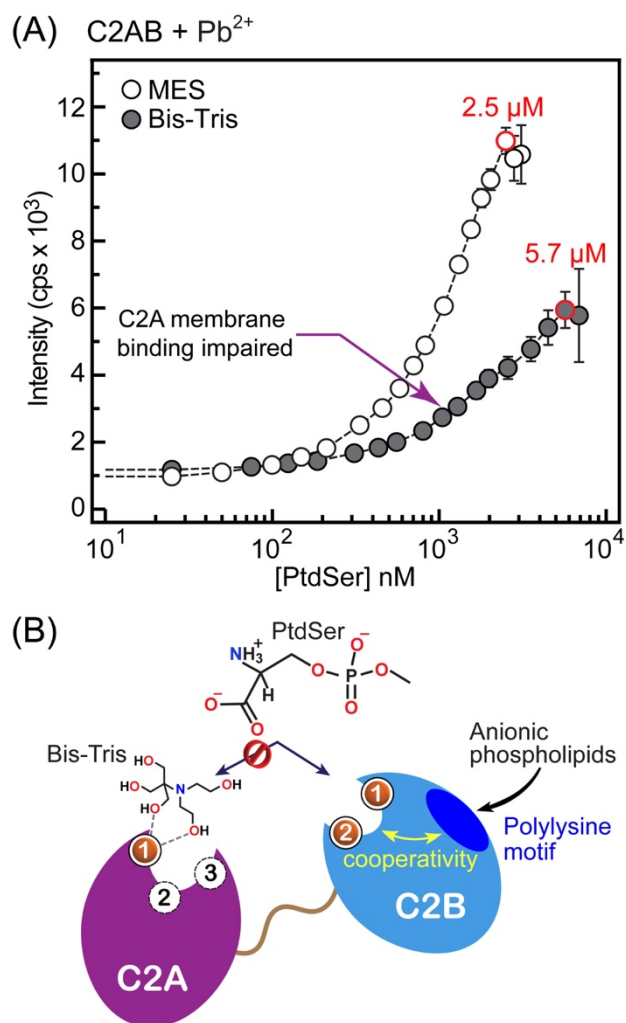
**Figure VI.6 Membrane association of C2AB reflects the differential effect of Bis-Tris on the individual C2 domains**

(A) C2AB-to-membrane binding curves plotted as a function of FRET efficiency versus concentration of accessible PtdSer in 100 nm LUVs. The concentration of C2AB and $Pb^{2+}$ are 0.5 μM and 500 μM, respectively. The composition of LUVs is PtdSer:PtdCho:dansyl-PE=73:20:7 (molar). The buffer conditions are 20 mM Bis-Tris (MES) at pH 7.0 (6.0) with 150 mM KCl. The clustering point, at which light scattering by LUVs precludes further FRET measurements, is marked in red. More than 50% intensity difference in the dansyl-PE fluorescence intensity at the clustering point is observed in Bis-Tris compared to MES. (B) Schematic representation of the C2AB-$Pb^{2+}$-anionic phospholipid interactions in the Bis-Tris environment. The association of anionic phospholipids with the polylysine cluster enables the population of Site 2 by $Pb^{2+}$ and the coordination of protein-bound $Pb^{2+}$ ions by PtdSer. Association of C2A with anionic membranes is extremely weak, because Bis-Tris interferes with $Pb^{2+}$ binding to Sites 2 and 3, and PtdSer coordination by Pb1.

## Conclusion

Identification of oxygen-rich sites that $Pb^{2+}$ could potentially target is essential for understanding how $Pb^{2+}$ interferes with the function of $Ca^{2+}$-dependent signalling proteins. Given low bioavailability of $Pb^{2+}$, distinguishing and isolating high- from low-affinity protein sites is essential. We demonstrated using two $Ca^{2+}$-sensing C2 domains of Syt1, that $Pb^{2+}$-chelating pH buffer Bis-Tris provides the means to achieve such isolation. $Pb^{2+}$ in Bis-Tris populates only one site per C2 domain. The implication for Syt1 is that two of its $Ca^{2+}$-binding sites (out of total five) are likely to be targeted by $Pb^{2+}$ in cellular milieu that contains natural chelators. The effect of Bis-Tris on the metal-ion dependent membrane interactions of C2 domains revealed their differential response to $Pb^{2+}$. Our results suggest that C2B rather than C2A mediates the $Pb^{2+}$-driven association of Syt1 with anionic membranes. Whether or not $Pb^{2+}$ can displace $Ca^{2+}$ from the membrane-bound C2 domains, isolated or in the context of full-length Syt1, remains to be investigated. Our data on the C2 domain from PKC$\alpha$[221] suggest that at least in the non-chelating environment this scenario is possible.

Since protein-metal ion interactions are at the core of many biological processes, extensive biochemical analysis of the corresponding binding equilibria is necessary. The use of non-chelating pH buffers is intuitively preferred, to avoid possible complications presented by metal ion chelation. This work provides a different perspective. If used in combination with non-chelating buffers, chelating pH agents, such as Bis-Tris, could potentially provide valuable mechanistic information that could otherwise be overlooked.

# References

[51] Fernandez-Chacon, R., Konigstorfer, A., Gerber, S. H., Garcia, J., Matos, M. F., Stevens, C. F., Brose, N., Rizo, J., Rosenmund, C., and Sudhof, T. C. (2001) Synaptotagmin I functions as a calcium regulator of release probability, *Nature 410*, 41-49.

[52] Katti, S., Nyenhuis, S. B., Her, B., Srivastava, A. K., Taylor, A. B., Hart, P. J., Cafiso, D. S., and Igumenova, T. I. (2017) Non-Native Metal Ion Reveals the Role of Electrostatics in Synaptotagmin 1-Membrane Interactions, *Biochemistry 56*, 3283-3295.

[54] Zhang, X., Rizo, J., and Sudhof, T. C. (1998) Mechanism of phospholipid binding by the C2A-domain of synaptotagmin I, *Biochemistry 37*, 12395-12403.

[144] Geppert, M., Goda, Y., Hammer, R. E., Li, C., Rosahl, T. W., Stevens, C. F., and Sudhof, T. C. (1994) Synaptotagmin I: a major Ca2+ sensor for transmitter release at a central synapse, *Cell 79*, 717-727.

[187] Katti, S., Her, B., Srivastava, A. K., Taylor, A. B., Lockless, S. W., and Igumenova, T. I. (2018) High affinity interactions of $Pb^{2+}$ with synaptotagmin I, *Metallomics 10*, 1211-1222.

[192] Perez-Lara, A., Thapa, A., Nyenhuis, S. B., Nyenhuis, D. A., Halder, P., Tietzel, M., Tittmann, K., Cafiso, D. S., and Jahn, R. (2016) PtdInsP2 and PtdSer cooperate to trap synaptotagmin-1 to the plasma membrane in the presence of calcium, *Elife 5*.

[212] Corbin, J. A., Evans, J. H., Landgraf, K. E., and Falke, J. J. (2007) Mechanism of specific membrane targeting by C2 domains: localized pools of target lipids enhance Ca2+ affinity, *Biochemistry 46*, 4322-4336.

[213] Caito, S., Lopes Ana Carolina, B. A., Paoliello Monica, M. B., and Aschner, M. (2017) 16. Toxicology of Lead and Its Damage to Mammalian Organs, In *Lead – Its Effects on Environment and Health*.

251

[214] Lidsky, T. I., and Schneider, J. S. (2003) Lead neurotoxicity in children: basic mechanisms and clinical correlates, *Brain 126*, 5-19.

[215] Bellinger, D. C. (2008) Very low lead exposures and children's neurodevelopment, *Current opinion in pediatrics 20*, 172-177.

[216] Gorkhali, R., Huang, K., Kirberger, M., and Yang, J. J. (2016) Defining potential roles of $Pb^{2+}$ in neurotoxicity from a calciomics approach, *Metallomics 8*, 563-578.

[217] Kirberger, M., Wong, H. C., Jiang, J., and Yang, J. J. (2013) Metal toxicity and opportunistic binding of $Pb^{2+}$ in proteins, *J. Inorg. Biochem. 125*, 40-49.

[218] Bouton, C. M., Frelin, L. P., Forde, C. E., Arnold Godwin, H., and Pevsner, J. (2001) Synaptotagmin I is a molecular target for lead, *J. Neurochem. 76*, 1724-1735.

[219] Scheller, K. H., Abel, T. H., Polanyi, P. E., Wenk, P. K., Fischer, B. E., and Sigel, H. (1980) Metal ion/buffer interactions. Stability of binary and ternary complexes containing 2-[bis(2-hydroxyethyl)amino]-2(hydroxymethyl)-1,3-propanediol (Bistris) and adenosine 5'-triphosphate (ATP), *Eur. J. Biochem. 107*, 455-466.

[220] Ferreira, C. M. H., Pinto, I. S. S., Soares, E. V., and Soares, H. M. V. M. (2015) (Un)suitability of the use of pH buffers in biological, biochemical and environmental studies and their interaction with metal ions – a review, *RSC Advances 5*, 30989-31003.

[221] Morales, K. A., Lasagna, M., Gribenko, A. V., Yoon, Y., Reinhart, G. D., Lee, J. C., Cho, W., Li, P., and Igumenova, T. I. (2011) $Pb^{2+}$ as modulator of protein-membrane interactions, *J. Am. Chem. Soc. 133*, 10599-10611.

[222] Long, D., and Yang, D. (2009) Buffer interference with protein dynamics: a case study on human liver fatty acid binding protein, *Biophys. J. 96*, 1482-1488.

[223] Seven, A. B., Brewer, K. D., Shi, L., Jiang, Q. X., and Rizo, J. (2013) Prevalent mechanism of membrane bridging by synaptotagmin-1, *Proc. Natl. Acad. Sci. U. S. A. 110*, E3243-3252.

[224] Katti, S., Nyenhuis, S. B., Her, B., Cafiso, D. S., and Igumenova, T. I. (2019) Partial metal ion saturation of C2 domains primes Syt1-membrane interactions, *bioRxiv*, 810010.

[225] Hothorn, M., D'Angelo, I., Marquez, J. A., Greiner, S., and Scheffzek, K. (2004) The invertase inhibitor Nt-CIF from tobacco: a highly thermostable four-helix bundle with an unusual N-terminal extension, *J. Mol. Biol. 335*, 987-995.

[226] Park, S. Y., Lee, W. R., Lee, S. C., Kwon, M. H., Kim, Y. S., and Kim, J. S. (2008) Crystal structure of single-domain VL of an anti-DNA binding antibody 3D8 scFv and its active site revealed by complex structures of a small molecule and metals, *Proteins 71*, 2091-2096.

[227] Do, H. T., Li, H., Chreifi, G., Poulos, T. L., and Silverman, R. B. (2019) Optimization of Blood-Brain Barrier Permeability with Potent and Selective Human Neuronal Nitric Oxide Synthase Inhibitors Having a 2-Aminopyridine Scaffold, *J. Med. Chem. 62*, 2690-2707.

[228] Duncan, K. (2009) Metallothioneins and Related Chelators. Metal Ions in Life Sciences Vol. 5., *48*, 7966-7967.

[229] Bai, J., Tucker, W. C., and Chapman, E. R. (2004) $PIP_2$ increases the speed of response of synaptotagmin and steers its membrane-penetration activity toward the plasma membrane, *Nat. Struct. Mol. Biol. 11*, 36-44.

[230] Xue, M., Ma, C., Craig, T. K., Rosenmund, C., and Rizo, J. (2008) The Janus-faced nature of the $C_2B$ domain is fundamental for synaptotagmin-1 function, *Nat. Struct. Mol. Biol. 15*, 1160-1168.

[231] van den Bogaart, G., Meyenberg, K., Diederichsen, U., and Jahn, R. (2012) Phosphatidylinositol 4,5-bisphosphate increases $Ca^{2+}$ affinity of synaptotagmin-1 by 40-fold, *J. Biol. Chem. 287*, 16447-16453.

[232] Perin, M. S., Brose, N., Jahn, R., and Sudhof, T. C. (1991) Domain structure of synaptotagmin (p65), *J. Biol. Chem. 266*, 623-629.

[233] Arac, D., Chen, X., Khant, H. A., Ubach, J., Ludtke, S. J., Kikkawa, M., Johnson, A. E., Chiu, W., Sudhof, T. C., and Rizo, J. (2006) Close membrane-membrane proximity induced by $Ca^{2+}$-dependent multivalent binding of synaptotagmin-1 to phospholipids, *Nat. Struct. Mol. Biol. 13*, 209-217.

[234] Herrick, D. Z., Kuo, W., Huang, H., Schwieters, C. D., Ellena, J. F., and Cafiso, D. S. (2009) Solution and membrane-bound conformations of the tandem C2A and C2B domains of synaptotagmin 1: Evidence for bilayer bridging, *J. Mol. Biol. 390*, 913-923.

[235] Ahamed, M., and Siddiqui, M. K. (2007) Low level lead exposure and oxidative stress: current opinions, *Clin. Chim. Acta 383*, 57-64.

[236] Gordy, W., and Thomas, W. J. O. (1956) Electronegativities of the Elements, *24*, 439-444.

[237] Dudev, T., Grauffel, C., and Lim, C. (2018) How $Pb^{2+}$ Binds and Modulates Properties of $Ca^{2+}$-Signaling Proteins, *Inorg. Chem. 57*, 14798-14809.

[238] Manalis, R. S., and Cooper, G. P. (1973) Letter: Presynaptic and postsynaptic effects of lead at the frog neuromuscular junction, *Nature 243*, 354-356.

[239] Carroll, P. T., Silbergeld, E. K., and Goldberg, A. M. (1977) Alteration of central cholinergic function by chronic lead acetate exposure, *Biochem. Pharmacol. 26*, 397-402.

[240] Minnema, D. J., Greenland, R. D., and Michaelson, I. A. (1986) Effect of in vitro inorganic lead on dopamine release from superfused rat striatal synaptosomes, *Toxicol. Appl. Pharmacol. 84*, 400-411.

[241] Minnema, D. J., Michaelson, I. A., and Cooper, G. P. (1988) Calcium efflux and neurotransmitter release from rat hippocampal synaptosomes exposed to lead, *Toxicol. Appl. Pharmacol. 92*, 351-357.

[242] Struzynska, L., and Rafalowska, U. (1994) The effect of lead on dopamine, GABA and histidine spontaneous and KCl-dependent releases from rat brain synaptosomes, *Acta Neurobiol. Exp. 54*, 201-207.

[243] Lasley, S. M., and Gilbert, M. E. (1996) Presynaptic glutamatergic function in dentate gyrus in vivo is diminished by chronic exposure to inorganic lead, *Brain Res. 736*, 125-134.

[244] Antonio, M. T., and Leret, M. L. (2000) Study of the neurochemical alterations produced in discrete brain areas by perinatal low-level lead exposure, *Life Sci. 67*, 635-642.

[245] Lasley, S. M., and Gilbert, M. E. (2002) Rat hippocampal glutamate and GABA release exhibit biphasic effects as a function of chronic lead exposure level, *Toxicol. Sci. 66*, 139-147.

CHAPTER VII SUMMARY AND FUTURE DIRECTIONS

## Summary

The primary goal of this work was to understand how conditional phospholipid-binding modules work. These domains have wide occurrence on the signaling complexes and show specific lipid/agonist preferences.[1] They ultimately control the membrane translocation of the signaling proteins in a regulated manner. Dysregulation of this process is at the very least disruptive to the signal transduction, at worst could lead to various disease states. Two such phospholipid-binding domains: C1 and C2 are studied in this work.

In chapter I, the general structural features, broad lipid/ligand preferences and the current understanding about the mechanisms of membrane translocation of these domains were briefly discussed. Using the stage set at this chapter, chapters II and III were focused on the experimental work done on C1A and C1B domains of protein kinase Cδ isoform respectively. In chapter II, the crystal structure of C1A domain with distinct diacylglycerol toggle-residue orientation was reported. We proposed and tested the resulting weak diacylglycerol dependence of this domain. On the other hand, the persistent phorbol ester sensitivity of C1A was evident of the highly disruptive nature of these tumor-promoting agents. In addition, a novel role of C1A domain as a putative PtdIns(4,5)P$_2$ sensor was uncovered.

In chapter III, we addressed a critical problem associated with obtaining atomic-resolution models of membrane associated C1-agonist complexes. NMR based experimental approach was proposed and successfully implemented to C1B domain of

protein kinase Cδ. The resulting experimental data provided unprecedented insight into the interactions of C1B with membranes mediated by diacylglycerol, phorbol esters, Prostratin, and Bryostatin-1. The results will guide the molecular dynamics simulations planned on these complex systems.

In chapters IV, V, and VI, the focus is switched to the $Ca^{2+}$-dependent C2 domains of Synaptotagmin 1 (Syt1). In chapter IV, using divalent cation $Cd^{2+}$ as a mimic of $Ca^{2+}$, we show that not only the electrostatic shift but also the direct metal ion-lipid interactions are essential to support Syt1 C2-membrane association. In chapter V, using yet another high-affinity divalent cation $Pb^{2+}$, we determine specific changes induced in the C2 domains upon saturation of metal-ion binding site 1. We present further extension of this study in chapter VI, demonstrating the mechanisms of cooperativity that govern the metal-ion occupancy and membrane association of the Syt1 C2 domains. The work done on C2 domains directly exhibits the valuable application of xenobiotic divalent cations in gaining mechanistic understanding of these modules.

## Future directions

### Understanding the role of individual C1 domains in PKCδ activation

After gaining insight into how individual C1 domains of PKCδ function, we want to study these domains in the context of their contribution to the overall membrane translocation of this isozyme. For PKCδ, the C2 domain is insensitive to $Ca^{2+}$. As a result, the detection of second messengers required for membrane translocation and subsequent kinase activation has to be mediated by C1 domains exclusively (**Figure VII.1**).
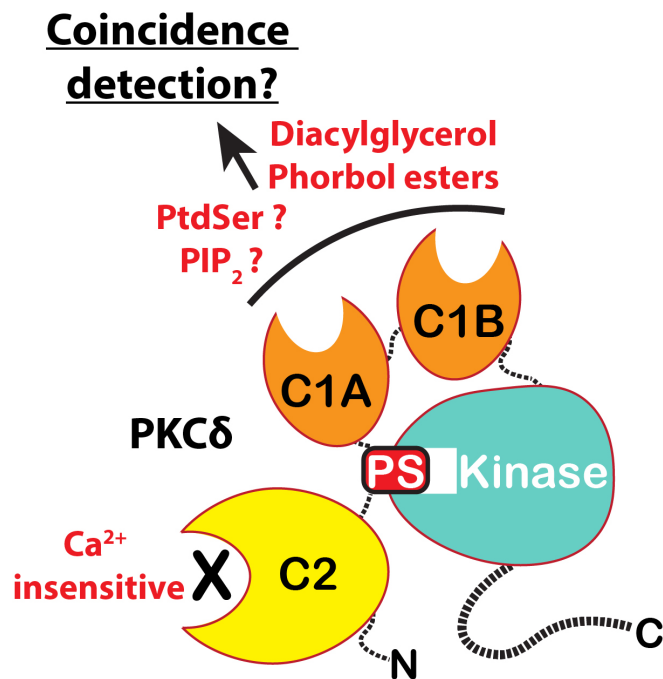
**Figure VII.1 The burden of detecting coincident lipid signals and membrane translocation of PKCδ falls upon C1 domains**
The schematic domain architecture of PKCδ is depicted to point out the importance of C1 domains as exclusive mediators of membrane translocation.


Based on the results we have obtained so far, we predict that C1A domain

conjoined with the pseudosubstrate region is likely responsible for mediating the

localization of the isozyme to the PtdIns(4,5)$P_2$-rich regions of the plasms membrane

**(Figure VII.2)**. We will test this by conducting membrane localization experiments in

live cells to determine the minimal modular unit necessary for PtdIns(4,5)$P_2$ sensitivity

of PKCδ.  This will be done using pseudosubstrate-C1A, isolated C1A and C1B, tandem

C1A-C1B, and the full pseudosubstrate-C1A-C1B constructs. We will also conduct

kinase activation assays where we will address whether the presence of PtdIns(4,5)$P_2$ can

contribute to the activation of PKCδ as a sole modulator as well as in combination with other second messengers and agonists. We will further test if the PtdIns(4,5)P$_2$-mediated activation of the enzyme can be attributed to C1A domain specifically by conducting the experiments with PKCδ mutants where the pseudosubtrate-C1A region predicted to interact will be altered.

To take it further, we will address the relative potency of two critical anionic lipids PtdSer and PtdIns(4,5)P$_2$ to modulate the membrane interactions of C1A and C1B domains in a comparative manner. This will be achieved by conducting the membrane-FRET (Förster resonance energy transfer) experiments where LUVs (Large unilamellar vesicles) of different molar ratios of these anionic lipids will be used to construct membrane binding profiles of C1A and C1B at fixed agonist concentrations (diacylglycerol and PDBu to begin with). The intrinsic fluorescence of the respective toggle-Trp residues will be used as a FRET-donor while membrane embedded dansyl-PE fluorophore will be used as an acceptor, providing a readout for membrane partitioning of these domains. The resulting profiles will be compared to gain quantitative insight into differential anionic lipid preferences of these C1 domains.

If C1A is in fact the PtdIns(4,5)P$_2$ binding module and can translocate in response leading to kinase activation as we hypothesize, we will test a subsequent aspect associated with such interaction. It is likely that this interaction can localize C1B in the vicinity of the region where diacylglycerol will be produced, as hydrolysis of PtdIns(4,5)P$_2$ by phospholipase C generates diacylglycerol **(Figure VII.2)**. Adding that to the intrinsic high affinity of C1B towards diacylglycerol, it is possible that C1B-

diacylglycerol interactions will then stabilize the membrane anchored activated kinase. One possible way such coupling can be achieved is if either of these domains or regions of PKCδ can interact with phospholipase C itself. We want to test the possibility of this interaction in future.
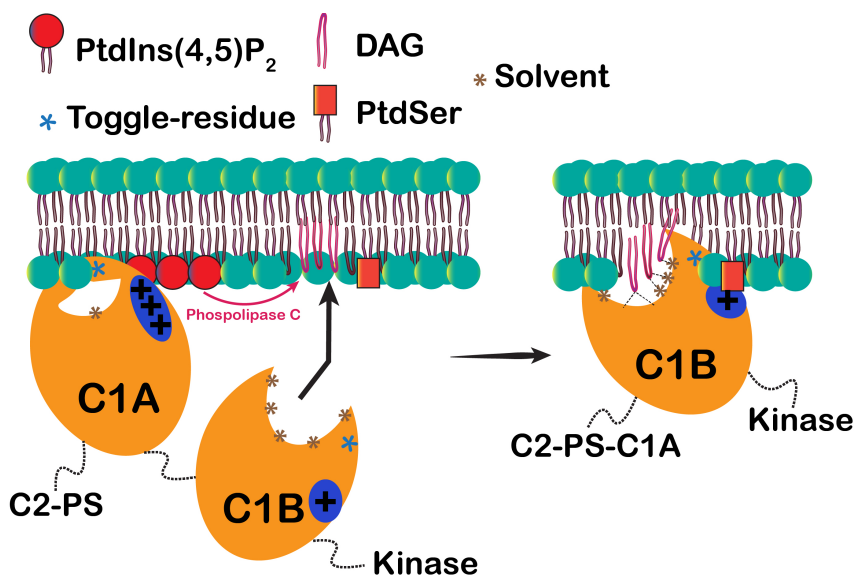


**Figure VII.2 Schematic model depicting one of the many possible mechanisms by which C1 domains differentially contribute to the detection of lipidic second messengers**

Finally, at the very fundamental and mechanistic level, we want to understand the specific factors that control the sensitivity of these domains to agonists like diacylglycerol, and anionic lipids. In the context of C1A and C1B domains of PKCδ, based on our work so far, we have identified certain key residues that likely play crucial roles (**Figure VII.3A)**. To verify, we will construct mutants of C1 domains, stating with C1A. The proposed mutations are aimed to convert C1A from a weak diacylglycerol sensing module to a potent one and modulate its anionic lipid preferences **(Figure**

**VII.3B and C)**. The behavior of these mutants will be analyzed experimentally as well as using *in silico* methods. If the desired effects are achieved upon mutations, it will validate the importance of these residues and allow us to reliably predict the behavior of other C1 domains sharing these structural features.

These proposed experiments should provide a comprehensive view of C1 domains and how they cooperate and complement each other to achieve the membrane translocation of PKCδ. In broader sense, the information obtained will clarify the mechanist differences between the activation of the $Ca^{2+}$-sensitive (conventional) and $Ca^{2+}$-independent (novel) PKC isoforms.
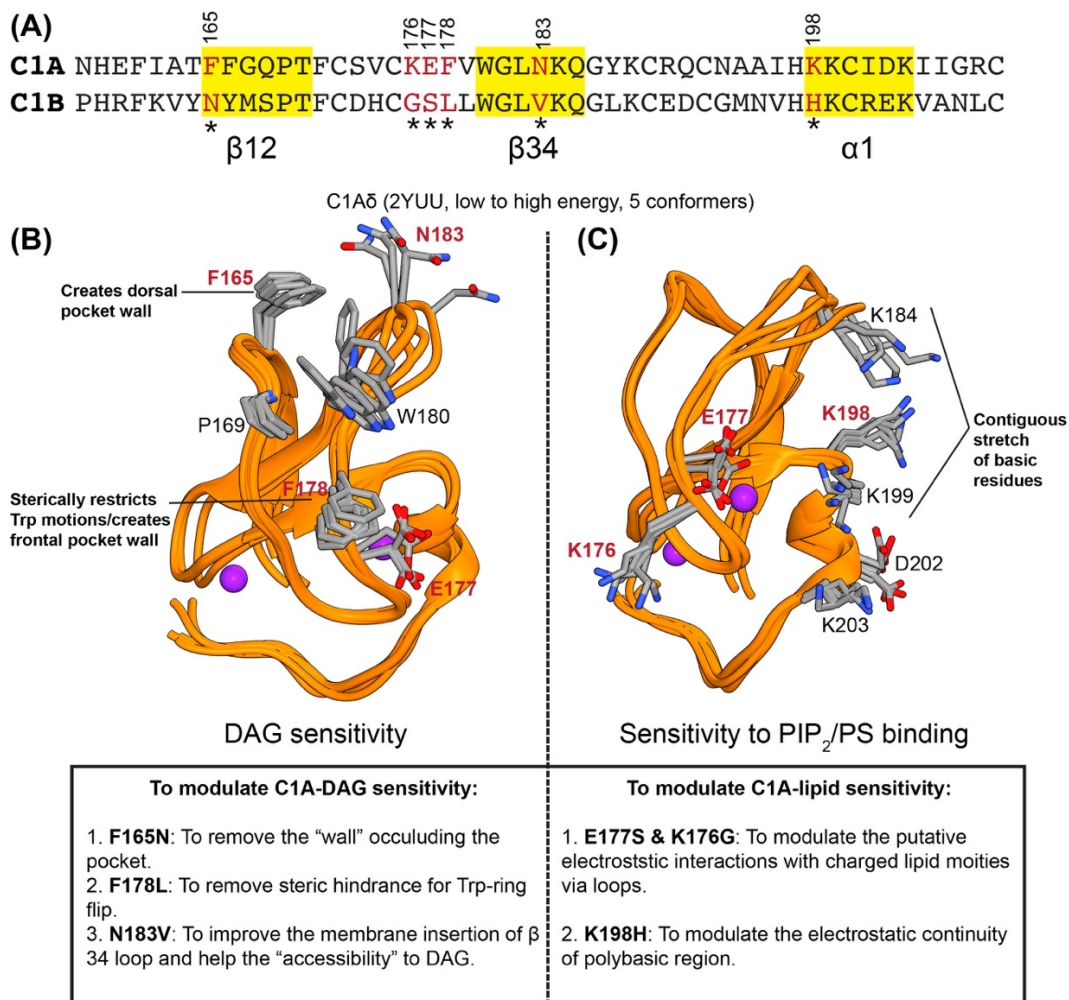
**Figure VII.3 Proposed mutations to modulate the diacylglycerol and anionic lipid preferences of C1A domain**

(A) Sequence comparison of C1A and C1B domains of PKCδ. Residues posited to play critical roles in DAG sensitivity and anionic lipid preferences of the domains are marked with asterisks. (B) Schematic representation of the proposed mutations and the reasoning behind the postulated effects is depicted.

262

<u>$^{19}$F NMR as a tool to study the phospholipid-binding C1 and C2 domains</u>

In addition to the experiments proposed above, we want to test a solution-state NMR approach that can be widely applicable to the phospholipid-binding domains, yet simple enough to implement as a preliminary exploration technique. $^{19}$F (Fluorine) NMR has been applied to address several biological problems involving those with the large-molecular weight systems.[246] This can be achieved due to the multitude of benefits associated with $^{19}$F NMR (**Figure VII.4**).[247]

The C1 and C2 domains are well suited for this technique. The membrane-binding regions of these domains typically possess aromatic residues that can partition efficiently into the membrane environments. C1 domains for instance have a toggle residue which, depending upon whether it is Tyrosine or Tryptophan, controls the diacylglycerol sensitivity.[22] In the $^{19}$F labelling scheme, these residues can be fluorinated and used directly as highly sensitive probes of membrane partitioning as well as agonist interactions.[248] This can be done via experimental scheme depicted in **Figure VII.5**. Specifically fluorinating the aromatic residues allows their exclusive detection (with the spectrometer capable of $^{19}$F detection) without any background signals. This is particularly useful when these domains bind to membranes, as the resulting large molecular weight complexes are challenging to probe using conventional labelling schemes ($^{13}$C/$^{15}$N) and acquisitions.
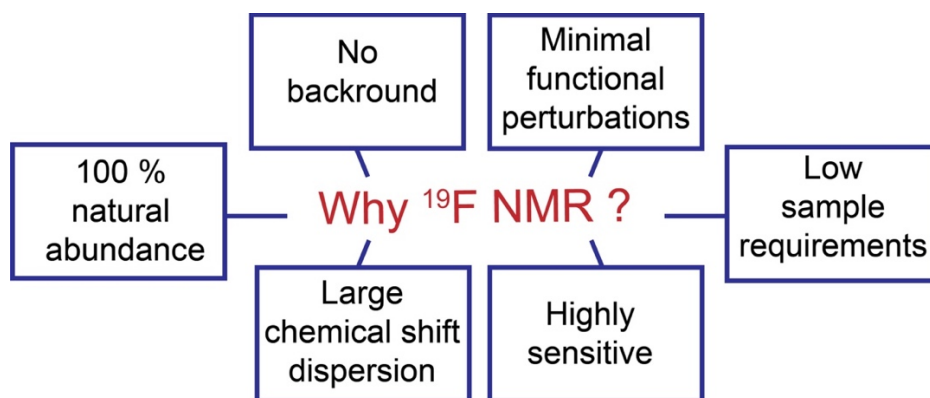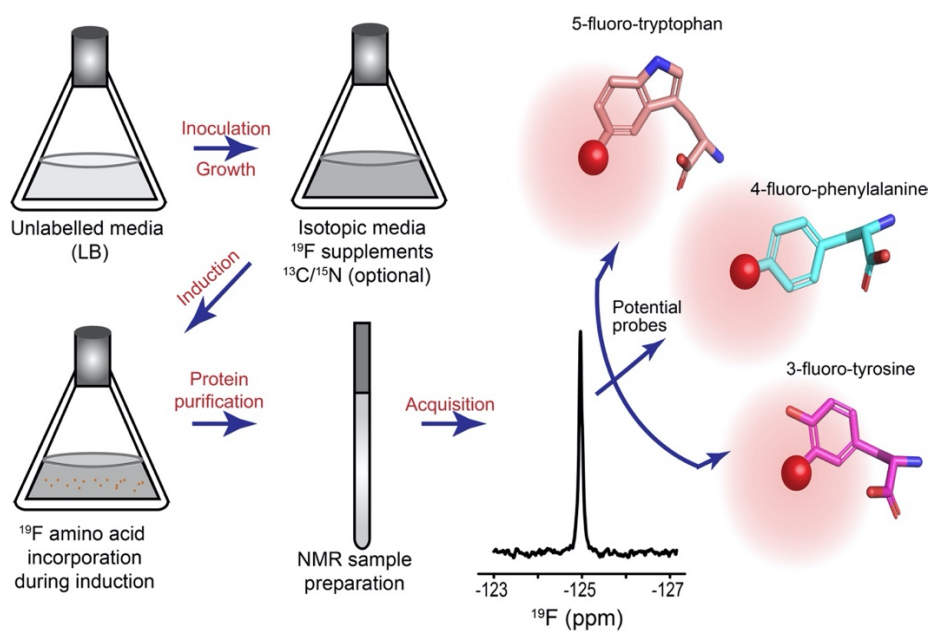
**Figure VII.4 Advantages of ¹⁹F NMR**



**Figure VII.5 Experimental schematic of ¹⁹F labelling scheme with aromatic residues that can be fluorinated**

As a preliminary proof of applicability, we tested this approach using the C1A domain of PKCδ. We incorporated the 5-fluoro-Trp in the growth media to make U-$^{15}$N labelled C1A domain that has fluorinated W180. This dual labelling scheme allows us to track the changes induced by membrane/agonist interactions using the $^{15}$N-$^{1}$H HSQCs as well as $^{19}$F 1-dimentional (1-D) spectra.

Based on our previous C1A experiments, we have established that the W180 side chain is localized at the intra-loop space. First, we wanted to determine where the fluorinated W180 side chain is likely localized by comparing the $^{15}$N-$^{1}$H HSQC spectrum with the non-fluorinated counterpart (**Figure VII.6A**). The chemical shift perturbations induced by $^{19}$F probe are typically confined to the site of incorporation and thus can be used as ambiguous readouts of W180 side chain location. The perturbations observed can be mapped to the loop residues (**Figure VII.6B and C**), consistent with the prediction that the W180 side chain is confined to this region.

Next, using isotropically tumbling bicelles as membrane mimics, we aimed to test whether we can detect with $^{19}$F NMR the membrane association of C1A (**Figure VII.7**). Specifically, we wanted to see if we can reliably distinguish between agonist-free and agonist-dependent membrane interactions. The $^{19}$F spectrum of the free C1A showed a single well resolved peak. Upon addition of PCPS bicelles, we observed a distinct chemical shift change for this peak. Partitioning into the membrane can occur via the loop where W180 is located (β34), as the side chain can sample multiple lipid-interacting states. The observance of a single $^{19}$F peak indicates that these states are in "fast" exchange with one another on chemical shift timescale.
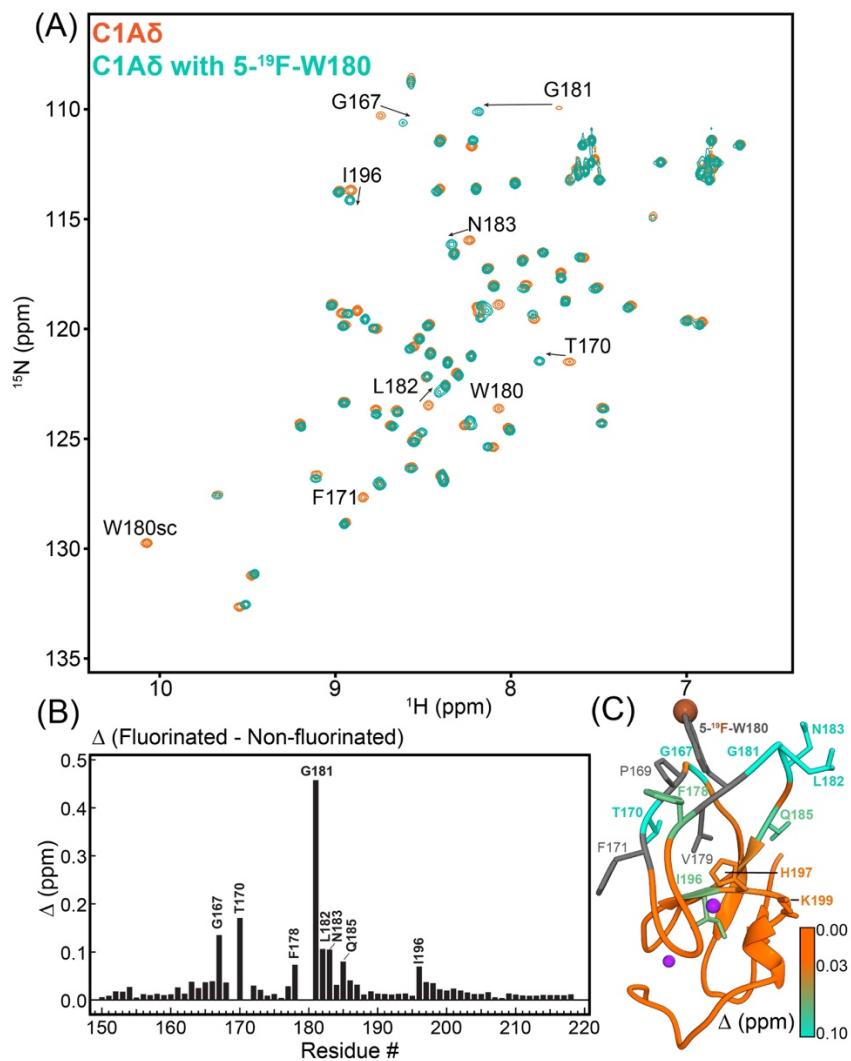
**Figure VII.6 Preparation of $^{19}$F-W180 C1A domain of PKCδ**

(A) The overlay of $^{15}$N-$^1$H HSQC spectra of U-$^{15}$N labelled C1A domain with and without fluorinated W180 residue. Select residues that show chemical shit perturbations due to the fluorination are labelled. (B) The fluorine-induced chemical shift perturbations are plotted as a function of primary sequence of C1A and mapped on the structure (2YUU, NMR lowest energy conformer) in (C). The perturbations are confined specifically to the loop region residue, suggesting the likelihood of fluorinated W180 side chain location.

Upon addition of agonist PDBu (1.2 fold to protein), we observe two distinct $^{19}$F resonances in the spectrum (**Figure VII.7**). The minor resonance peak has identical chemical shift as the agonist-free, bicelle-bound protein while the major peak is identical in chemical shift to the free-protein W180 resonance. This observation suggests that binding of PDBu changes the chemical exchange regime from "fast" to "slow" and the state of W180 identical to free protein is conformationally selected for by PDBu. Addition of more PDBu (2.5 fold to protein) completely shifts this equilibrium, further supporting the PDBu induced conformational selection. One possible mechanistic explanation for this observation would be the potential stacking interaction between PDBu and W180 side chain, that confines the side chain motions. Addition of PDBu to free protein without the bicelles leads to no detectable change in the chemical shift of the $^{19}$F signal, further suggesting that PDBu does not alter and in fact prefers the endogenous W180 orientation of C1A (between intra-loop space). Further experiments will be conducted to verify the validity of this suggested model and possible alternative interpretations.

These observations are highly informative and clearly demonstrate the applicability $^{19}$F NMR. In the context of C1A as well as other C1 domains, we will apply this approach in the future to test membrane interactions in presence of different agonists. In particular, we want to conduct the similar set of experiments for C1B domain where the W252 (analogous to W180) has distinctly different initial orientation from that of C1A. The highly sensitive nature of $^{19}$F NMR will also allow us to study the domains in tandem, where both domains are on the same polypeptide chain (C1A-C1B).
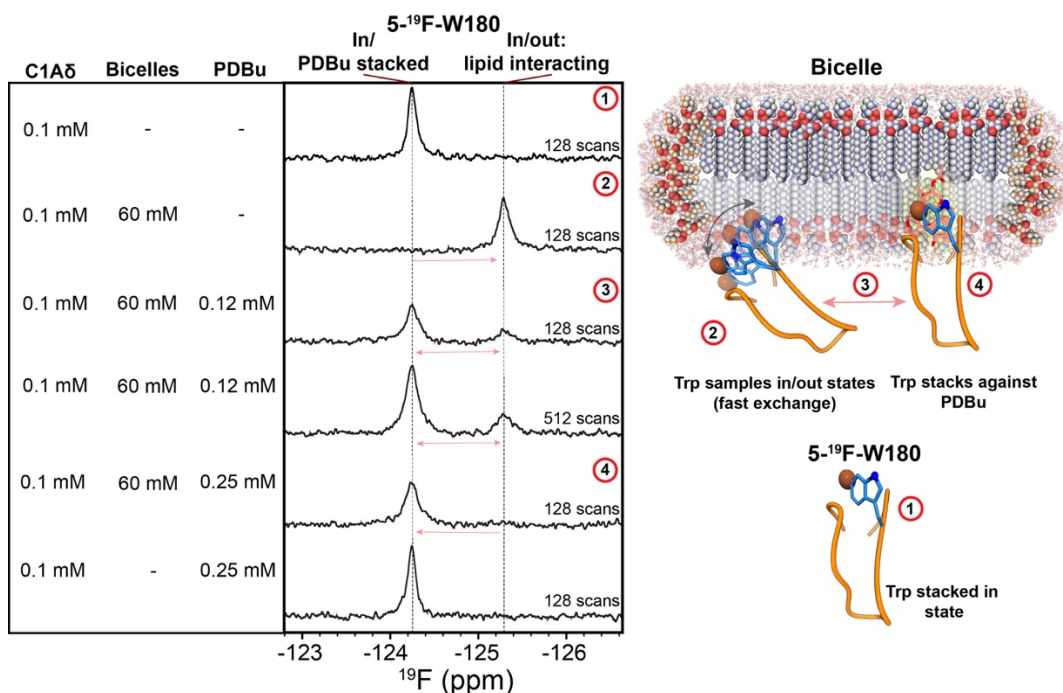
**Figure VII.7 Application of $^{19}$F NMR to study membrane partitioning and agonist interactions of C1A domain**
The $^{19}$F spectra of $^{19}$F-W180 C1A domain collected at different bicelle and agonist (PDBu) conditions are compared. The schematic model correlates the numbered spectra with the putative interaction modes of C1A.

C2 domains also possess aromatic residues at strategic locations that make them ideal probes of $^{19}$F NMR to study metal-ion and specific lipid interactions (**Figure VII.8)**. We will fluorinate these sites to test the applicability of $^{19}$F NMR to the C2 domains in future. The simplicity of this technique is lucrative and should be exploited to further our understanding of these phospholipid-binding domains.
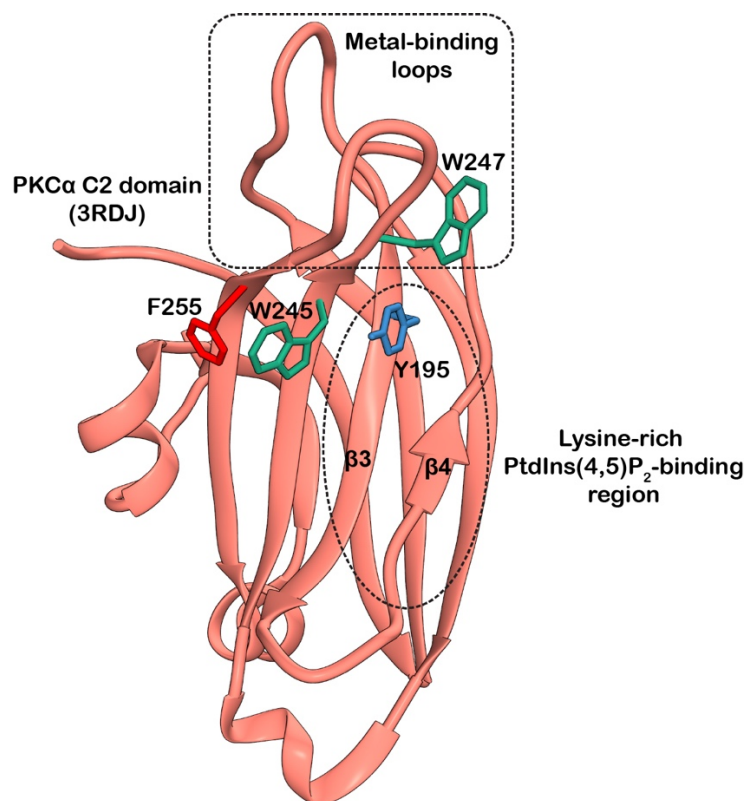
**Figure VII.8 Presence of aromatic residues at strategic positions on C2 domains make them amenable to $^{19}$F NMR**

PKCα C2 domain is depicted with specific regions that are involved in metal-ion and anionic lipid interactions. Proximal to these regions are aromatic residues that can be fluorinated to gain insight into the C2-metal ion binding, membrane partitioning, and specific anionic lipid interactions.

# References

[1] Lemmon, M. A. (2008) Membrane recognition by phospholipid-binding domains, *Nat Rev Mol Cell Biol 9*, 99-111.

[22] Dries, D. R., Gallegos, L. L., and Newton, A. C. (2007) A single residue in the C1 domain sensitizes novel protein kinase C isoforms to cellular diacylglycerol production, *J Biol Chem 282*, 826-830.

[246] Rose-Sperling, D., Tran, M. A., Lauth, L. M., Goretzki, B., and Hellmich, U. A. (2019) 19F NMR as a versatile tool to study membrane protein structure and dynamics, *400*, 1277.

[247] Chen, H., Viel, S., Ziarelli, F., and Peng, L. (2013) 19F NMR: a valuable tool for studying biological events, *Chemical Society Reviews 42*, 7971-7982.

[248] Gee, C. T., Arntson, K. E., Urick, A. K., Mishra, N. K., Hawk, L. M. L., Wisniewski, A. J., and Pomerantz, W. C. K. (2016) Protein-observed 19F-NMR for fragment screening, affinity quantification and druggability assessment, *Nature Protocols 11*, 1414-1427.